A STUDY OF FRACTURE

IN

BRITTLE LAMINAR COMPOSITES

THAT

CONTAIN WEAK INTERLAYERS

By

COLIN SCOTT, B.Sc.(Eng)

A Thesis

Submitted to the School of Graduate Studies

in Partial Fulfillment of the Requirements

for the Degree

Ph.D.

McMaster University

FRACTURE IN BRITTLE LAMINAR COMPOSITES

Ph.D. (2001)

(Materials Engineering)

TITLE: A Study of Fracture in Brittle Laminar Composites that Contain Weak Interlayers.

AUTHOR: Colin Scott, B.Sc.(Eng) (Queen's University)

SUPERVISOR: Professor P.S.Nicholson

NUMBER OF PAGES: xxv, 273

Abstract

Ceramics have material properties that make them useful for many industrial applications. They are strong, hard, and chemically inert. Their refractoriness gives them an advantage over metals and polymers for use at high temperature. Unfortunately, the inherent brittleness of ceramics limits their use in structural applications.

One way to improve the toughness of ceramics is to combine them with other materials to make composites. The correct combination of materials can lead to synergism, and a significant improvement in properties. In this work, brittle laminates that contain weak interlayers are considered. The weak interlayers lead to crack deflection, and *can* result in non-catastrophic failure of the material. The requirements for consistent crack deflection and non-catastrophic failure are not fully understood.

This work is an attempt to explain the observed fracture behaviour in brittle laminar composites that contain weak interlayers. A combination of experimental work, fracture mechanics modeling and finite element modeling has been used to predict the requirements necessary for non-catastrophic failure.

The work shows the size of flaws in the surface of the composite, in the weak interlayer, and in subsequent strong layers in the material, all play an

important role in the fracture behaviour. Control and understanding of the effect of the various flaw sizes *can* be used to achieve non-catastrophic failure and increased work of fracture in these composites.

Acknowledgments

I would first like to thank my supervisory committee; Professors Patrick Nicholson, David Wilkinson and David Weaver. Their different backgrounds have lead to different contributions to this work, and to my approach to science. Thanks to Professors Dick Hoagland, Tony Evans and Yves Brechet (from outside of McMaster) for useful and encouraging comments on my fracture mechanics and finite element modeling efforts. Thank you also to Professors David Embury, Gary Purdy and George Weatherly. They have not been directly involved in this project, but have always been helpful and given me confidence in my work.

Thank you to everyone in A203, for friendship and company over the last few years. Thanks to Dr Partho Sarkar, Connie Barrie and Dwayne Ritcey for help with experiments, particularly at the beginning of my stay at McMaster. Thanks to Dr Debnath De for discussions on elasticity and regression analysis, which have been helpful in clarifying my modeling efforts. Thanks to summer student Ewa Szymanski for working on the plaster-of-Paris project, which paralleled my own composite experiments.

Thanks to Marwan Hassan, from the mechanical engineering

department, for his help in confirming the validity of my finite element work.

Thanks to my Uncle John, for providing me with his FitAll software, used for the *non*-linear regression analysis. Thanks also for many much-needed rest cures during the frustrating times.

Thanks to Ena, Betty, Veronika, Helen, Lori, Ginny and Jan for taking care of all my administrative and paper work problems along the way. A sad farewell to Veronika, I know that she is on a lot of people's appreciation pages.

Last of all, thank you to all the friends I've made at McMaster; this includes the people with whom I've had intelligent conversations, and more importantly, the people with whom I have *not* had intelligent conversations. I think it would be best if I put them all in the same list, in no particular order; Andrew, Brian, Chad, Christine, Dave, Dave, Denis, Dwayne and Shelley, Jeff and Amy, Jeff and Patty, Joey and Erin, John, John, Justin and Angie, Kelly, Kevin, Kevin, Kim, Kristin, Mike, Stu and Liz...and all my friends from the Misfits softball team, and the McMaster rugby teams.

Table of Contents

List of Figures

List of Tables

List of Symbols

$\underline{a}$	displacement vector for finite element nodes
a	main crack size
a_0	initial main crack size at the onset of fracture
a_{crit}	critical main crack size for pre-cracking of the weak interlayer
a_{ind}	half-diagonal size of a Vicker's hardness indent
a_{rad}	half-diagonal size of a Vicker's hardness indent's radial cracks
A	regression parameter that combines strength and toughness terms
b	breadth of bend test specimen
c	weak interlayer (half-) crack size
c_0	initial weak interlayer (half-) crack size at the onset of propagation
c_{crit}	critical weak interlayer (half-) crack size for multi-stage fracture behaviour
c_{ext}	extent of weak interlayer crack propagation during catastrophic failure of strong surface layer
C	specimen compliance
E	Young's modulus
$\underline{f}$	load vector for finite element nodes

G	strain energy release rate
G_C	critical strain energy release rate for fracture (toughness)
G_a	strain energy release rate of main crack (in normalized terms)
G_{aC}	critical strain energy release rate of main crack (in normalized terms)
G_c	strain energy release rate of weak interlayer crack (in normalized terms)
G_{cC}	critical strain energy release rate of weak interlayer crack (in normalized terms)
G_{SC}	critical strain energy release rate for fracture of strong material
G_{SS}	steady state strain energy release rate for delamination
G_{WC}	critical strain energy release rate for fracture of weak interlayer
h	height of bend test specimen
H	hardness
I_2	second moment of area of second layer in bilayer composite
I_C	second moment of area of bilayer composite
$[K]$	stiffness matrix for finite elements
K	stress intensity factor
K_C	critical stress intensity factor for fracture (toughness)
K_{effW}	effective stress intensity factor on weak interlayer crack
K_i	stress intensity factor, mode "i" loading
K_{iC}	critical stress intensity factor, mode "i" loading
K_{iW}	stress intensity factor on weak interlayer crack, mode "i" loading

ℓ	surface layer thickness (must be smaller than "h")
L	length of bend test specimen
m	Weibull modulus
m_{eff}	effective Weibull modulus
M_i	moment on "i^{th}" region of a cracked beam
n	regression parameter
P_1	load at failure of surface layer
P_2	load after failure of surface layer
P_3	load at failure of "next" layer in composite
P_f	fracture load
P_{ind}	applied indent load
P_S	survival probability
r	radial distance, for polar coordinates
R	thermal shock resistance
S	specimen stiffness
t_i	layer thickness of material "i" in composite
u	horizontal displacement of finite element node
U_0	stored elastic energy in an uncracked plate
$U_{elastic}$	change in elastic energy on introduction of a crack
$U_{surface}$	surface energy of a crack
U_{total}	total energy of a system

v	vertical displacement of finite element node
V	volume
V_0	regression parameter for Weibull analysis
x	horizontal direction
y	vertical direction
Y	compliance (or geometric) factor
α	thermal expansion coefficient
α_D	Dundur's parameter
β	an indentation constant
β_i	regression coefficient "i"
χ	an indention constant
δ	deflection
δ_i	vertical displacement of "i^{th}" region of a cracked beam
ϕ	Airy stress function
γ	surface energy
ν	Poisson's ratio
θ	rotation angle, for polar coordinates
ρ	crack tip radius, *or* material density
$\sigma_{applied}$	applied stress
σ_f	fracture stress

σ_{max} maximum stress

σ_{xx} normal stress in the x-direction (horizontal)

σ_{xy} shear stress in the x-y plane

σ_{yy} normal stress in the y-direction (vertical)

ζ an indentation constant

Chapter 1. Introduction

"An unbaked vase, when broken, may be repaired,

but a baked one may not."

Leonardo da Vinci,

Folio 38 Recto, Codex Trivulzianus.

Ceramics have been used as structural materials throughout history. They are strong, hard, chemically inert, and can be made using several processing techniques into a variety of shapes. Their high melting points make them particularly suited to high temperature applications. Metals and polymers either soften or melt at higher temperature, or undergo chemical reactions that severely degrade their structural properties. The one disadvantage of ceramics is that they are brittle. This limits their use in many industrial applications.

Both ceramics and metals have theoretical strengths that are much higher than seen in practice. In metals the strength is limited by plasticity. Shear stresses cause dislocations in the crystal structure to move, and the material yields macroscopically. In many situations, the bonding in ceramics does not

allow such stress redistribution. The stress concentrates at defects within the material, breaks inter-atomic bonds, and leads to catastrophic failure.

Stress concentrations that build up in brittle materials are very sensitive to the size of defects. Failure originates from regions in the material that are highly stressed and/or contain large defects. The natural distribution of flaws from sample to sample results in a significant reliability problem. Not only do ceramics fail catastrophically, but they also do so under loading conditions that can be difficult to predict. The increase in flaw size due to impact or thermal shock in service exacerbates this problem.

The ultimate test of a structural material is its ability to bear load under service conditions. The strength of ceramics can be improved by refining the grain structure, which results in smaller defects and a higher load bearing capacity. Toughness, or the ability to absorb damage during failure, is more difficult to achieve.

One strategy to improve the toughness of materials is to look to nature. Natural materials such as bone, wood, seashell, mica and jade have layered structures. These layers allow crack deflection along weak interfaces, which can prevent complete catastrophic failure. Engineering ceramics can be developed with similar crack deflecting structures. While catastrophic failure cannot be avoided, a safety mechanism is put in place that allows the bulk of the material to continue to bear load. The energy required for complete material failure can be

increased several-fold.

The aim of this work is to determine the criteria required for consistent and successful crack deflection along weak interfaces in laminate composites subjected to flexure. Previous researchers have developed models, but they fail to account for the observed mechanical behaviour in some composites systems. A model is required that can predict the conditions necessary to achieve non-catastrophic failure in composites. The materials chosen, their properties, and the loading conditions, are expected to be very important to performance.

In this work, *interlayers* are considered. An interlayer is a thin layer of one material, which is sandwiched between thicker layers of a different material. It differs from an interface, which is the two dimensional plane between two layers of different material. An interlayer can be approximated as an interface for mechanical analysis, if sufficiently thin. The terms will be used interchangeably.

This work is a combination of fracture mechanics modeling, finite element analysis and experimental work. The approaches used are based on the same assumptions, and bear self-consistent results. Each leads to a better understanding of crack deflection phenomena, and a more educated design of composite materials.

Chapter 2. Background and Literature Review

2.1 Brittle Fracture

Fracture occurs when a solid material is subjected to enough tensile stress to physically rupture the chemical bonds that hold it together. In the case of ductile materials, the motion of dislocations within the crystal relieves strain energy and precedes the fracture. This plasticity reduces stress concentrations and delays the bond rupture. The material yields macroscopically and so the fracture is forewarned. The material absorbs energy through the accumulation of damage, and is said to be *tough*. In the case of brittle fracture no plastic deformation occurs. The material cannot absorb energy, except by creating new surface area. The failure is sudden and catastrophic. The difference in stress-strain behaviour during mechanical testing of the two types of materials is shown schematically as Figure 2.1-1.

Failure in a given sample originates where the stress is the highest. In brittle materials this is at the tips of microscopic (or macroscopic) flaws. Tensile forces cannot be transferred across the free surfaces of these cracks, and so the

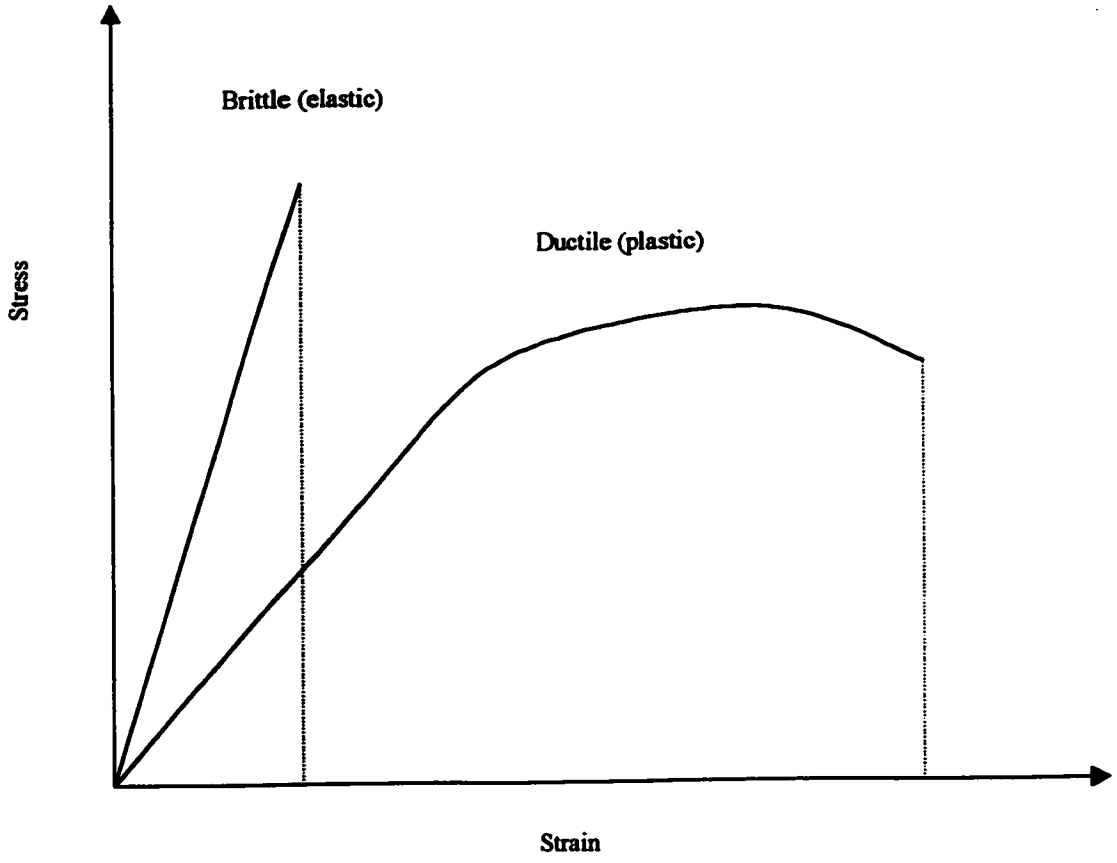

Figure 2.1-1. A schematic of the stress-strain behaviour of ductile and brittle materials.

"excess" load is concentrated at the tips. The larger the stress or the larger the flaw, the larger the resulting stress concentration and the weaker the material.

Inglis (1913) first estimated the magnitude of stress concentration at a crack tip. Consider an infinite flat plate containing a through-thickness elliptical flaw (see Figure 2.1-2), stressed perpendicular to the major axis. The stress concentration at the end of the major axis is given by;

$$\sigma_{max} = \sigma_{applied}\left(1+2\sqrt{\frac{a}{\rho}}\right) \qquad (2.1\text{-}1)$$

where σ_{max} is the maximum stress at the crack tip, $\sigma_{applied}$ the applied stress, a the semi-major axis, and ρ the radius of curvature at the ends of the major axis. If the crack is sharp, then $\rho \to 0$ and $\sigma_{max} \to \infty$. The effective stress at the tips of cracks can be many times the applied stress. This ultimately leads to rupture of the inter-atomic bonds.

2.1.1 Chemical Bonding in Solids

Three primary types of chemical bonding exist in solids; metallic, ionic and covalent. Bonds are not necessarily purely of one type. There may be mixed metallic-covalent or ionic-covalent combinations. In metallic bonding, valence electrons from each atom in the solid contribute to the bond. The result is positive ion cores held together by a region of delocalized electrons. This form of bond

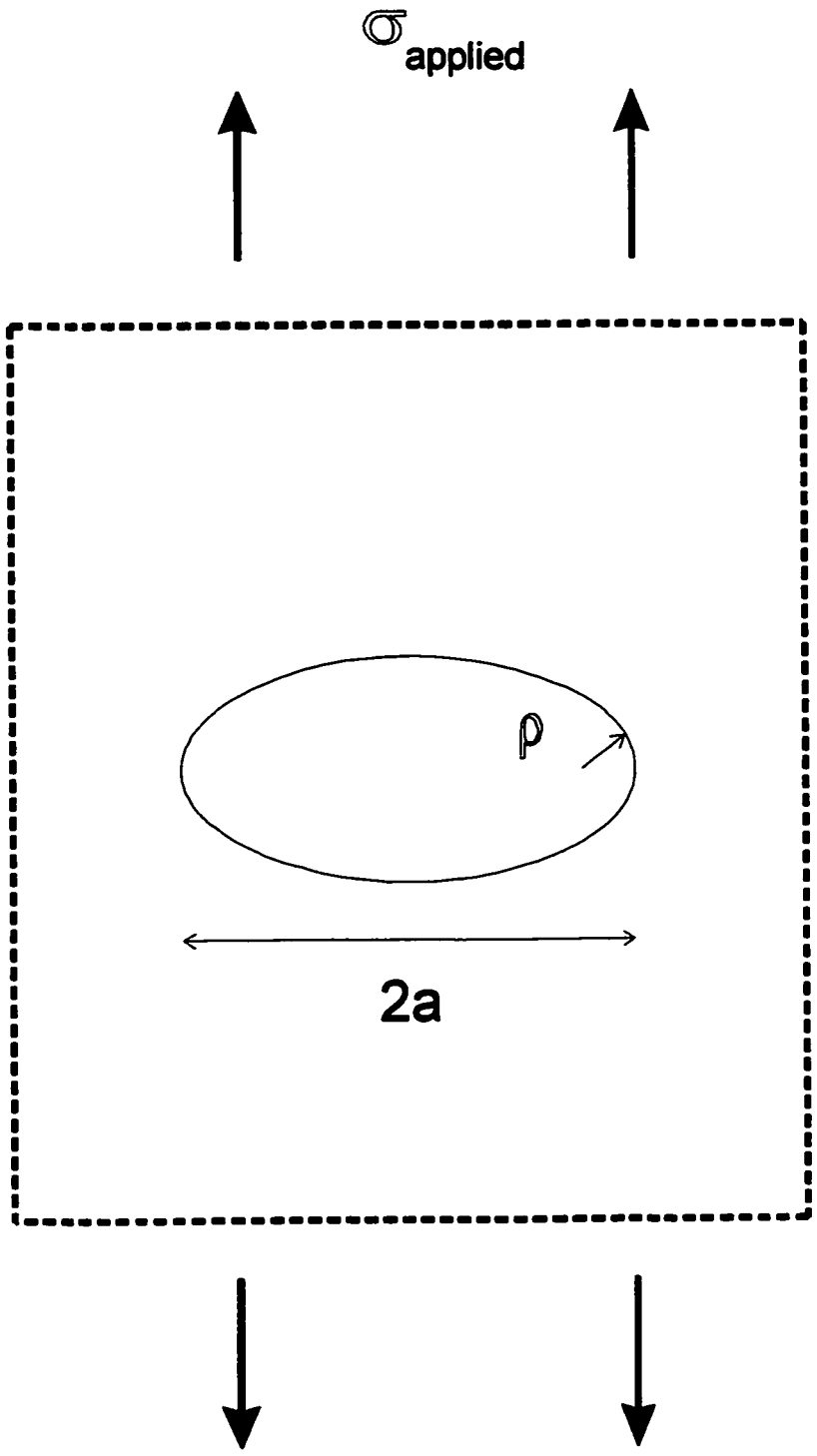

Figure 2.1-2. A schematic of the Inglis elliptical crack geometry.

has relatively low energy and is non-directional. In ionic bonds, the metal atoms give up their valence electrons to non-metal atoms. The resulting metal cations and non-metal anions are attracted by Coulombic forces. The bonds are strong and non-directional. In covalent bonding valence electrons are shared between two specific atoms in the solid. The bonds are strong and directional.

Metallic bonding can be used to explain the plastic behaviour exhibited by metals. The non-directional bonds do not resist shear, and so planes within the crystal lattice are free to move relative to one another. This allows dislocations (planar defects) in the crystal structure to move and dissipate stress. The macroscopic result is that many metals deform before fracture.

Ionic and covalent bonding can be used to explain the brittle behaviour exhibited by ceramics and glasses. Ionic solids consist of alternating cations and anions in the crystal structure. High shear stresses are necessary to overcome the Coulombic repulsion between like ions as they move relative to one another, so dislocations are difficult to move. The requirement for electrical neutrality in the dislocation makes the defect geometrically complex. Bond rupture becomes energetically more favourable than plastic yielding, so fracture is more likely. Covalent solids contain highly directional bonds that are highly resistant to shear. The directionality of bonds leads to geometrically complex dislocations. Like ionic bonds, bond rupture is energetically more favourable than plastic yielding.

The ionic and covalent bonding in ceramics is the source of their brittleness, but is also the source of their hardness, chemical nobility and high

melting points. The bonding in brittle materials cannot be changed, so toughening strategies must rely on other avenues.

2.1.2 The Thermodynamics of Crack Propagation

Fracture is a thermodynamic process. Work by Griffith (1920) is the basis of modern mechanical thermodynamics. Griffith considered an infinite plate containing a perfectly sharp crack, subjected to an applied stress (see Figure 2.1.2-1), similar to the work by Inglis. The total energy of the system can be calculated;

$$U_{total} = U_0 + U_{elastic} + U_{surface} - W_{external} \qquad (2.1.2\text{-}1)$$

where U_{total} is the total energy of the system, U_0 the stored strain energy in the (uncracked) plate, $U_{elastic}$ the change in elastic strain energy on introducing the crack, $U_{surface}$ the surface energy of the crack, and $W_{external}$ the work done by external forces. Assuming a cylindrical region around the crack is stress free, the total energy attributable to the presence of the crack can be calculated as;

$$U_{total} = \left(\frac{-\sigma^2 \pi a^2}{2E} \right) + 4a\gamma \qquad (2.1.2\text{-}2)$$

where σ is the applied stress, a the half crack size, E the Young's modulus of the material, and γ the surface energy of the crack.

The strain energy release rate is defined as the derivative of the strain energy with respect to the crack size, that is;

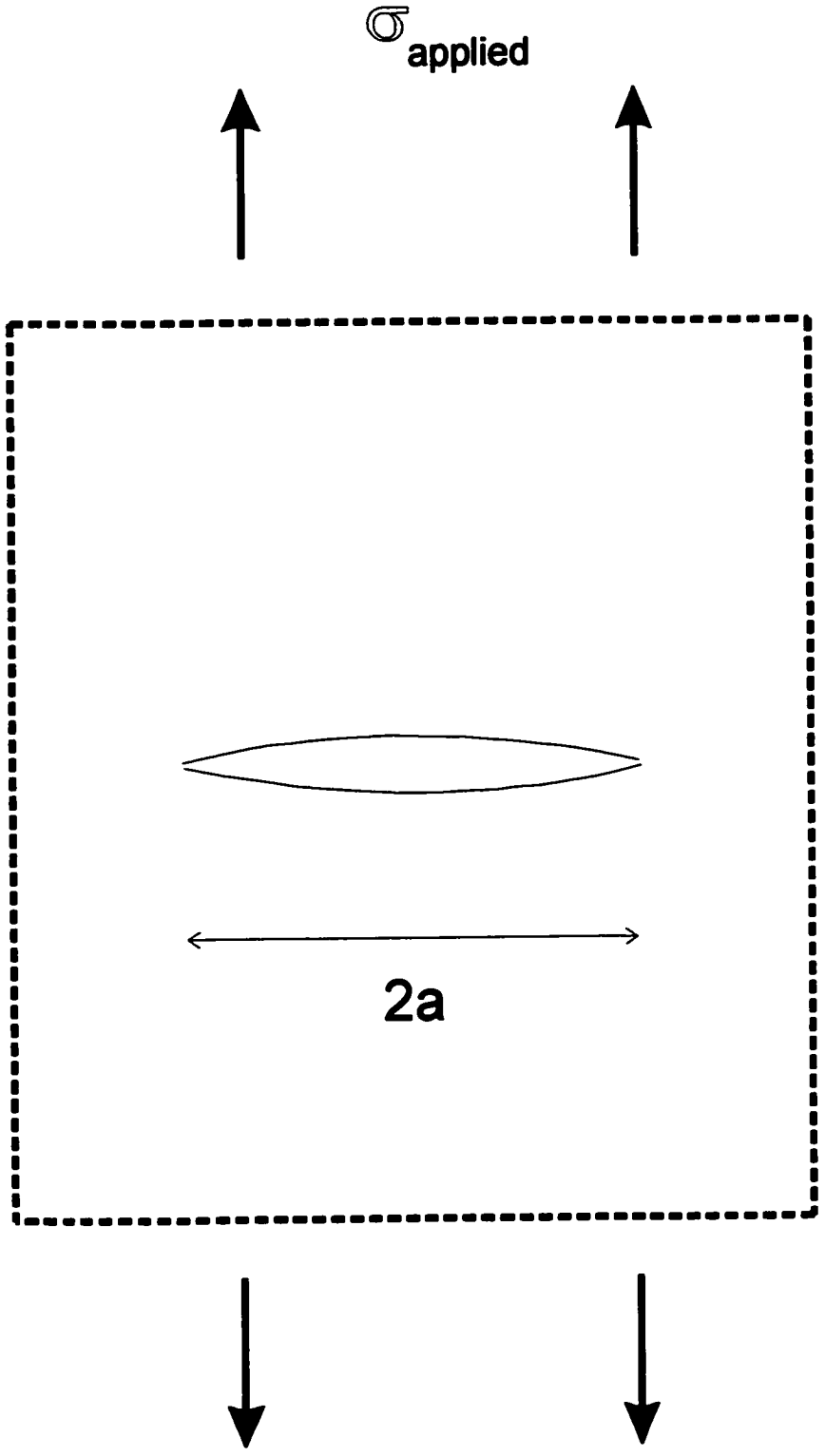

Figure 2.1.2-1. A schematic of the Griffith sharp crack geometry.

$$G = \frac{dU_{elastic}}{da} = \frac{-\sigma^2 \pi a}{E} \qquad (2.1.2\text{-}3)$$

Griffith argued that the crack would only propagate if it were thermodynamically favourable. As the crack extends, its surface energy increases and the total system strain energy is reduced. When the derivative of the *total* energy equation equals zero, the rate of change of these two components is equal. This defines the critical strain energy release rate for the material and the fracture stress;

$$G_C = 2\gamma = \frac{\sigma_f^2 \pi a_0}{E} \qquad (2.1.2\text{-}4)$$

where G_C is the critical strain energy release rate, σ_f the fracture stress, and a_0 the initial half crack size. The critical strain energy release rate is an intrinsic material parameter for purely linear elastic materials, whereas the strength is a function of crack size.

If a material is stressed such that its strain energy release rate is above the critical value, the crack will propagate. As the strain energy release rate is proportional to the crack size, *a*, the crack propagates unstably and the material fractures catastrophically. The strength of the material is inversely proportional to the square root of the initial crack size. If the strain energy release rate is below the critical value, then theoretically the crack will heal. This does not usually occur in practice.

Griffith validated the theory experimentally. Cracks of known size were introduced into glass samples. The strength of each sample, plotted versus the

inverse of the square root of the crack size, yields a linear relationship (Figure 2.1.2-2).

Crack propagation is dependent on loading geometry. Obreimoff (1930) showed brittle fracture can be non-catastrophic. Consider the cleavage of a mica flake by wedging (see Figure 2.1.2-3). For this geometry;

$$U_{elastic} = \left(\frac{E\delta^3 h^2}{8a^3} \right) \qquad (2.1.2\text{-}5)$$

where δ is the deflection caused by the wedge and h the height of the flake. Therefore;

$$G = \frac{dU_{elastic}}{da} = \left(\frac{-3E\delta^3 h^2}{8a^4} \right) \qquad (2.1.2\text{-}6)$$

In this case the strain energy release rate decreases as the crack propagates. At some point the value falls below the critical value for the material and the crack arrests. If the wedge is driven further into the sample the crack propagates stably. The crack maintains a constant length. The work done in driving the wedge is exactly compensated by surface energy in the cleaved mica. This experiment allowed the surface energy of the mica to be calculated.

An alternate approach to calculating the strain energy release rate is to consider the change in work done during crack propagation;

$$G = \frac{d}{da}\left(\frac{1}{2} P\delta \right) \qquad (2.1.2\text{-}7)$$

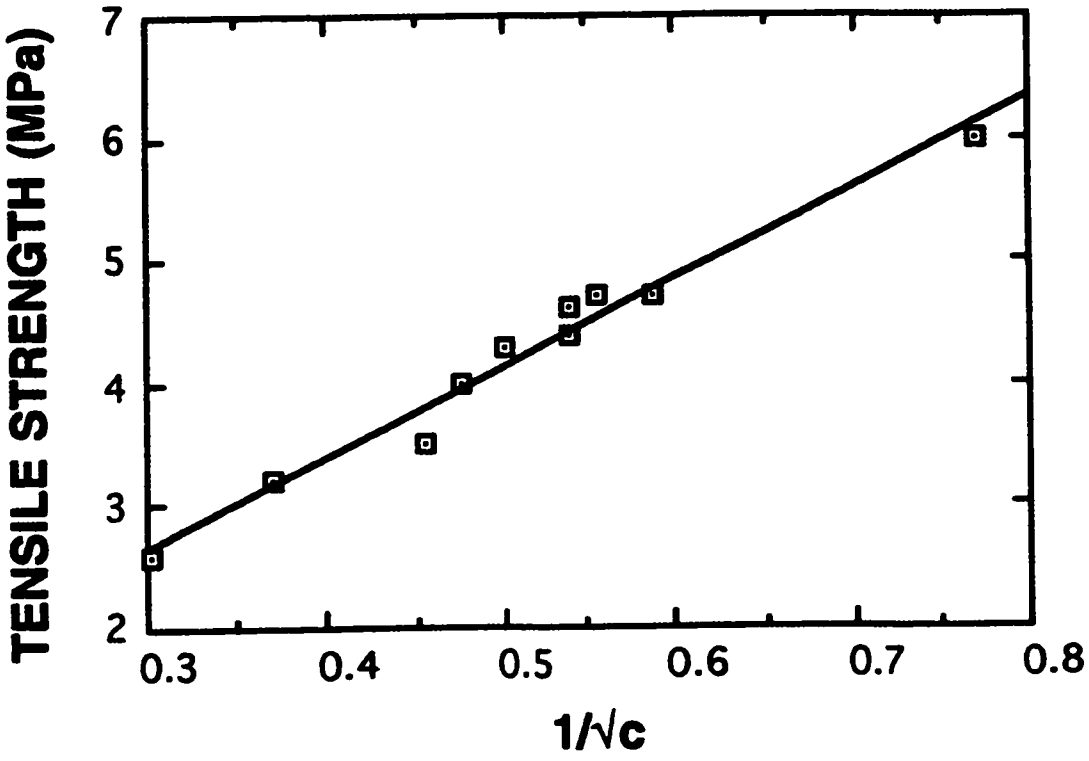

Figure 2.1.2-2. The Griffith data, used to show the relationship between strength and crack size (Green, 1998).

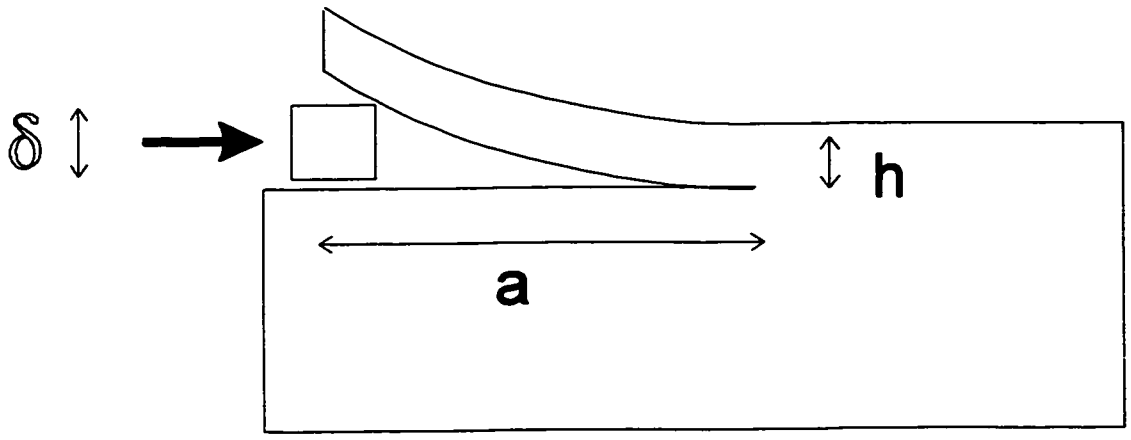

Figure 2.1.2-3. A schematic of the Obriemoff cleavage experiment.

where P is the applied load, and δ the displacement. Mechanical testing is often done under load or displacement controlled conditions. The strain energy release rate can be calculated in terms of the change in compliance, or stiffness, of the test sample;

$$C = \frac{1}{S} = \frac{\delta}{P} \qquad (2.1.2\text{-}8)$$

where C is the compliance and S the stiffness. For constant loading conditions;

$$G = \frac{1}{2} P^2 \frac{dC}{da} \qquad (2.1.2\text{-}9)$$

For constant displacement conditions;

$$G = \frac{1}{2} \delta^2 \frac{dS}{da} \qquad (2.1.2\text{-}10)$$

The stability or instability of the crack depends on the geometry of the test specimen, and whether the compliance (or stiffness) is increasing or decreasing.

Other loading geometries have been designed that allow cracks to stabilize. These will be discussed in later sections. The ability to stabilize a brittle crack provides a strategy for toughening brittle materials. If a crack can be arrested, then complete fracture can be prevented. The criterion for stabilization of a propagating crack is (as long as $G<G_C$);

$$\frac{dG}{da} \leq \frac{dG_C}{da} \qquad (2.1.2\text{-}11)$$

Both terms in the equation can be manipulated. Either the geometry of the material can be designed to reduce the strain energy release rate as the

crack propagates, or the crack can be forced to propagate into regions in the material of higher toughness.

Irwin (1958) rearranged the Griffith equation to develop a fracture criterion based on stress intensity rather than energy;

$$K = Y\sigma\sqrt{\pi a} \qquad (2.1.2\text{-}12)$$

where *K* is the stress intensity factor, and *Y* a compliance function, which is dependent on the loading geometry. Similarly;

$$K_C = Y\sigma_f\sqrt{\pi a_0} \qquad (2.1.2\text{-}13)$$

where K_C is the critical stress intensity factor, or the *toughness* of the material. Similar to G_C, the critical stress intensity factor is an intrinsic material parameter for perfectly linear elastic materials. The two approaches are related by;

$$K^2 = EG \qquad (2.1.2\text{-}14)$$

Three basic loading modes can be identified (see Figure 2.1.2-4), termed modes *I*, *II*, and *III*. When all three are considered the *K* and *G* relationship becomes more complex. For plane strain conditions, which are appropriate for the mechanical testing of ceramics;

$$G = \frac{K_I^2\left(1-\nu^2\right)}{E} + \frac{K_{II}^2\left(1-\nu^2\right)}{E} + \frac{K_{III}^2(1+\nu)}{E} \qquad (2.1.2\text{-}15)$$

where ν is the Poisson's ratio of the material, and the subscripts represent the three loading modes.

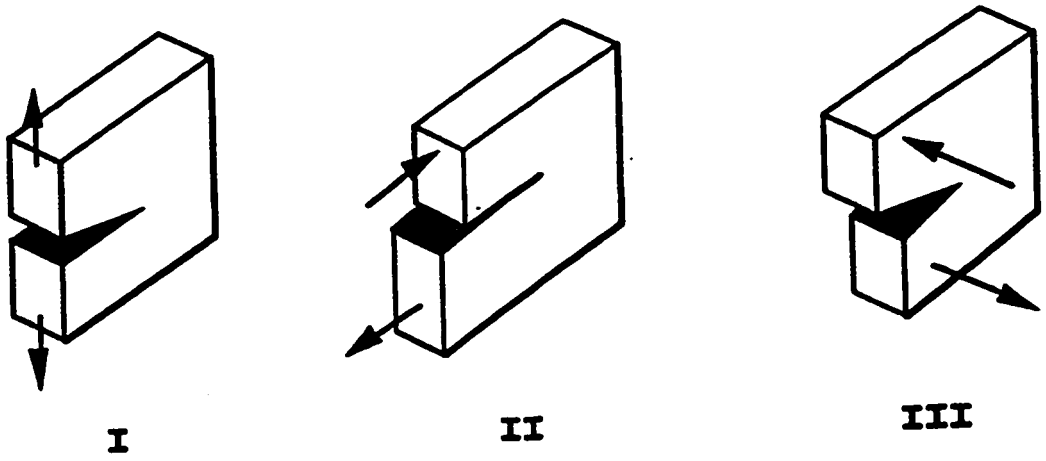

Figure 2.1.2-4. The three loading modes considered in crack propagation (Green, 1998).

Mott (1948) modified the Griffith energy approach to estimate the velocity of a propagating crack. A kinetic energy term was added to Equation 2.1.2-1, of the form;

$$U_{kinetic} = \frac{k\rho a^2 \left(\frac{da}{dt}\right)^2 \sigma^2}{2E^2} \qquad (2.1.2\text{-}16)$$

where $U_{kinetic}$ is the kinetic energy term, k a constant, ρ the density of the material, and t time. The kinetic energy can be related to the difference between the *critical* strain energy release rate and the *instantaneous* strain energy release rate of a propagating crack. This leads to an expression for the velocity of the crack;

$$\left(\frac{da}{dt}\right) = \sqrt{\frac{2\pi}{k}}\sqrt{\frac{E}{\rho}}\sqrt{1-\frac{a_0}{a}} \approx 0.38\sqrt{\frac{E}{\rho}}\sqrt{1-\frac{a_0}{a}} \qquad (2.1.2\text{-}17)$$

Experimentally calculated velocities (Roberts and Wells, 1954) tend to be below this theoretical prediction, though this has been attributed to a difficulty in achieving the exact conditions specified in derivation of the equation. Other researchers (Berry 1960, Dulaney and Brace 1960) have developed similar analyses, resulting in similar equations. Experimental errors have made each approach difficult to validate.

The above approach is *quasi-static*. The equation is developed based on theory that specifies equilibrium conditions. At the onset of crack propagation, when $a=a_0$, the velocity and acceleration are zero, which can not be true. This

undermines the approach. It can also be argued that, at high crack velocities, the inertia of matter surrounding the crack tip influences the strain energy release rate. The maximum velocity of an unstable crack is the Rayleigh speed, which describes the velocity of surface waves in the material. This leads to the development of dynamic stress intensity factors, and the consideration that the critical strain energy release rate of the material is velocity dependent. Solutions to the problem exist, but are sensitive to the assumptions made in each calculation and the geometry of interest (Kanninen and Popelar, 1985, Chapter 4).

Consideration of the kinetics of propagating cracks has implications for the strategies used to toughen brittle materials. A material containing a small flaw that initiates fracture will initially have a high elastic strain energy. This energy is converted to surface and kinetic energy during fracture. To slow, or even arrest the crack, the strain energy release must be reduced to a rate below the critical value defined by the material. The excess kinetic energy must also be absorbed if a dynamic approach is considered, so the release rate must be well below the critical value. A material containing a large flaw will store less elastic energy, and so will produce less kinetic energy during propagation. To arrest the crack, the strain energy release rate must be below the critical strain energy release rate for the material, but there is less kinetic energy for which to compensate. The overall result is that initially large flaws propagating are more easily arrested than initially

small flaws propagating. This aspect of crack propagation has not been fully exploited in the design of tough brittle materials.

2.1.3 Weibull Statistics

Equations 2.1.2-4 and 2.1.2-5 show the strength of brittle materials is sensitive to the initial flaw size. Samples containing large flaws are weaker, and samples containing small flaws stronger. Fracture will always initiate at the crack tip in the sample that suffers the highest stress intensity. The strength is sensitive to both the loading mode and the orientation of cracks. The natural variation of flaw size and orientation in samples results in a variation in strength.

Weibull (1951) developed a probability function that can be used to describe the reliability of brittle materials. The method was originally developed as an empirical equation, but it can be related to gamma-type continuous probability functions. The simplest form of the equation is;

$$P_S = \exp\left\{-\frac{V}{V_0}\left(\frac{\sigma}{\sigma_0}\right)^m\right\} \qquad (2.1.3\text{-}1)$$

where P_S is the probability of the sample surviving a given applied stress, V the volume of the sample, σ the applied stress, m the Weibull modulus, V_0 a reference volume and σ_0 a constant determined by regression. A number of specimens are tested to failure, and their strengths calculated. The Weibull modulus is determined by linear regression of the data to the equation;

$$\ln\ln\left(\frac{1}{P_S}\right)=m\ln\sigma_f+\text{constant} \qquad (2.1.3\text{-}2)$$

A high Weibull modulus (~100) indicates a reliable material, whereas a low value (~5) indicates an unreliable material. Engineering ceramics tend to have low moduli, in the range ~10-20.

The strength of a given ceramic sample is dependent on its volume. A large sample has a high probability of containing large flaws, so is more likely to be weak. The opposite is true for small samples, which have a low probability of containing large flaws and so are more likely to be strong. This relationship was demonstrated by Griffith (1920), who showed the strength of glass fibres under tension increases with decreasing diameter. It was also shown by Leonardo da Vinci (referenced by Timoshenko, 1953), who reported the strength of steel increases with decreasing wire length.

Strength also depends on the loading geometry. Equation 2.1.3-1 holds for specimens subjected to tensile stress. If a sample is biaxially stressed there is a higher probability that a natural, randomly oriented, flaw will suffer a critical stress. A number of samples will be weaker, on average. Conversely, only a small region of a sample subjected to a bend test endures its calculated maximum stress, so a number of samples will be stronger on average. A loading factor can be included in Equation 2.1.3-1 to account for the effect of loading geometry on the Weibull modulus.

The reliability of an engineering ceramic is ultimately based on its load bearing capacity. Design of brittle components for service must account for flaw size distributions, sample size and loading geometry.

2.1.4 Strength and Toughness Testing

The strength of a material is the maximum *nominal* stress endured before fracture. The strength of a brittle material is sensitive to flaw size, so an average strength is usually quoted with either a calculated error, or the Weibull modulus.

The usual strength test for a ceramic is a four-point bend test (see Figure 2.1.4-1). The test sample is supported by four loading pins; two on either side. The assembly is pushed together, with the centre of the span subjected to pure bending stresses (no shear is involved). The strength is calculated from the load required to fracture the sample.

Tensile tests are not favoured as the loading grips may scratch the surface of the material and lead to error, and the alignment is too critical. Three-point bend tests are often used industrially, but these tend to over-estimate the strength, as only the centre of the beam is subjected to the maximum calculated stress. Fracture may initiate elsewhere in the sample depending on its unknown and random distribution of flaws. A four-point test subjects the portion between

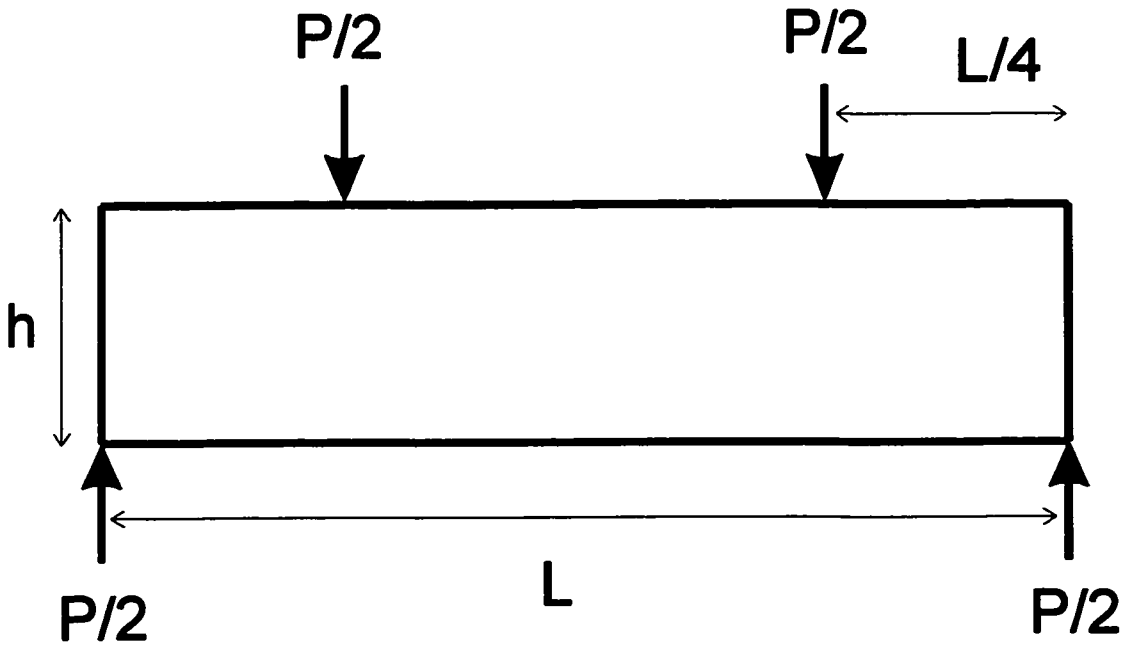

Figure 2.1.4-1. The four-point bend test geometry.

the inner pins to the maximum calculated stress, and avoids the problem of significant damage by the loading assembly.

For the test geometry shown in Figure 2.1.4-1, the maximum stress can be calculated using classical beam theory;

$$\sigma = \frac{3PL}{4bh^2} \qquad (2.1.4\text{-}1)$$

where P is the total load applied at the loading pins, L the outer span, b the breadth of the beam, and h the height. The strength is calculated at fracture;

$$\sigma_f = \frac{3P_fL}{4bh^2} \qquad (2.1.4\text{-}2)$$

where σ_f and P_f are the fracture strength and load respectively. Note that these equations assume the inner span of the loading pins is half that of the outer span, and that the beam is slender enough to ignore any possible shear effects.

Fracture usually initiates at the surface of the sample during bend testing. Derivation of the Griffith equation (Equation 2.1.2-4) considered the initial *half* crack size. For a surface crack the *whole* crack size is considered, and the compliance factor is >1 (Equation 2.1.2-12), so the stress intensity factor is larger for a surface crack than an internal crack. Thermal residual stresses caused by processing can result in fracture initiating at an internal crack.

The *fracture toughness* of a material is the maximum stress intensity factor a material can endure before fracture. Unlike strength, it is an intrinsic material parameter. Various tests can be performed to calculate the value. These

tend to give slightly different results, so the test method must be quoted with the calculated toughness.

A common technique for ceramics is the single-edge-notched-beam (SENB) test. A three- or four-point bend sample is prepared, a notch of known depth is cut into the tensile surface, and the sample bend tested to failure. The critical stress intensity factor is then calculated using Equation 2.1.2-13. For a three-point test;

$$Y = 1.93 - 3.07\left(\frac{a}{h}\right) + 14.53\left(\frac{a}{h}\right)^2 - 25.11\left(\frac{a}{h}\right)^3 + 25.8\left(\frac{a}{h}\right)^4 \qquad (2.1.4\text{-}3)$$

For a four-point bend test;

$$Y = 1.99 - 2.47\left(\frac{a}{h}\right) + 12.97\left(\frac{a}{h}\right)^2 - 23.17\left(\frac{a}{h}\right)^3 + 24.8\left(\frac{a}{h}\right)^4 \qquad (2.1.4\text{-}4)$$

These compliance factors were calculated by regression of polynomials to the experimental data (Brown 1966, Tada et al 1973). One problem with the test is that a notch cut from a saw does not produce a perfectly sharp crack. This leads to an over-estimation of the toughness of a given material.

2.1.5 Indentation

Indentation allows the toughness and hardness of a sample to be measured. Hardness is the resistance of a material to indentation, and is related to the yield strength of the material. Brittle materials resist yielding, so have higher hardness.

Indentation involves applying a known load to the surface of a sample with a rigid indenter. The size of the region deformed by the indenter is used to calculate the hardness of the material. The smaller the deformed region (for a given load) the harder the material. In the case of brittle materials the test also results in stable cracks running from the edges of the indent. These can be used to calculate the toughness of the material. The cracks also affect the strength of a given sample. Various tests are possible, but the only one considered here is the Vicker's hardness test. In this case the load is applied via a pyramid-shaped diamond indenter.

The hardness of a material is calculated using;

$$H = 1.854 \frac{P_{ind}}{a_{ind}^2} \qquad (2.1.5\text{-}1)$$

where H is the hardness, P_{ind} the indentation load, and a_{ind} the length of the diagonal of the impression left by the indenter (see Figure 2.1.5-1). The indentation is measured using an optical microscope. Resolution may lead to errors in the measured lengths.

If the material is brittle, the indentation also leads to radial cracks that form during unloading. The toughness of the material can be calculated (Cook and Lawn, 1983) by measuring the size of these radial cracks;

$$K_C = \frac{\chi P_{ind}}{a_{rad}^{3/2}} = \beta \sqrt{\frac{E}{H}} \frac{P_{ind}}{a_{rad}^{3/2}} \qquad (2.1.5\text{-}2)$$

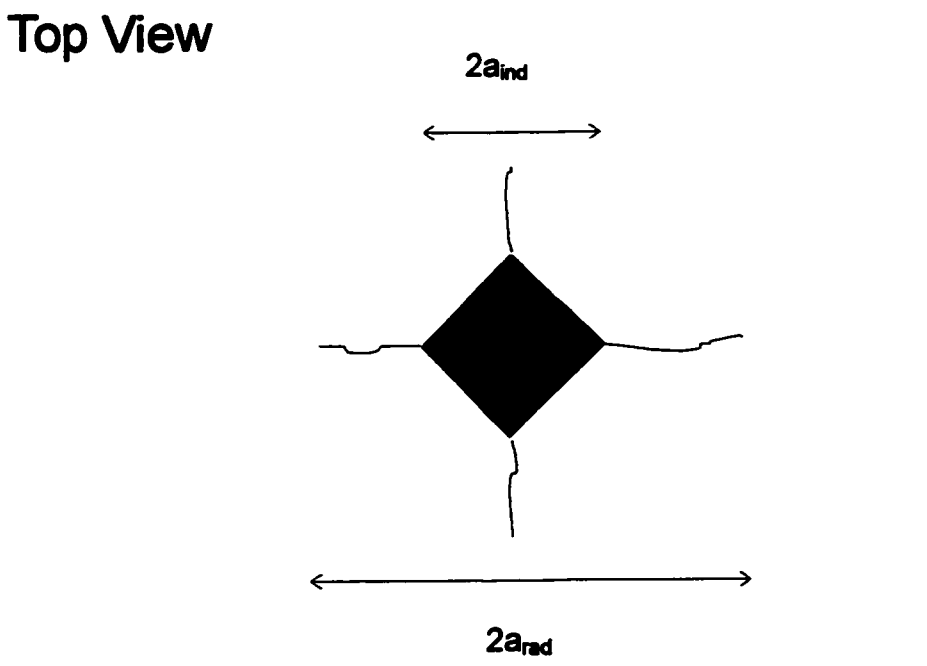

Figure 2.1.5-1. A schematic of a hardness indent in a brittle material.

where χ and β are constants, and a_{rad} the size of the radial cracks (indentation centre to tip). The parameter β has been determined from calibration tests, and is taken as ~0.016.

An alternative to measuring the radial crack size is to bend test the indented sample. During bend testing, the radial crack grows stably under the influence of both the applied load and the residual stress left by the indentation. The sample eventually fails catastrophically, because the stress intensity rises as the crack grows. At the point of fracture it can be shown that;

$$\sigma_f = \frac{0.47K_C^{4/3}}{Y(\chi P_{ind})^{1/3}} \qquad (2.1.5\text{-}3)$$

The compliance factor used is that for a semi-circular crack; $Y=2/\pi$. This can be combined with Equation 2.1.5-2 and rearranged to give;

$$K_C = \zeta\left(\frac{E}{H}\right)^{1/8}\left(\sigma_f P_{ind}^{1/3}\right)^{4/3} \qquad (2.1.5\text{-}4)$$

where;

$$\zeta = \left(2.27Y\beta^{1/3}\right)^{3/4} \qquad (2.1.5\text{-}5)$$

This parameter has been calculated by calibration tests, and is taken as $\zeta \approx 0.59$. Following Equation 2.1.5-3, a plot of log strength versus log indent load yields a straight line with a slope of –1/3. This is true only for a perfectly brittle material, and has been demonstrated by Lawn (1993) – see Figure 2.1.5-2. If plotted data does not have a slope of –1/3 it is a non-ideal brittle material. If a material has a

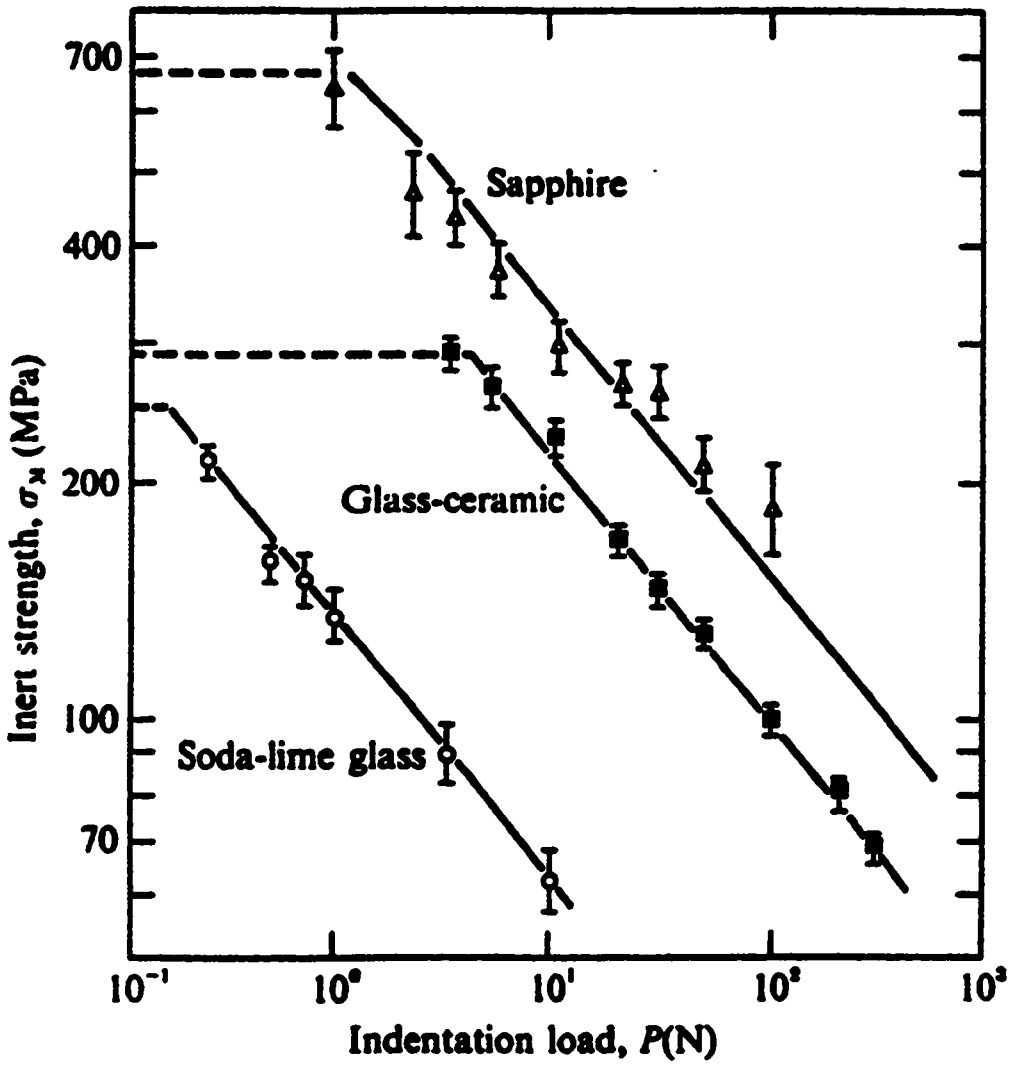

Figure 2.1.5-2. A plot of log strength versus log indent load for an ideally brittle material (Lawn, 1998).

slope of greater than -1/3, then the strength is greater than predicted for a given indent load or crack size. Such a material is said to exhibit 'R-curve' behaviour.

One advantage of indentation testing is that both hardness and toughness can be calculated. The other is that cracks of a known size can be introduced into a sample under controlled conditions. This reduces the strength of the material as the cracks are larger than natural flaws, but in some experiments the consistency of the crack size is paramount. The effective Weibull modulus is increased significantly. The desire to have a "deterministic" strength will be discussed later.

2.1.6 Elastic Crack Tip Stress Fields

Fracture always initiates at a highly stressed crack tip. The stress intensity experienced near a stressed crack tip can be calculated by finding a complex solution of the Airy stress function, which must be satisfied for all elastic stress fields.

The solution to any elastic stress field problem must satisfy mechanical equilibrium and strain compatibility. The requirement for mechanical equilibrium ensures that forces within the material are mutually balanced. For the simple 2-dimensional case;

$$\frac{\partial \sigma_{xx}}{\partial x} + \frac{\partial \sigma_{yx}}{\partial y} + f_x = 0 \qquad (2.1.6\text{-}1)$$

and;

$$\frac{\partial \sigma_{yy}}{\partial y}+\frac{\partial \sigma_{xy}}{\partial x}+f_y=0 \qquad (2.1.6\text{-}2)$$

where the σ's are stresses, the f's body forces, and the x's and y's are the horizontal and vertical directions. The requirement for strain compatibility ensures the strains are mutually consistent, and give continuous displacement functions. These two restrictions are satisfied by;

$$\frac{\partial^2 \varepsilon_{xx}}{\partial y^2}+\frac{\partial^2 \varepsilon_{yy}}{\partial x^2}=\frac{2\partial^2 \varepsilon_{xy}}{\partial x \partial y} \qquad (2.1.6\text{-}3)$$

where the ε's are strains. Hooke's Law, a constitutive relation gives the relationship between the stress and strain in an elastic material, which, in its simplest form is;

$$E=\frac{\sigma}{\varepsilon} \qquad (2.1.6\text{-}4)$$

Equations 2.1.6-1 to 2.1.6-4 can be combined to form the Airy stress function;

$$(\nabla^2)^2 \phi = 0 \qquad (2.1.6\text{-}5)$$

where ϕ is the Airy stress function (a function in both x and y). The stresses and shears are given by;

$$\sigma_{xx}=\frac{\partial^2 \phi}{\partial y^2} \qquad (2.1.6\text{-}6)$$

$$\sigma_{yy}=\frac{\partial^2 \phi}{\partial x^2} \qquad (2.1.6\text{-}7)$$

and;

$$\sigma_{xy} = -\frac{\partial^2 \phi}{\partial x \partial y} \qquad (2.1.6\text{-}8)$$

Any mathematical equation that satisfies the Airy stress function *and* the boundary conditions of a given problem, is a legitimate mathematical solution to the problem. This has the advantage that many solutions may be found. The disadvantage is that the "true" solution may be a combination of several super-imposed functions.

The Airy stress function approach to solving elasticity problems can be used to determine the stress and strain fields around sharp cracks. Several researchers have contributed solutions to this of the same general form problem (Westergaard 1939, Williams 1954, Irwin 1958, Cook and Gordon 1964). The accepted form of the mode I stress distribution near a crack tip is given by;

$$\begin{Bmatrix} \sigma_{xx} \\ \sigma_{yy} \\ \sigma_{xy} \end{Bmatrix} = \frac{K_I}{\sqrt{2\pi r}} \cos\frac{\theta}{2} \begin{Bmatrix} 1 - \sin\frac{\theta}{2}\sin\frac{3\theta}{2} \\ 1 + \sin\frac{\theta}{2}\sin\frac{3\theta}{2} \\ \sin\frac{\theta}{2}\cos\frac{3\theta}{2} \end{Bmatrix} \qquad (2.1.6\text{-}9)$$

where the σ's are stresses, and r and θ polar coordinates of the point of interest, as shown in Figure 2.1.6-1. K_I is the stress intensity factor given by Equation 2.1.2-12. It is possible to modify Equation 2.1.6-9 to account for mode II or III loading.

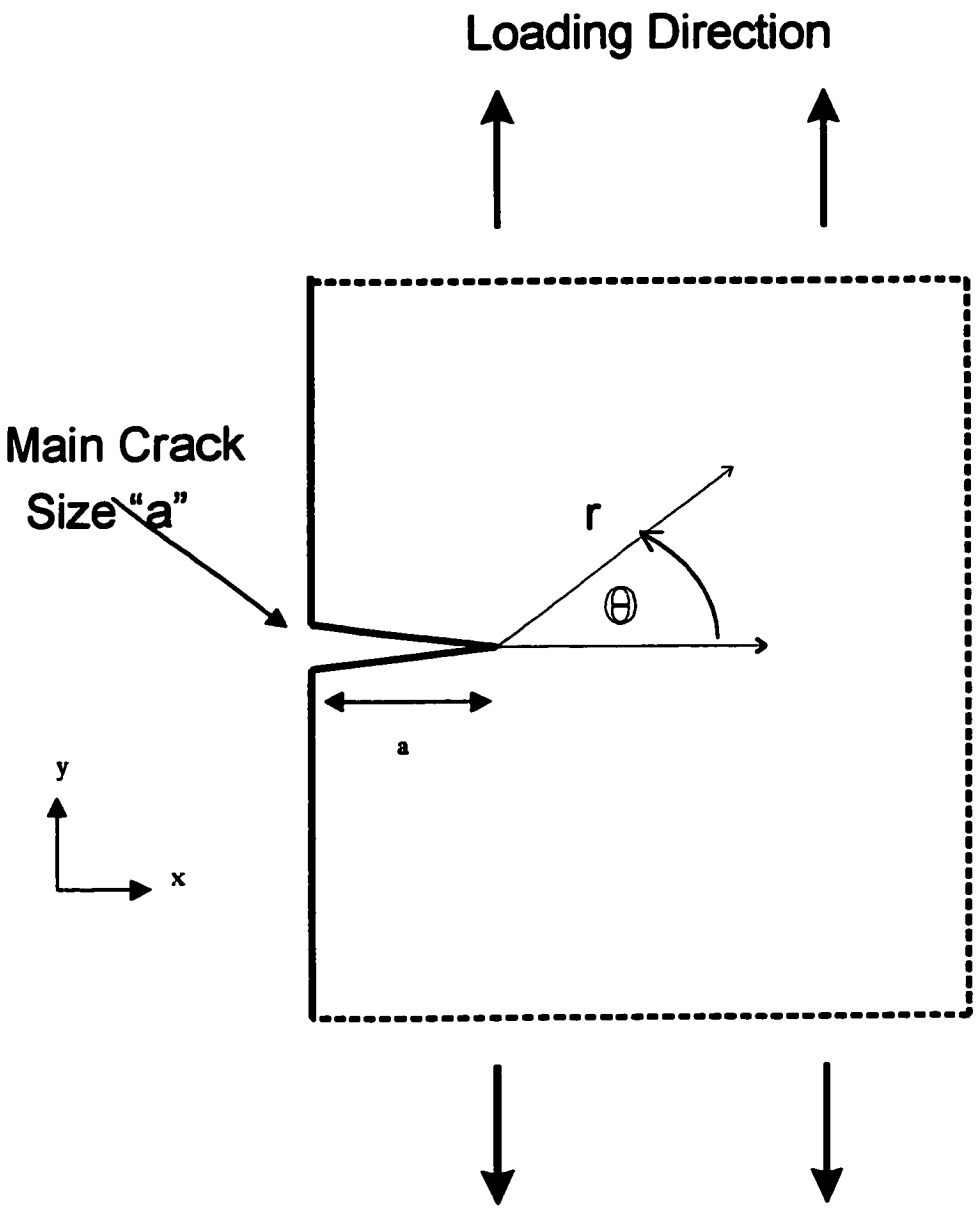

Figure 2.1.6-1. A schematic of the crack tip geometry.

Equation 2.1.6-9 is the leading term in an equation comprised of several super-imposed functions. The remaining terms are usually ignored as the most important stresses to the fracture process are those at the crack tip, that is, σ_{yy} at $r=0$. If toughening is to be achieved using weak interfaces, the stresses away from the crack tip and parallel to the plane of the crack are important, that is, σ_{xx} at $r>0$. Unfortunately, these terms have not been accurately determined. One term in the solution, referred to as the "T-stress", is a stress parallel to the plane of the crack that is independent of the distance from the tip. The magnitude of this stress has been calculated for various geometries. The T-stress is estimated as ~3% the applied stress, for a three-point bend test (Larsson and Carlsson, 1973). This is not expected to have a significant effect on the fracture behaviour.

Equation 2.1.6-9 was derived assuming the crack is subjected to a uniform stress. It is possible to determine the stress concentration at the tip of a crack subjected to a non-uniform stress distribution. Consider a crack, of length $2a$, subjected to a stress field described by the function $\sigma_{yy}=f(x)$ (see Figure 2.1.6-2). The stress intensity factor at the tip of the crack is calculated using a *Green* integral function (Tada, Paris and Irwin 1973);

$$K_I = \frac{1}{\sqrt{\pi a}} \int_{-a}^{a} \frac{\sigma_{yy}(x)}{\sqrt{1-\left(x/a\right)^2}} dx \qquad (2.1.6\text{-}10)$$

Similar equations can be developed to account for mode II or mode III loading of the crack.

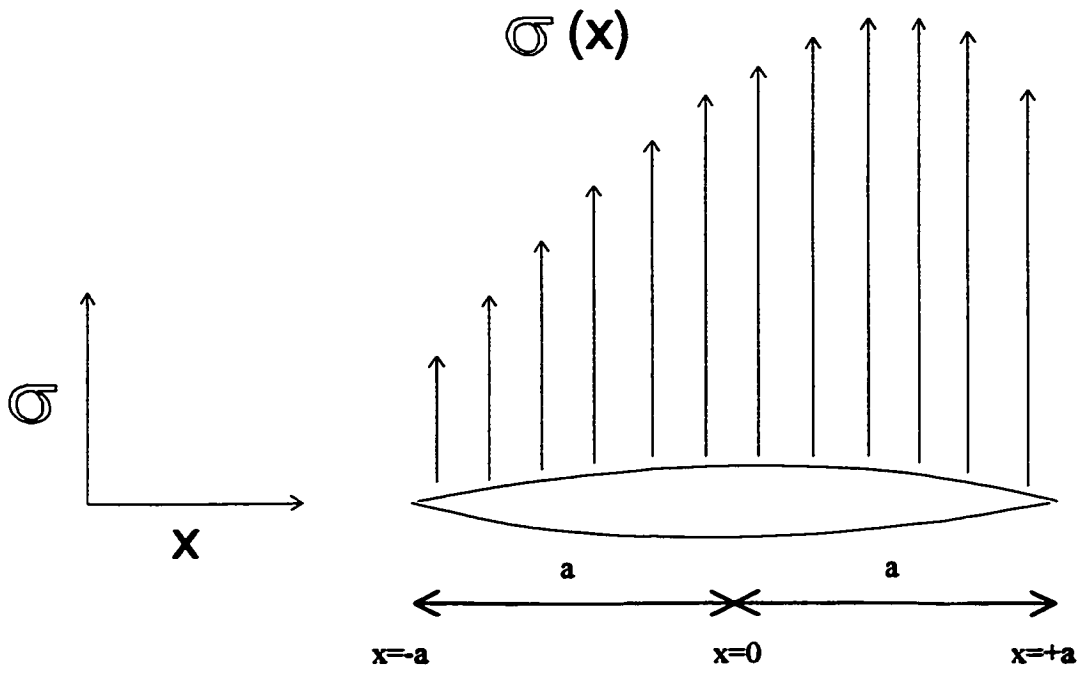

Figure 2.1.6-2. A schematic of a stress concentration solved using a Green integral function. The stress field does not act on the crack face, but represents the stress field that would exist if the crack were not there.

An important feature of the equations is the singularity at the crack tip – theoretically the stress is infinite. This is true only for perfectly sharp cracks, which have infinitesimal crack tip radii. A more realistic minimum crack tip radius is a value comparable to the lattice parameter of the material.

Cook and Gordon (1964) considered the stresses near an elliptical hole in an infinite plate, to calculate more realistic maximum stresses in the region of the crack tip. Their work was similar to that of Inglis (1913), but used the complex mathematical forms developed by others. They found a more realistic stress concentration at the crack tip is ~200x the applied stress perpendicular to the crack plane (σ_{yy}). The stress parallel to the crack plane (σ_{xx}) was found to be ~40x the applied stress, with a maximum just ahead of the crack tip. This suggested a hypothetical interface, perpendicular to the crack plane, would itself also crack provided the interfacial toughness was less than ~20% that of the bulk material. If a brittle material could be designed consisting of weak interfaces, there may be crack deflecting capabilities and nominal toughening. This was not experimentally verified. The effect of the size of flaws in the interface was not considered.

2.1.7 Crack Deflection

The work of Cook and Gordon (1964) suggested crack deflection and nominal toughening could be achieved by designing a material to crack in "non-

catastrophic" directions. The ability to prevent cracks from propagating directly through brittle materials has long been sought as a toughening strategy. Increased crack deflection leads to a larger fracture area, which means an increased work-of-fracture.

A crack always propagates such as to maximize the strain energy release rate from the material (Nuismer, 1973). Of the three modes of loading, mode I fracture releases the most strain energy for a given crack growth increment. Cracks will deflect so they propagate primarily in mode I. Mode II loading provides a driving force to turn the crack during mixed-mode propagation. The phase angle (He and Hutchinson, 1989) of a given crack, ψ, indicates the tendency for it to deflect, where;

$$\psi = \tan^{-1}\left(\frac{K_{II}}{K_I}\right) \qquad (2.1.7\text{-}1)$$

Cracks subjected to high shear stress (mode II) are likely to deflect to maximize their strain energy release rate. The source of the shear can be heterogenities in the microstructure, second phase particles, or thermal or elastic mismatch stresses. The shear experienced during four-point bend testing is negligible, so no crack deflection is expected. Cracking of a weak interface as suggested by Cook and Gordon (1964) is not simply *deflection* of the main crack, but *bifurcation*, splitting of the crack along the interface. The terms are often used interchangeably.

Following the work of Cook and Gordon, Kendall (1975) considered the criteria for crack deflection based on energy considerations. The calculations predicted crack deflection along an interface provided that;

$$\frac{G_{int,C}}{G_{bulk,C}} < \frac{1}{4\pi\left(1-\nu^2\right)} \qquad (2.1.7\text{-}2)$$

where the *G*'s are the critical strain energy release rates for the interface and bulk materials. This requirement is more restrictive than other predictions. The theoretical work was verified by testing crack deflection in brittle rubber laminates. In addition, it was experimentally shown the crack propagation speed influences the toughness of both the interface and bulk material, and the deflection behaviour. Slower cracks were more easily deflected.

He and Hutchinson (1989a) predicted the criteria for the deflection of a crack at an interface between two solids with dissimilar elastic properties. They considered several cases; cracks perpendicular or at an angle to the interface, cracks propagating along or across the interface, and the effect of the difference in elastic properties of the two materials. Complex solutions to the Airy stress function were used to calculate the change in strain energy with either crack deflection or penetration of the material across the interface.

The general result is that cracks are more likely to deflect along an interface if they approach it at an angle, the interface is considerably less tough than the bulk material, and/or the material across the interface is stiffer than the material containing the original crack. Kendall also noted the latter point.

He and Hutchinson (1989, I) used their calculations to "map" the expected crack path, as a function of elastic modulus difference and interface toughness/material toughness ratio. The difference in elastic moduli is usually quoted using the Dundurs' parameter (Dundurs, 1969), which is a normalized value;

$$\alpha_D = \frac{E_1' - E_2'}{E_1' + E_2'} \qquad (2.1.7\text{-}3)$$

where α_D (or simply α) is the parameter, *1* denotes the material across the interface, and *2* the material containing the crack. A positive Dundurs' parameter indicates a crack crossing an interface into a stiffer material (Figure 2.1.7-1). A negative parameter indicates a crack approaching a more compliant material. The interface toughness (G_i/G_p) is the ratio of the critical strain energy release rate of the interface (crack deflection) divided by the critical strain energy release rate of material 1 (crack penetration).

Figure 2.1.7-2 was developed to predict the deflection behaviour of a crack in material *2*, perpendicular to the interface. It is a plot of the interfacial toughness ratio as a function of the Dundurs' parameter. The curves in the figure represent critical interface toughness ratios for crack deflection as a function of the modulus difference. If the interface toughness is high (represented by the region above the curves), penetration of the crack across the interface is predicted. If the interface toughness is low (represented by the region below the

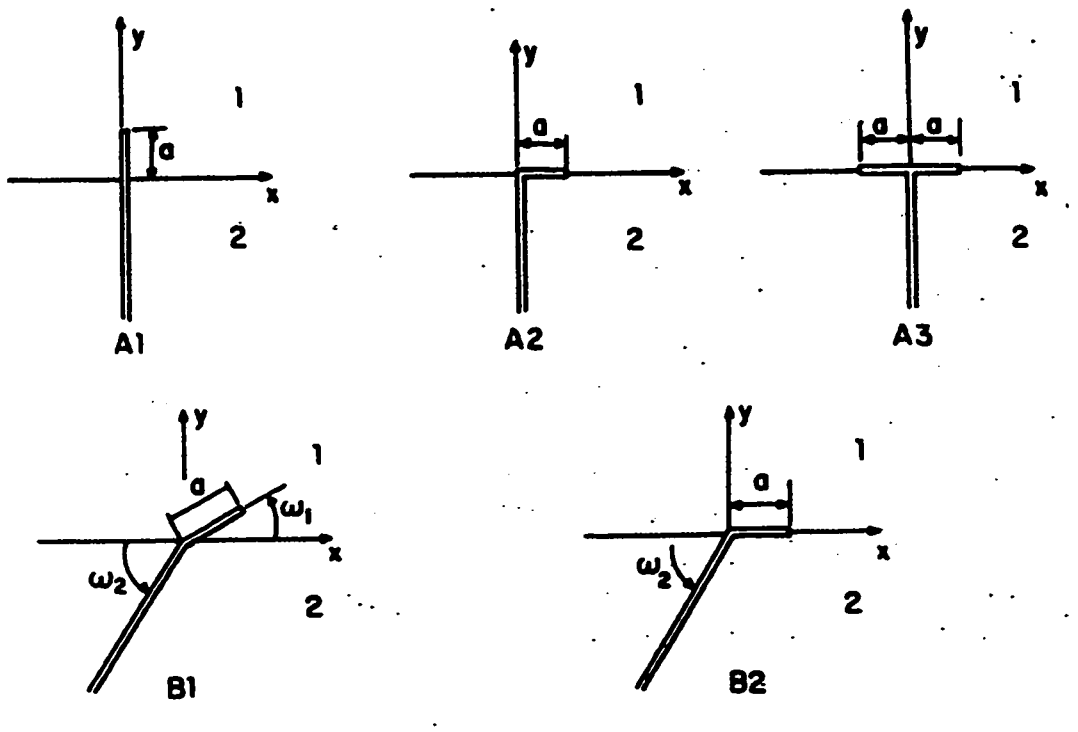

Figure 2.1.7-1. A schematic of the crack geometries used for the crack path predictions (He and Hutchinson, 1989a). A1: straight crack penetrating interface, A2: straight crack singly deflected, A3: straight crack doubly deflected (bifurcated), B1: angled crack penetrating, B2: angled crack deflecting.

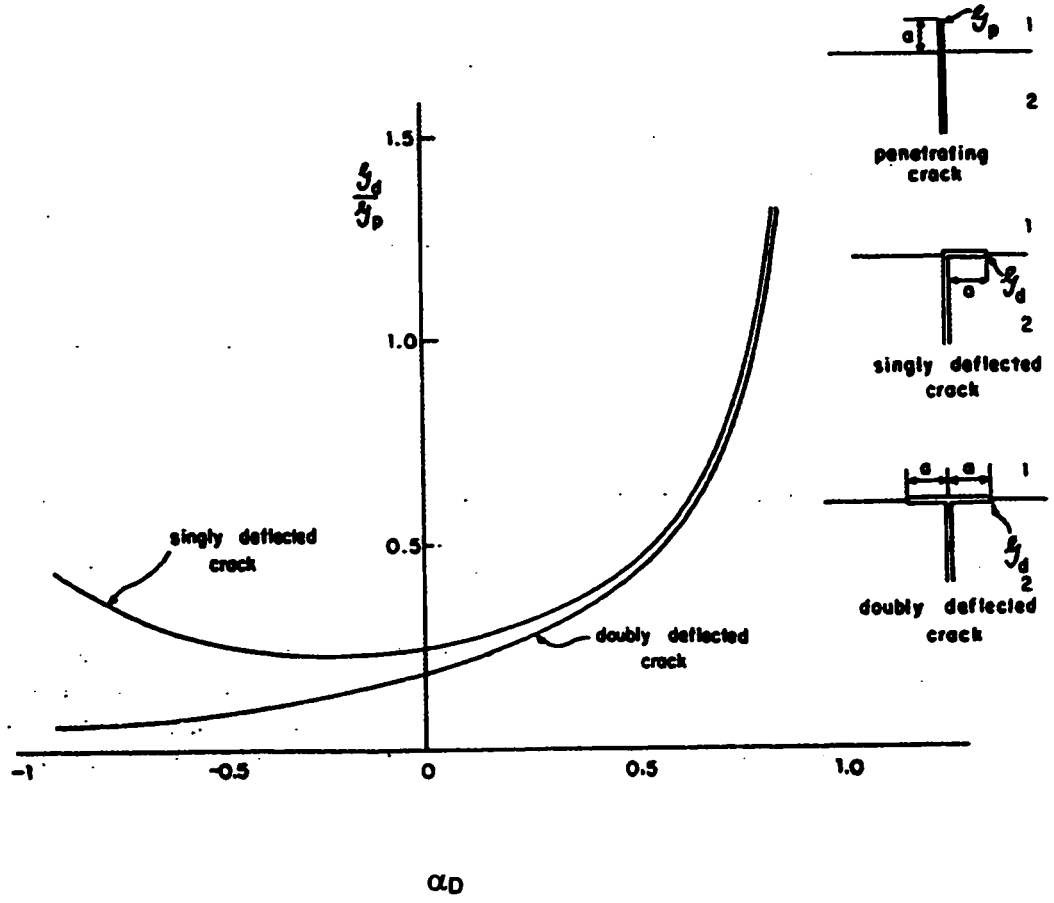

Figure 2.1.7-2. Critical energy release rate ratios as a function of Dundurs' parameter (He and Hutchinson, 1989a). Critical curves for both singly and doubly deflected cracks, and the crack geometries of interest are given.

curves), deflection is predicted. The difference in elastic properties has an effect on the deflection criterion.

If one considers the situation of a crack perpendicular to a weak interface between two equivalent elastic solids, the deflection criteria is similar to that determined by Cook and Gordon (1964). They predicted a critical interfacial toughness of ~20% that of the bulk material toughness was required for deflection.

He et al (1994) further modified the work to consider the effect of thermal residual stresses on the deflection criteria. They used the same approach as He and Hutchinson (1989a), but a thermal residual stress was super-imposed on the solution. Figure 2.1.7-3 is equivalent to Figure 2.1.7-2, but accounts for a thermal residual stress perpendicular to the crack. Again, the upper and lower regions in the figure represent predictions of penetration and deflection respectively. η_t is a non-dimensional parameter used to describe the magnitude of this thermal stress. It is defined as the crack tip stress intensity associated with the thermal stress divided by that associated with the applied stress; a positive value indicates tension, negative compression.

If η_t is negative, the critical curve for deflection is raised. This physically means that a higher interface toughness will still lead to deflection. Cracks are more likely to deflect along interfaces if the material across the interface is subject to a residual thermal compression. The converse is also true. A positive

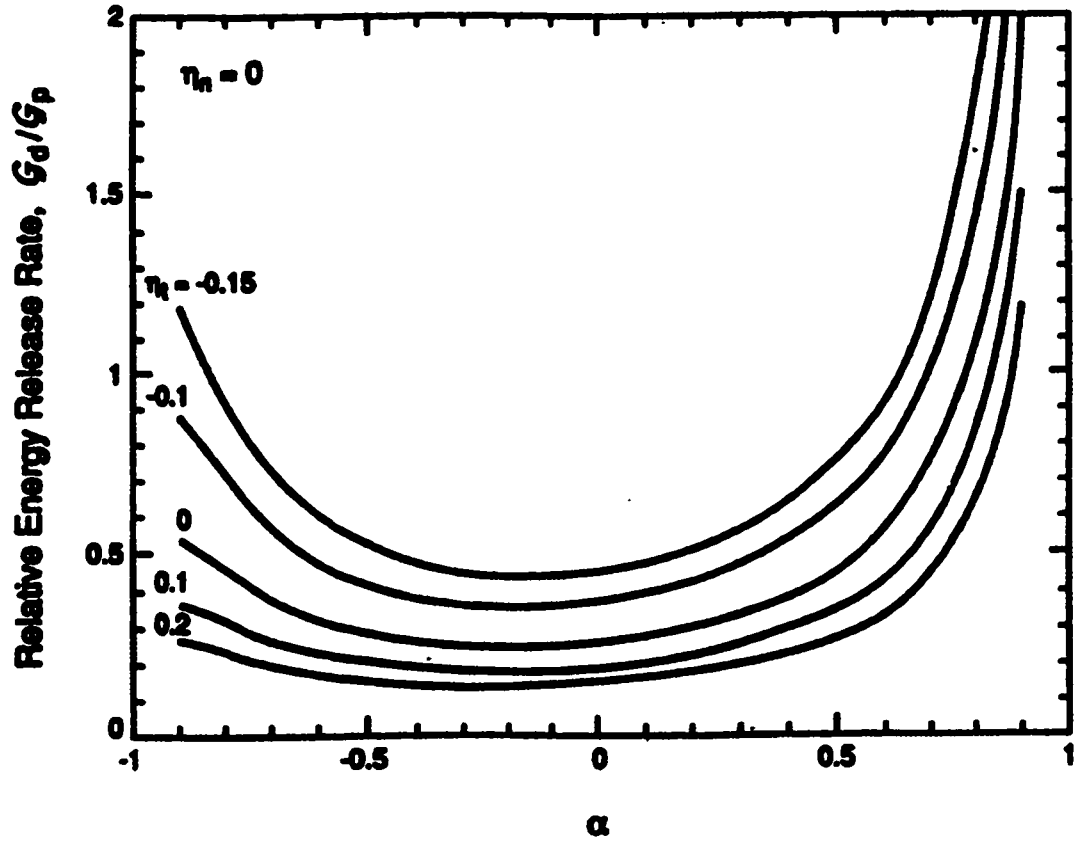

Figure 2.1.7-3. Critical energy release rate ratios as a function of Dundurs' parameter and thermal residual stress (He, Hutchinson and Evans, 1989a). Zero thermal stress perpendicular to the layers is assumed.

η_t lowers the critical curve, so a lower interfacial toughness is necessary for crack deflection.

It is important to note that these criteria assume the crack tip is *at* the interface. A propagating crack has a strain energy release rate above its critical value, and this will affect the predictions. Flaws within the interface, and their effect on main crack deflection, were not considered.

He and Hutchinson (1989b) also considered the requirements for a crack in an interface to deflect back out, and penetrate the second material. Figure 2.1.7-4 is a plot of the minimum material/interface toughness ratio (G_{2i}/G_{0c}) required to prevent a crack from kinking out of an interface (note that in this case the material after the interface is subscripted as "2", and the interface toughness is subscripted as "0"). Deflection out of an interface is more likely if the crack would deflect into a more compliant material, though this is dependent on the phase angle of loading. If the two materials sandwiching the interface are equally stiff, the crack will remain in the interface provided the interface toughness is equal to or less than ~1/2 that of the bulk material. Given that this is higher than the interfacial toughness required to deflect a crack into an interface, it is likely the crack will not kink out.

Mammoli et al (1995) considered a crack approaching an interface containing a flaw (Figure 2.1.7-5). They used a similar mathematical approach to He and Hutchinson (1989, a and b) and He et al (1994). The presence of flaws enhances the likelihood of crack deflection toward the interface, provided the

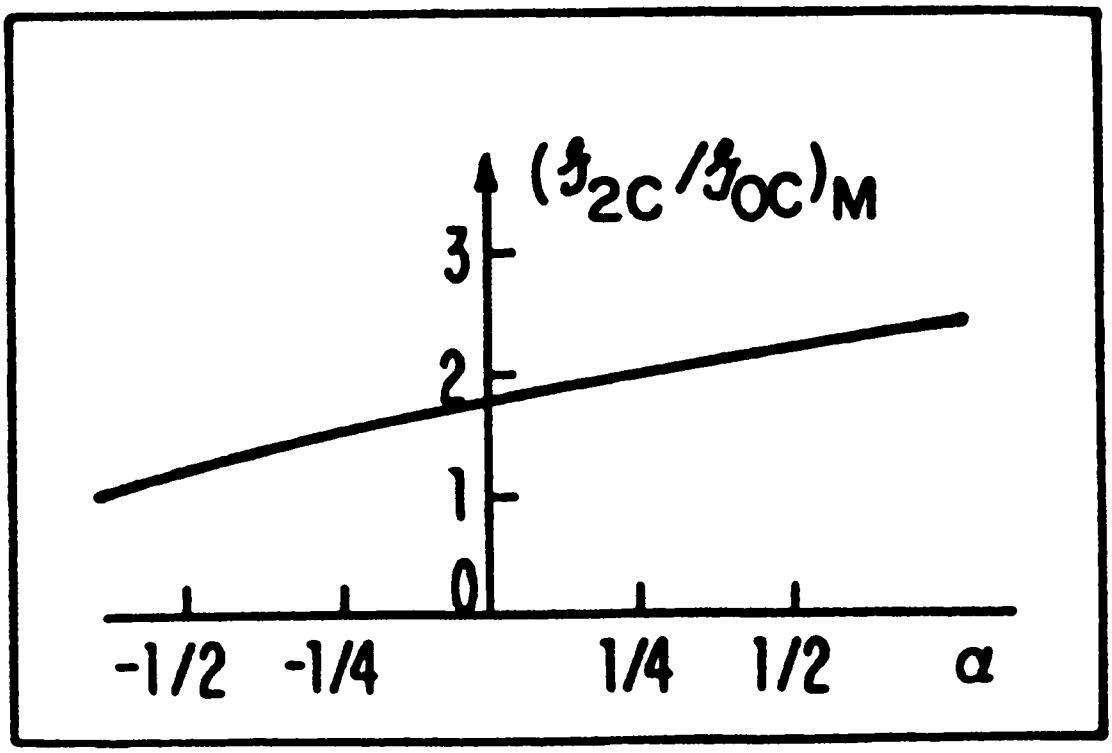

Figure 2.1.7-4. A plot of the minimum material/interface toughness ratio required to prevent a crack from kinking out of an interface, as a function of Dundurs' parameter. The toughness ratio refers to the material which the crack kinks into (material 2) and the interface. The upper region predicts interface fracture, the lower region predicts kinking out of the interface (He and Hutchinson, 1989b).

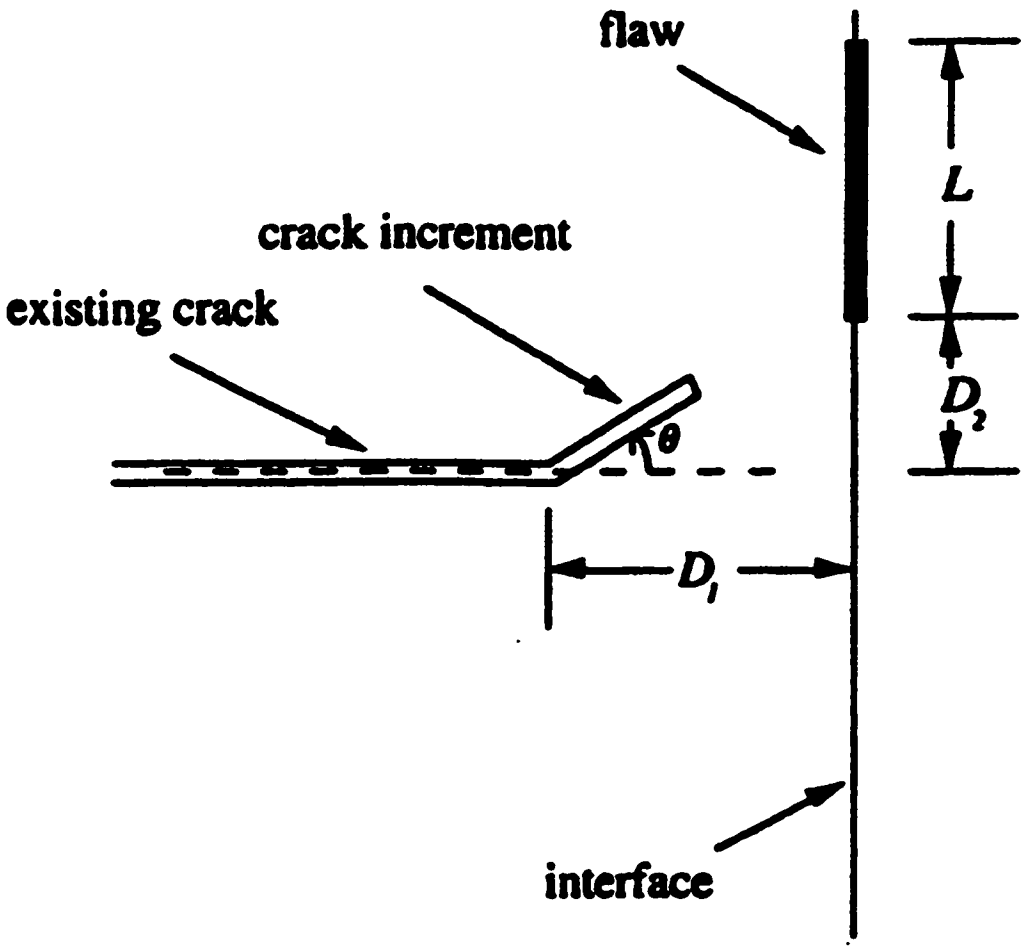

Figure 2.1.7-5. A schematic of the crack geometry used to calculate the effect of an interface flaw on a crack path (Mammoli et al, 1995). No modulus difference is included.

main and interface cracks are close. This is due to the interaction of crack tip stress fields, which result in shear. If the main crack is drawn into the interface, the loading mode changes from mode I to mixed modes I and II. This may lead to deflection back out of the interface if its toughness is moderate.

2.1.8 Delamination Testing

The ratio of the interface toughness to bulk material toughness is important in determining the propensity of the interface to crack. Bend or indentation testing can be used to calculate the toughness of the bulk material, as described in Sections 2.1.4 and 2.1.5. Calculation of the interface toughness requires other techniques.

Charalambides et al (1989) developed a technique for determining the interfacial toughness of a bilayer composite. The method involves bending a specimen that has had the layer on the tensile bend side cut through to the interface (see Figure 2.1.8-1). The sample is loaded in four-point bending. At some point during the loading the interface opens and the tensile layer delaminates, provided the interface is weak enough. The interface cracks under steady-state conditions due to the loading geometry (similar to the Obriemoff experiment discussed earlier). The load at which the delamination occurs can be determined from the load-displacement curve (see Figure 2.1.8-2). This load, the geometry of the sample, and the material properties of the two layers, can be

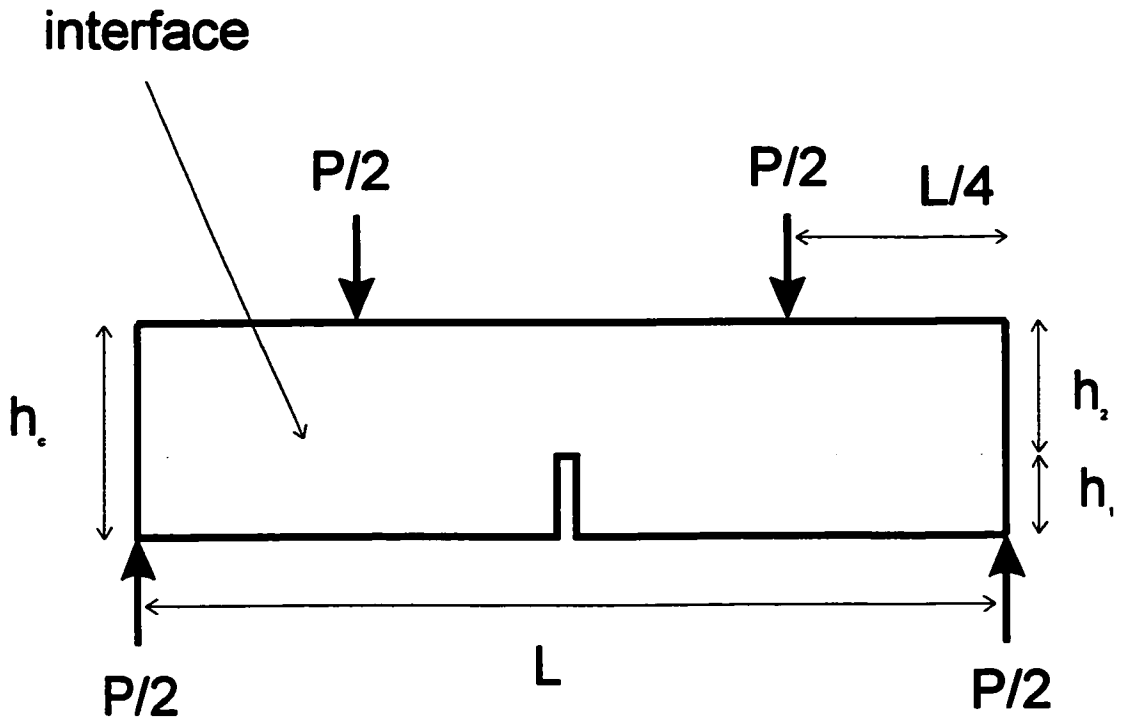

Figure 2.1.8-1. A schematic of the bilayer specimen geometry used in the Charalambides delamination test. The cut layer is material 1, the intact layer material 2.

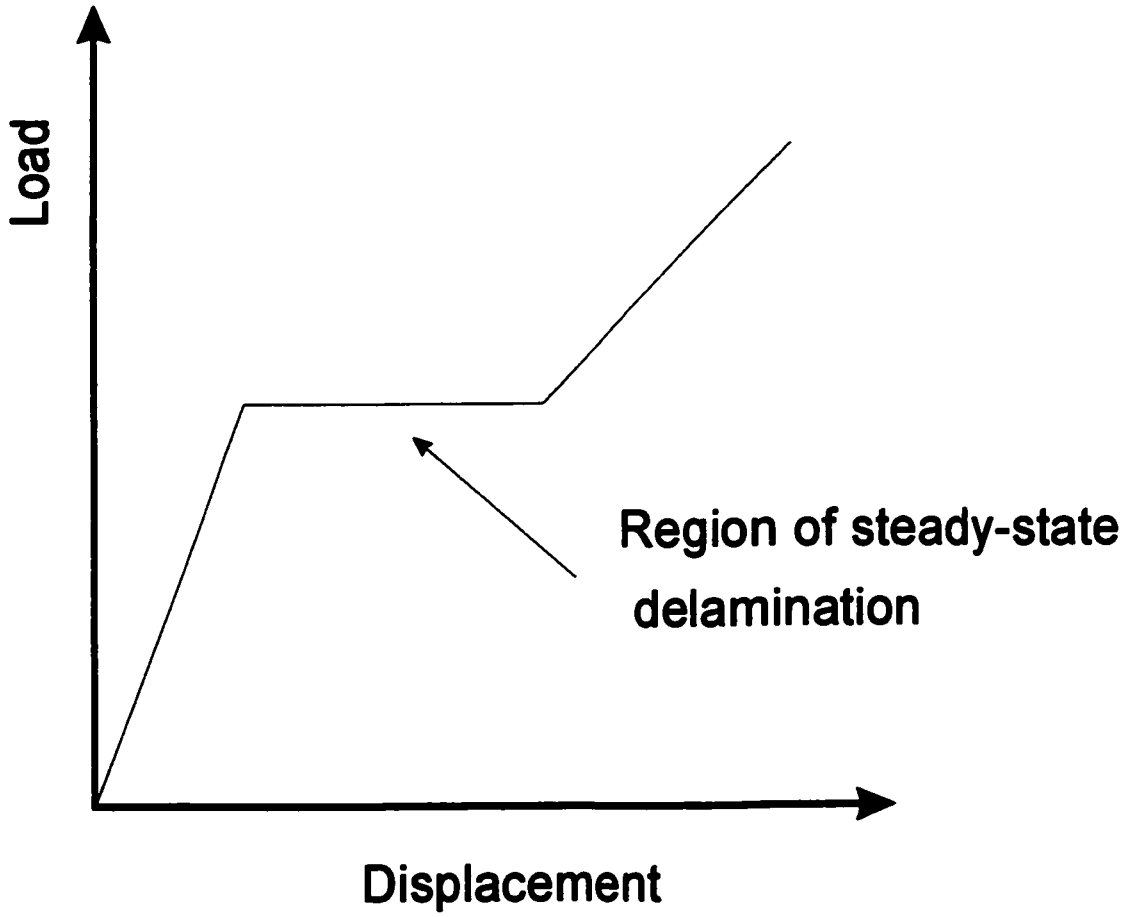

Figure 2.1.8-2. A schematic of a load-displacement curve from a Charalambides delamination test.

used to calculate the interfacial toughness;

$$G_{ss} = \frac{M^2(1-\nu_2^2)}{2E_2}\left(\frac{1}{I_2} - \frac{\lambda}{I_c}\right) \qquad (2.1.8\text{-}1)$$

where G_{ss} is the steady-state strain energy release rate, M the applied moment, E_2 and ν_2 the elastic properties of the second layer (intact layer), and I_2 and I_c the second moment of area of the second layer and total bilayer respectively. The λ is a term that represents the difference in elastic properties of the two materials in the bilayer;

$$\lambda = \frac{E_2(1-\nu_1^2)}{E_1(1-\nu_2^2)} \qquad (2.1.8\text{-}2)$$

In the case of two layers of the same material sandwiching a weak interface, $\lambda=1$.

The work was supported by finite element analysis. Eight-noded isoparametric elements were used, with sufficient crack tip mesh refinement to estimate stress intensity factors and displacement changes during crack propagation (Figure 2.1.8-3). The results were consistent with experimental measurements taken during delamination testing of aluminum/PMMA bilayers (Figure 2.1.8-4). A value of K_c~0.26(±0.01)MPa$\sqrt{m}$ was determined for the composite interface, which is similar to the value of K_C~0.4MPa$\sqrt{m}$ determined by Hardwick et al (1986). The difference can be attributed to the bonding procedures used by the two groups. There may also be an influence due to the phase angles of the techniques. The Charalambides delamination test involves a

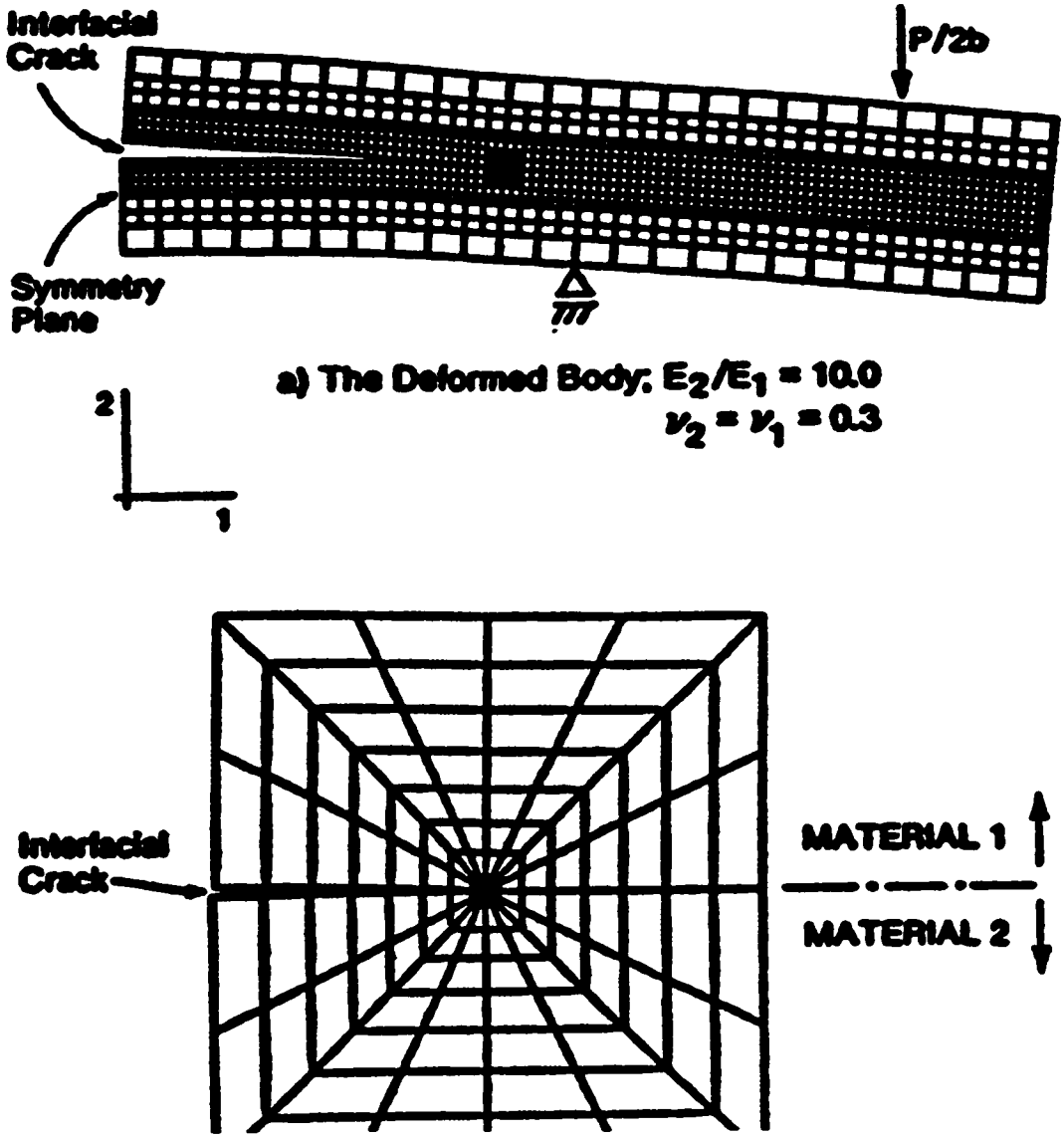

Figure 2.1.8-3. A schematic of the mesh used by Charalambides et al for their finite element analysis (Charalambides et al, 1989). The lower mesh is a magnification of the crack tip region in the upper mesh.

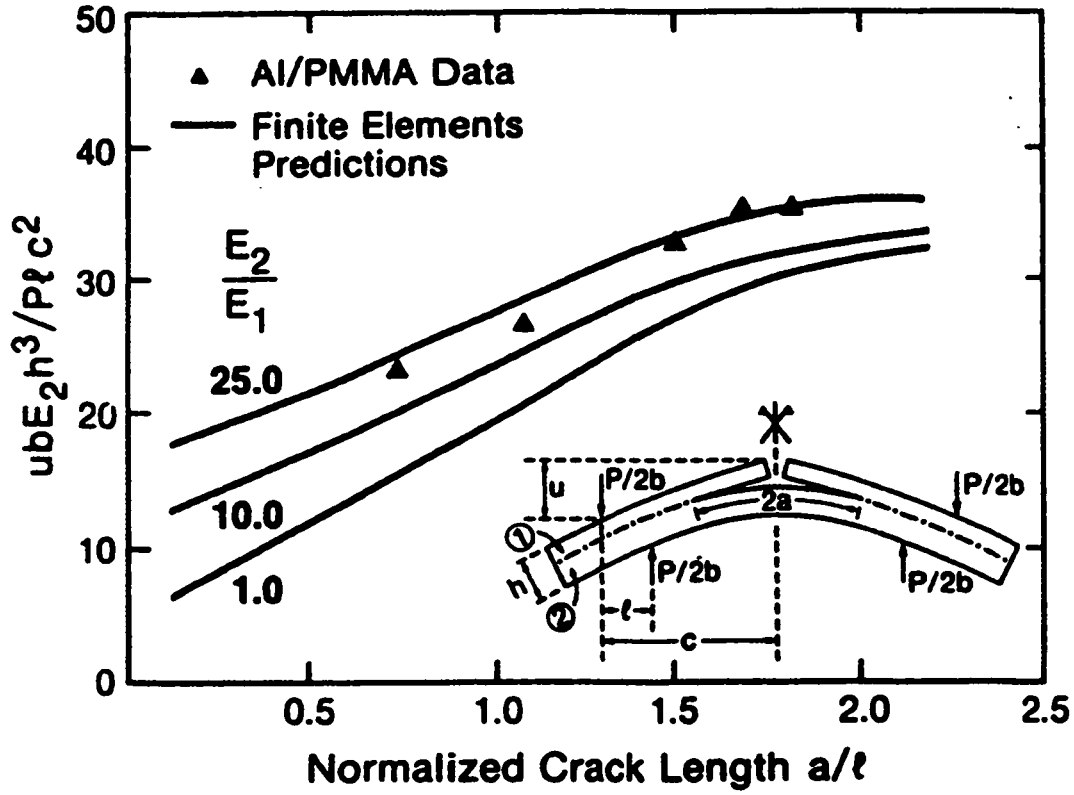

Figure 2.1.8-4. Experimental and finite element results of Charalambides et al (1989). The vertical axis is normalized vertical displacement term.

phase angle of 40-50° acting on the interfacial crack, that is, there is a shear component.

2.1.9 Thermal Shock

Up to this point, it has been assumed that ceramics fracture only as a result of an applied load. Stresses can also be generated by thermal gradients in the material caused by quenching. If the gradient in the material is high enough, crack propagation and fracture can result. This "thermal shock" is a serious problem for ceramics in many applications, so is an important parameter in material selection.

Thermal shock is the result of both a rapid drop in temperature and a low thermal conductivity. The surface of the material attempts to contract during the quench due to its thermal expansion coefficient. The low thermal conductivity leads to a high strain gradient in the material, and therefore also a high stress gradient. A high tensile stress may cause propagation of surface cracks into the material. Unlike the fractures discussed earlier, the crack propagation may not be catastrophic. The stress on the crack tip reduces as the crack propagates, and the stress intensity may drop below the critical stress intensity for the material.

Although the thermal shock may not fracture the material, the increased crack size weakens material. Materials show no change in strength for small

changes in temperature, as the stresses that develop during cooling are insufficient to cause crack propagation. As the temperature changes are increased, the stresses also increase. It is possible to define a critical temperature drop that results in crack propagation and a significant weakening of the material. This provides a parameter that can be used to compare the relative thermal shock resistance of materials (Hasselman, 1969);

$$\Re = \Delta T_c = \frac{\sigma_f (1-\nu)}{\alpha E} \qquad (2.1.9\text{-}1)$$

where $\Re$ is the thermal shock resistance, ΔT_c the temperature change, and α the thermal expansion coefficient. Thermal shock provides a technique to introduce large cracks into ceramic specimens.

2.2 Laminated Composites

Various toughening strategies involve the use of composites, which are materials made up of two or more materials with different properties. The choice of materials and their configuration affect performance. Differences in strengths, moduli and thermal expansion coefficients can be exploited to maximize the overall mechanical properties. Many researchers have shown crack deflection, and therefore toughening, is possible. Architectures available in composite design include spherical, whisker, or platelet particle reinforcement, uniaxial fibre or weave reinforcement, and laminates. Each structure can provide improvement of different mechanical properties.

Laminates are the focus of this work. They consist of alternating layers of two or more materials. The properties of the materials chosen and the thickness of the layers will affect the composite performance. The laminate structure has specifically been shown to improve flexural properties.

Many researchers have shown that improvements in toughness are possible. In some cases the interfaces between the layers are strong, and improvements are made via crack deflection due to differences in elastic or thermal properties. In some cases the interfaces are weak, and improvements are made by sacrificing one layer in the laminate for the good of the remaining layers. Both cases can lead to an increased work-of-fracture.

The work-of-fracture is a measure of the total energy required to fracture a material, normalized to the *nominal* cross-sectional area of the sample. It is determined by calculating the total area under a load-displacement curve, and dividing by the measured cross-sectional area of the sample. When crack deflection is used to toughen a material, the increased area of fracture surface may improve the work-of-fracture, but the nominal cross-sectional area remains the same. If a crack is deflected sequentially along several weak interfaces, the work-of-fracture can improve a hundred-fold (Clegg et al, 1990). The critical stress intensity factor or critical strain energy release rate will not necessarily be affected, and this must also be considered.

An important feature of laminates is the residual thermal stresses that form in the layers during processing. Their magnitudes can be estimated using the elastic and thermal properties of the materials selected. Consider a laminate consisting of alternating layers of material 1 and material 2, as shown in Figure 2.2-1. The composite is processed at high temperature, and then cooled to room temperature. If the interfaces in the composite are strong, the two materials must contract an equal amount during cooling. A difference in their thermal expansion coefficients will lead to residual stresses parallel to the layers. These stresses must satisfy mechanical equilibrium;

$$\sigma_1 t_1 + \sigma_2 t_2 = 0 \qquad (2.2\text{-}1)$$

where the σ's are the average stresses in the two materials and the t's the thickness of each material. Unit width of samples is assumed. If the layers

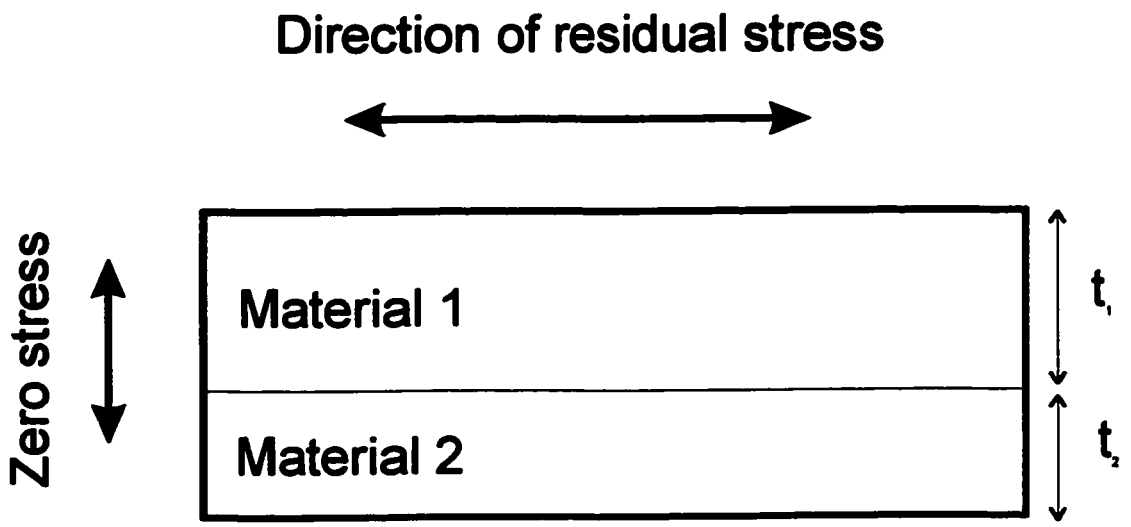

Figure 2.2-1. A schematic of a laminate used for thermal residual stress calculations.

remain strongly bonded at their interfaces, the stresses in the layers must have equivalent strains;

$$\frac{\sigma_1}{E_1'}+\alpha_1\Delta T=\frac{\sigma_2}{E_2'}+\alpha_2\Delta T \qquad (2.2\text{-}2)$$

where the α's are the thermal expansion coefficients of the two materials, and ΔT the temperature change (final minus initial). The primes on the moduli denote that a modified modulus must be used to account for the biaxiality of the stresses in the layers, that is; E'=E/(1-ν). Combining Equations 2.2-1 and 2.2-2 leads to;

$$\sigma_1=\frac{(\alpha_2-\alpha_1)\Delta T}{\frac{1}{E_1'}+\left(\frac{t_1}{t_2}\right)\frac{1}{E_2'}} \qquad (2.2\text{-}3)$$

and;

$$\sigma_2=-\left(\frac{t_1}{t_2}\right)\sigma_1 \qquad (2.2\text{-}4)$$

Note that one of the materials is in tension, the other in compression. This can have a significant effect on the strength of the composite.

2.2.1 Laminates with Strong Interfaces

Whitehead (1994) reported improvements in toughness for room temperature tested alumina/zirconia (TZ3Y) non-planar laminates. The composites consisted of alternating thick (~10μm) alumina layers and thin (~3μm) zirconia layers. No significant change in strength was reported. The

toughness was K_C= 4.57(±0.73) MPa$\sqrt{m}$, a 57% increase over monolithic alumina. In this case a chevron notch bend test was used, which makes comparisons to other work difficult.

Prakash et al (1995) tested composites consisting of both 95% zirconia (TZ3Y)+5% alumina, and 95% alumina +5% zirconia. The strength of zirconia increased from 950MPa to 995MPa on addition of thin alumina layers. The strength of the alumina decreased from 556MPa to 488MPa. Errors were not reported. The thermal expansion coefficients of alumina and zirconia are ~8μ/°C and ~11μ/°C respectively. The result (using 2.2-3 and 2.2-4) is thermal residual tension in the zirconia and compression in the alumina. The changes in strength are contrary to expectations, though this result was not discussed. Significant crack deflection at the interfaces was shown by fractography, but changes of the calculated work-of-fracture were not reported.

A similar series of experiments was performed by Huang et al (1997) on silicon nitride/titanium nitride laminates. The flexural strength of monolithic silicon nitride was increased from ~730MPa to ~960MPa by adding alternating layers of silicon nitride and a silicon nitride/titanium nitride mixture, though this was dependent on the number of layers in the laminate (Figure 2.2.1-1). The thermal expansion coefficients of silicon nitride and titanium nitride were quoted as 3μ/°C and 8μ/°C respectively. Compressive thermal residual stress in the surface silicon nitride layers lead to an increase in strength, though an increased number of layers in the composite lead to high tension in the mixed layers, which initiated

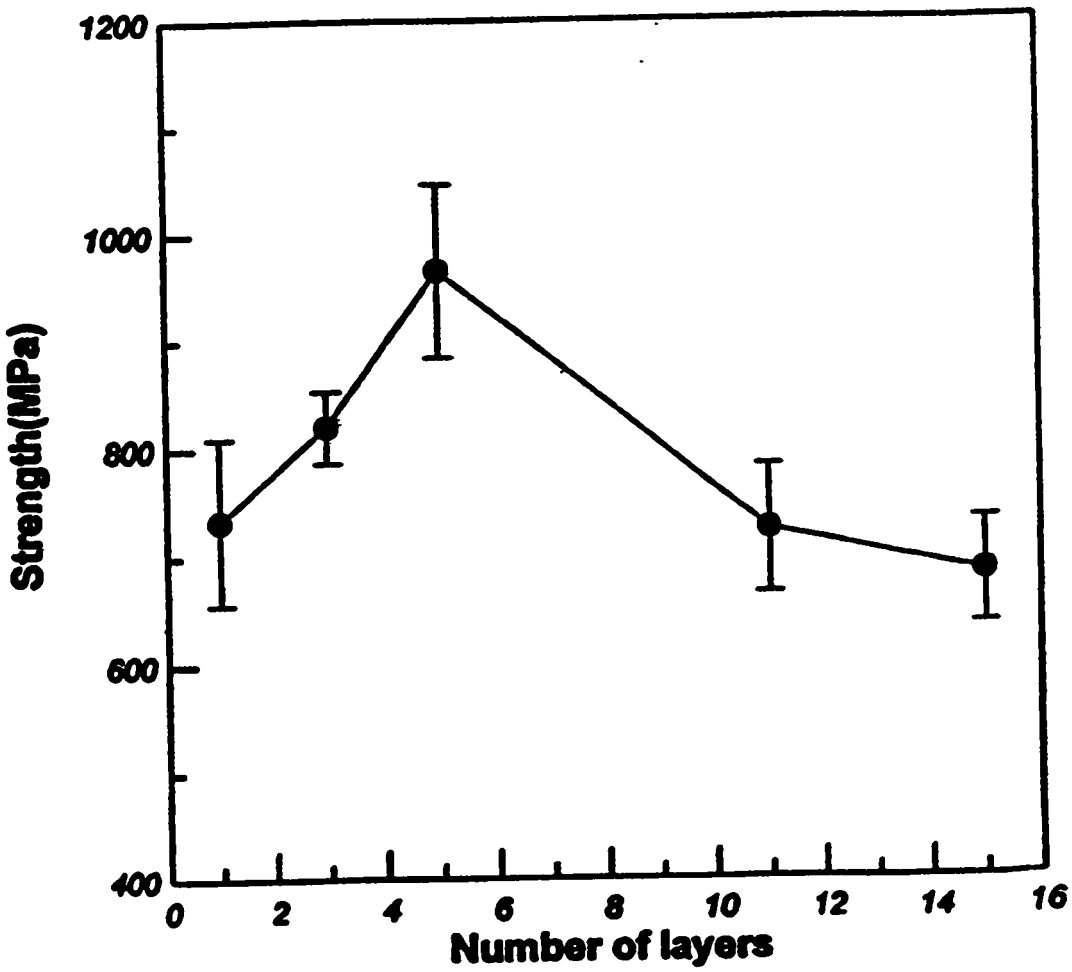

Figure 2.2.1-1. The flexural strength of silicon nitride/titanium nitride composites as a function of number of layers (Huang et al, 1997).

fracture at internal flaws. Similarly, fracture toughness increased (Figure 2.2.1-2), though this was also dependent on the number of layers in the laminate.

Significant crack deflection was observed as cracks propagated across interfaces. Thermal residual shear stresses at the interface would cause crack deflection, though this was not discussed. The relationship between the indent depth and layer thickness, and its effect on the crack propagation, was not considered. If the depth of the indent crack was comparable to the layer thickness, there may have been deflection or blunting of the crack prior to bend testing. This would influence the fracture behaviour and/or the strength.

Although these examples showed improvements in the calculated critical stress intensity factors, all samples suffered catastrophic failure. The nominal increase in toughness can be attributed to an increase in strength caused by thermal residual compression in the surface layers. The fracture toughness of the material was not changed, only the stress state surrounding critical flaws. The increases in calculated toughness do not prevent the possibility the material will fail catastrophically in service.

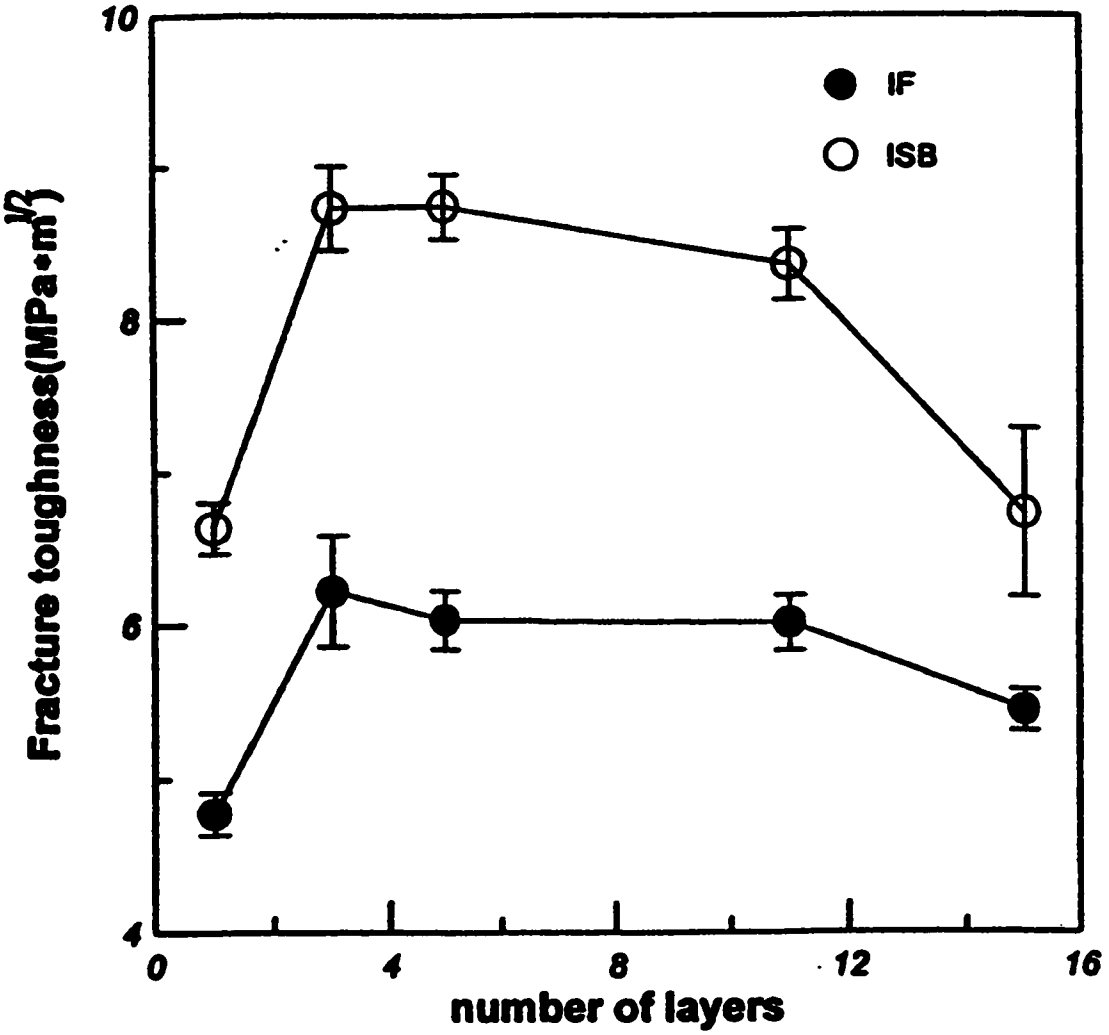

Figure 2.2.1-2. The fracture toughness of silicon nitride/titanium nitride composites as a function of number of layers (Huang et al, 1997). IF: indentation fracture (crack length) method, ISB: indentation strength in bending method.

2.2.2 Laminates with Weak Interfaces

The mechanical properties of composites containing weak interfaces are significantly different to those with strong ones. The strategy is not to increase the critical stress intensity factor for the material, but to prevent fatal failure in service. Significant increases in the work-of-fracture are also possible.

Consider a ceramic laminate consisting of alternating strong layers and weak interfaces subjected to a bend test (see Figure 2.2.2-1). At some point during the loading the stress in the tensile surface exceeds the fracture strength of the strong material, and the *layer* fails catastrophically. If the interface is weak enough, the propagating crack deflects along it. The deflection absorbs energy, lowers the load experienced by the sample, and allows the remaining portion of the beam to continue to support load. In effect, the surface layer is sacrificed to save the rest of the beam. Continued loading causes the next strong layer to fracture and the cycle repeats. This strategy provides a "safety net" for the material in service.

The improvement in the work-of-fracture of these composites is apparent in their load-displacement curves. The fracture of sequential layers leads to an instantaneous increase in compliance of the beam and a corresponding load drop. The result is a "zig-zag" reduction in the load rather than a catastrophic drop (see Figure 2.2.2-2). This type of failure is often referred to as "graceful" failure. In this work it will be referred to as "multi-stage" failure.

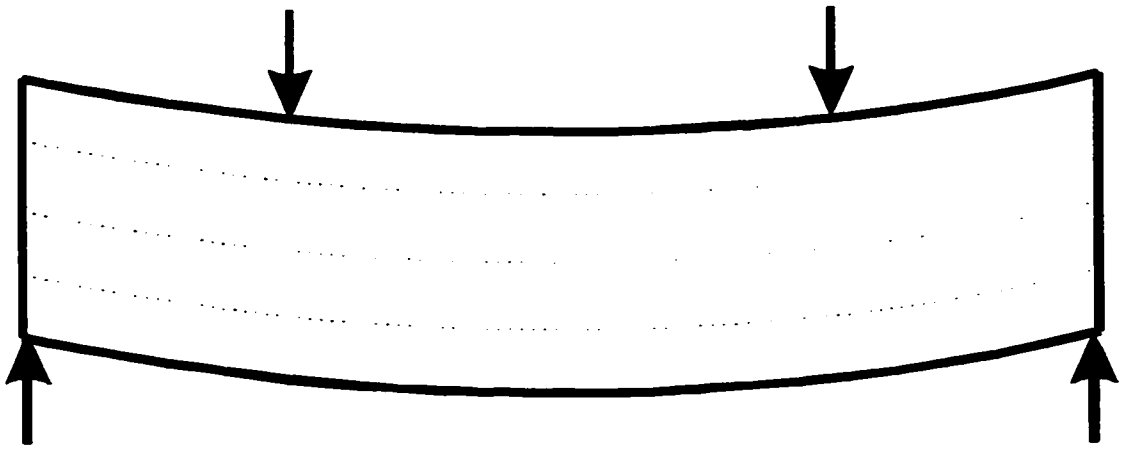

Figure 2.2.2-1. A schematic of a laminate containing weak interlayers (shown by dotted lines) subjected to a bend test. Loading (shown by the arrows) is perpendicular to the layers.

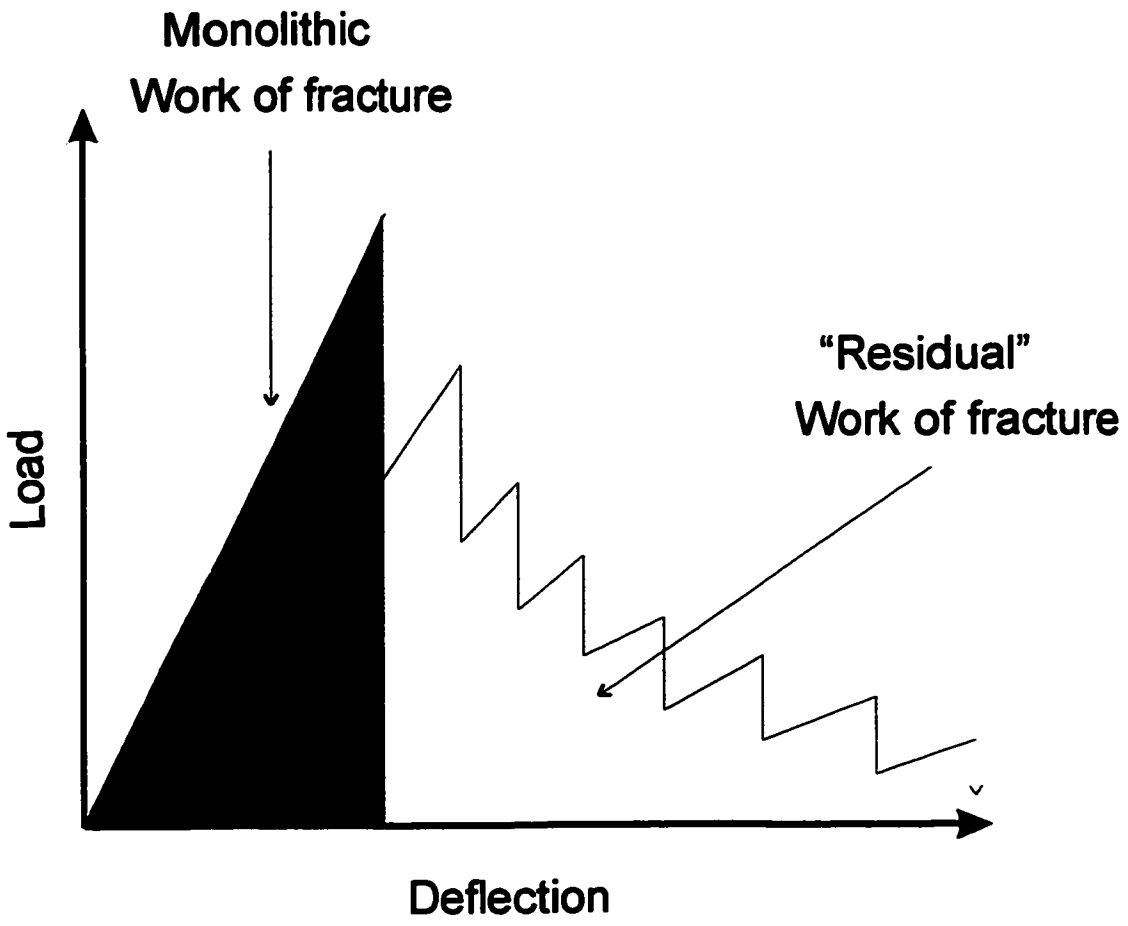

Figure 2.2.2-2. A schematic of a load –displacement curve for a brittle laminate containing weak interfaces showing multi-stage failure. The shaded region represents the work-of-fracture for a monolithic brittle material. The residual work-of-fracture is available only through crack deflection along several weak interfaces.

The technique of weak interface toughening does not work under all conditions. The stress on the beam must drop as the surface layer fractures. If the test is done under displacement controlled conditions, the compliance of the beam increases and the load decreases. The load drop reduces the stress on the remaining portion of the beam to below the strength of the material. If the test is done under load controlled conditions, the displacement of the loading pins is increased to offset the increasing compliance and maintain load. The remaining portion of the beam can not withstand the same load as the full beam, so it continues to fail catastrophically. Fracture initiated by either impact or thermal shock is similar to displacement controlled conditions. This would allow the strategy to take effect.

Composites can be designed consisting of alternating strong and weak layers. The interfaces between the two types of layers are strong, but crack deflection *within* the weak layers is possible due their low toughness and/or large inherent flaws. In this case, the composite consists of weak *interlayers* rather than weak interfaces. The analysis is the same, so the terms can be used interchangeably. The reasons for this will be discussed later.

Weak interlayer toughening was first reported by Clegg et al (1990). Silicon carbide sheets, ~200μm thick, were coated in graphite and stacked to form green bodies ~2mm thick. The samples were sintered under argon to 98% theoretical density. Non-graphite coated sheets were also used, to produce

monolithic silicon carbide samples for comparison. The samples were cut into bend bars and three-point bend tested to *complete* failure.

The strength of the composites was 633MPa, an increase over the 500MPa strength of the monoliths. Errors were not included. The strength increase was not explained.

Notched specimens were used to compare the toughness of the monolith and composite. The toughness of the monolith was 3.6 MPa$\sqrt{m}$, and that of the composite 15 MPa$\sqrt{m}$. The monolithic sample failed catastrophically, whereas the composite exhibited multi-stage fracture behaviour (Figure 2.2.2-3).

The apparent improvement in toughness was due to geometry rather than an improvement in the material properties. In the composite sample, a notch cut to the depth of one of the interfaces allowed the graphite layer to crack preferentially. The deflection of the (notch) crack along the interlayer effectively eliminated the notch. Fracture of the remaining portion of the beam then initiated at a natural flaw in the "next" silicon carbide layer. The toughness was calculated using Equation 2.1.2-13. The crack size used in the calculation was that of the notch, but the strength used was due to a natural flaw. The calculated toughness value is therefore notch size dependent.

The major improvement in the properties reported was the work-of-fracture. The energy absorbed during fracture of the monolithic samples was 62J/m^2, while that of the composites was 4625J/m^2. The load-deflection curves

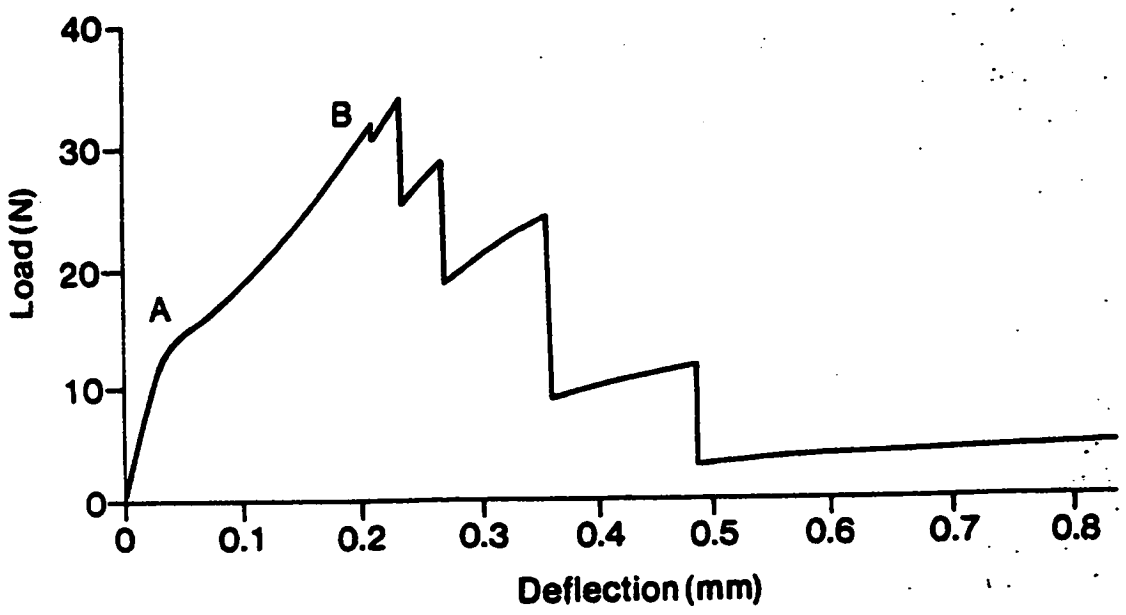

Figure 2.2.2-3. Multi-stage fracture behaviour in silicon carbide/graphite composites (Clegg et al, 1990). The compliance change at *A* is due to delamination of the notched, tensile surface layer. Catastrophic failure of the first (intact) strong layer occurs at *B*, followed by alternating crack deflection along weak interlayers and catastrophic failure of strong layers.

showed multiple non-catastrophic load drops. This result lead to further work by other researchers.

The phenomenon of weak interface toughening was first modeled by Phillipps et al (1993a). They developed a numerical model to predict the mechanical properties of these composites, based on the properties of their constituents. The parameters of interest were the critical strain energy release rates of the strong material and weak interface, the total work of fracture for the composite, the work of fracture associated with interfacial surface energy, the strength and modulus of the strong material, and the geometry of the bend tests.

The model (Figure 2.2.2-4) was designed to evaluate the compliance of a hypothetical composite beam for a given applied displacement. It was assumed the tensile surface layer failed catastrophically. The possibility of subsequent bulk or interfacial fracture was then predicted based on competing strain energy release rates. A Monte Carlo method was used to account for the varying strengths of layers. Iteration of the computer program allowed the work-of-fracture to be calculated for a given set of material properties and sample geometry. The model program was run for a variety of material property combinations. Comparisons were done to optimize the work-of-fracture.

The work provided several insights into the mechanical behaviour of this type of composite. Iteration of the model suggested increasing the layer strength, and decreasing the layer thickness and interfacial toughness could

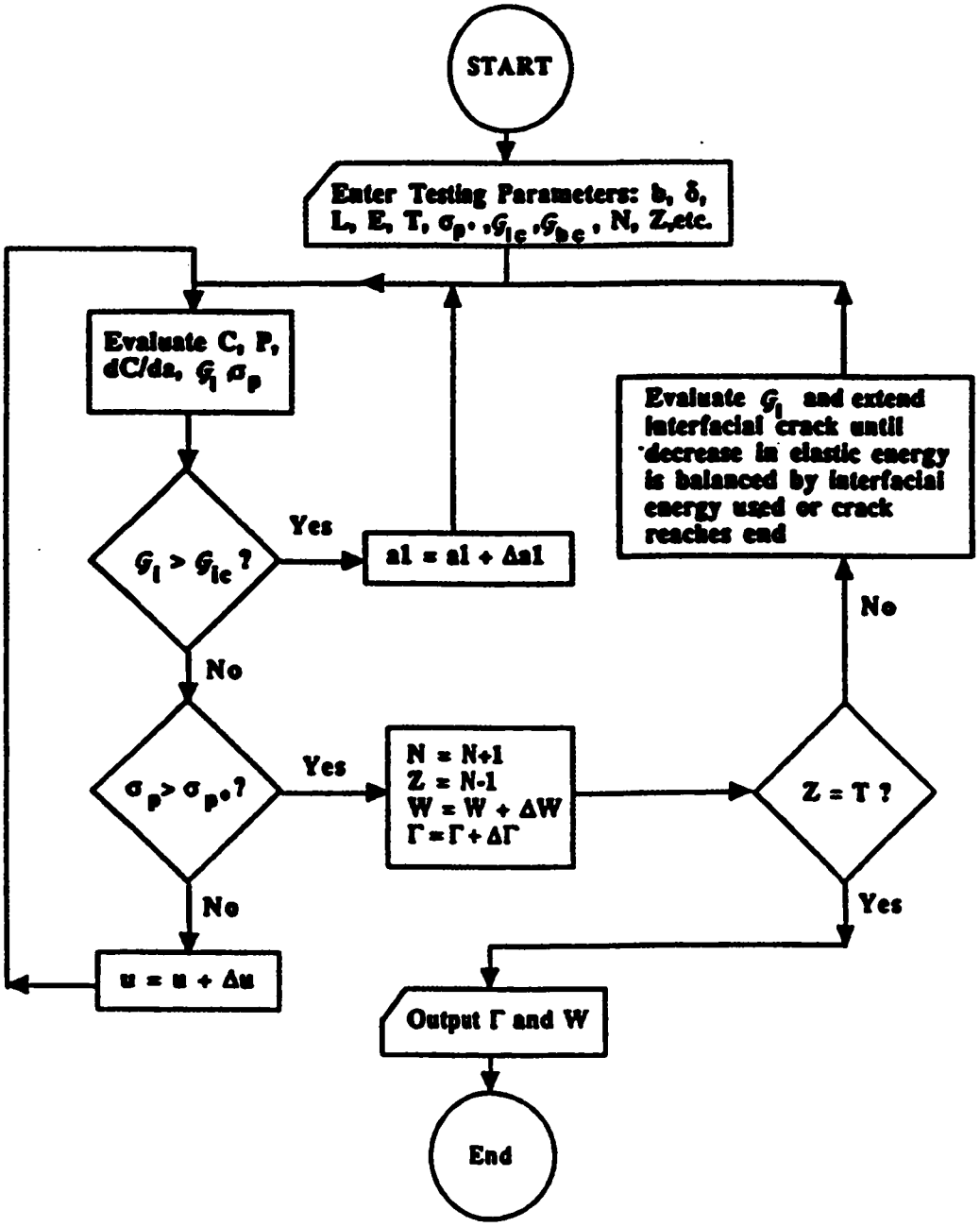

Figure 2.2.2-4. The algorithm implemented in the numerical model (Phillipps et al, 1993a). *a* is interfacial crack size, *C* compliance, *N* total number of strong layers, u vertical displacement, *W* total work of fracture per unit volume, *Z* number of interfacial cracks, Γ interfacial work and σ_p failure stress.

maximize the work of fracture. The work was also found to be inversely proportional the modulus of the strong material.

The model was experimentally verified by Phillipps et al (1993b) using silicon carbide/graphite laminates. The flexural fracture behaviour of the composite showed good agreement with that predicted by the model (Figure 2.2.2-5). The experimental work of fracture of 146kJ/m^3 for a given laminate was in close agreement with the numerically-predicted value of 150kJ/m^3.

The model did not account for cracking of the interfaces before complete fracture of the tensile surface layers. The stress concentrations associated with crack propagation in the strong layers will later be shown to influence propagation of the interfacial cracks.

Folsom et al (1996a) reported similar modeling work. They predicted composite stress-strain responses for both tensile and flexural tests. For the flexural test calculations, it was assumed strong layers that failed supported *zero* load. This tacitly assumes that the interface toughness is zero, which is unrealistic, but provides the simplifications necessary to make initial predictions.

Classical beam equations were used to plot two loci; one of the expected stress-strain relationship prior to fracture of sequential layers of the laminate, and one after fracture of each layer. They assumed an instantaneous increase in compliance during fracture at constant displacement, then continued bending until all layers had failed. The result is a "zig-zag" curve that oscillates between the two loci.

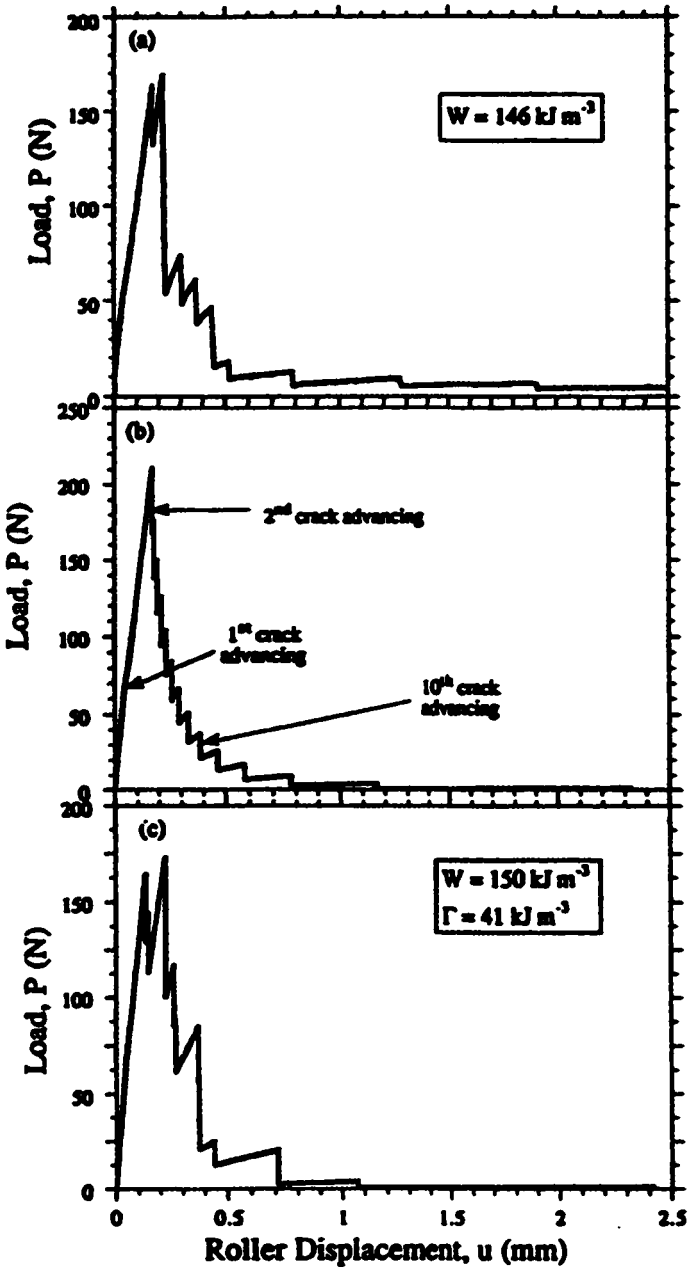

Figure 2.2.2-5. A comparison of experimental and theoretical (numerically modeled) load-displacement curves (Phillips et al, 1993b). The second and third curves are for determinate and Monte Carlo simulated strengths respectively.

This curve was compared to the expected stress-strain behaviour of brittle material subjected to pure tension (Figure 2.2.2-6). The modeling was initially done assuming a deterministic (known) strength of the layers.

The Weibull modulus was later incorporated to estimate the reliability of the materials. The work showed the flexural strength of the laminates is significantly higher than the tensile strength. This is consistent with Weibull statistics, so the result should not be considered typical of only this class of composites. More significantly, it was shown that the average work-of-fracture of the composites (area under the fracture curve) is less dependent on the Weibull modulus if tests are flexural rather than tensile (Figure 2.2.2-7). This suggests the reliability of the composites is improved.

The modeling results were validated by work on glass/thermoplastic adhesive laminates (Folsom et al, 1996b). Glass plates (microscope slides) were coated in a thin layer of thermoplastic adhesive and stacked to form multi-layered beams. The samples were uniaxially hot-pressed (175°C, 350kPa) before four-point bend testing. In some cases the plates were indented with up to 10kg using a Vicker's indenter prior to bonding, so the layers would exhibit a deterministic strength. Results of the bend tests were broadly consistent with the predictions of the modeling work. Figure 2.2.2-8 is a typical stress-strain curve of one of the four-layer glass/thermoplastic specimens.

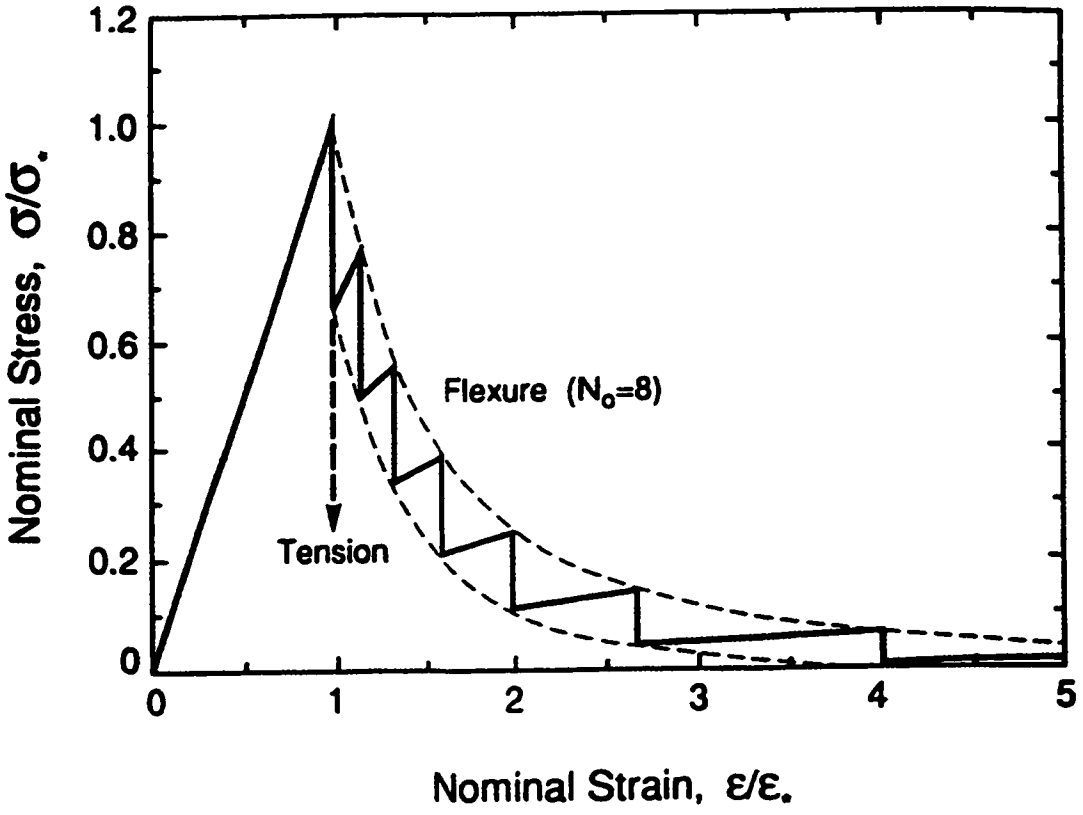

Figure 2.2.2-6. Comparison of the tensile and flexural stress-strain curves of a system comprising eight brittle layers (Folsom et al, 1994a). The vertical dashed line and arrow represent catastrophic failure of a monolithic sample under tension. The curved dotted lines are the loci calculated to envelop the "zig-zag" behaviour of a brittle laminate containing weak interfaces (or interlayers).

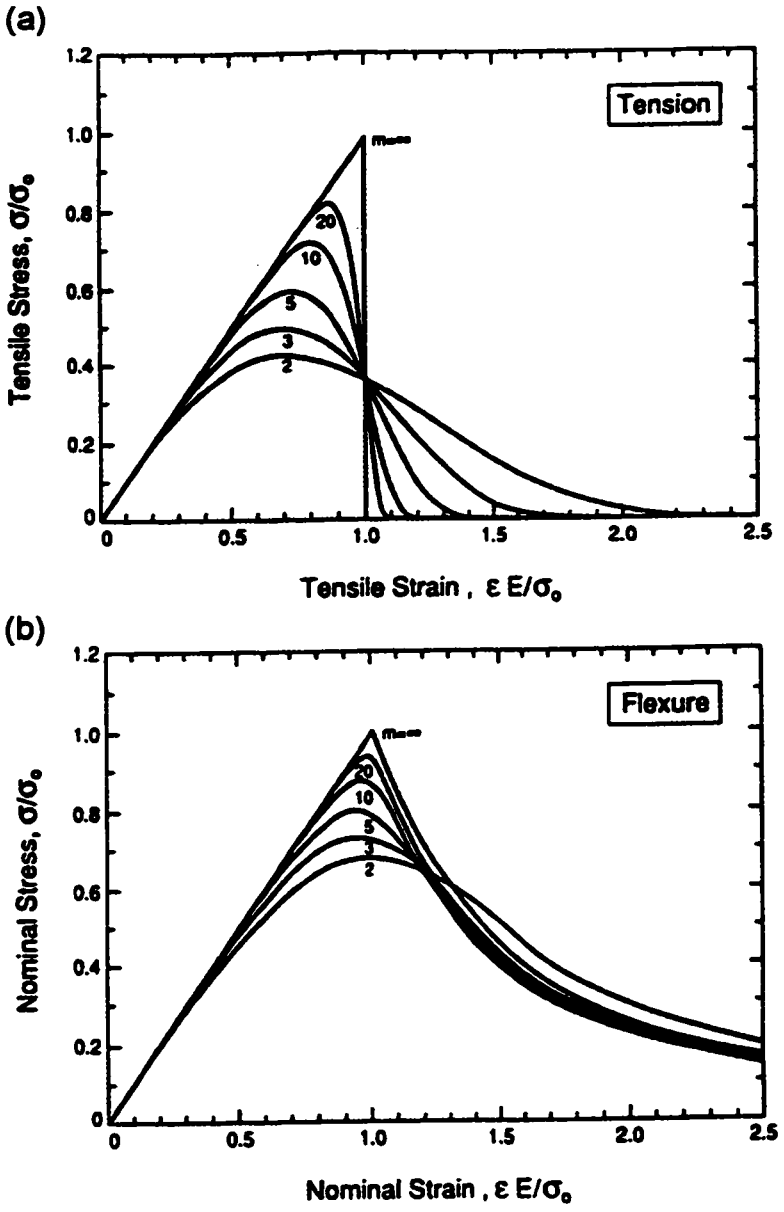

Figure 2.2.2-7. Influence of the Weibull modulus on the (a) tensile and (b) flexural stress-strain response of laminates (Folsom et al, 1994a). The work-of-fracture (area under the curve) is increased for flexure. The *m*-values refer to the Weibull modulus.

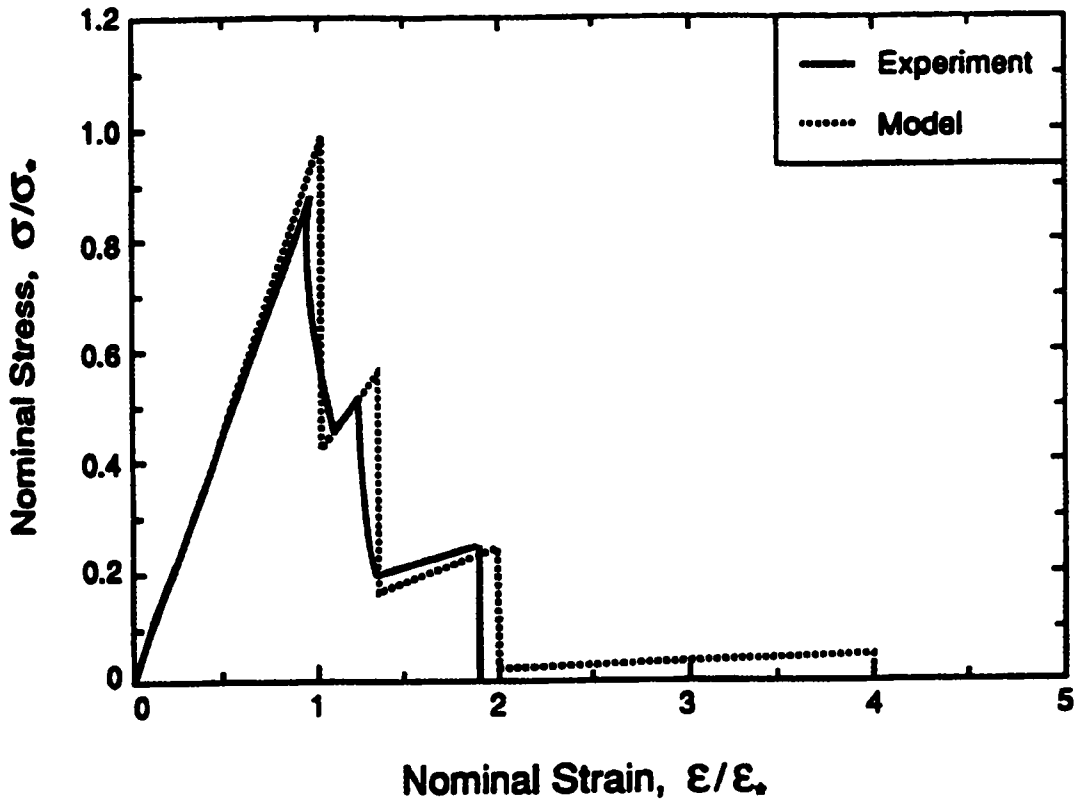

Figure 2.2.2-8. The flexural response of a four-layer glass/thermoplastic specimen, indentation load of 10kg (Folsom et al, 1994b). The model (dotted line) is based on the predicted fracture behaviour given as Figure 2.2.2-6.

The work by Folsom et al (1996) confirmed the stress-strain behaviour of laminates could be predicted by classical beam theory. Their model did not attempt to predict the criteria necessary for crack deflection, nor the effect of interfacial properties on the fracture behaviour.

Before 1995, the only engineering ceramic composites to exhibit multi-stage failure were silicon carbide/graphite. The combustion of graphite prevents the use of these materials at high temperature. If structural ceramics are to be used at temperature, where their refractoriness gives them an advantage over metals and alloys, the chemical stability problem must be addressed. This lead to several researchers attempting to design an all-oxide laminate with multi-stage fracture capabilities.

Bissinger (1995) made zirconia/lanthanum-aluminate laminates by electrophoretic deposition. Zirconia was selected as relatively tough ceramic (K_c~5-12MPa$\sqrt{m}$) due to its transformation toughening capabilities. In some cases alumina platelets were co-deposited to encourage crack deflection. Lanthanum-aluminate was selected for the interlayers as it's toughness is <20% that of zirconia, so should show the crack deflecting behaviour predicted by Cook and Gordon (1964) and He and Hutchinson (1989a). Lanthanum-aluminate forms *in situ* during the sintering of alumina and lanthanum oxide mixtures. The anisotropy of the material results in a platey, porous structure, ideal for crack deflection.

The experimentation involved indentation, electron microscopy, strength testing and (K_C) toughness testing. Indentation parallel to the layers and microscopy showed the lanthanum-aluminate layers must be ≥8μm to deflect cracks. Below this thickness the platey grains are constrained, and do not form a sufficiently porous microstructure for crack deflection. Flexural tests showed an improvement in strength of alumina platelet reinforced zirconia from 702(±35) to 784(±42)MPa by lamination with lanthanum-aluminate. Similarly, toughness was increased from 7.08(±0.62) to 8.28(±0.51)MPa√m. Despite the apparent increase in critical stress intensity factor and obvious crack deflection during the tests, *none* of the samples failed in a multi-stage fashion. This result suggests factors other than interlayer toughness must be considered in the design of laminates.

Electrophoretic deposition was also used by Vanderperre et al (1998), to synthesize silicon-carbide/graphite laminates. Multi-stage fracture behaviour was observed during three-point bend testing, and a nominal toughness of 17.7MPa√m was reported. This is an improvement over the expected value for silicon carbide of ~3-4MPa√m. Fracture of the surface layer was preceded by failure of the interlayer by shear. This makes comparisons to other work and the development of mechanical models difficult.

Mechanical properties of the laminates were studied by performing three-point bend tests on laminates, and compression tests on laminate rings. Figure 2.2.2-9 is a load-displacement curve for a ring compression test, showing extensive multi-stage fracture behaviour. The work-of-fracture was not reported.

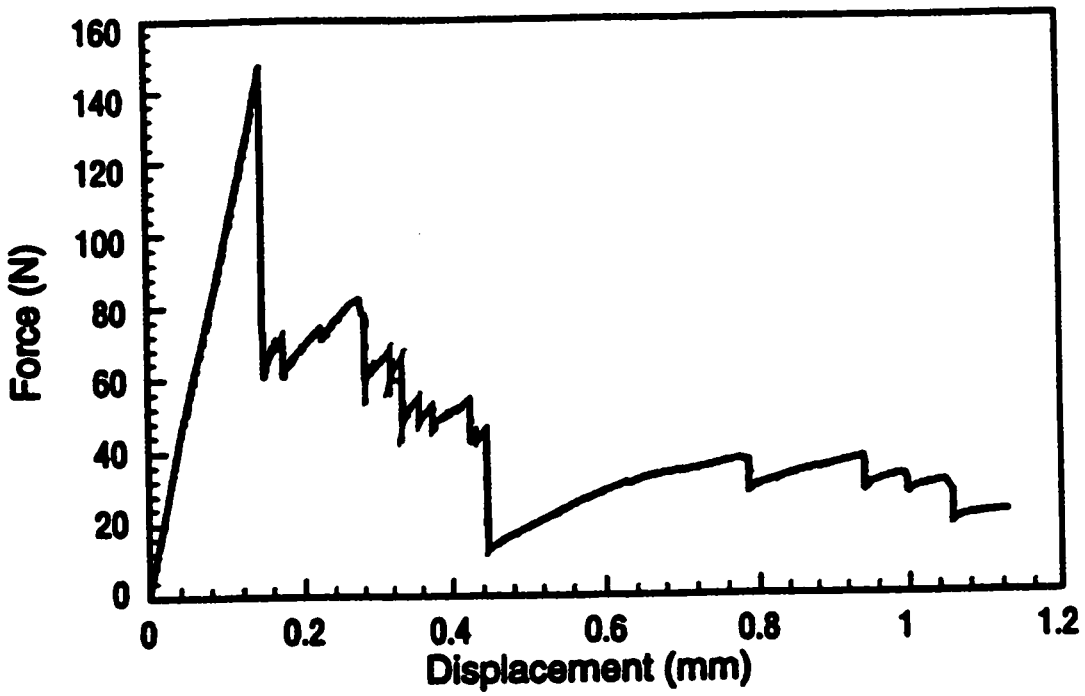

Figure 2.2.2-9. Load-displacement curve for a laminated ring compression test (Vanderperre et al, 1998). Load is applied to the ring across its diameter. Stress distribution within the sample is complex, and can *not* be easily compared with a simple three-point bend test.

Oeschner et al (1996) attributed crack deflection to thermal residual stresses developed when cooling from sintering to room temperature during processing. Earlier work by Ho et al (1995) showed residual stresses can cause cracking at the surface edges of interlayers, parallel to the layers (see Figure 2.2.2-10). This occurs only if the compression in the interlayer is high and the interlayer thickness is over a critical value determined by the properties of the material, that is;

$$t_C = \frac{G_C E}{0.34\left(1-\nu^2\right)\sigma_R^2} \qquad (2.2.2\text{-}1)$$

where t_C is the critical interlayer thickness, σ_R the residual thermal stress in the interlayer, and the other terms refer to the bulk material. They predicted crack bifurcation would occur only if the interlayer thickness were above this critical value.

Oeschner et al (1996) achieved multi-stage failure in zirconia/alumina laminates. Bend tests were performed on laminates consisting of alternating thick zirconia layers and thin, mixed alumina/zirconia layers. In this case the interlayers were subjected to an estimated ~ 2GPa of compression. They reported a correlation between successful crack bifurcation and interlayer thickness. The experimental results supported their predictions. The testing of samples that had notched surface layers was stopped mid-test to examine crack deflection. The role of the notch in the fracture behaviour was not investigated.

The Oeschner predictions were supported by the work of Hatton (1998).

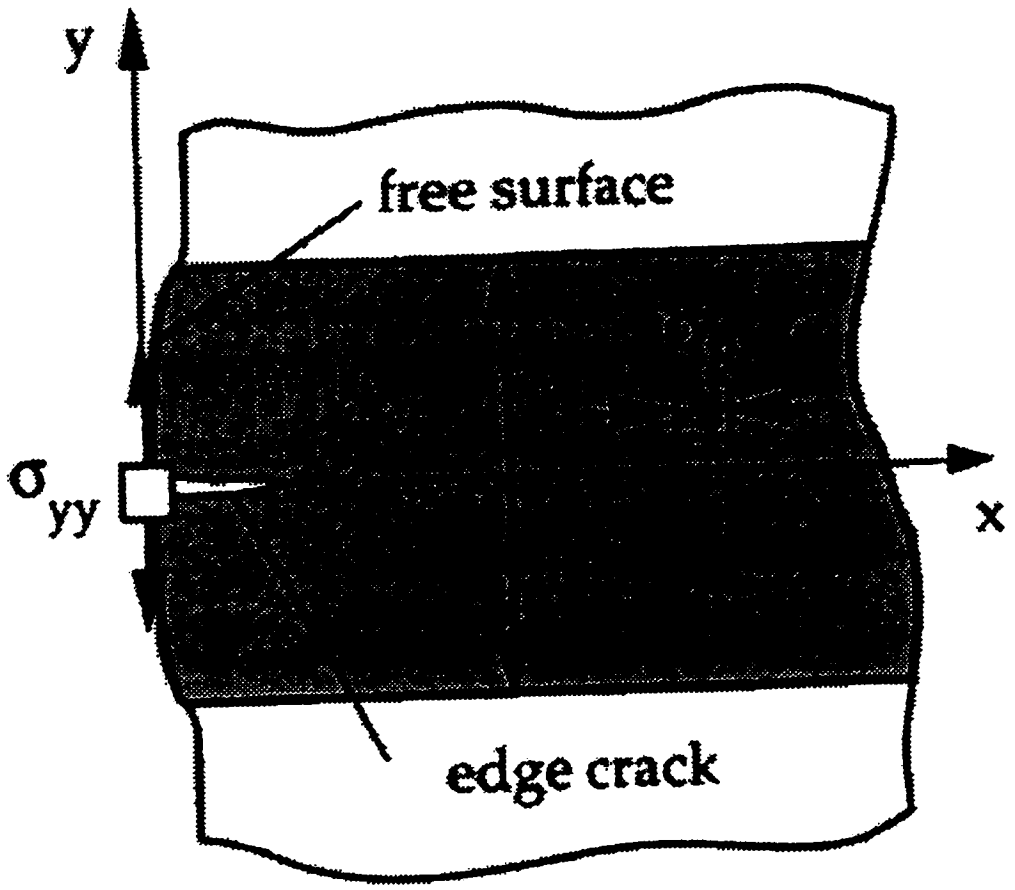

Figure 2.2.2-10. A schematic of the tensile stress at the free surface of an interlayer under thermal residual compression (Oeschner et al, 1996). The white layers are under tension, the dark layer under compression. The σ_{yy} stress causes edge cracking along the free surface of the interlayer.

Various composites consisting of thick zirconia layers and thin alumina layers were bend tested at both room and elevated (~1300°C) temperature. Several samples showed multi-stage fracture behaviour at room temperature, depending on the layer thickness combinations selected. None of the samples exhibited multi-stage fracture at high temperature. These results supported the Oeschner work, which predicts catastrophic failure due to lack of thermal stresses to deflect the crack along the interlayer.

At room temperature zirconia has a strength of ~900MPa, whereas alumina has a strength of ~500MPa. The Hatton composites consisted of stronger, thick layers of zirconia and weaker, thin layers of alumina. At temperatures ~1300°C the relationship is reversed; zirconia has a strength of ~150MPa and alumina has a strength of ~300MPa. This means that the composite consisted of weak thick layers and strong thin layers. This change was not discussed, and questions the validity of the comparison.

The Oeschner prediction was also supported by Sánchez-Herencia et al (1999), who performed bend tests on laminates consisting of thick layers of tetragonal zirconia and thin layers of mixed tetragonal/monoclinic zirconia. This combination was selected as it allows both the layer thickness and the residual thermal stresses to be varied. The stresses were varied by changing the tetragonal-to-monoclinic zirconia ratio in the interlayer. The tests were performed at room temperature.

The zirconia composite results also supported the Oeschner work. Both layer thickness and thermal residual stress affected the fracture behaviour. The results of bend tests performed on a variety of composites were plotted to demonstrate the cracking behaviour as a function of thermal residual stress (which relates to interlayer composition) and interlayer thickness (see Figure 2.2.2-11).

Three regions of cracking behaviour were identified. The delamination region represents conditions that cause catastrophic failure *during processing*. The high monoclinic zirconia content in the interlayers leads to high residual compression on cooling from the higher processing temperature. The high residual stress and relatively thick interlayer cause cracks that propagate through the entire composite. These samples could not be bend tested. The other two regions represent the difference in cracking behaviour predicted by Equation 2.2.2-1. If the monoclinic zirconia content in the interlayers is low (the left side of the figure), the thermal residual stresses developed in the interlayer are insufficient to cause surface cracking and bifurcation. A higher monoclinic zirconia content (the right side of the figure) causes edge cracking and bifurcation, *for a given interlayer thickness*. It was reported there was no significant affect on composite strength.

The tetragonal-to-monoclinic ratio will not only affect the thermal stresses, but will also affect the strength of the interlayer. This was not considered. Monoclinic zirconia is very weak due to a phase transformation that occurs

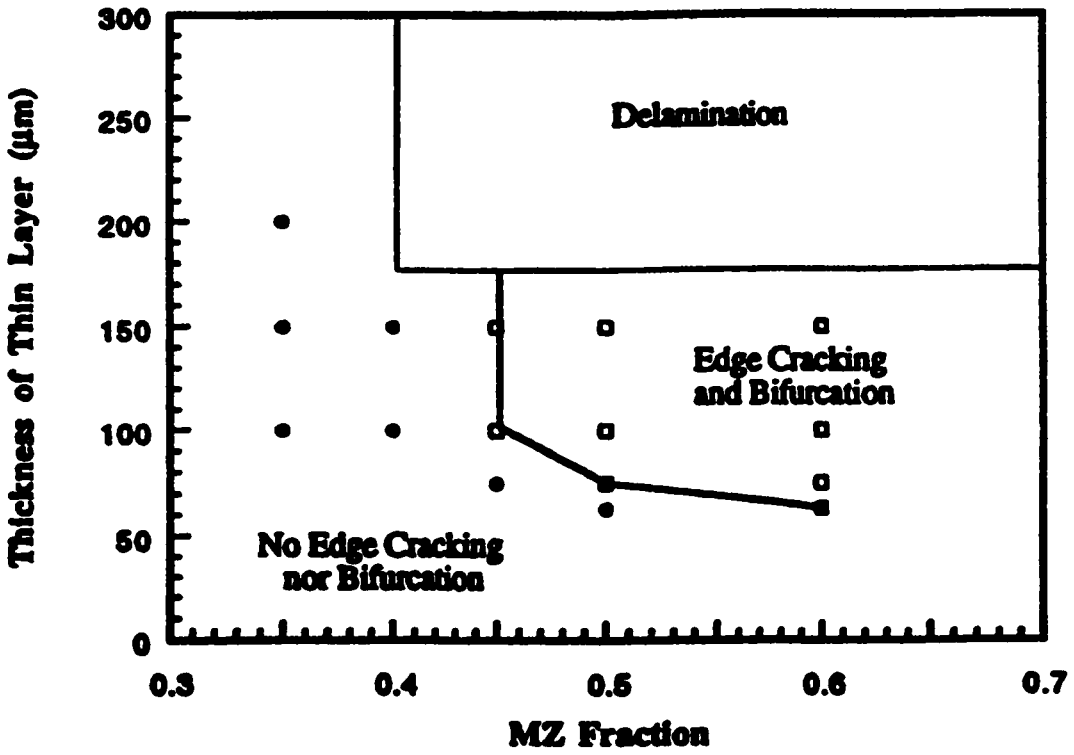

Figure 2.2.2-11. A summary of the cracking behaviour of zirconia composites (Sánchez-Herencia et al, 1999). The three region predict (fatal) delamination during processing, edge cracking and bifurcation, or neither edge cracking nor bifurcation.

during processing. This will be discussed later. The affect of the changing interlayer *strength* on the fracture behaviour was not considered.

Lee et al (1996) showed the assumption that the main crack reaches the weak interface before bifurcation occurs is incorrect. The stress intensity in the vicinity of a main crack tip is high enough to cause propagation in weak interface cracks *before* the main crack arrives at the interface. This was first noticed by Ignat and Clegg (1995), and Lee (1996).

Lee et al (1996) studied the pre-cracking phenomenon by wedge loading PMMA laminates. The wedge loading allowed cracks to propagate stably, and allowed observation of interface cracking behaviour (Figure 2.2.2-12). The results showed the interface fracture energy could be as high as ~60% that of the strong layers and bifurcation would occur. Wedge loading provides a stress concentration at a crack tip that is different to that of uniaxial tensile loading or bending. In the former case, a wedge is physically driven into the crack, so the crack surfaces are subjected to compression. In the latter case, the loading is remote and the crack surfaces remain traction free.

Lee et al (1996) supported their experimental work with finite element analysis. Meshes were developed to simulate wedge loading, tension, and three- and four-point bending. Eight-noded bi-quadratic elements were used for the bulk of the mesh, with quarter-point node elements used to simulate the crack tip stress singularity. The finite element calculations under-estimated the interface crack driving forces. Phase angle calculations were broadly consistent with

Figure 2.2.2-12. A photograph showing pre-cracking of an interface ahead of a main crack (Lee et al, 1996). The PMMA sample has a notch on the top surface. The darker, central region, is a (pre-) crack plane between two strong layers in the laminate.

comparable predictions made by Suo and Hutchinson (1990).

Kuo and Kriven (1997) achieved successful multi-stage fracture in a composite consisting of zirconia, mixed zirconia/alumina, and weak yttrium phosphate layers. The alumina was added to modify the thermal expansion of the zirconia layers and prevent cracking during processing. One of the laminates tested had a strength of 358MPa, and an apparent work-of-fracture of 8.2kJ/m^2 due to multi-stage fracture behaviour (Figure 2.2.2-13). This strength is lower than monolithic zirconia (~900MPa) due to thermal residual tension. The advantage of this material is the work-of-fracture was ~2x that of monolithic zirconia. Data was quoted for *one* four-point bend test, so the reliability of the work must be questioned.

Kovar et al (1998) studied crack propagation and deflection in silicon nitride/boron nitride laminates. The strong layers were silicon nitride, and the weak interlayers consisted of varying ratios of silicon nitride and born nitride. A strength of 500MPa and work of fracture of 5000J/m^2 were achieved. It was shown that the composition of the interlayer had a significant effect on the mechanical behaviour (Figure 2.2.2-14). Samples with tougher interlayers exhibited less multi-stage fracture.

Kovar et al (1998) also incorporated the predictions of He et al (1991) into their work to differentiate between crack kinking and delamination. Kinking occurs when a crack deflects along an interface briefly, but does not prevent catastrophic failure. Delamination involves extensive crack deflection and multi-

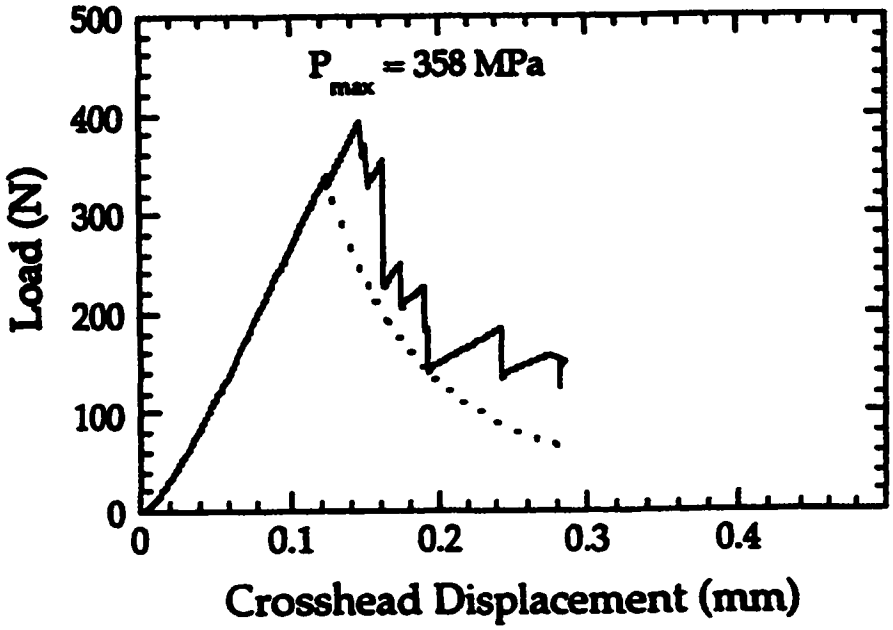

Figure 2.2.2-13. The load-displacement curve for a yttrium phosphate-zirconia-alumina laminate (Kuo and Kriven, 1997). Crack deflection along the weak yttrium phosphate interlayers lead to multi-stage fracture behaviour, and a significant improvement in the work-of-fracture.

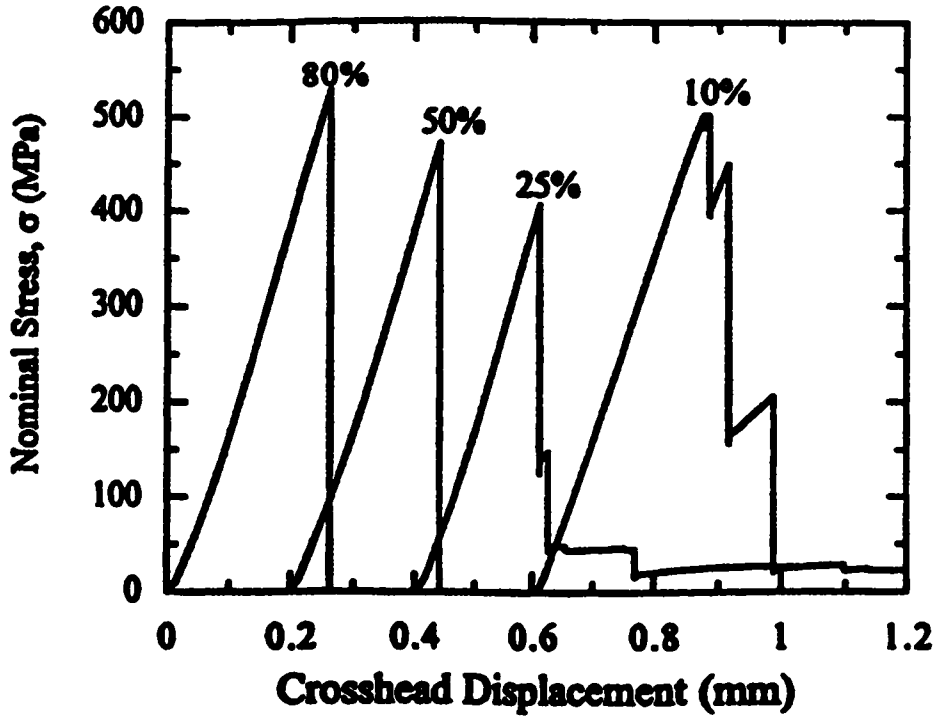

Figure 2.2.2-14. Load-displacement curves for silicon nitride/boron nitride laminates (Kovar et al, 1998). The compositions of the interlayers were 80%, 50%, 25% and 10% silicon nitride, with the balance boron nitride. A higher (weak) boron nitride content lead to crack deflection, and multi-stage fracture behaviour. The strength of samples was consistent.

stage fracture. The behaviour was shown to be dependent on the toughness of the interlayer, and the critical flaw size in the (strong) material (Figure 2.2.2-15). Samples with stronger interlayers and/or large critical flaws exhibited crack kinking (right side of figure), whereas samples with weaker interlayers and/or small critical flaws exhibited delamination (left side of figure). This work is consistent with the idea that stronger interlayers resist cracking and limit toughening ability.

Mawdsley et al (2000) studied crack deflection behaviour in alumina/monazite ($LaPO_4$) composites. Laminates were tested in four-point flexure. Un-notched laminates exhibited catastrophic failure despite apparent crack deflection. Notched laminates exhibited sporadic crack deflection, and failed non-catastrophically (Figure 2.2.2-16). Mawdsley et al (2000) predicted the fracture behaviour of their system; similar to the technique used by Kovar et al (1998) (Figure 2.2.2-15). They predicted no crack deflection if the interlayer toughness was more than half that of the strong layers (Figure 2.2.2-17).

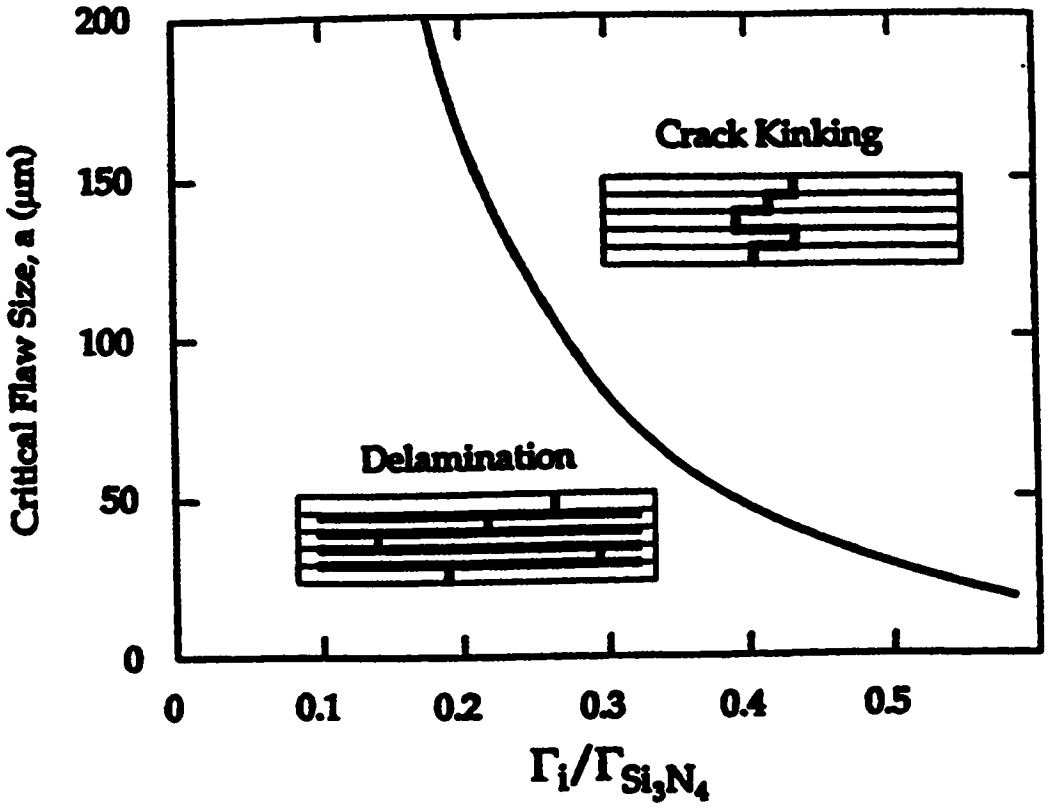

Figure 2.2.2-15. Predicted fracture behaviour as a function of critical flaw size and interlayer toughness (Kovar et al, 1998). The Γ's are toughness values for the weak interlayer and strong silicon nitride layers.

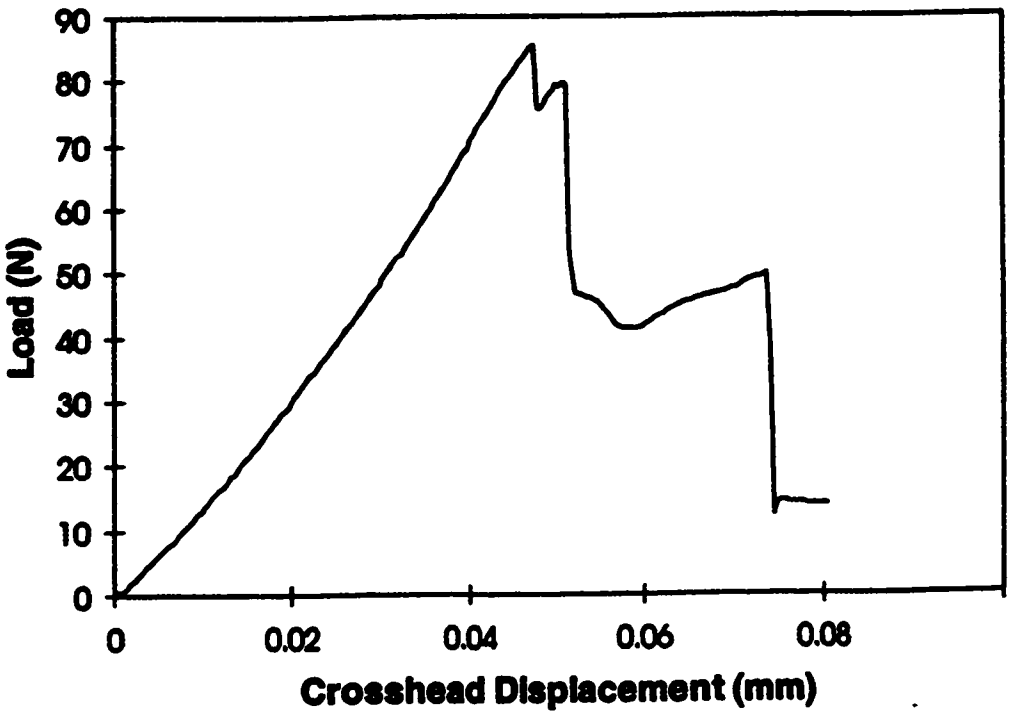

Figure 2.2.2-16. A load-displacement curve for a notched alumina/monazite laminate (Mawdsley et al, 2000). The weak monazite interlayers lead to crack deflection, and multi-stage fracture behaviour.

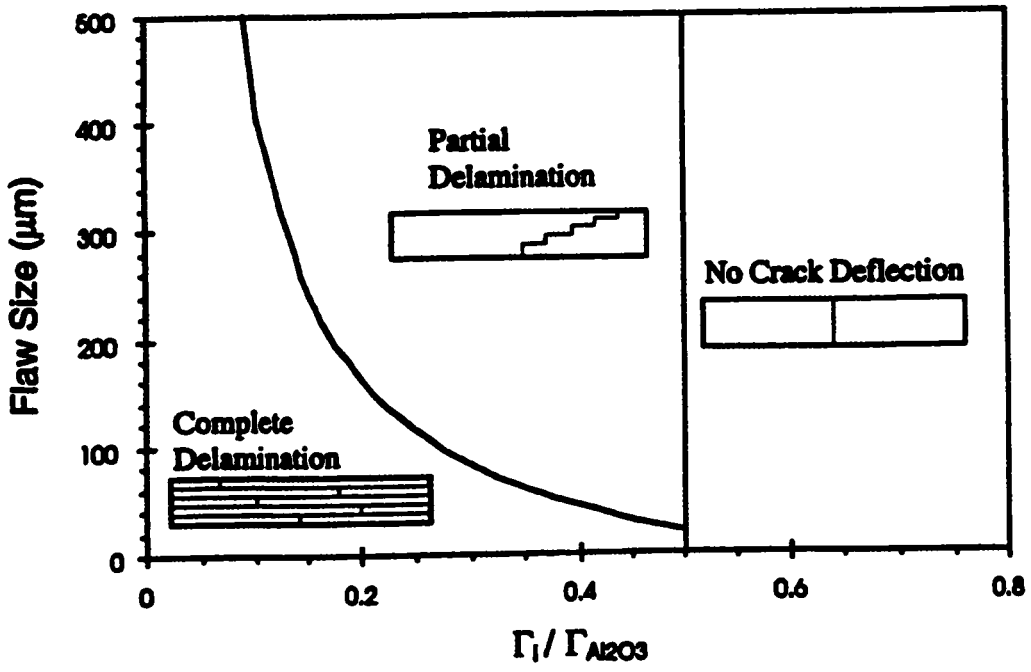

Figure 2.2.2-17. Predicted fracture behaviour as a function of flaw size and interlayer toughness (Mawdsley et al, 2000). The Γ's are toughness values.

2.3 Composite Materials

2.3.1 Powder Processing of Ceramics

The powder processing of ceramics is important to their final properties. Several common techniques exist; slip casting, pressure casting, tape casting and centrifugal casting. The process used for this work was electrophoretic deposition, which is a recently developed technique for ceramic laminates. Each method involves mixing of a slip (or suspension), shaping of a part, and finally sintering of the green ceramic to form a dense material.

The goal of all powder processing techniques is material homogeneity, in the shape necessary for a given application. For structural ceramics, the most important feature is the distribution of unavoidable flaws. While these flaws can never be eliminated completely, every effort is made to ensure that the flaws are as small as possible, to provide the maximum possible strength. A small powder size results in a fine structure of pores and grains. This leads to small flaws and high strength. The starting powder size is therefore important to the final properties. A fine powder also allows the material to be sintered at a lower temperature or for shorter times, which is industrially favourable. Finer powders are expensive, so are only used for critical components.

The powder is mixed with water or organic materials, then milled to break up agglomerates and ensure a finer grain size. The resulting suspension may be stabilized by adding salts or polymers. Particles are mutually repelled by coulombic forces or steric hindrance respectively.

Electrophoretic-deposition (EPD) is a processing technique developed in the nineteenth century (Ruess, 1837), that has only recently been exploited in the fabrication and design of engineering ceramics. The technique has some advantages over other processing routes. EPD is quick, relatively inexpensive, and can be used to form various shapes. Its principal advantage is that it can be used to make variety of ceramic composites; particle-, platelet- or fibre-reinforced materials, laminates, and functionally graded materials.

A slip is mixed using the powder and a suspension medium. Most powders that have previously been used have been oxides, though there has been recent work on silicon carbide (Vanderperre et al, 1998) and silicon nitride (Fukada, 2001). The suspension medium must have a high dielectric constant for the electrophoresis, so water or alcohol is used. The slip is stabilized using either acid or base. Ions dissociate in the liquid, and adsorb onto the particles according to;

$$MOH + H^{+} \rightarrow MOH_2^{+} \quad \text{(acid)} \qquad (2.3.1\text{-}1)$$

or

$$MOH + (OH)^{-} \rightarrow MO^{-} + H_2O \quad \text{(base)} \qquad (2.3.1\text{-}2)$$

where *MOH* is a metal oxide particle containing a naturally adsorbed hydroxide ion, and H^{+} and $(OH)^{-}$ are dissociated ions from the acid or base. The result of the adsorption is that the particle is charged, either positively or negatively. The like charges in the suspension repel and prevent particle agglomeration.

The electrophoretic-deposition occurs when two electrodes are immersed in the suspension, and a DC current passed between them (see Figure 2.3.1-1, Sarkar and Nicholson 1996). Electrophoresis is the movement of particles within a suspension under the influence of an applied electric field. The particles move to the either the cathode or the anode, depending on their charge. A dense cake forms on the deposition electrode. When the desired thickness of deposit is achieved, it is removed from the suspension, then dried and sintered.

One advantage of the EPD process is that the thickness of layers can be tailored. The mass of ceramic deposited is proportional to the charge passed, so timing the process can control thickness. If a laminate is required, two or more different suspensions are prepared, and the electrodes alternately immersed in each. Different particles types deposit at different rates (Whitehead 1994, Bissinger 1995), and so rate calibration is necessary if specific thickness of layers in the laminate is required.

2.3.2 Zirconia/Lanthanum-Aluminate Composites

Zirconia/lanthanum-aluminate composites were designed by Bissinger (1995) in an attempt to achieve multi-stage fracture behaviour. Zirconia (zirconium oxide, ZrO_2) became popular as a structural ceramic after the discovery of transformation toughening (Garvie et al, 1975). Effective control of the microstructure can be used to produce ceramics with a room temperature

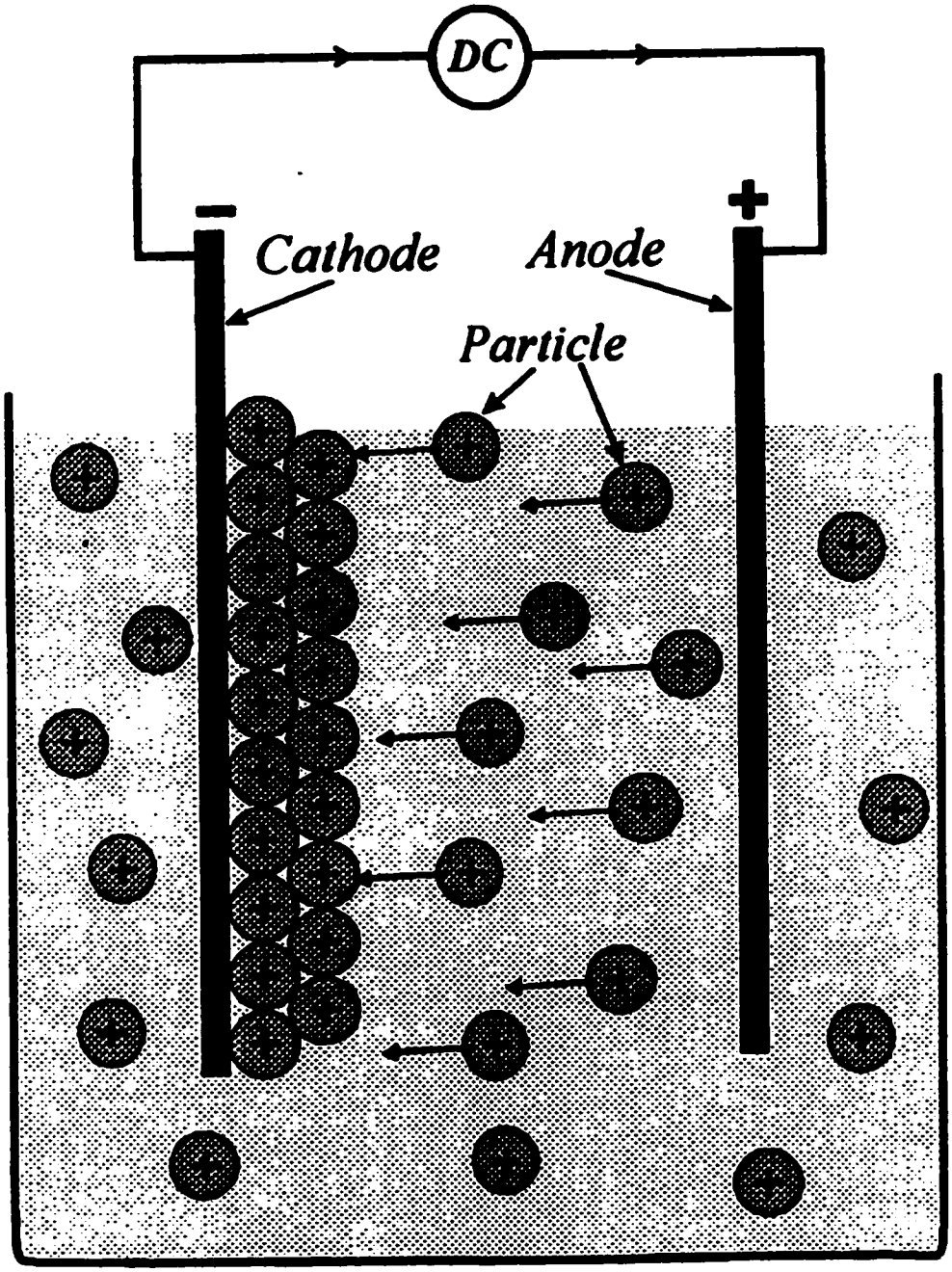

Figure 2.3.1-1. A schematic of an EPD cell (Sarkar and Nicholson, 1996).

strength over 2GPa, and toughness of up to 35MPa$\sqrt{m}$ (Green, 1998). The toughening technique relies on a phase transformation in the material during fracture.

Zirconia has three stable phases. It is monoclinic at room temperature, tetragonal at ~1000-1500°C and cubic over ~1500°C. The structure is that of face-centred "cubic" zirconium atoms, with oxygen at the eight tetrahedral interstitial sites (see Figure 2.3.2-1). Transformation of the phases leads to significant strains. The most important of the transformations is tetragonal to monoclinic, which involves a ~4% volumetric strain. This strain is sufficient to cause fatal cracking of zirconia during processing, unless the material is stabilized appropriately.

Zirconia ceramics are doped using yttrium, calcium, magnesium or cerium. The amount and type of dopant influences the temperatures at which the transformations occur. The tetragonal phase can be stabilized at room temperature. The result is either partially stabilized zirconia (PSZ) or tetragonal zirconia polycrystals (TZP). Alternatively, the material is heavily doped to produce a stable cubic phase at room temperature.

The presence of the tetragonal phase at low temperature is critical to the toughening mechanism. If the material is stressed, the stress concentration at the tips of microscopic cracks in the material is enough to induce the transformation to the monoclinic phase. The transformation requires a volume increase that is

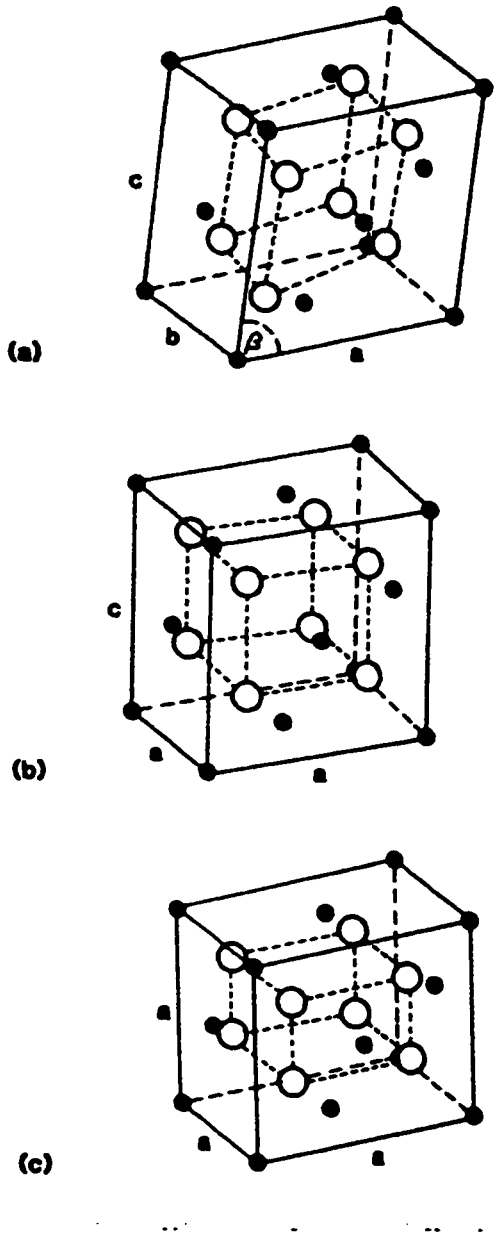

Figure 2.3.2-1. The crystal structures of the three phases of zirconia; (a) monoclinic, (b) tetragonal, and (c) cubic (Green et al, 1989). The black circles are zirconium atoms, the white ones oxygen.

constrained by surrounding grains. During the transformation, the new monoclinic phase is subjected to large compressive forces that act to close the crack. This reduces the effective stress acting on the crack, and nominally toughens the material. The grain size in the material must be below a critical radius to prevent the transformation from occurring spontaneously.

The transformation toughening technique also strengthens the ceramic. The grains on the surface of the material are not constrained on all sides by neighbouring grains, which can allow transformation. The resulting compressive stress closes surface cracks. Fracture of the material then requires an "extra" stress to negate this residual stress.

The zirconia used in this work was 3 mole% yttrium doped (TZ-3Y). Bissinger (1995) previously characterized this material, made by EPD. A (room temperature) strength of 935±54Mpa, a toughness of 5.5 MPa$\sqrt{m}$, a Young's modulus of 221.8±2.5GPa, a Poisson ratio of 0.31, and a thermal expansion coefficient of 11.3μ/°C were reported.

Lanthanum-aluminate ($La_2O_3 \cdot 11Al_2O_3$) is a β"-alumina type structure that forms *in situ* during the sintering of lanthanum oxide and alumina powder mixtures. The ceramic forms long, platey grains as a result of the crystallographic anisotropy. The random orientation of these grains leads to a porous structure, which is advantageous if the material is to be used as a weak interlayer. Lanthanum aluminate densities of only ~77% theoretical were achieved by

Bissinger (1995), even after sintering at 1550°C for six hours. A flexural strength of 100±30MPa and an elastic modulus of 112GPa were reported.

Composites were made by immersion of the deposition electrodes alternately in appropriate suspensions of zirconia and lanthanum aluminate. This technique was used by Bissinger (1995) to fabricate multilayer laminates with a zirconia layer thickness of ~200-300μm and a lanthanum aluminate interlayer thickness of ~10μm. Bissinger added alumina platelets to the zirconia suspensions. The difference in elastic and thermal properties leads to crack deflection. The crack deflection does not prevent catastrophic failure.

In the present work, the EPD technique is used for composite fabrication, but only single interlayers are used in the laminates. The strong layers are zirconia (TZ-3Y). The weak layers are lanthanum-aluminate/alumina, with the same composition as the materials produced by Bissinger. Alumina platelets were added to seed the growth of the lanthanum-aluminate grains and elongate pores for added weakness.

2.3.3 Glass/Epoxy Composites

Folsom et al (1996, II) showed that multi-stage fracture is possible in glass/thermoplastic adhesive composites. This is a practically convenient way to fabricate samples in a quick and consistent manner. Indentation of the glass slides prior to bonding allows better control of the strength of individual layers.

Glass behaves in a purely brittle manner, and the adhesive interlayers are sufficiently thin to allow brittle behaviour. Fracture has been shown to follow the trends predicted by elastic calculations (as discussed Section 2.2.2).

Fleck et al (1991) considered the propagation of cracks in brittle adhesive layers, in a manner similar to the theoretical work of He and Hutchinson (1989b). The calculations showed that interlayer cracks tend to remain trapped if the residual stresses are minimal. The crack may oscillate between interfaces *or* propagate within the interlayer, but will not deflect out unless there are extreme residual stresses or loading conditions. The theoretical predictions were consistent with the experimental results of Cao and Evans (1989), Chai (1987), and Wang and Suo (1990).

Glass/epoxy composites have also been used in the present work. This allows the study of a system in which there are no (or negligible) thermal residual stresses. It is assumed that the temperature change in the epoxy due to polymerization is minimal. Residual thermal stresses were used as the basis of the crack deflection model proposed by Oeschner et al (1996). The multi-stage fracture behaviour exhibited by glass/epoxy composites suggests other factors are important. The thermal residual stresses are only important in that they induce large cracks, which weaken the interlayer. The interlayer weakness is acknowledged as being an important feature of this class of materials.

The two componenets of the glass/epoxy system have a large difference in elastic moduli; glass is ~25x stiffer than epoxy (~65-75GPa versus ~2-5GPa).

In this work, the effect of the modulus on the fracture behaviour is assumed negligible, so the difference is not included in the calculations. This will be discussed in detail in Chapter 3.

2.3.4 Plaster-of-Paris Composites

Plaster-of-Paris was used by Szymanski* (2000) to study crack deflection along porous interlayers. Plaster forms when calcium sulfate hemi-hydrate is mixed with water;

$$CaSO_4.½H_2O + 1½H_2O \rightarrow CaSO_4.2H_2O \qquad (2.3.4\text{-}1)$$

The properties of plaster vary with water content, but one can expect a flexural strength in the range 3-8MPa, a toughness of 0.14-0.16MPa$\sqrt{m}$, and a modulus of 4.5-8GPa (CMS Software, 1994). The advantage of using this material is that composites can be made with neither modulus difference or thermal residual stresses. Samples are easy to fabricate, and properties such as interlayer strength and sample geometry can be readily adjusted.

Szymanski (2000) made both monolithic and composite plaster samples. Composites were made by inserting a row of straight wires into the mold before

* The work by Szymanski (2000) was a collaborative project with the author. The experiments were designed to parallel the author's work with zirconia/lanthanum-aluminate and glass/epoxy composites.

pouring in the pre-mixed plaster slurry. The wires were removed after curing, to leave a uniform row of holes. The mold was designed to allow the ℓ/h ratio of the sample to be adjusted (where ℓ is the distance between the tensile surface and interlayer, and h the total height of the sample – see Figure 3.1-2). A hacksaw was used to cut notches of various depths into the tensile surface of the samples.

The strength of the monolithic plaster was 5.4(±0.7)MPa. Notches of 4 and 6mm reduced the strength to 2.0(±0.1) and 1.8(±0.2)MPa respectively. A toughness of K_C =0.25(±0.02)MPa$\sqrt{m}$ was calculated, based on the notched sample bend tests. The weak layers had no significant effect on strength. For samples with a 4mm notch and a weak layer 6mm from the tensile surface, a strength of 1.7(±0.4)MPa was reported.

The catastrophic and multi-stage behaviour of the composite samples showed a distinct trend. Samples with small notches and/or large ℓ/h ratio failed catastrophically. Sample with large notches and/or small ℓ/h ratios showed multi-stage fracture behaviour (Figure 2.3.4-1).

A delamination test (à la Charalambides et al, 1989) was attempted to determine the critical strain energy release rate of the weak layers. All samples failed catastrophically, so no value was calculated. A toughness of G_C=8.9J/m^2 can be calculated, based on the K_{IC} and measured modulus (7GPa) of the plaster.

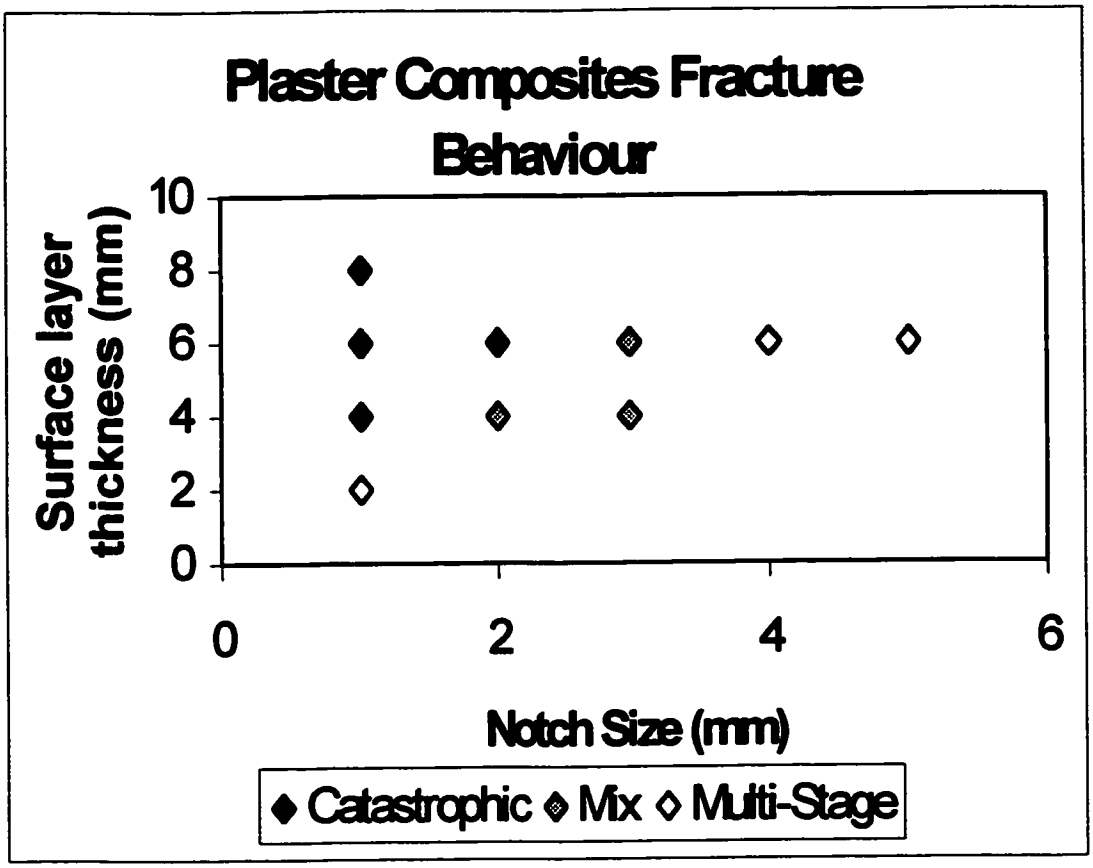

Figure 2.3.4-1. The fracture behaviour of plaster-of-Paris composites (data from Szymanski 2000). Two behaviour zones are evident; a catastrophic zone (upper left), and a multi-stage fracture zone (lower right). The central region is a mixture of behaviour.

Samples were also subjected to thermal shock tests. After heating for three hours at 100°C and quenching, the strength reduced to 2.7(±0.7)MPa. Results revealed the interlayers crack stably during quenching. This suggests multi-stage fracture behaviour can be encouraged by service conditions. The strength degradation remains a problem.

2.4 Finite Element Analysis

Fracture mechanics modeling requires several simplifications and approximations to make predictions possible. An alternate approach is finite element analysis, which produces accurate predictions for complex geometries. The technique is purely mathematical. It allows one to define a complex geometric shape, simulate applied loads or displacements, and calculate the resulting displacements or loads (respectively) based on the elastic properties of the chosen material. The displacements are in turn used to calculate stresses and strains in various parts of the shape.

The finite element method involves mathematically defining a shape that is sub-divided into many smaller elements to produce a "mesh". The elements can vary in shape, but in the present work square elements (constant strain quadrilaterals) are used for all the calculations. The square elements have nodes at the corners that are subjected to simulated loads or displacements, in both the horizontal and vertical directions. The relationship between the loads and resulting displacements (or vice versa) is determined by the elastic properties of the material, and is expressed as an 8x8 stiffness matrix, *[K]*. The deformation of each element is described using eight load components and eight displacement components (for two directions and four nodes). To satisfy Hooke's law, the matrix and two vectors are related by;

$$\underline{f} = [K]\underline{a} \qquad (2.4\text{-}1)$$

where $\underline{f}$ and $\underline{a}$ are the load and displacement vectors, and *[K]* the elemental stiffness matrix (Stolle, 1999).

Neighbouring elements share nodes, so must have equivalent loads and displacements. This allows construction of a global stiffness matrix, which represents the behaviour of the entire shape. Simulated loads or displacements can then be applied, and the matrix solved for the unknowns. Considering elements ***not*** having shared nodes can simulate cracks.

Estimated errors are important to finite element calculations. There are two main techniques that are used to improve the accuracy. The first is to use high order elements; that is, elements with a greater number of nodes. This allows the displacements of the nodes to vary parabolically or cubically *within* each element, which gives them greater versatility in situations with complex stress and strain gradients. Higher order elements require more complex meshing and involve larger matrices, which leads to longer computing times. An alternate route is to use more elements. This also leads to larger matrices and longer computing times, but mesh generation remains simple.

The present work involves the calculation of fracture criterion for brittle laminates that contain weak interlayers. The are two ways finite element analysis can be used to assist in these calculations; direct methods, and indirect methods (Broek, 1982).

Direct methods involve calculation of stress intensity factors at crack tips. Stresses in the neighbourhood of the crack tip are calculated using finite element

methods, and the stress intensity *at* the crack tip determined using Equation 2.1.6-9. Theoretically, the stresses at the tips of sharp cracks are infinite. The finite element method can not yield an infinite solution, so stresses are limited to a finite value. Stress values in the neighbourhood of the crack tip are *under*-estimated. The technique requires extrapolation to determine the stress intensity *at* the crack tip, so there is an error associated with the calculated value.

Refining the mesh near the crack tip can mitigate the error associated with direct methods. The increased number of elements allows the sharp stress gradient at the crack tip to be better modeled. Chan et al (1970) calculated the stress intensity factor at a crack tip in a compact tension specimen using direct methods, and studied the effect of mesh refinement on the accuracy of the solution. Increased mesh refinement led to a more accurate result, but the theoretical solution (determined by collocation) was not achieved. A discrepancy of ~5% was reported (Figure 2.4-1).

Hybrid elements have been developed, which calculate stress intensity factors directly (Walsh, 1971). The elements are designed to relate nodal displacements to a stress intensity factor, rather than a series of loads. These elements require complicated meshing in the neighbourhood of the crack tip. The technique produces more accurate results than mesh refinement.

Indirect methods involve calculation of strain energy using finite element analysis. The strain energy release rate can be determined by calculating the strain energy for two crack sizes, and dividing the difference by the crack size

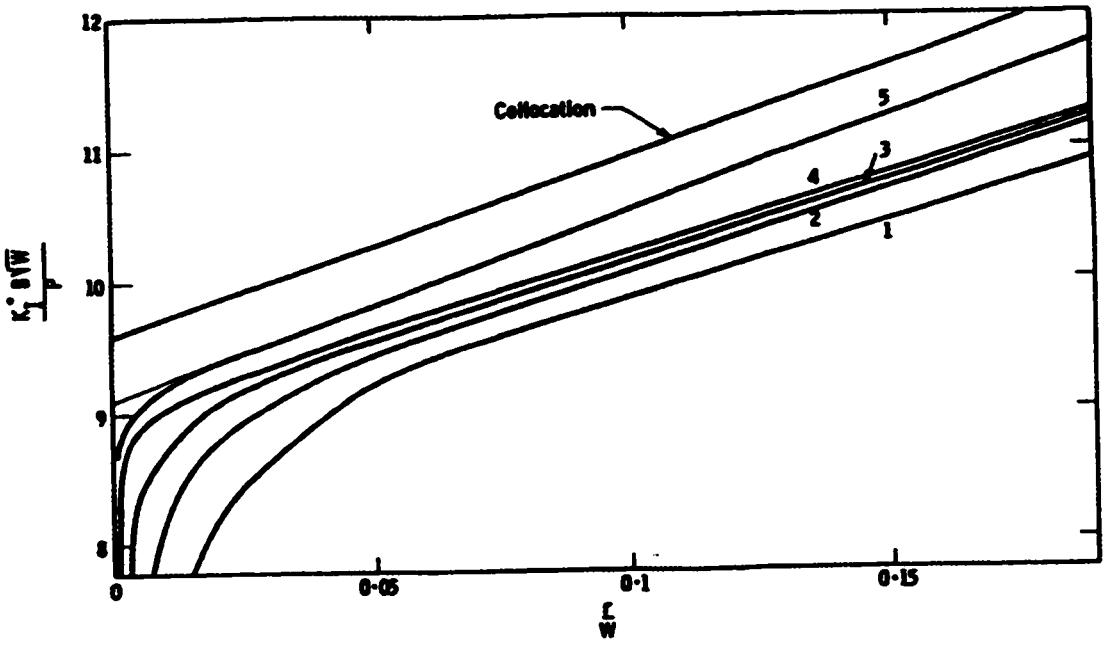

Case	Element size†-A/a^2 Inner (10^{-3})	Outer (10^{-2})
1	312	2
2	78	2
3	20	2
4	1·20	2
5	1·20	1

†A—Element area, a—Crack-length.

Figure 2.4-1. The effect of element size on accuracy of K for a compact tension specimen (Chan et al, 1970). Each curve represents a calculated stress intensity as a function of distance from the tip. The crack tip stress intensity is the (extrapolated) intercept on the left axis of the figure. Cases 1 to 5 use an increasing number of elements in the calculation. None reach the expected value given by collocation.

increment. The stress intensity is related to the strain energy release rate using Equation 2.1.2-14.

This technique was first developed by Mowbray (1970) to calculate the stress intensity of cracks in a single edge notch in tension. Errors as low as 0.2% were achieved using a moderately coarse mesh. No refinement was necessary at the crack tip. There are two reasons for the accuracy. The first is that stress under-estimation (as in the direct methods) is avoided by not calculating the stresses. Calculations based on the strain energy are accurate, as small errors are balanced out over the entire mesh. The second reason for the accuracy is that strain energy calculations converge to the correct solution much more quickly than stress calculations. Energy calculations are inherently more accurate than stress or strain calculations, for a given mesh size.

Indirect methods do have limitations. There is error associated with the differentiation procedure. The magnitude of this will vary with complexity of the shape of interest and the regression equation used to fit the calculated energies. Another problem is, if a crack is subjected to shear, the fracture modes (I and II) can not always be separated from the single strain energy release rate calculated.

2.5 Thesis Objectives

Several researchers have shown it is possible to incorporate weak interlayers into ceramics to give them non-catastrophic fracture behaviour. This is a major improvement in their mechanical properties. Various researchers have predicted the criteria required to achieve multi-stage fracture behaviour, but each model is incomplete. The interfacial toughness guideline proposed by Cook and Gordon, and later supported by He and Hutchinson, failed the zirconia/lanthanum-aluminate laminates designed by Bissinger. The thermal residual stress model proposed by Oeschner et al does not account for multi-stage fracture in glass/epoxy laminates. It is true the thermal residual stresses will increase the flaw size in the interlayers, but this will not necessarily guarantee crack deflection. The supporting work by Hatton, and Sánchez-Herencia et al, fails to adequately account for the effect of interlayer strength on fracture behaviour.

The aim of the present work is to develop a model that will predict catastrophic or multi-stage fracture in laminates containing weak interlayers, which is effective for *all* composites. The important parameters considered in the model are the testing geometry, the two materials' mechanical properties, and the flaw sizes in the materials. It is proposed that three separate flaw sizes have an influence on the fracture behaviour; the surface layer crack size, the interlayer crack size, and the crack size in the "next" layer in the composite. As three cracks influence the behaviour, reliability is expected to be an important issue.

Several assumptions must be made to make the problem manageable, and these are acknowledged.

The model does not consider the effect of thermal or elastic mismatch, and it is assumed the interlayers are thin enough to be treated as interfaces. This will be discussed in Chapter 3. The composite is treated as a material containing a two-dimensional plane that has a lower toughness. The stress distribution in the composite during loading will be equal to that in a monolith, except for the presence of interlayer cracks.

The model presumes that during catastrophic failure of the surface layer of a composite during flexural testing, the stress concentration in the vicinity of the propagating crack is sufficient to cause pre-cracking of the interlayer. This pre-cracking was experimentally shown by Lee et al, and will be shown to be theoretically justifiable. The model then considers the extent of pre-cracking necessary to reduce stress concentration in the next layer in the composite, to prevent total catastrophic failure.

A "quasi-static", or "kinetic", approach has been used. The calculations account for changing strain energy release rates of cracks during their propagation, and the complimentary changes in kinetic energy. The technique does *not* consider the effects of the inertial effects of material at the crack tip, or the effect of shock waves in the system.

The model has been developed using standard fracture mechanics equations, with complimentary work done using finite element analysis. These

approaches are self-consistent, and provide similar predictions. Experimental work has been done using three different composite systems to demonstrate the versatility of the model. The three systems are;

i) zirconia/lanthanum-aluminate (elastic mismatch and thermal residual stresses),

ii) glass/epoxy (elastic mismatch, but no thermal residual stresses), and

iii) plaster-of-paris (no elastic mismatch, and no thermal residual stresses).

The work has important implications on the future design of composites consisting of weak interlayers. The objective is to understand the brittle fracture behaviour of this class of materials to allow for design of strength and reliability.

Chapter 3. Modeling

3.1 Mathematical Modeling Using Fracture Mechanics

This modeling work is an attempt to explain the observed fracture behaviour of ceramic laminates that contain weak interlayers. The attempts of other researchers have failed to give consistent predictions of whether a given sample will fracture in catastrophic or multi-stage manner. The work of Cook and Gordon (1964), Kendall (1975) and He and Hutchinson (1989a) used theoretical calculations to determine a critical interface toughness ratio required for crack deflection. This criterion was not sufficient to promote multi-stage fracture in the zirconia/lanthanum aluminate laminates fabricated and tested by Bissinger (1995). The predictions based on thermal residual stress measurements proposed by Oechner et al (1996) fail to explain the fracture behaviour of glass/epoxy composites.

The focus of this work is a consideration of the cracks involved in the fracture process. It is important to realize that crack deflection within a weak interlayer is only half of the solution to the problem of catastrophic failure. Multi-stage fracture behaviour is only possible if all *other* cracks in the material are prevented from propagating unstably. This modeling work deals with three

different cracks; (i) the main ("primary") crack responsible for failure of the surface layer of the composite, (ii) the weak interlayer crack ("secondary"), which reduces load significantly during deflection, and (iii) the ("tertiary") crack in the next strong layer, which must be prevented from propagating. These cracks are shown schematically in Figure 3.1-1.

If a weak layer is sufficiently thin (~1% of beam thickness) it can be treated as a weak interface. The difference in moduli of the two materials will have a negligible affect on the overall stiffness of the beam, so it can be ignored in the load/deflection calculations. The composite is treated as a monolithic material that contains a two-dimensional plane of weakness. Crack tip stress concentrations surrounding the main crack, the effect of modulus mismatch, and thermal residual stresses must all be considered before the simplification can be made. The approach is legitimate only for thin interlayers and/or relatively large interlayer crack sizes.

The stress perpendicular to the layers is important to fracture behaviour as it is responsible for opening cracks in the weak interlayer. Stresses must be equal on either side of the (two-dimensional) interfaces between materials, to ensure mechanical equilibrium. If the interlayer is thin there is a negligible change in this perpendicular stress *across* the interlayer. Thermal residual stresses are zero in this direction.

The stress parallel to the layers affects propagation of the main crack, but does not affect the weak interlayer cracks. The thermal residual stresses

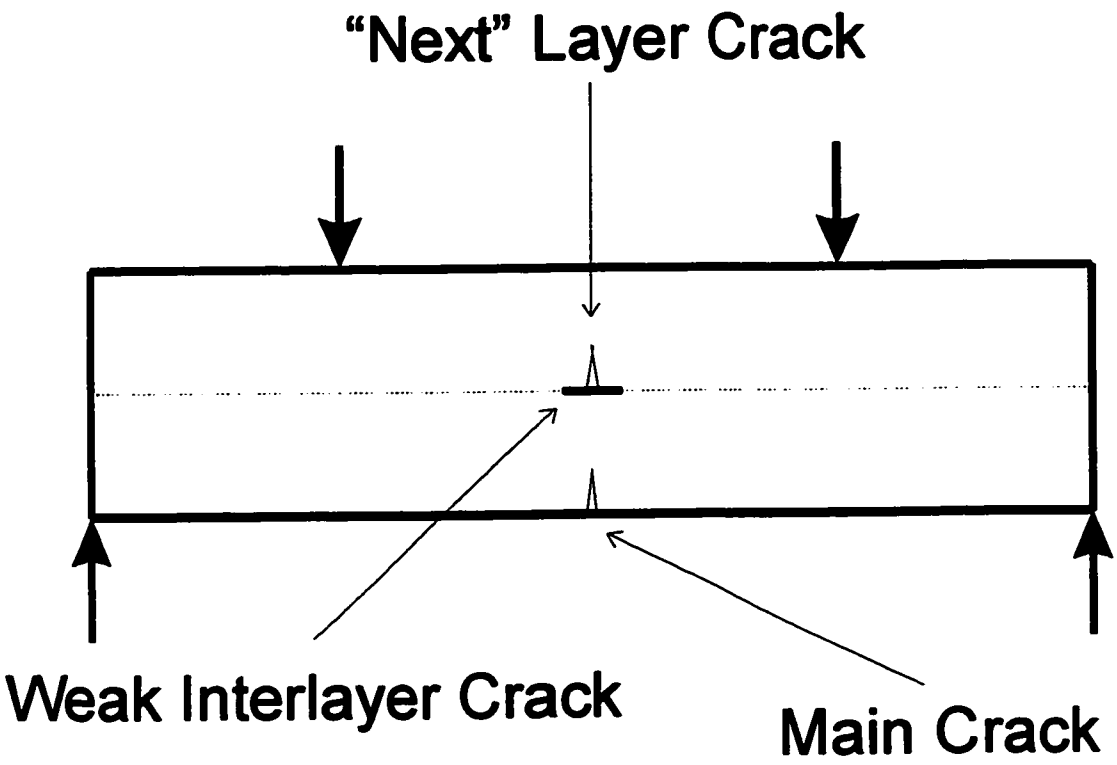

Figure 3.1-1. A schematic of the three cracks under consideration in the modeling work.

in the strong layers are negligible, due to the thickness ratio of the composites. This will have no significant effect on the overall strength of the composite. Thermal residual shear on the interlayers can also be neglected. Shear *forces* act in the same direction on either side of the interlayers. Therefore, the shear stress changes sign across the interlayer. In the centre the shear stress is zero.

In this modeling, it is assumed the three cracks are all in the centre of the beam. This is not always correct, but is necessary to simplify the problem. The entire inner span is subjected to the maximum calculated stress during four-point bend testing. If the surface layer fails at the centre of the beam, either by chance or due to indentation, the calculations are relatively accurate. If the surface layer fails near to one of the loading pins, the calculations are less accurate due to the asymmetry of the geometry. The positions of the weak interlayer and "next" strong layer cracks have a comparable influence.

All three cracks will affect the fracture behaviour of the composite. The primary crack governs the overall load/stress on the material before fracture. It will be shown this crack also influences the initiation of the weak interlayer crack propagation. The secondary crack determines the weakness of the interlayer, and therefore influences the extent of deflection. The tertiary crack determines the strength of the "next" layer in the laminate. This final crack is perhaps the most critical, in that it must *not* propagate if multi-stage fracture is to be achieved. Flaw sizes are difficult to control, so fracture mechanics modeling can only

predict trends in behaviour. The statistical nature of flaw size distributions can have a significant effect.

Consider a composite "sandwich", consisting of two strong layers with an infinitely thin weak interlayer, as shown in Figure 3.1-2. The interlayer is treated as a two-dimensional plane (or interface) of low toughness material. It is assumed the interlayer is sufficiently thin to ignore its modulus in both beam calculations and crack tip stress fields, as discussed earlier. Before fracture of the first layer, the composite can be analyzed as a monolithic beam subjected to a four-point bend test. The deflection of the beam for a given load can be calculated using classical beam mechanics (Timoshenko and Gere, 1973);

$$\delta = \frac{P_1 L^3}{8Ebh^3} \qquad (3.1\text{-}1)$$

where δ is the deflection of the loading points, P_1 the load at the onset of fracture, L the outer span, b the breadth and h the height. In this case the inner span is half the outer span.

The load experienced by the material drops during fracture of the surface layer and its subsequent delamination. The change is effectively instantaneous, so calculations assume a constant deflection. The new load on the cracked beam can be approximated using classical beam mechanics. The calculation ignores stress concentrations associated with the initial deflection of the crack, and assumes zero stress in the delaminated portions of the cracked layer.

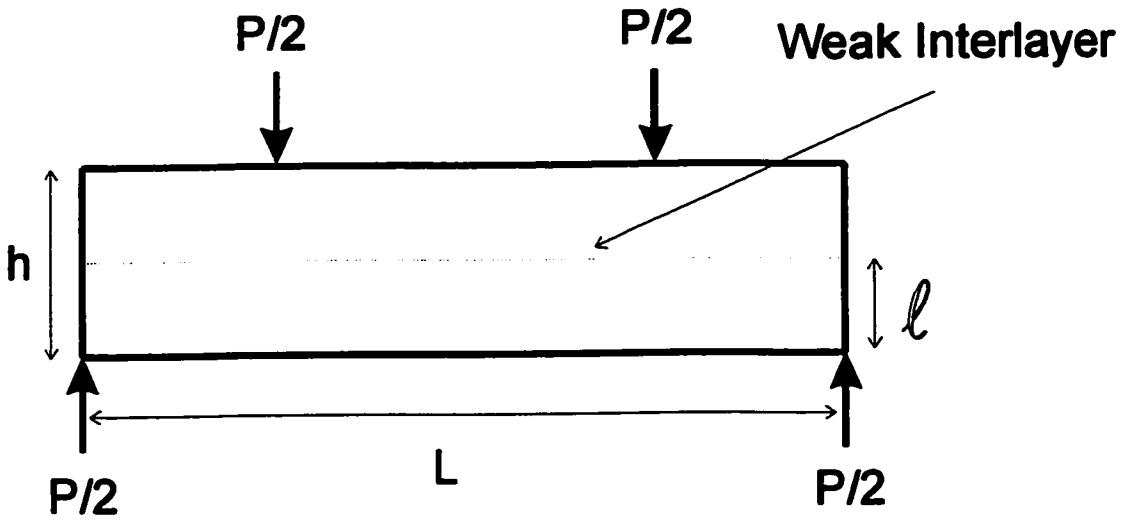

Figure 3.1-2. A schematic of an uncracked composite "sandwich". The beam is long and slender enough (L/h≥8) to use classical beam equations in the analysis; shear in the centre span is zero.

The beam is now treated as three sections, as shown in Figure 3.1-3. The three sections are defined by *x*, the distance along the beam *from its centre point*. Consider; (i) the central cracked region, where $0 \le x \le c$, (ii) the central uncracked region, where $c \le x \le L/4$, and (iii) the outer span, where $L/4 \le x \le L/2$. Note that for this derivation $c \le L/4$.

For Region 1 (using classical beam mechanics);

$$M_1 = \frac{P_2 L}{8} \tag{3.1-2}$$

where M_1 is the moment acting at the point *x*, and P_2 the load on the beam after cracking. This leads to;

$$\theta_1 = \int \frac{M_1}{EI_1} dx = \frac{3P_2 Lx}{2Eb(h-\ell)^3} + C_1 \tag{3.1-3}$$

and

$$\delta_1 = \int\int \frac{M_1}{EI_1} dx^2 = \frac{3P_2 Lx^2}{4Eb(h-\ell)^3} + C_1 x + C_2 \tag{3.1-4}$$

where θ_1 is the slope of the beam and δ_1 the deflection of the beam at point *x*, I_1 the second moment of area, ℓ the thickness of the surface layer, and the *C*'s are integration constants. Note, the subscript denotes the region under consideration.

Similarly, for Region 2;

$$M_2 = \frac{P_2 L}{8} \tag{3.1-5}$$

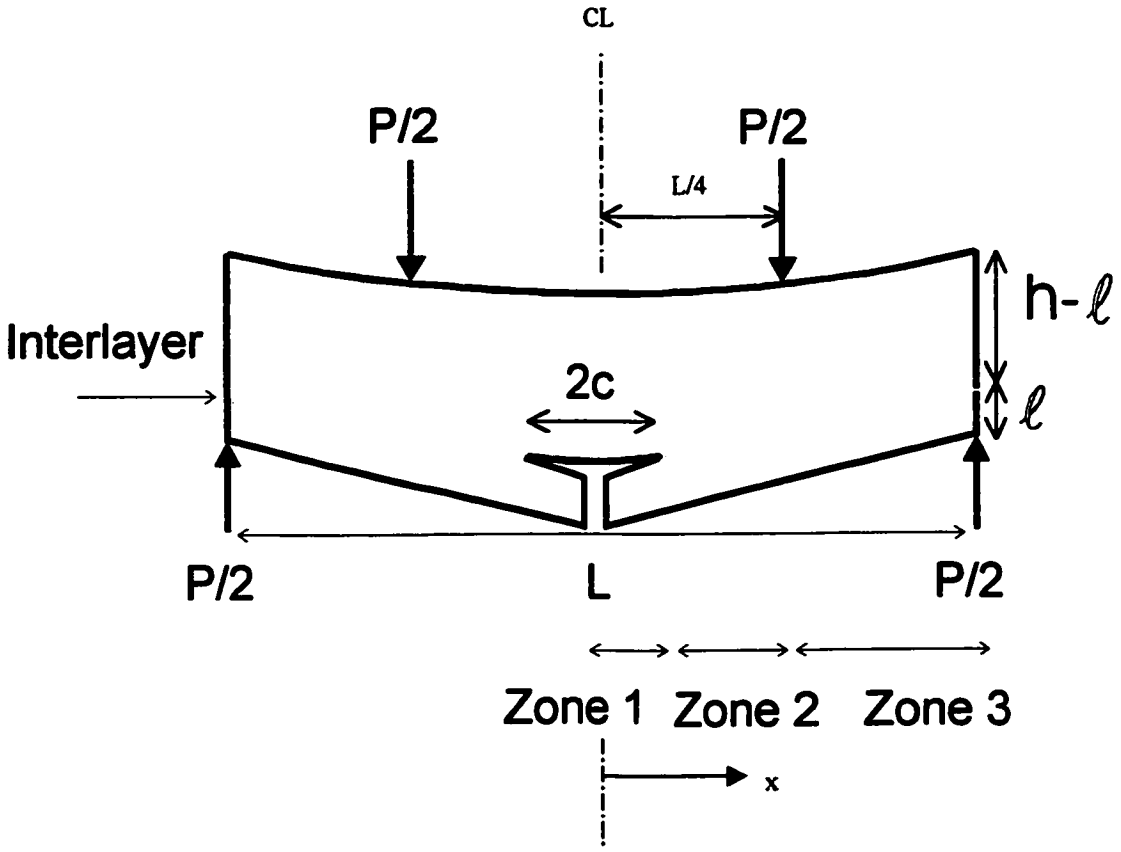

Figure 3.1-3. A schematic of a cracked composite "sandwich". Although similar in geometry, this is *not* the same as the work of Charalambides (1989). This case considers the load drop during catatstrophic failure and subsequent delamination of an *un-notched* surface layer, at constant deflection. Charalambides considered the steady state strain energy release rate of a *cut-through* surface layer, at constant load.

$$\theta_2 = \int \frac{M_2}{EI_2} dx = \frac{3P_2 Lx}{2Ebh^3} + C_3 \qquad (3.1\text{-}6)$$

$$\delta_2 = \int\int \frac{M_2}{EI_2} dx^2 = \frac{3P_2 Lx^2}{4Ebh^3} + C_3 x + C_4 \qquad (3.1\text{-}7)$$

and Region 3;

$$M_3 = \frac{P_2}{2}\left(\frac{L}{2} - x\right) \qquad (3.1\text{-}8)$$

$$\theta_3 = \int \frac{M_3}{EI_3} dx = -\frac{3P_2 x^2}{Ebh^3} + \frac{3P_2 Lx}{Ebh^3} + C_5 \qquad (3.1\text{-}9)$$

$$\delta_3 = \int\int \frac{M_3}{EI_3} dx^2 = -\frac{P_2 x^3}{Ebh^3} + \frac{3P_2 Lx^2}{2Ebh^3} + C_5 x + C_6 \qquad (3.1\text{-}10)$$

The integration constants can be calculated by equating the deflections and slopes of Regions 1 and 2 at $x=c$, and Regions 2 and 3 at $x=L/4$. The slope is zero at $x=0$ (symmetrical beam) and the deflection zero at $x=L/2$. The change in load during instantaneous fracture can be calculated;

$$\frac{P_2}{P_1} = \frac{1}{1 + \frac{3c}{L}\left(\frac{h^3}{(h-\ell)^3} - 1\right)} \qquad (3.1\text{-}11)$$

Note that the equation is not valid for $c \approx 0$. The maximum relative stress on the centre span of the beam becomes;

$$\frac{\sigma_2}{\sigma_1} = \frac{1}{1 + \frac{3c}{L}\left(\frac{h^3}{(h-\ell)^3} - 1\right)} \frac{h^2}{(h-\ell)^2} \qquad (3.1\text{-}12)$$

It is this stress which is critical to the fracture behaviour of the composite. If the stress σ_2 is greater than the fracture stress of the centre span, the next layer in the laminate will fracture, *regardless* of the crack deflection. The strength of this region varies, depending on the flaw size distribution in the material.

The extent of interlayer cracking clearly has a major effect on the behaviour of the material. Significant cracking reduces the load (and stress) on the material, which encourages multi-stage fracture. However, if the interlayer cracking is minimal, the region of material subjected to high stress is small. Small stressed regions are, on average, stronger than large stressed regions (according to Weibull statistics). This indirectly encourages multi-stage fracture. The complex stress field in the region of the crack tip in the initial stages of deflection complicates the calculation of the balance point of these offsetting effects.

It is possible to calculate the extent of weak interlayer cracking necessary for multi-stage fracture based on the relative strengths of the two layers. Manipulation of Equation 3.1-12 yields;

$$\left(\frac{c}{L}\right)_{crit} = \frac{1}{3}\frac{\sigma_{f1}}{\sigma_{f2}}\frac{\left(\dfrac{h^2}{(h-\ell)^2}-1\right)}{\left(\dfrac{h^3}{(h-\ell)^3}-1\right)} \qquad (3.1\text{-}13)$$

where $(c/L)_{crit}$ is the critical extent of weak interlayer cracking necessary for multi-stage fracture, and σ_{f1} and σ_{f2} the strengths of the surface and "next" layer respectively. Figure 3.1-4 is a plot of the critical (c/L) ratio as a function of the

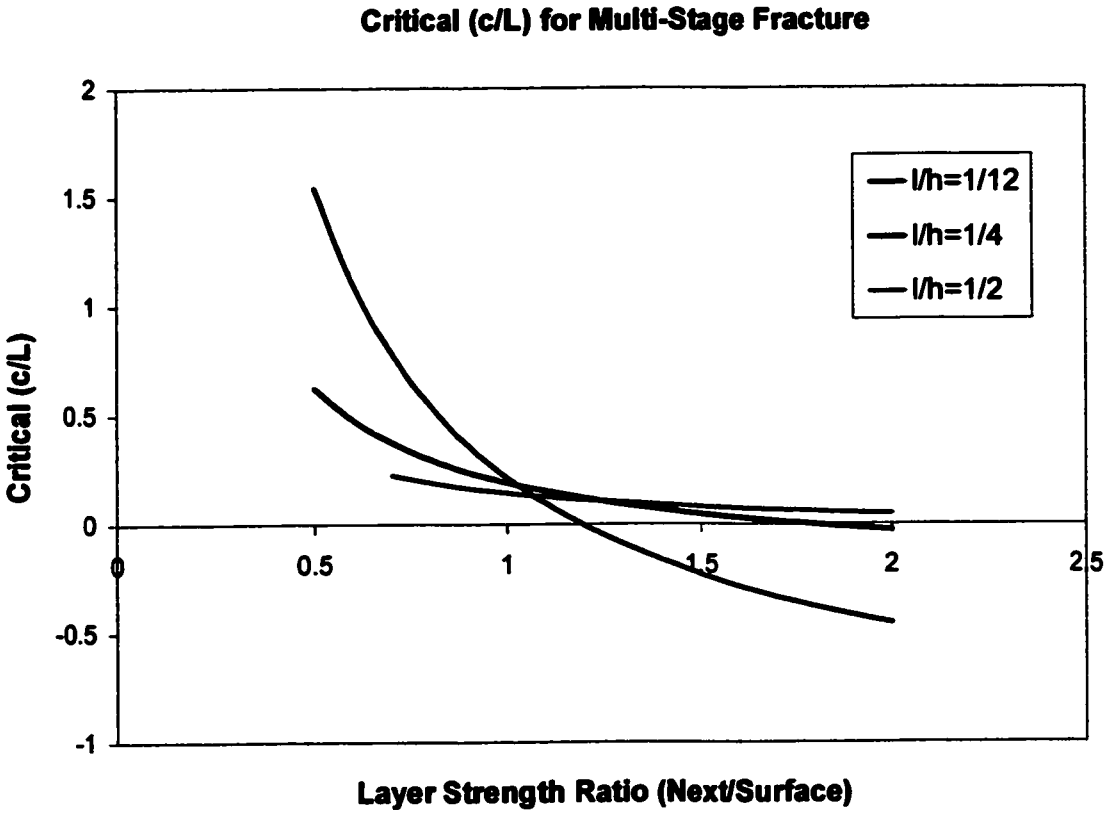

Figure 3.1-4. The critical (c/L) ratio for multi-stage fracture as a function of layer strength ratio. The stronger the next layer in the composite (right side of figure), the less interlayer cracking is necessary for multi-stage fracture behaviour.

layer strength ratio. The next step in the modeling is to determine appropriate values for the two strengths.

Indents were used on sample surfaces during the experimental work (Chapter 4) to provide a variety of crack sizes (and therefore strengths). Following Equation 2.1.5-3, experimental data points and non-linear regression analysis (FitAll Non-Linear Regression Analysis, MTR Software) were used to calculate the strength of samples as a function of indent load;

$$\sigma_{fl} = A \cdot P_{ind}^{\,n} \tag{3.1-14}$$

where P_{ind} is the indent load, and A and n regression constants. The initial flaw size is then calculated by manipulation of Equation 2.1.2-13;

$$a_0 = \frac{1}{\pi}\left(\frac{K_{SC}}{Y\sigma_{fl}}\right)^2 \tag{3.1-15}$$

where a_0 is the initial flaw size, and K_{SC} the critical stress intensity (toughness) of the strong surface layer material. The compliance factor, Y, is that of a semi-circular flaw.

The *"a"* crack size increases and the load on the beam decreases during fracture of the surface layer. The load change experienced by the beam can be approximated as;

$$\frac{P_2}{P_{fl}} \approx 1 - \left(\frac{a}{h}\right)^2 \tag{3.1-16}$$

where P_2 is the load on the beam during fracture, P_{fl} the initial fracture load, a the propagating crack size, and h the height of the beam. This equation is a

simplification of a theoretically justifiable equation that will be derived in Section 3.2.

The stress intensity at the tip of the propagating crack can then be approximated using Equations 2.1.2-12, 2.1.4-1 and 3.1-16;

$$\frac{K}{K_C} = Y\frac{3\left[1-\left(\frac{a}{h}\right)^2\right]L}{4bh^2}\sqrt{\pi a} \qquad (3.1\text{-}17)$$

where K is the stress intensity at the crack tip, K_C the critical stress intensity (toughness) of the strong surface material, and a the size of the propagating crack.

The stress intensity at the tips of the weak interlayer crack is estimated using Green integral functions (Equation 2.1.6-2). For the mode I component;

$$K_{IW} = \frac{2}{\sqrt{\pi c}}\int_0^{c_0}\frac{\sigma_x(y)dy}{\sqrt{1-\left(y/c_0\right)^2}} \qquad (3.1\text{-}18)$$

For the mode II component;

$$K_{IIW} = \frac{2}{\sqrt{\pi c}}\int_0^{c_0}\frac{\tau_{xy}(y)dy}{\sqrt{1-\left(y/c_0\right)^2}} \qquad (3.1\text{-}19)$$

where K_{IW} and K_{IIW} are the stress intensities on the interlayer crack tips due to the presence of the main crack tip, and c_0 the initial interlayer half crack size. The normal stress σ_x and shear τ_{xy} are the near-crack tip stresses, given earlier as Equation 2.1.6-9. In this case there must be a conversion from polar to Cartesian

coordinates. The weak interlayer is perpendicular to the main crack tip, at a distance "ℓ-a" away (see Figure 3.1-5). Along the plane of the interlayer;

$$x = \ell - a \tag{3.1-20}$$

$$y = (\ell - a)\tan\theta \tag{3.1-21}$$

The two stress intensities are used to calculate the effective stress intensity at the tips of the weak crack;

$$K_{effW}^2 = K_{IW}^2 + K_{IIW}^2 \tag{3.1-22}$$

When this value equals the critical stress intensity of the weak material, the weak interlayer crack also propagates.

It must be noted that this is an approximation. The actual stress field equations are comprised of several terms, all of which are ignored except the leading term, which is expected to dominate. No attempt has been made to adjust the equations to account for bending of the beam. It is assumed that the main crack tip is close to the interlayer before secondary cracking, and that the leading term overwhelms other minor terms. This approximation is also addressed in Section 3.2.

As the main crack tip propagates the stress intensity increases. If the interlayer is sufficiently weak, then it too cracks. This interlayer cracking reduces the overall stress experienced by the beam and prevents stress concentrating on cracks in the next strong layer. The size of the main crack, at the point at which the interlayer crack begins to propagate is termed "a_{crit}".

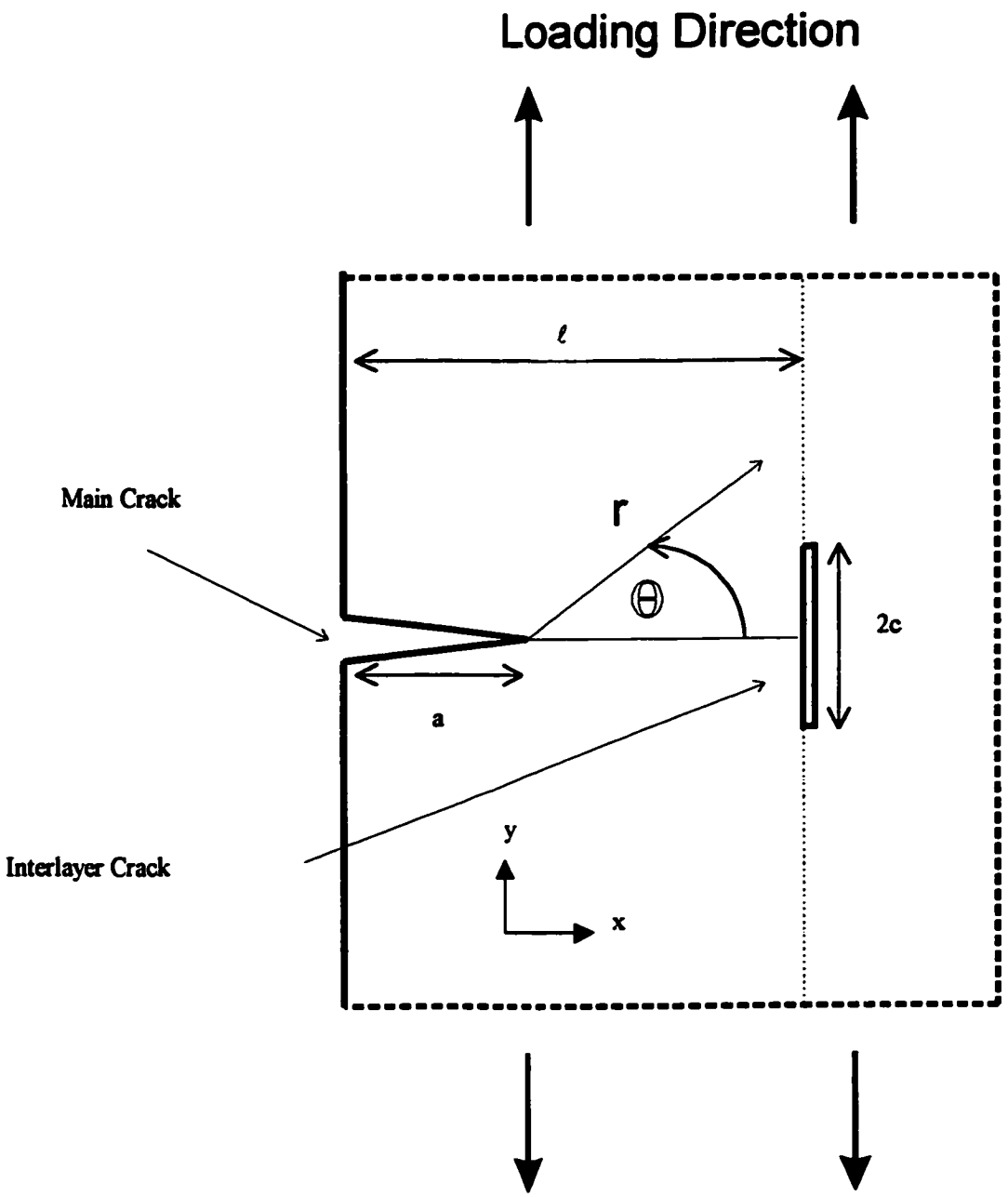

Figure 3.1-5. A schematic of the crack tip and weak interlayer crack geometry.

The two cracks propagate simultaneously. Based on the work of Mott (1948), and others, it is possible to estimate the velocity of the propagating cracks as a function of crack size (see Section 2.1.2). The presence of a weak interlayer will affect crack velocity calculations, but it is assumed the change will be minimal. In this work the equations of Dulaney and Brace (1960) are used, which simplify the mathematics;

$$\frac{da}{dt} \approx 0.38\sqrt{\frac{E}{\rho}}\left(1-\frac{a_0}{a}\right) \tag{3.1-23}$$

By integration it is possible to estimate the time for the main crack to completely fracture the surface layer, *after* initiation of the weak interlayer crack propagation;

$$0.38\sqrt{\frac{E}{\rho}}\int_0^t dt = \int_{a_{crit}}^{\ell} \frac{da}{\left(1-\frac{a_0}{a}\right)} \tag{3.1-24}$$

and

$$\Delta t \propto (\ell - a_{crit}) + a_{crit} \ln\left|\frac{\ell - a_0}{a_{crit} - a_0}\right| \tag{3.1-25}$$

where Δt is the crack propagation time. Note, this time depends on several factors; the surface layer thickness, the initial flaw size (and therefore strength of the beam), and indirectly on the weak interlayer crack size and toughness.

An equivalent calculation can be done for the weak interlayer crack. The crack stability conditions are considerably different to those of the main crack, but the necessary equations are not available to determine an accurate time of propagation. An equation in the form of 3.1-25 is deemed an acceptable

approximation. It will be shown in Section 3.2 that the weak interlayer crack propagates unstably.

The modulus and density used in both calculations are those of the strong material. The bulk of the strain energy shed during crack propagation is associated with the strong layers. This assumption also relies on thin interlayers.

The two cracks propagate for the same amount of time. Equating the two time equations allows the extent of weak interlayer cracking to be estimated. This influences the fracture behaviour of the composite. The estimated value is compared to that calculated using Equation 3.1-13. If the extent of interlayer cracking is sufficient, then multi-stage fracture is achieved. If insufficient, the stress on the next layer in the composite is high enough to cause a fatal stress concentration on one of its inherent flaws, and the composite fails catastrophically *despite* crack deflection along the weak interlayer.

The fracture is dependent on the strength of the next strong layer in the laminate. As discussed in Section 2.1.3, the Weibull modulus is an important parameter for gauging mechanical reliability. As the weak interlayer crack deflects, there is both a changing load suffered by the beam *and* a changing volume of material suffering that load. Following Equation 2.1.3-1, the fracture strength of the next layer in the composite is estimated as;

$$P_S = \exp\left[-\frac{c/L}{L}\left(\frac{\sigma_{f2}}{\sigma_0}\right)^{m_{eff}}\right] \qquad (3.1\text{-}26)$$

where σ_0 and m_{eff} are determined by linear regression of experimental data. This equation is a simplification. It does not account for bending, and assumes test samples are the same geometry. The effective Weibull modulus, m_{eff}, is a useful approximate value calculated by regression analysis from experimental data.

The above equations are combined to determine a critical (ℓ/h) ratio for multi-stage or catastrophic failure, as a function of indent load applied to the surface layer. The geometry of the beam and mechanical properties of the two materials in the composite must also be considered in the calculation. The result is a "map" of fracture behaviour (see Figure 3.1-6).

The fracture map determined by the model consists of two zones; the catastrophic zone and the multi-stage zone. The critical boundary adjusts with composite material choice, but the shape is consistent. The catastrophic zone is the upper left area on the map, representing small surface flaw sizes and/or thick surface layers. Under these conditions the fracture strength of the composite is very high, and insufficient load is shed to prevent fracture of the relatively thin (and therefore weak) next strong layer. The main crack accelerates quickly, not allowing the interlayer to propagate appreciably. The multi-stage zone is the lower right area on the map, representing large surface layer flaw sizes and/or thin surface layers. The fracture strength of the composite is low, but the relatively thick (and therefore strong) next layer can withstand the load transfer. The main crack accelerates relatively slowly, giving the interlayer crack sufficient time to propagate and further reduce load.

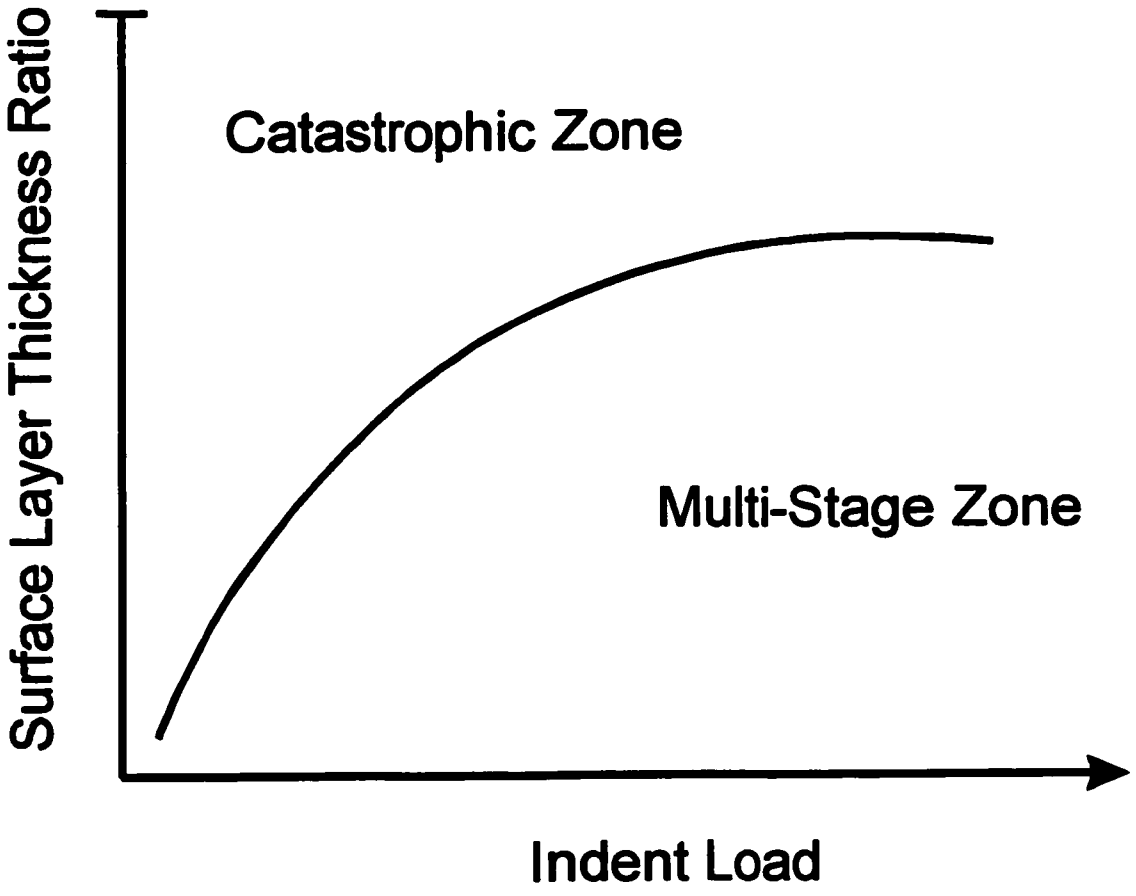

Figure 3.1-6. A schematic of the fracture map determined using the model.

The critical boundary shown in Figure 3.1-6 is based on the average strength of the strong material. The natural distribution of flaw sizes will affect the position of this boundary. If the next layer in the composite is stronger or weaker than average, the curve must be adjusted accordingly. Dashed line curves can be added to the fracture map to show the affect of strength variability.

A typical method of demonstrating reliability is to show error bars on data points. Error bars typically represent a spread of one standard deviation. One standard deviation theoretically encompasses 68% of the data values used to calculate the average. When using Weibull statistics, and Equation 3.1-26 in particular, this represents survival probabilities of P_S=16% and P_S=84%. Recalculation of the critical boundary in the model using these values adjusts the relative position of the curve. A similar calculation can be done for two and three standard deviations (95% and 99.8%). The "error" curves show the mechanism of multi-stage fracture is very sensitive to the Weibull modulus of the strong material. This must be considered in analysis of experimental data.

Determination of the critical ℓ/h ratio results in a transcendental function which cannot be solved by standard mathematical techniques. A computer program was written in Pascal 7.0 to solve the problem. A flow chart for the program is given as Figure 3.1-7, and the code is included as Appendix I.

The program determines the critical boundary using an iterative approach. The material properties and geometry of the composite are defined at

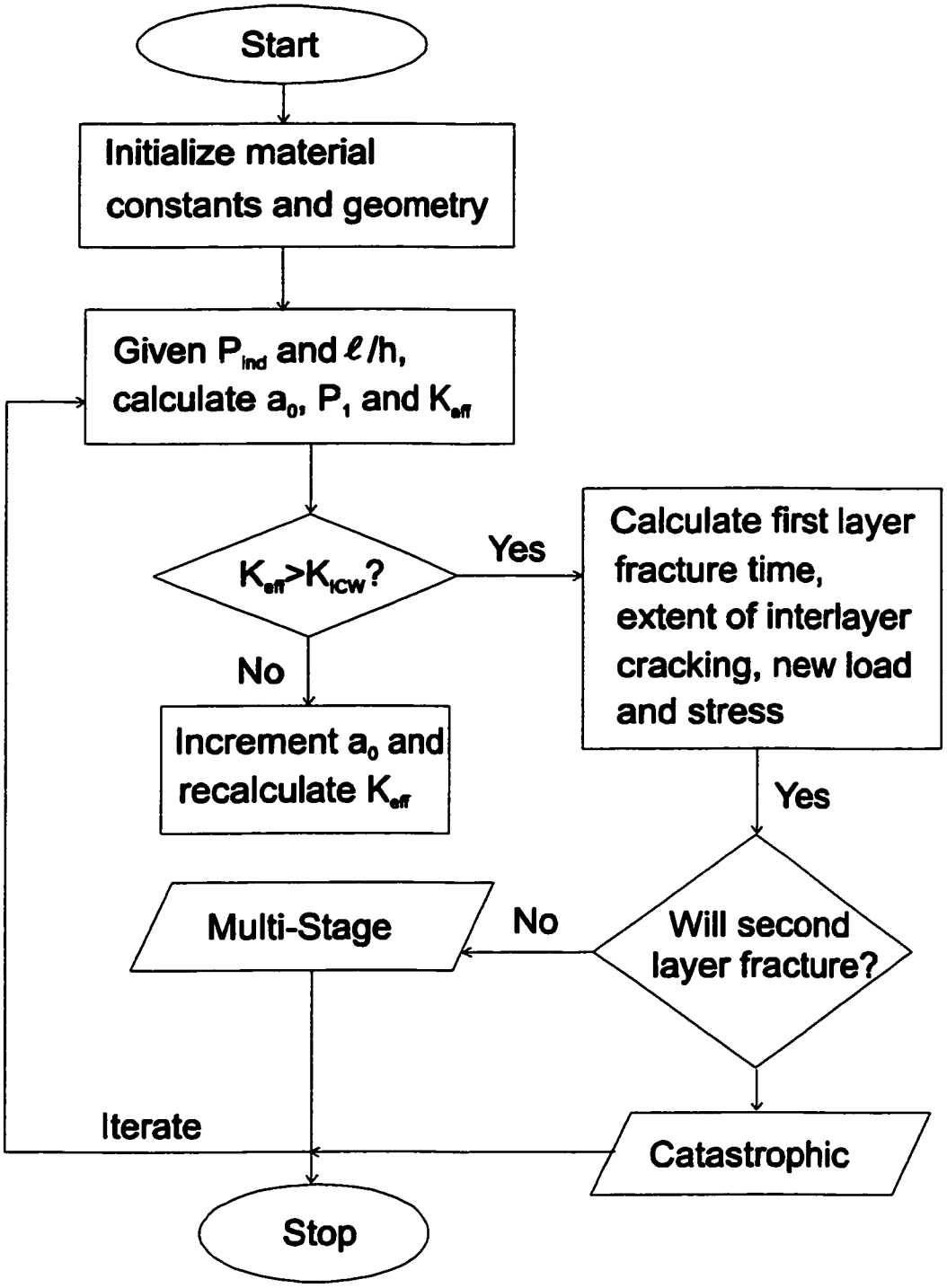

Figure 3.1-7. A flow chart for the program used to calculate the critical ℓ/h boundary.

the start at the program. An initial surface layer flaw size is estimated as a function of indent load, and the fracture stress and load calculated. The critical extent of weak interlayer cracking required for multi-stage fracture is determined, based on the layer thickness (ℓ/h) ratio. The stress intensity at the main crack tip is calculated, and then used to estimate the stress intensity at the interlayer crack tips. The program iterates, recalculating the stress intensities as the main crack propagates. When the weak interlayer cracks begin to extend, the velocity equations are invoked to estimate the extent of weak interlayer cracking. This is compared to the calculated critical value. The comparison determines whether the composite fails in a catastrophic or multi-stage fashion. The program is iterated for various combinations of initial indent load and layer thickness ratio. The program is repeated to produce the "error bar" curves.

3.2 Finite Element Analysis

Finite element analysis is particularly well suited to the present work. The complex geometry of beams containing both surface and interlayer cracks requires that assumptions be made if a fracture mechanics approach is used. The complex geometry of the present work can be easily defined mathematically, and a compliance (or stiffness) equation developed as a function of both crack sizes. This equation can be used to predict the onset of both surface and interlayer cracking, and the strength and reliability of the composite.

In this work the fracture of laminates is considered. Bend tests are conducted under displacement controlled conditions so multi-stage fracture behaviour is possible. The fracture is effectively instantaneous, it is assumed that constant displacement conditions are valid. The beam is defined using an appropriate mesh, and subjected to a simulated loading-pin displacement. The global stiffness matrix is constructed and solved. The most important value calculated is the load associated with the simulated pin displacement. The process can be iterated for beams with various crack configurations but the *same simulated pin displacement*. The calculated pin loads are then used to construct stiffness functions for the various geometries, or compared to theoretical expectations. All values are normalized to simplify comparisons.

The finite element calculations were done using custom software, written using Matlab 5.0. A flowchart for the code is given as Figure 3.2-1, and the code

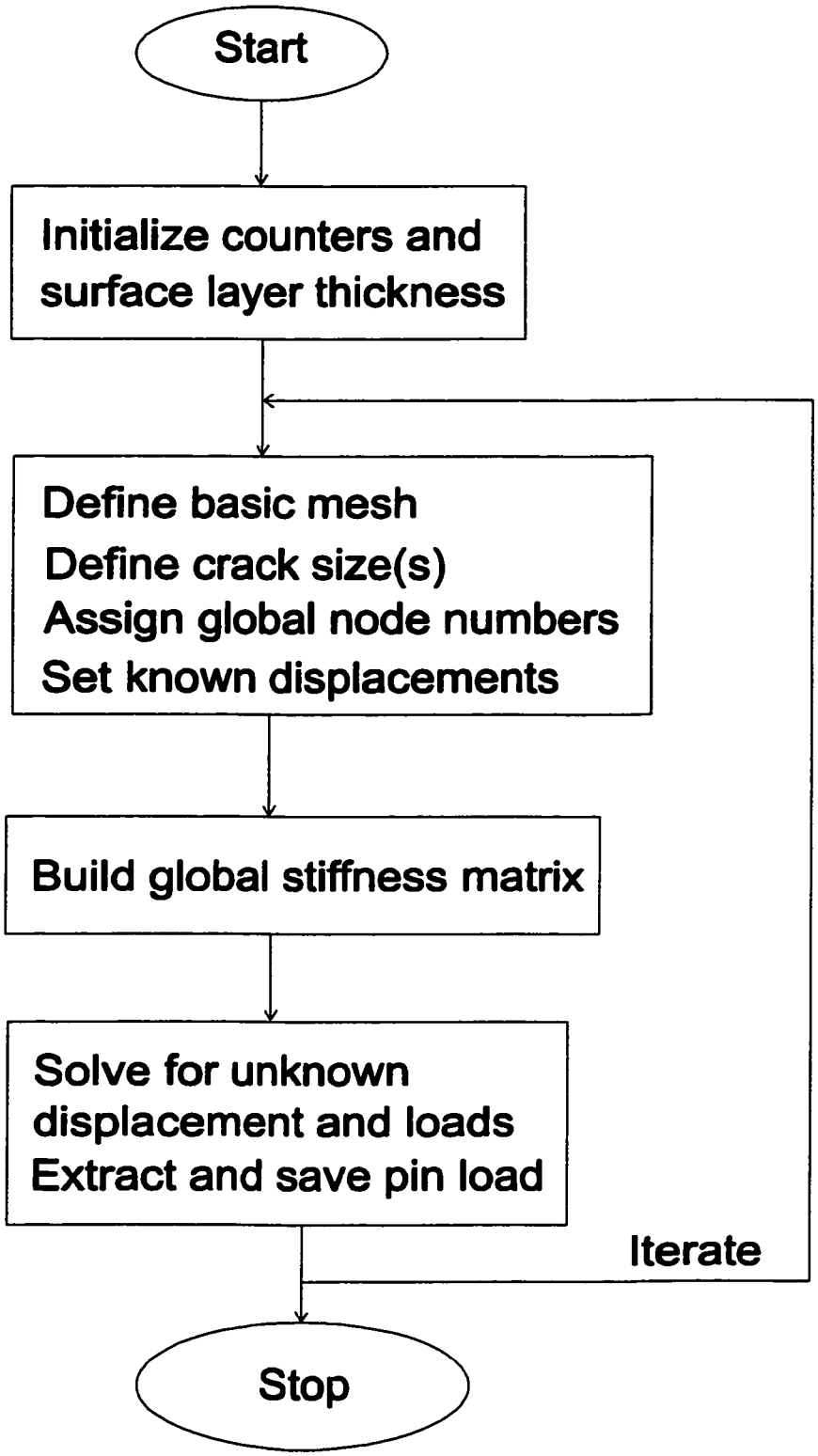

Figure 3.2-1. A flowchart for the custom finite element code.

given as Appendix II. Only half of the beam is considered in each case, due to the symmetry of the beams and the desire for calculation efficiency.

The accuracy of finite element calculations depends on the number of elements used. More elements yield a more accurate solution, but cost more in computing time. Simple beam deflection calculations were done using various mesh sizes to determine an appropriate number of elements to use in the simulations. It was decided to use 720 elements in each calculation. This represents a <1% error on load calculations, compared to theoretical. Normalization of all values further reduces this problem.

Three different scenarios were considered; (i) catastrophic failure of a beam, (ii) delamination after fracture of a surface layer, and (iii) pre-cracking of the weak interlayer during surface layer crack propagation. Sample meshes for the three scenerios are given as Figure 3.2-2. The details of the modeling are explained in the following sections.

3.2.1 Catastrophic Failure

The finite element code was used to calculate the load required to deform a given beam a given displacement. This can be used to calculate the work done on the beam;

$$W = \frac{1}{2}P\delta \qquad (3.2.1\text{-}1)$$

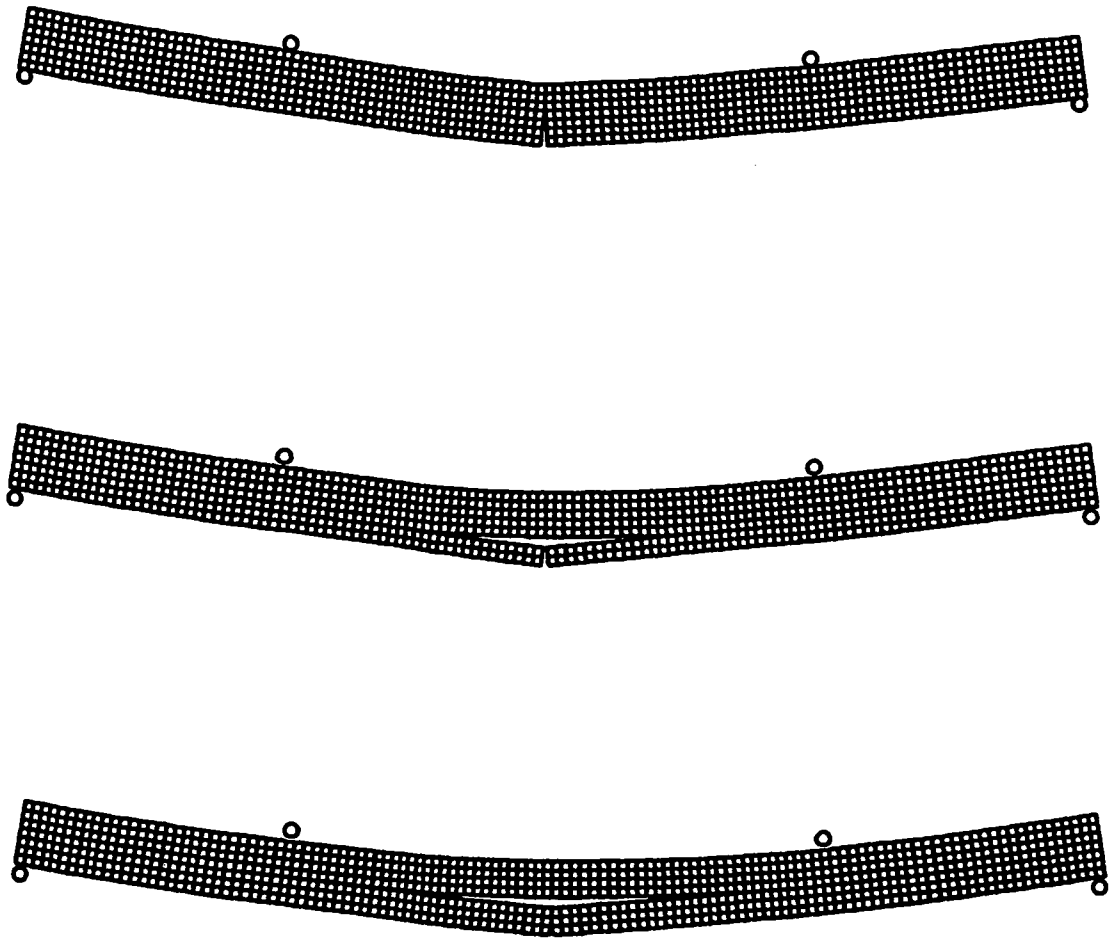

Figure 3.2-2. Sample meshes for the three scenerios simulated using finite element methods.

where W is the work done by the loading pins, P the load and δ the applied displacement. This is equivalent to the strain energy in the beam. Therefore, the strain energy release rate can be determined as the derivative of the work done with respect to crack size. For constant displacement conditions, this leads to;

$$G_a \propto -\frac{dP}{da} \tag{3.2.1-2}$$

where G_a and a are the strain energy release rate and size of the main crack. This can also be related directly to the strain energy. Following Equation 2.1.2-3;

$$G_a = -\frac{Y^2\sigma^2\pi a}{2E} \propto Y^2P^2a \tag{3.2.1-3}$$

where Y is the compliance function, σ the stress and E the modulus. Combining Equations 3.2.1-2 and 3.2.1-3 yields;

$$\frac{dP}{P^2} \propto -Y^2ada \tag{3.2.1-4}$$

This can be integrated to calculate the change in load as a crack propagates. Initially, it is assumed the compliance function is not a function of the crack length. Consider the following;

$$\int_{P_1}^{P_2} \frac{dP}{P^2} \propto -Y^2 \int_0^a ada \tag{3.2.1-5}$$

This serves as a first order approximation. This leads to;

$$\frac{P_2}{P_1} \approx 1 - Y^2a^2 \tag{3.2.1-6}$$

Given the boundary condition that $P_2 \rightarrow 0$ as $a/h \rightarrow 1$, an appropriate compliance function is $Y=1/h$. Therefore, the finite element calculated load values were compared to the simple parabolic equation;

$$\frac{P_2}{P_1} \approx 1 - \left(\frac{a}{h}\right)^2 \qquad (3.2.1\text{-}7)$$

This can be related to Equation 3.2.1-2 to calculate the strain energy release rate during catastrophic failure of the beam.

$$G_a \propto -\frac{dP}{da} \approx \frac{2a}{h^2} \qquad (3.2.1\text{-}8)$$

Fracture occurs when the strain energy release rate exceeds the critical value for the strong material, G_{aC}. The strain energy release rate increases as the crack size increases, so the crack propagates unstably.

The strain energy release rate can also be used to derive a term for the crack velocity. The difference between the instantaneous and critical strain energy release rates is proportional to the kinetic energy of the propagating crack,

$$U_{kinetic} \propto v_a{}^2 \propto G_a - G_{aC} \qquad (3.2.1\text{-}9)$$

where v_a is the main crack velocity. Therefore;

$$v_a{}^2 \propto \frac{2a}{h^2} - \frac{2a_0}{h^2} = \frac{2}{h^2}(a - a_0) = \frac{2}{h^2}\left(1 - \frac{a_0}{a}\right) \qquad (3.2.1\text{-}10)$$

and

$$v_a \propto \sqrt{1-\frac{a_0}{a}} \qquad (3.2.1\text{-}11)$$

The velocity equation derived is the same form as Equation 2.1.2-17.

The assumption that the compliance function is not a function of crack size is an acknowledged approximation, so the load values calculated by finite element analysis were fitted to regression equations in the form;

$$\frac{P_2}{P_1} = 1 + \beta_1\left(\frac{a}{h}\right)^2 + \beta_2\left(\frac{a}{h}\right)^4 + \ldots + \beta_n\left(\frac{a}{h}\right)^{2n} + \text{error} \qquad (3.2.1\text{-}12)$$

where the βs are regression coefficients. Only even numbered exponents were used. The load equation is differentiated to determine the strain energy release rate, and then square rooted to determine the stress intensity factor. A linear term cannot be included, as it would violate the requirement that $G_a=0$ at $a/h=0$. The above equation corresponds to an equivalent *"nth"* order simple polynomial compliance function for a stress intensity factor. The higher order terms allow a steeper gradient to be fitted to the data, and leads to a more refined solution. The effect of increasing order of polynomial was considered in selecting the order of the regression equations used in Section 3.2.3.

The convergence of regression equations with respect to the number of elements was also considered for the simple four-point bend test geometry. The finite element calculation of load values for increasing crack size was repeated using an increasing number of elements. The resulting sets of data were regressed to a fourth order polynomial equation. Convergence of the regression

equations was used to determine the number of elements necessary for an acceptable solution.

3.2.2 Delamination Fracture

The second scenario considered was that of delamination after complete fracture of the surface layer. The change in load was determined earlier in Section 3.1, and given as a function of interlayer crack size and beam geometry as Equation 3.1-11. The finite element code was used to define appropriate meshes and calculate loading-pin loads. Again, constant displacement of the pins was assumed. Calculated values were normalized and compared to Equation 3.1-11.

The load equation can also be used to calculate a strain energy release rate of the interlayer crack (after initial fracture of the surface layer). Similar to Equation 3.2.1-8;

$$G_c \propto -\frac{dP}{dc} = \frac{\frac{3}{L}\left(\frac{h^3}{(h-\ell)^3}-1\right)}{\left[1+\frac{3c}{L}\left(\frac{h^3}{(h-\ell)^3}-1\right)\right]^2} \qquad (3.2.2\text{-}1)$$

where G_c is the strain energy release rate of the interlayer crack. Fracture occurs while this exceeds the critical strain energy release rate for the weak interlayer material, G_{cC}. In this case the strain energy release rate decreases as the crack extends and so the crack may be stabilized.

Equation 3.2.2-1 can be used to estimate the point at which the delamination crack stops propagating. There are two approaches to this calculation. The first is to assume static conditions; the crack stops when its strain energy release rate falls below the critical value for the interlayer material;

$$G_{cC} \geq -\left.\frac{dP}{dc}\right|_{c_{stat}} = -\left.\frac{dP}{dc}\right|_{c_0} \qquad (3.2.2\text{-}2)$$

where c_{stat} is the crack arrest point based on static conditions. This provides a lower estimate of the crack extension. The second approach to the calculation assumes dynamic conditions; the crack momentum propagates the crack further until the kinetic energy is absorbed by fracture. This requires the solution of an integral equation;

$$\int_0^{c_{stat}} \left[\left(-\left.\frac{dP}{dc}\right|_c\right) - \left(-\left.\frac{dP}{dc}\right|_{c_0}\right)\right] dc = \int_{c_{stat}}^{c_{dyn}} \left[\left(-\left.\frac{dP}{dc}\right|_{c_0}\right) - \left(-\left.\frac{dP}{dc}\right|_c\right)\right] dc \qquad (3.2.2\text{-}3)$$

where c_{dyn} is the crack arrest point based on dynamic conditions. The first term represents the kinetic energy that gives the crack momentum. The second term represents this "excess" energy that must be absorbed by fracture beyond equilibrium.

The crack velocity of a delamination crack can also be derived using the strain energy release rates. Following the derivation in Section 3.2.1;

$$v_c \propto \sqrt{\frac{3}{L}\left(\frac{h^3}{(h-\ell)^3}-1\right)\left[\frac{1}{\left[1+\frac{3c}{L}\left(\frac{h^3}{(h-\ell)^3}-1\right)\right]^2}-\frac{1}{\left[1+\frac{3c_0}{L}\left(\frac{h^3}{(h-\ell)^3}-1\right)\right]^2}\right]} \qquad (3.2.2\text{-}4)$$

where v_c is the velocity of the delamination crack. The velocity reduces as the crack extends. This calculation assumes static conditions, so beyond c_{stat} the velocity becomes imaginary.

3.2.3 Pre-Cracking of the Weak Interlayer

The final scenario considered was that of a beam containing both a surface crack and an interlayer crack. This is the most complex geometry, and therefore the most difficult to model using fracture mechanics. As in the other cases, load values were calculated for a constant displacement. Various combinations of both crack sizes were attempted.

No equation was available for comparison, so linear regression analysis was used to find an empirical equation. The form of the regression equation was based on two functions. The first was Equation 3.2.1-12, to account for the change in load associated with cracking of the surface layer;

$$f_1 = f(a) = 1 + \beta_i\left(\frac{a}{h}\right)^2 + \beta_j\left(\frac{a}{h}\right)^4 + \text{error} \qquad (3.2.3\text{-}1)$$

The second was in the same form, and represents the interlayer crack;

$$f_2 = f(c) = 1 + \beta_k\left(\frac{c}{L}\right)^2 + \beta_1\left(\frac{c}{L}\right)^4 + \text{error} \qquad (3.2.3\text{-}2)$$

The two functions were combined to form the regression equation (3.2.3-3);

$$P = P(a,c) = \beta_1 + \beta_2\left(\frac{a}{h}\right)^2 + \beta_3\left(\frac{a}{h}\right)^4 + \beta_4\left(\frac{c}{L}\right)^2 + \beta_5\left(\frac{c}{L}\right)^2\left(\frac{a}{h}\right)^2 + \ldots$$

$$\ldots + \beta_6\left(\frac{c}{L}\right)^2\left(\frac{a}{h}\right)^4 + \beta_7\left(\frac{c}{L}\right)^4 + \beta_8\left(\frac{c}{L}\right)^4\left(\frac{a}{h}\right)^2 + \beta_9\left(\frac{c}{L}\right)^4\left(\frac{a}{h}\right)^4 + \text{error} \qquad (3.2.3\text{-}3)$$

where the β's are regression coefficients. The final equation is the result of trial and error. In each case the calculated and regression values were compared, and the form of the equation manipulated to find an appropriate fit. Equation 3.2.3-3 does not fit the calculated load values perfectly, but errors are ≤1.2%. The equation is valid for $a/h=0\rightarrow\ell/h$ and $c/L=0\rightarrow 1/8$.

The final load equation determined can be used in several ways to predict the properties of this class of composite laminates. The strength, reliability, nominal toughness, onset of main crack propagation, onset of weak interlayer crack propagation, extent of interlayer crack propagation, and crack velocities can all be inferred from the load equation. The calculations assume quasi-static conditions are approximately valid. Comparisons of relative values are considered more important than perfectly accurate solutions. This allows predictions to be made on the behaviour of composites, which allows for improved design of materials.

The strength of laminates can be predicted using Equations 2.1.2-12 and 2.1.2-13. Comparing the two yields;

$$\sigma_{fl} \propto P_{fl} = K_{aC}\left(\frac{P}{K}\right) \tag{3.2.3-4}$$

where σ_{fl} is the strength of the laminate, P_{fl} the fracture load, and K_{aC} the critical stress intensity factor (toughness) of the strong material. The load, P, and the stress intensity factor, K, can be determined from the regression curve. Based on Equations 2.1.2-14 and 3.2.1-2;

$$K \propto \sqrt{-\frac{\partial P}{\partial a}} \tag{3.2.3-5}$$

Therefore, the relative strength of a given laminate, as a function of both crack sizes, is given by;

$$\sigma_{fl} \propto \frac{P}{\sqrt{-\frac{\partial P}{\partial a}}} \tag{3.2.3-6}$$

The equation can be easily evaluated for various values of "a" and "c". This allows the effect of crack sizes and surface layer thickness on strength to be determined.

The reliability of the material cannot be predicted in the usual way. The Weibull modulus gives a measure of the range of strengths of a series of samples, which is due to a range of critical flaw sizes. In these composites, two different flaw sizes must be considered. A qualitative approach to predicting the reliability involves considering the two terms;

$$\frac{\partial}{\partial a}\left(\frac{P}{\sqrt{-\frac{\partial P}{\partial a}}}\right) \quad \text{and} \quad \frac{\partial}{\partial c}\left(\frac{P}{\sqrt{-\frac{\partial P}{\partial a}}}\right) \tag{3.2.3-7}$$

The first term indicates the sensitivity of the strength to the main crack size. A small value suggests the strength is not greatly affected by a change in flaw size, whereas a large value suggests the strength is highly sensitive. Similarly, the reliability of the laminates can be inferred from the second term, and the effect of weak interlayer flaw size. A simple way to gauge the reliability is to examine the gradient of strength versus crack size curves.

The regression curve can also be used to predict the onset of crack propagation. Assume that a laminate initially contains a main crack of size a_0 and an interlayer crack of size c_0. The main crack propagates when the strain energy release rate exceeds the critical strain energy release rate for the strong material;

$$G_a \geq G_{aC} \propto -\left.\frac{\partial P}{\partial a}\right|_{a_0 c_0} \tag{3.2.3-8}$$

The main crack propagates with an increasing strain energy release rate. At some point, the strain energy release rate of the interlayer crack exceeds its critical value, and it also propagates;

$$G_c \geq G_{cC} \propto -\left.\frac{\partial P}{\partial c}\right|_{a_{crit} c_0} \tag{3.2.3-9}$$

In this case, the main crack size is a_{crit}, the same critical crack size which was determined using an alternate method in Section 3.1. The two strain energy

release rates can be related using the ratio of the critical strain energy release rates of the two materials;

$$\left.\frac{\partial P}{\partial c}\right|_{a_{crit}c_0} = \left(\frac{G_{cC}}{G_{aC}}\right)\left.\frac{\partial P}{\partial a}\right|_{a_0c_0} \qquad (3.2.3\text{-}10)$$

The point at which the interlayer crack propagates will be a function of both crack sizes, and the relative toughness of the interlayer and strong materials.

Another possibility is that the interlayer cracks before the main crack. A comparable calculation can be done;

$$\left.\frac{\partial P}{\partial a}\right|_{a_0c_{crit}} = \left(\frac{G_{aC}}{G_{cC}}\right)\left.\frac{\partial P}{\partial c}\right|_{a_0c_0} \qquad (3.2.3\text{-}11)$$

This will occur if;

$$\frac{\left.\frac{\partial P}{\partial c}\right|_{a_0c_0}}{\left.\frac{\partial P}{\partial a}\right|_{a_0c_0}} \geq \left(\frac{G_{cC}}{G_{aC}}\right) \qquad (3.2.3\text{-}12)$$

The stress on the beam decreases as the two cracks propagate. It was shown that the extent of interlayer cracking has a significant effect on the fracture behaviour of the composites in Section 3.1 and Equation 3.1-13. The extent of interlayer crack propagation can be estimated from the stiffness equation. In Section 3.1 the crack velocities were used. A similar approach can be developed, based on the relative crack propagation rates of the main and interlayer cracks.

The regression equation can be used to predict the velocities of the simultaneously propagating cracks. Assuming the two cracks propagate such

that the reduction of total strain energy of the system is maximized, the relative velocities of the cracks can be calculated using;

$$-\nabla P(a,c) = -\left\langle \frac{\partial P}{\partial a}, \frac{\partial P}{\partial c} \right\rangle = \langle G_a, G_c \rangle \qquad (3.2.3\text{-}13)$$

The load can be represented mathematically by a surface, which is a function of *a* and *c* (see Section 5.2.3). The path of steepest *descent* will trace the size of the two cracks. Note that this approach is constrained by the critical strain energy release rates of the two materials. Individual crack velocities can be determined, provided the strain energy release rates are above their critical values;

$$v_a \propto \sqrt{\left(-\frac{\partial P}{\partial a}\Big|_{ac}\right) - \left(-\frac{\partial P}{\partial a}\Big|_{a_0 c_0}\right)} \qquad (3.2.3\text{-}14)$$

and

$$v_c \propto \sqrt{\left(-\frac{\partial P}{\partial c}\Big|_{ac}\right) - \left(-\frac{\partial P}{\partial c}\Big|_{a_{crit} c_0}\right)} \qquad (3.2.3\text{-}15)$$

If the strain energy release rates fall below their critical values, the solutions to these equations become complex (that is, imaginary). The crack velocities can be used to estimate c_{ext}, the extent of interlayer cracking.

3.2.4 Crack Tip Mesh Refinement

It could be argued that accurate crack tip stress intensities can only be accurately determined using extensive mesh refinement. Comparable load and

stress calculations were done for a variety of cracked beam geometries, using IDEAS commercial software*. The load values calculated were compared to equivalent values produced by the author's custom software. The crack tip stress values calculated were used to calculate stress intensity factors. Extrapolation of data and Equation 2.1.6-9 were necessary. The stress intensity factors were compared to equivalent calculations using the load-regression technique.

* The IDEAS commercial software calculations were done by Marwan Hassan, of the Department of Mechanical Engineering, McMaster University.

Chapter 4. Experimental

4.1 Monolithic Zirconia

Monolithic zirconia bend bars were made by electrophoretic deposition. The zirconia was 3 mole% yttria stabilized (Tosoh Corporation, TZ-3Y), which is tetragonal at room temperature. The same starting material and processing conditions were used for all of the monolithic zirconia and zirconia/lanthanum aluminate composite samples. The powder was size analyzed using a Horiba CAPA-700 Particle Analyzer.

The powder was mixed with distilled water and dispersed using a sonic dismembrator (Fisher Model 300). The suspension was centrifuged (Beckman GS-15) and the supernatant decanted. This process was repeated until the conductivity of the supernatant was comparable to that of distilled water. Conductivity was measured using an impedance analyzer (Hewlett-Packard 4192A LF). The zirconia powder required ~10-12 washings.

The powder was dried overnight at ~110°C (Fisher 800W Oven) to remove the water, then mixed with absolute ethyl alcohol to a thick slurry. Grinding media (zirconia balls, ~3mm diameter) were added, and the slurry vibro-

milled overnight to break up agglomerates. The grinding media were filtered out, and the slurry diluted to 5 vol% solids with ethanol.

The zirconia/ethanol slurry was used for deposition suspensions. The suspension was stabilized with diluted (1:4) acetic acid (glacial, Caledon), to reduce the pH to ~4.5. Diluted (1:9) hydrochloric acid (Fisher Scientific) was added drop-wise to reduce the pH to ~3.2-3.6. Four or five drops of nitrocellulose were added to each 300ml suspension to act as a binder and assist in post-deposition drying.

Deposition electrodes were made by made cutting ~3x4cm strips from 1mm thick teflon sheets. Equally sized graphite sheets, ~250μm thick, were cut and bonded to the teflon with Krazy™ glue. The graphite sides of the electrodes were cleaned with acetone, then dilute graphite powder/ethanol slurry sprayed onto each. The alcohol was allowed to evaporate, to leave a fine graphite powder that allowed easy green body removal after deposition.

The graphite/teflon electrode and a strip of stainless steel were immersed in the pH-balanced suspension. The power source (Keithley 237 High Voltage Source Measure Unit) was connected so that the stainless steel electrode was the anode and the graphite/teflon the deposition cathode. The circuit was similar to that given earlier as Figure 2.3.1-1.

Electrophoretic deposition of the zirconia was done under constant current conditions. Most deposition was done at 2mA, with a starting voltage of ~50V. The resistance of the circuit increased during deposition, with final

voltages as high as ~80-100V. Deposition continued until the green bodies were 1.5-2mm thick.

After deposition was complete, the power was turned off and the cathode removed from the suspension. Excess material was cut away from the edges of the deposit to prevent constraint during drying. The material was saturated with ethanol and wrapped in Saran Wrap™. The ethanol slowly bled off, and the deposit dried over ~7-10 days.

Dry deposits were placed on a flat bed of coarse alumina and sintered in air at 1550°C for six hours in a furnace (CM Model 1700S). Heating and cooling rates were 300°C per hour. A flat, previously fired sample was placed on top of each green body to reduce sintering curvature.

The samples were cut using a diamond-coated high speed saw to produce bend bars, nominally ~1.5x2x25mm. The bars were ground on each side to ensure flat and even samples. One side of each bar (the ~2mm width side) was polished to 1μm diamond. The samples were then annealed in air at 1250°C for ten hours to remove residual machining stresses.

Several samples were tested without indentation. Others were indented with loads up to 10kg, using a Vicker's hardness tester (Zwick Model 3212). The load was applied to the polished surface with a diamond-tipped indenter for a 10-second count.

The samples were four-point bend tested to failure (the polished surfaces subjected to tension) using a Wykeham Farrance 5000kg Stepless

Compression Test Machine. The load cell used had a 500lb range (Kulite Semiconductor Type TC2000). A loading rate of 100μm/minute was used for all tests. Load-deflection time plots were constructed using a chart recorder. Deflections were calculated from the loading times.

The stiffness of the test rig was calculated as 0.05μm /N. This was later used to correct the deflection calculations. The time scale on the chart recorder was calibrated using a linear variable displacement transducer (LVDT), and found accurate to ±1%. Errors in the load calculations were estimated as ±1%, and the stress and deflection calculations as ±1.5%.

A series of non-indented and indented samples were tested to fracture. In each case the strength was calculated using Equation 2.1.4-2, and the critical stress intensity factor (K_{IC} toughness) using Equation 2.1.5-4. The work of fracture was calculated by measuring the area under the load-deflection time curves, converting to an energy term, and dividing by the cross-sectional area of the sample.

The strength of each sample was plotted versus indent load (applied prior to bend testing). Following Equations 2.1.5-3 and 3.1-14, non-linear regression analysis (FitAll, MTR Software v5.7) was used to determine the strength as a function of indent load, that is, the *A* and *n* parameters. The non-indented sample strengths were not included in the regression.

The strengths of a series of non-indented samples were plotted versus fracture probability. Linear regression analysis was used to determine a Weibull modulus for the zirconia using Equation 2.1.3-2.

The dimensions of the hardness indents and their radial cracks were measured optically, for several indent loads. The hardness of each sample was calculated using Equation 2.1.5-1, and critical stress intensity factor (K_{Ic} toughness) using Equation 2.1.5-2.

Zirconia samples were thermally shocked from 400, 600, 800 and 1000°C. Samples were heated to the appropriate temperature and given a fifteen minute soak time. The samples were removed from the furnace and sprayed with water at room temperature until completely cooled. The bars were bend tested to complete failure under the same test conditions as the indented samples.

The fracture surfaces of some of the samples were studied using a Electroscan 2020 Environmental Scanning Electron Microscope.

4.2 Zirconia/Lanthanum Aluminate Composites

The zirconia/lanthanum aluminate composites were made in a similar fashion to the monolithic zirconia. The sample preparation procedures were repeated, the only difference being the zirconia deposition was interrupted mid-way to deposit a ~10μm layer of lanthanum aluminate.

The lanthanum aluminate suspension consisted of 20wt% alumina platelets (Elf Atochem, α-Al_2O_3, 7-10μm), 66wt% alumina (AKP-50, Sumitomo Chemical Co Ltd) and 14wt% lanthanum oxide (Cerac Inc, Pure Advanced Specialty Inorganics, 200 mesh). This mixture was selected following from the work of Bissinger (1995), as it had a high porosity after sintering. The alumina platelets were added to seed the *in situ* growth of lanthanum aluminate, parallel to the composite layers. This was done to elongate the pores and promote high stress concentrations in the weak layers. The powder mixture was vibro-milled prior to the addition of the platelets to avoid platelet fracture. The suspension was placed in an ultrasonic bath for ~30 minutes before pH balancing to disperse the platelets.

The composites were made following the same procedure as for the monolithic zirconia. Part way through the zirconia deposition, the suspension was exchanged for the lanthanum aluminate suspension. A ~10μm layer of the weak interlayer material was deposited, and the suspensions exchanged again to finish the deposition. The result was zirconia samples containing a *single* weak interlayer.

The steady-state strain energy release rate of the weak interlayer was calculated using the Charalambides method outlined in Section 2.1.8. Composite samples were prepared as usual. A notch was cut to the depth of the interlayer (on the polished/tensile side) using a Beuhler Isomet slow speed saw, with a diamond-coated 300μm thick blade. The samples were bend tested using the

same conditions as for the monolithic zirconia. The "plateau" loads from the load-deflection curves and Equation 2.1.8-1 were used to calculate the strain energy release rate. The critical stress intensity factor (toughness) of the interlayer was estimated using Equation 2.1.2-14.

The remaining composite "sandwich" bars were bend tested to *complete* failure. In some cases the samples failed catastrophically and the load and deflections were calculated as per the monolithic samples. In some cases the samples failed in a multi-stage fashion. The failure mode was noted. Three loads and two deflections were calculated (see Figure 4.2-1). The first of the loads, P_1, was used to calculate the initial fracture strength of the composite. The second load, P_2, was used to estimate the extent of weak interlayer fracture, using Equation 3.1-11. The third load, P_3, was used to calculate the residual strength, after multi-stage fracture of the first layer. The initial strength depends on the indent load applied to the surface layer before bend testing, and the residual strength depends on both the natural flaw size in the second strong layer and the layer thickness ratio (ℓ/h). The three loads and two deflections were used to estimate the work of fracture of the samples.

4.3 Glass

The glass used was microscope slides (Fisher Scientific Co, Plain #12-550A) and cover glasses (Corning Labware and Equipment). The slides were

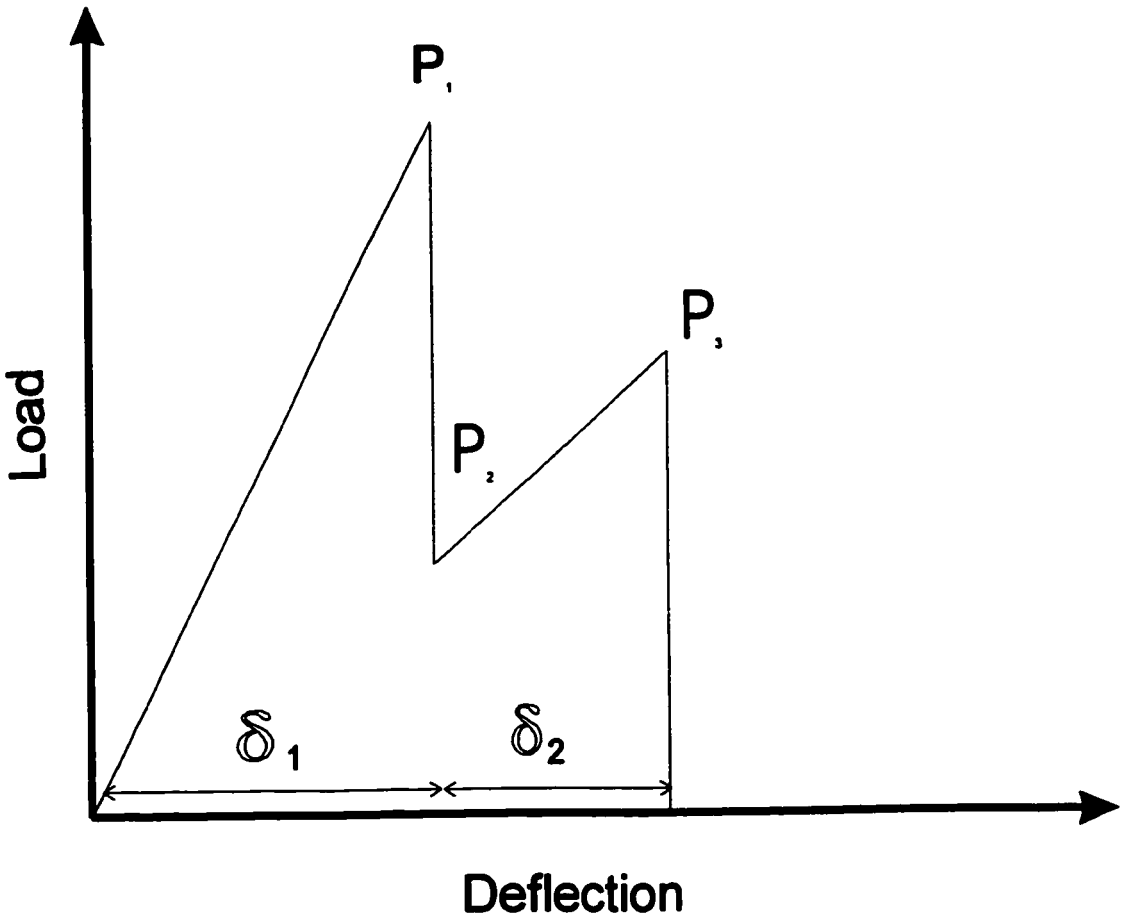

Figure 4.2-1. A schematic of a load-deflection curve for a sandwich sample suffering multi-stage failure.

originally 1x25x75mm in size. The slides were scored using a silicon nitride machining tool, and carefully cracked to produce 1x25x25mm glass plates. The cover glasses were 0.16x22x22mm.

The same tests were performed on the glass samples as the monolithic zirconia samples. Indents of up to 7kg were applied to the slide glass, but only 0.5kg to the thinner cover glass. Hardness was calculated using the indentation crack length method – Equation 2.1.5-1. The samples were coated with a thin layer of gold (SPI-MODULE sputter coater) prior to indentation to allow measurement of the indent and radial cracks.

The samples were bend tested to failure under the same conditions as the monolithic zirconia. The load cell had a 100lb range cell (Kulite Semiconductor Type TC2000-100). The strength, modulus, (indentation) toughness and work of fracture of each sample were calculated from the load and deflection time data recorded. A series of non-indented samples was tested to calculate a Weibull modulus. Non-linear regression analysis was performed to determine the strength of the glass as a function of the applied indent load.

4.4 Glass/Epoxy Composites

Glass/epoxy sandwich composites were made by bonding together either two slides, or a slide and a cover glass. The adhesive was Mastercraft epoxy (67-1420-6). Even amounts of resin and hardener were mixed for one

minute and spread evenly on one glass plate. The second plate was pressed on top. The plates were rubbed firmly against one another to ensure spreading of the adhesive, before being allowed to set. Sets of samples were made in random order to minimize accidental mixing inconsistencies. The composites were allowed to cure overnight. The steady-state strain energy release rate was determined using the Charalambides method.

Some composites were made using non-indented glass slides. Others were made by indenting either one or both of the plates before bonding. In all cases the composites were made and tested with the indents on the tensile side of the bend bars. In this work the surface indent on the first glass slide will be referred to as the "outer" indent. The indent on the second glass slide (initially in compression) is termed the "inner" indent (see Figure 4.4-1).

Most laminates were constructed of two glass slides, giving an ℓ/h ratio of ½. Some were made using the cover glasses, giving an ℓ/h ratio of either ~1/7 or ~6/7. Unless otherwise specified, the ℓ/h ratio is ½.

4.5 Plaster-of-Paris

Plaster-of-Paris composites were fabricated and tested by Ewa Szymanski, as a project to parallel the ceramic laminate and glass/epoxy work. The highlights of this work were discussed in Section 2.3.4.

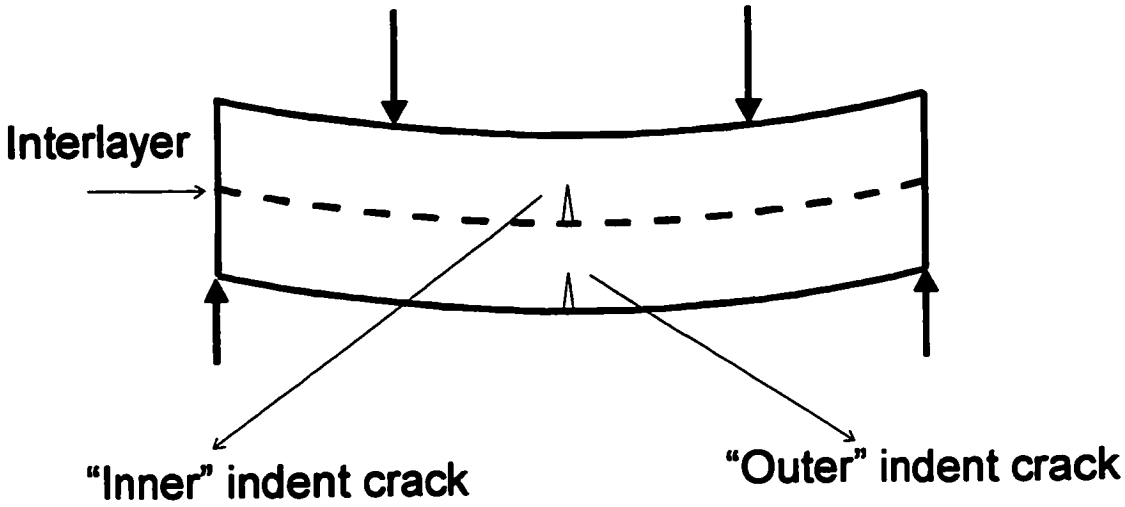

Figure 4.4-1. A schematic of the "inner" and "outer" indents in the composite test bars.

Chapter 5. Results and Discussion

5.1 Experiments

5.1.1 Monolithic Zirconia

The size distribution of the zirconia powder is given as Figure 5.1.1-1. The median particle diameter was 0.17μm, with a standard deviation of 0.38μm. The range of particle size adversely affects both sintering behaviour and strength.

The flexural strength of the zirconia was 895(±71)MPa. This is lower than the value reported by Bissinger (1995) for electro-phoretically deposited zirconia, but within experimental error. The Weibull modulus was m=9.9(±0.7), and the hardness H=12.5(±0.3)GPa.

Regression of the strength/indent load data yielded parameters; A=901(±68)MPa·kg^{-n}, and n=-0.46(±0.06) – see Figure 5.1.1-2. The measurement error on individual data points is ±1.5%. The exponential factor for an ideally brittle material is –1/3, which suggests significant error in the calculation. Transformation toughening of the zirconia leaves the surface of the material in residual compression. This will affect the exponential factor. The crack

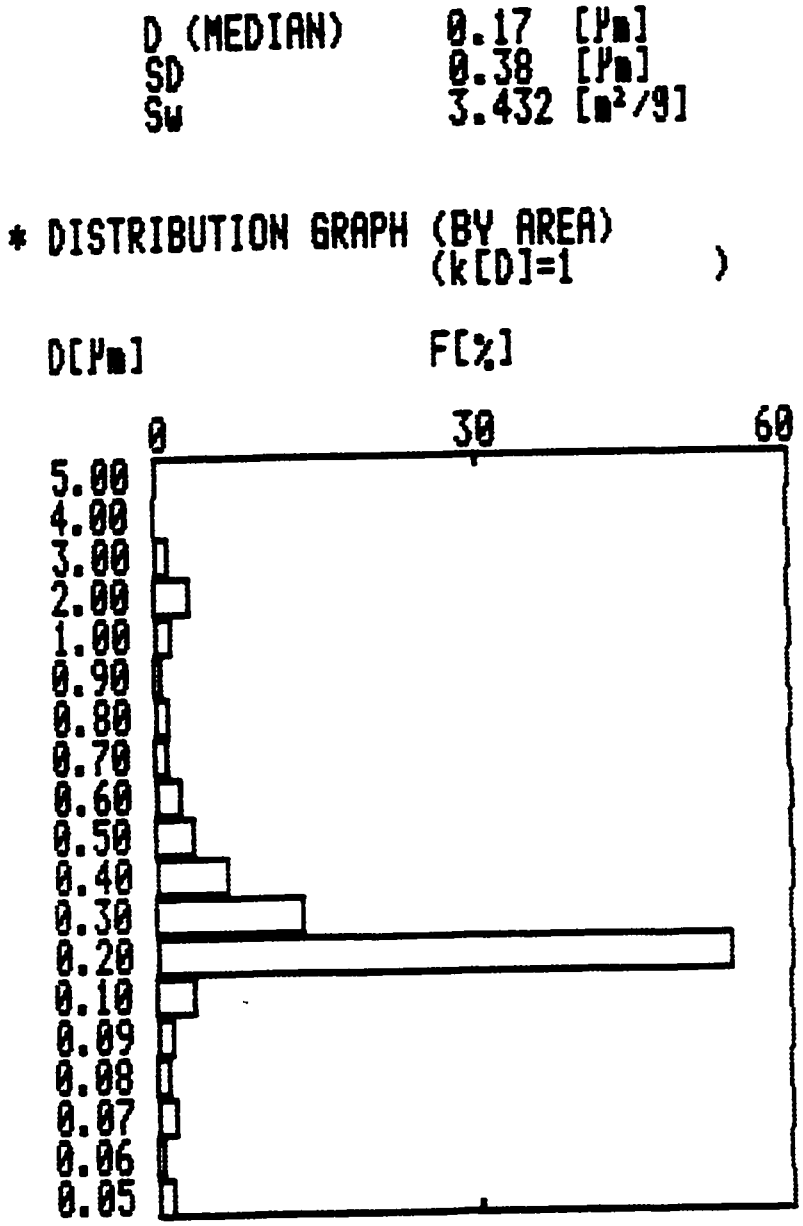

Figure 5.1.1-1. The size distribution of the zirconia powder.

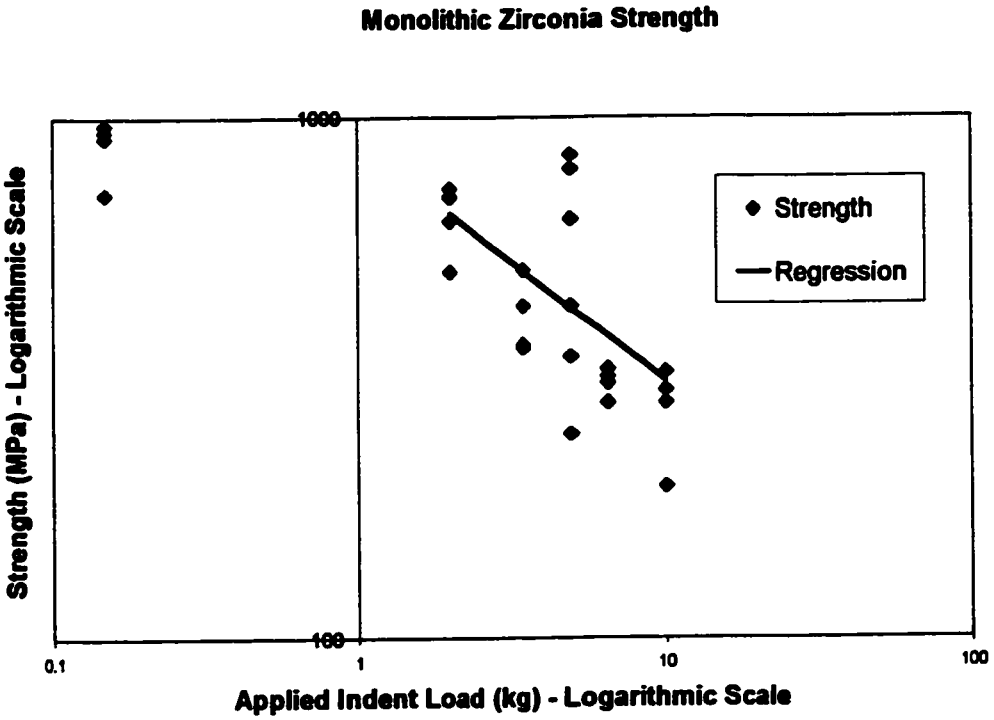

Figure 5.1.1-2. The strength-indent load relationship for the monolithic zirconia.

size resulting from a small indent load will be less than expected, due to the compression. The opposite is true for a large indent load – the stress field reaches the tensile sub-surface region, which leads to cracks that are larger than expected.

Two techniques were used to determine the toughness of the zirconia. The indentation-crack-length toughness was K_{IC}=6.6(±0.3)MPa$\sqrt{m}$, and the indentation-strength-in-bending toughness K_{IC}=6.6(±0.6)MPa$\sqrt{m}$. The average values are equivalent, but the indentation-strength-in-bending calculations were less consistent. The discrepancy suggests there may be sub-surface flaws influencing the strength of the material.

The work-of-fracture of the monolithic zirconia is given as Figure 5.1.1-3. The measurement error on individual data points is ±2.4%. The work-of-fracture is calculated from the area under the load-displacement curve. The value is sensitive to flaw size, which affects both the fracture load value and compliance of a given sample. The variation is comparable, or higher, than that associated with the Weibull modulus. The average work of fracture of the non-indented samples was 7510(±2080)J/m^2. The work-of-fracture of the indented samples varies with their strength.

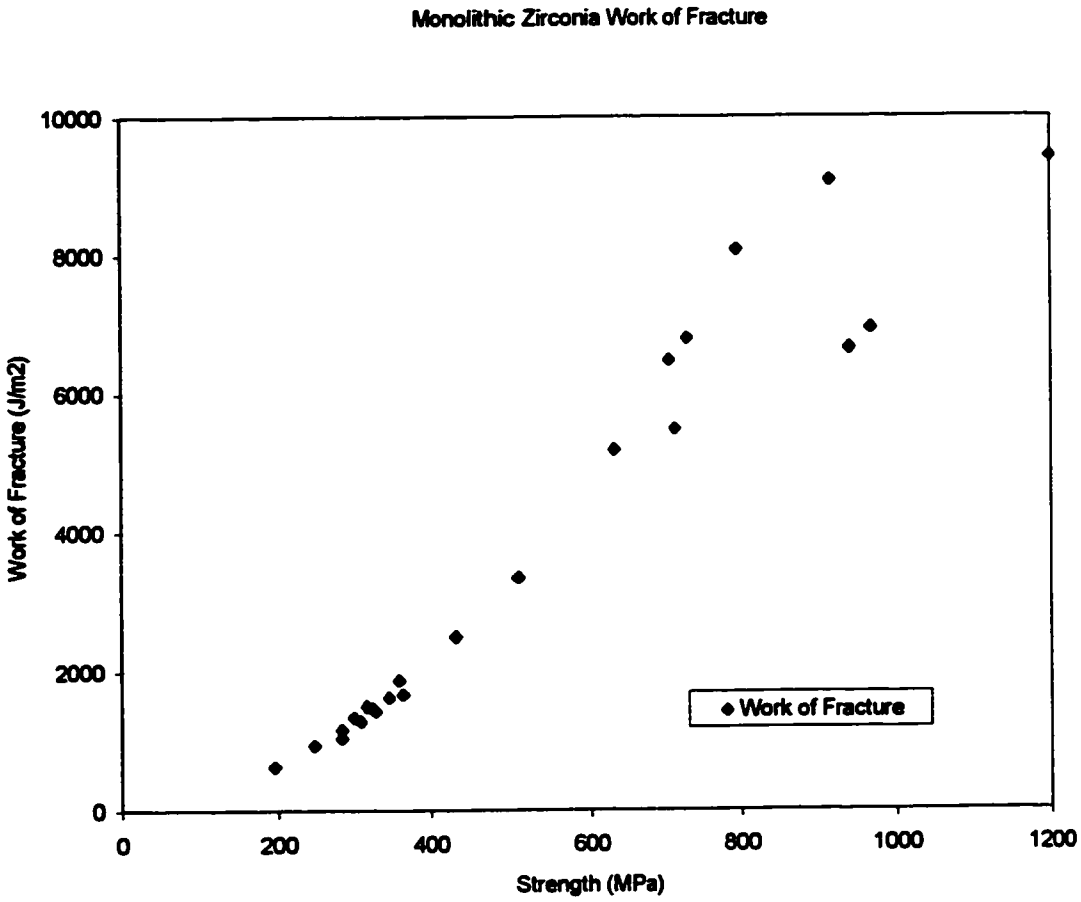

Figure 5.1.1-3. The work of fracture of the monolithic zirconia as a function of strength.

5.1.2 Zirconia/Lanthanum Aluminate Composites

The delamination tests yielded a steady-state strain energy release rate for lanthanum aluminate of G_{ss} =17.2(±4.5)J/m^2. This is equivalent to $K_c \approx 2.1 MPa\sqrt{m}$. This value, and the strength, toughness and Weibull modulus values quoted above, were used as material parameters in the crack deflection model.

The crack deflection model program was run repeatedly. Parameters were adjusted to determine the sensitivity of each value to the fracture zone boundary. The strength of the *next* layer in the laminate had the greatest effect. Reasonable changes in strong or weak interlayer toughness values, or initial interlayer flaw size, had less effect. This suggests the critical factor in determining the fracture behaviour of the sandwich laminates is the strength ratio of the two *strong* layers.

The zirconia/lanthanum aluminate composite suffered both catastrophic and multi-stage failure. This is a progression from the work of Bissinger (1995), in which all of the samples failed catastrophically.

Figures 5.1.2-1 and 5.1.2-2 are (environmental) scanning electron microscope micrographs that clearly show crack deflection within the lanthanum aluminate interlayers. The zirconia/lanthanum-aluminate interfaces are strong. Note the assumptions of the model ignore which of the pathways crack, but rely on a consistent and measurable critical strain energy release rate.

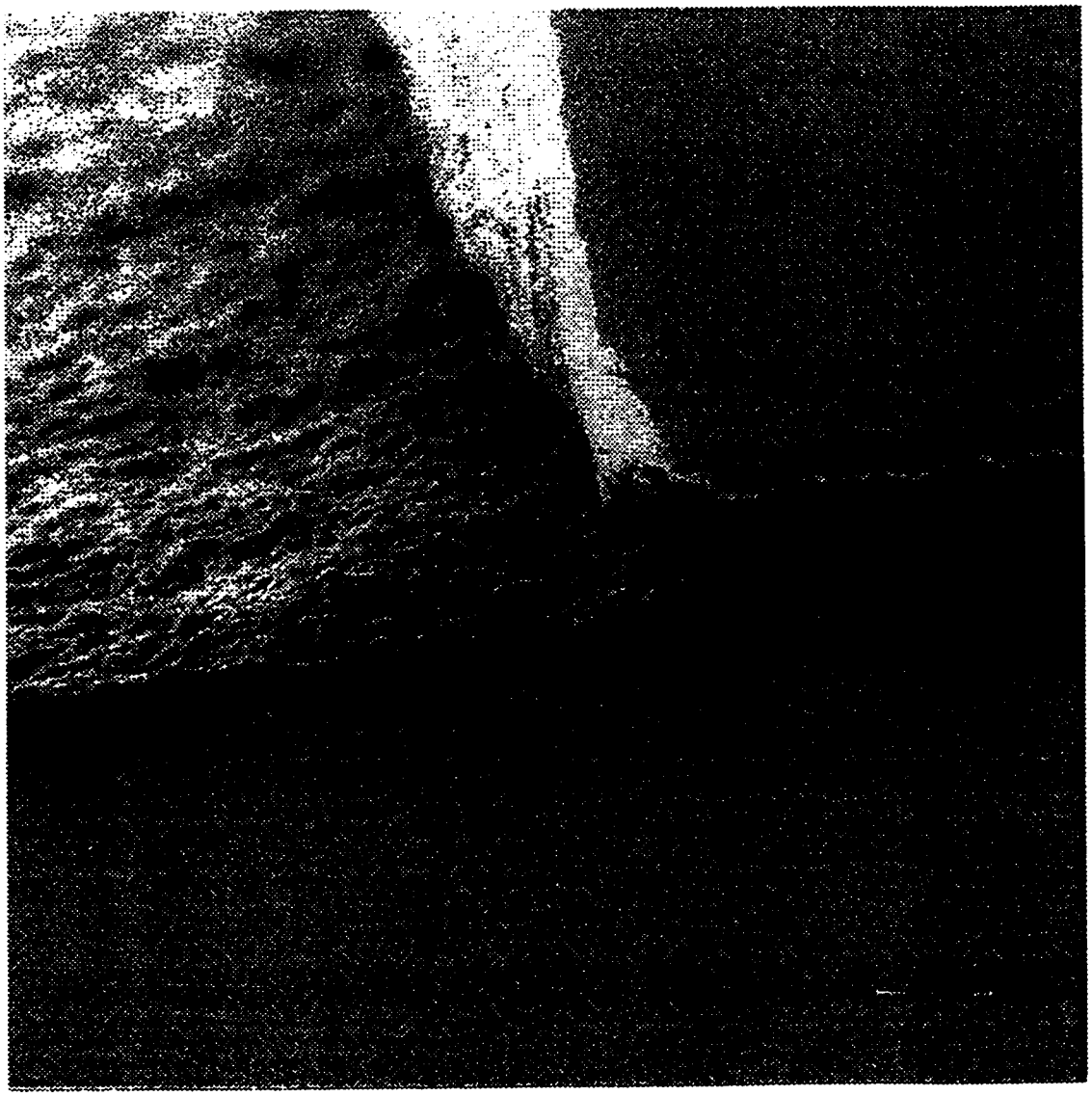

Figure 5.1.2-1. A micrograph of the crack bifurcation region of a composite that failed in a multi-stage manner (~100X).

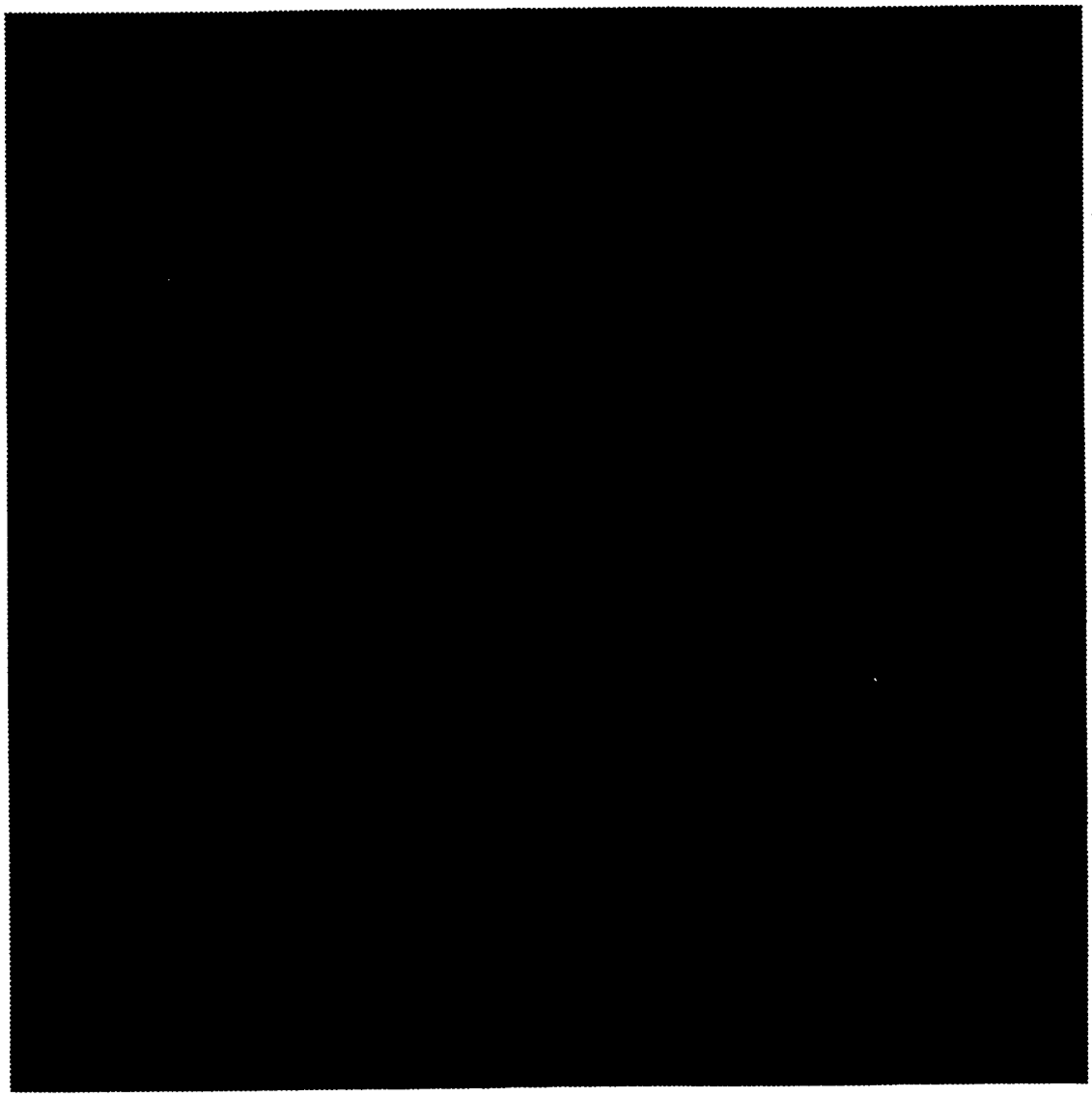

Figure 5.1.2-2. A micrograph of a crack within a lanthanum-aluminate interlayer (~1000X).

The test results are plotted with the fracture mechanics modeling results, as Figure 5.1.2-3. The results show a trend consistent with the model prediction. The region near the critical boundary, within the first dotted lines, the behaviour is expected to be unpredictable. Minor deviations in the strength of the next strong layer in the composite (due to natural variations of flaw size) affect the behaviour of the composite. Further away from the critical boundary the behaviour is increasingly more predictable.

The error lines included are based on the Weibull modulus of the strong material, which influences the strength of the next layer in the beam, and therefore the fracture mechanism. Errors associated with the indent strength or toughness calculations have not been included. Considering these factors would further spread the dotted lines. It is also assumed that initial weak interlayer cracks are equal in all samples, and directly ahead of the main indent cracks. This is not true, but necessary to simplify the modeling work.

Considering the assumptions of the model, the predictions are good. Most samples that contained a small initial flaw size and/or a thick surface layer failed catastrophically. Most samples that contained a large initial flaw size and/or a thin surface layer failed in multi-stage fashion.

Regression of the strength/indent load data for all the composites yielded A=692(±25)MPa·kg^{-n} and n=-0.29(±0.02) – see Figure 5.1.2-4. These values are significantly different from those determined for the monolithic zirconia. The result suggests the interlayer significantly weakens the material. Intuitively,

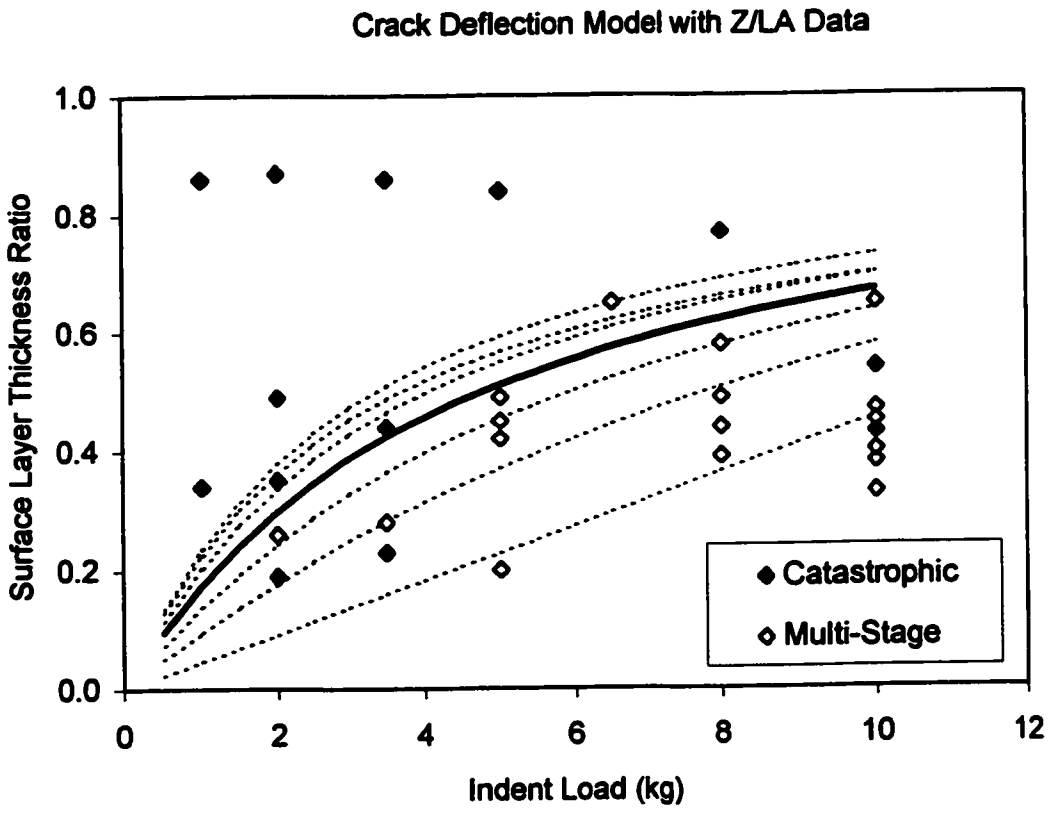

Figure 5.1.2-3. The results of the zirconia/lanthanum aluminate composite bend tests, compared to the fracture mechanics model. The solid line represents the critical boundary, assuming an average strength in the next strong layer. The dotted lines represent errors associated with the Weibull modulus of the (strong) material.

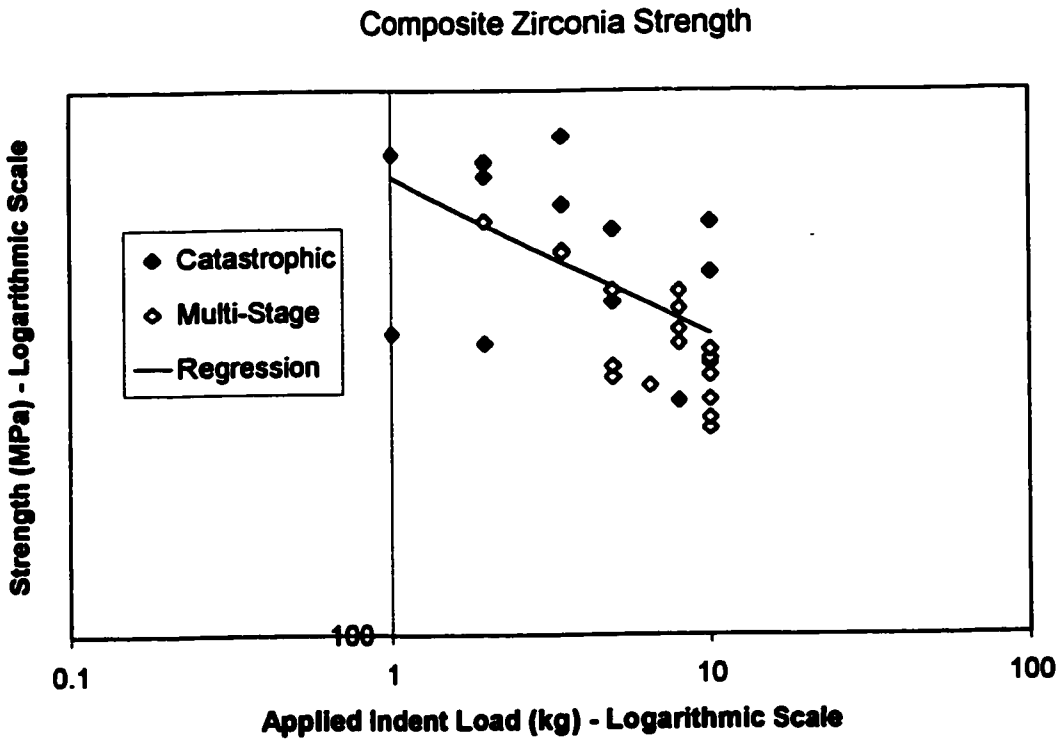

Figure 5.1.2-4. The strength-indent load relationship for the zirconia-lanthanum aluminate composites.

addition of a weak layer should weaken a material. In this case the surface flaw is in the strong material, and the applied stress parallel to the interlayer, so there should be no effect. The interlayer may affect the formation of the indent crack.

Considering the variation in strength with indent size, it is appropriate to redefine the fracture mechanics model in terms of layer thickness ratio and *strength*. Figure 5.1.2-5 shows a comparison of the composite bend test results to the model. The data and horizontal axis were adjusted accordingly, using Equation 3.1-14. The trend is comparable to that shown by Figure 5.1.2-3.

The residual strength after multi-stage fracture is also of interest. In this case the nominal residual strength has been calculated, which is based on the load bearing capability after multi-stage fracture, but the *initial* sample thickness. Following Equation 2.1.4-2, the nominal residual strength should be proportional to the square of the remaining sample thickness. Figure 5.1.2-6 shows the residual strength plotted versus $"[1-(\ell/h)]^2"$, and an appropriate line to represent the expected theoretical relation. There is scatter in the data, but the trend is consistent with theory.

A nominal residual strength *increase* may be predicted considering the Weibull relation (Equation 2.1.3-1). When the weak interlayer cracks, it may not propagate as far as the inner loading pins of the test rig. Therefore, the volume of material subjected to the maximum stress will be less than for the (non-indented) strength tests. The apparent strength is appropriately higher. This reasoning leads to a paradox. Extensive crack deflection lowers the load (and therefore

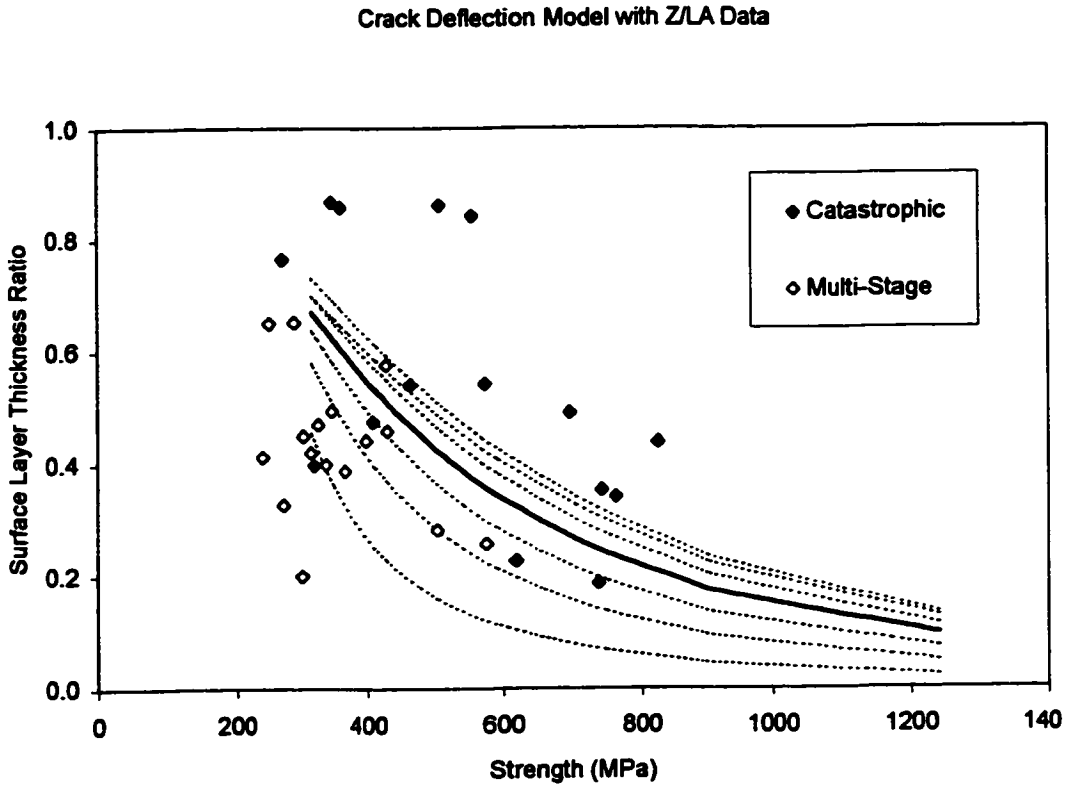

Figure 5.1.2-5. The results of the zirconia/lanthanum aluminate composite bend tests compared to the fracture mechanics model - in terms of strength rather than applied indent load.

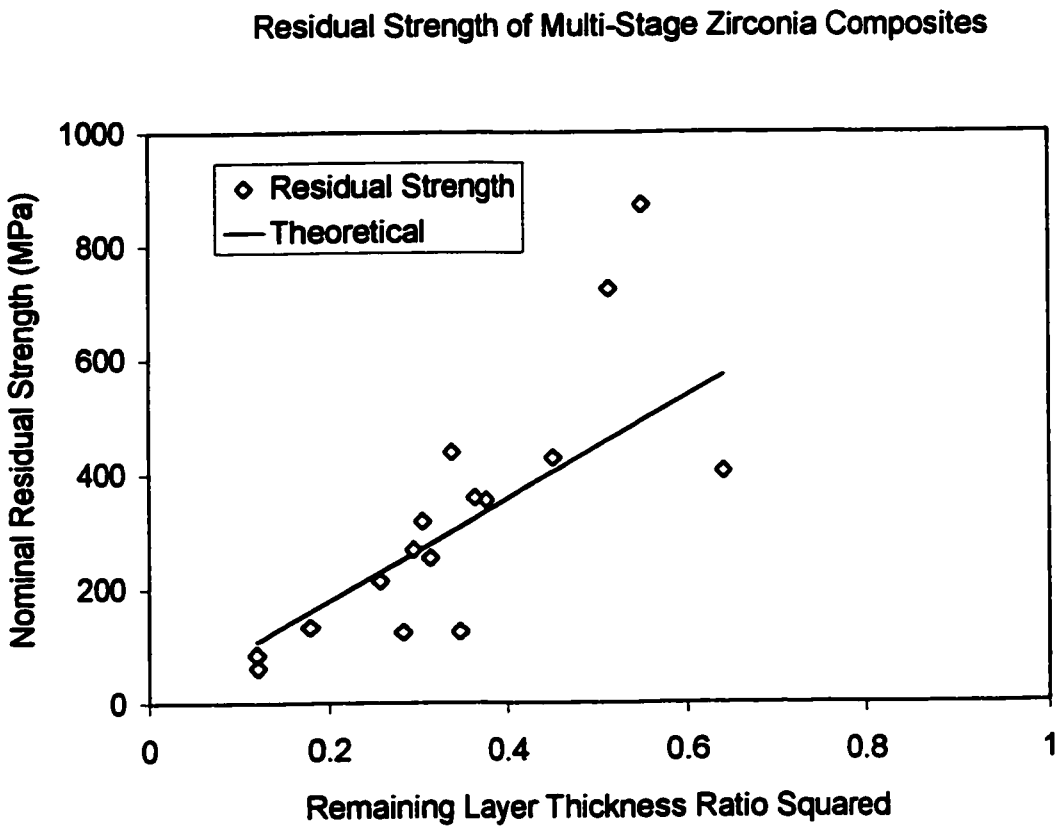

Figure 5.1.2-6. Residual strength of the multi-stage composites as a function of remaining sample thickness.

the stress) on the remaining layer in the composite. This encourages multi-stage fracture behaviour. However, the Weibull relation results in a lower strength in the beam, which encourages catastrophic behaviour. The converse can also be argued. Less crack deflection results in the remaining beam being subjected to a higher stress, but the lower volume of material is stronger. It may be possible to estimate an optimal extent of crack deflection to ensure multi-stage fracture behaviour. The complex stress field in the region of the bifurcated crack and the natural distribution of flaws in the next strong layer in the composite make this a difficult problem. If this issue could be solved, it may be possible to tailor the weakness of the interlayer to improve the reliability of the composites.

The important feature of the weak interlayer toughening mechanism is the work-of-fracture can be improved. This leads to difficulties when the results of Figures 5.1.2-3 and 5.1.2-5 are considered. A high strength in a monolith is advantageous as the material stores more elastic energy before fracture, so has a higher work-of-fracture. Similarly, a weak monolith has a low work-of-fracture. In the case of the composites, the weakness of the surface layer influences whether the material will fail in a multi-stage or catastrophic manner. A composite with a weak surface layer will have the low work-of-fracture associated with a comparable monolith, but is more likely to have a large work-of-fracture associated with its residual strength. Conversely, a strong surface layer leads to a high initial work of fracture but no residual strength. There may be an optimum

surface layer strength that will maximize the work-of-fracture. The work-of-fracture is plotted as a function of (initial) strength in Figure 5.1.2-7.

There is considerable variation in the data. For the samples that failed in a catastrophic manner, the work-of-fracture varies with the strength, as shown earlier with the monolithic samples. The variation for the multi-stage composites is more difficult to explain. There is a component of the work-of-fracture that relates directly to its strength, but there is another component that relates to the residual strength following multi-stage fracture.

The residual strength in the next layer in the beam depends on the surface layer thickness ratio (ℓ/h), and the extent of interlayer cracking, as discussed earlier. This also explains the variability in the data. A high residual strength is advantageous, but this implies a low initial strength is necessary to ensure multi-stage fracture behaviour. Similarly, a sample that fails catastrophically has zero residual strength, but a high work-of-fracture due to its high initial strength. The results indicate a concession is necessary if multi-stage fracture is to occur. A high work-of-fracture and a "safety-net" against material failure are only possible if the surface layer strength is reduced.

The thermally shocked zirconia samples exhibited severe strength degradation after 600°C water quench. Samples shocked 400°C had strengths comparable to monolithic zirconia. The strength/fracture behaviour relationship predicted by the model suggests the shock may increase the work-of-fracture.

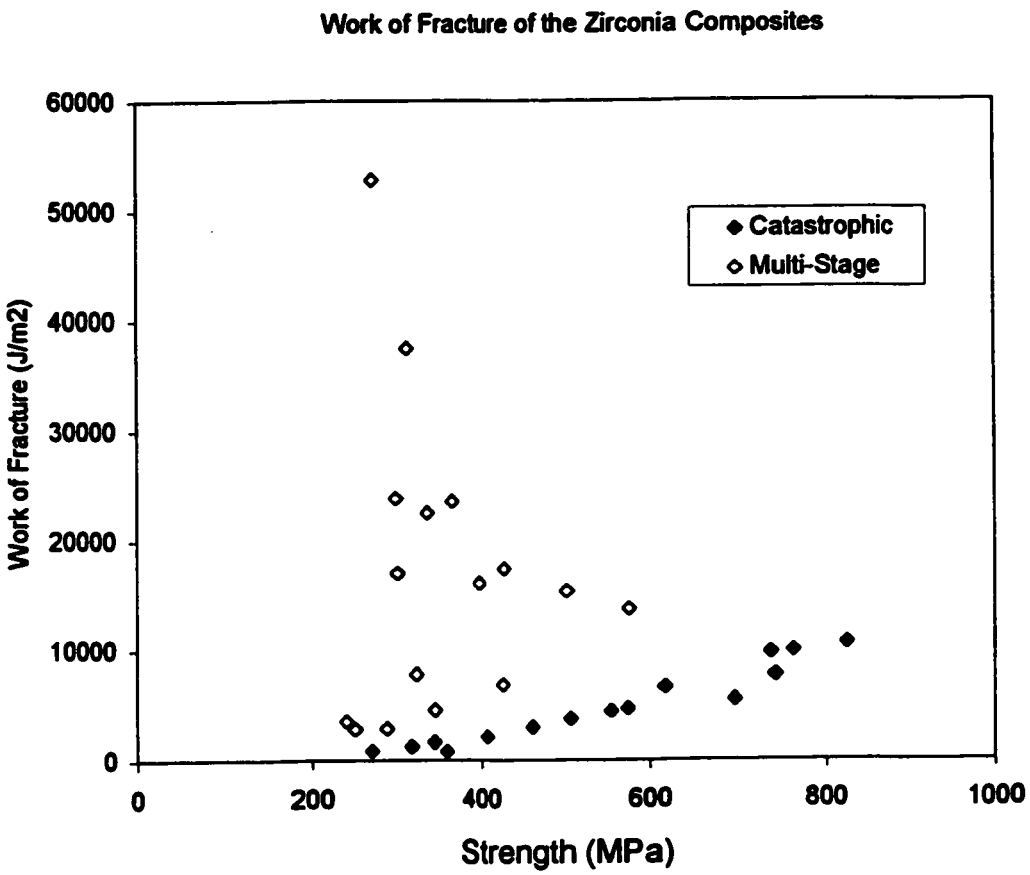

Figure 5.1.2-7. The work of fracture of the composites as a function of (initial) strength.

The strength of the samples as a function of thermal shock is given as Figure 5.1.2-8. The strengths of the quenched samples exhibit considerable variation. The catastrophic/multi-stage behaviour relationship is not as apparent as it was in Figures 5.1.2-3 and 5.1.2-5. Some samples quenched 600 or 800°C failed in a multi-stage manner, but none quenched from 1000°C behaved in this manner.

Multi-stage fracture relies on part of the delaminated surface layer bearing some of the load. In the case of severely shocked samples, the surface layer is too damaged. In effect the sample is a monolith with many large flaws. Multi-stage fracture behaviour is only possible in samples subjected to moderate (~600-800°C) thermal shock.

There is a considerable variation in the works-of-fracture of the thermally shocked samples (Figure 5.1.2-9). The same arguments can be made for these samples as for the indented samples. The only expected difference is that the extremely shocked samples have no residual strength.

The work of Lange et al (1998) suggested the thermal residual stress in the composite is critical to its fracture behaviour. In the present work a series of samples have shown both multi-stage and catastrophic behaviour, despite having comparable interlayer thickness and thermal residual stress (estimated +3.2MPa in zirconia, and –480MPa in lanthanum aluminate). The difference is the surface layer thickness ratios (ℓ/h) and flaw sizes (a_0) were varied. These two features strongly influence fracture behaviour.

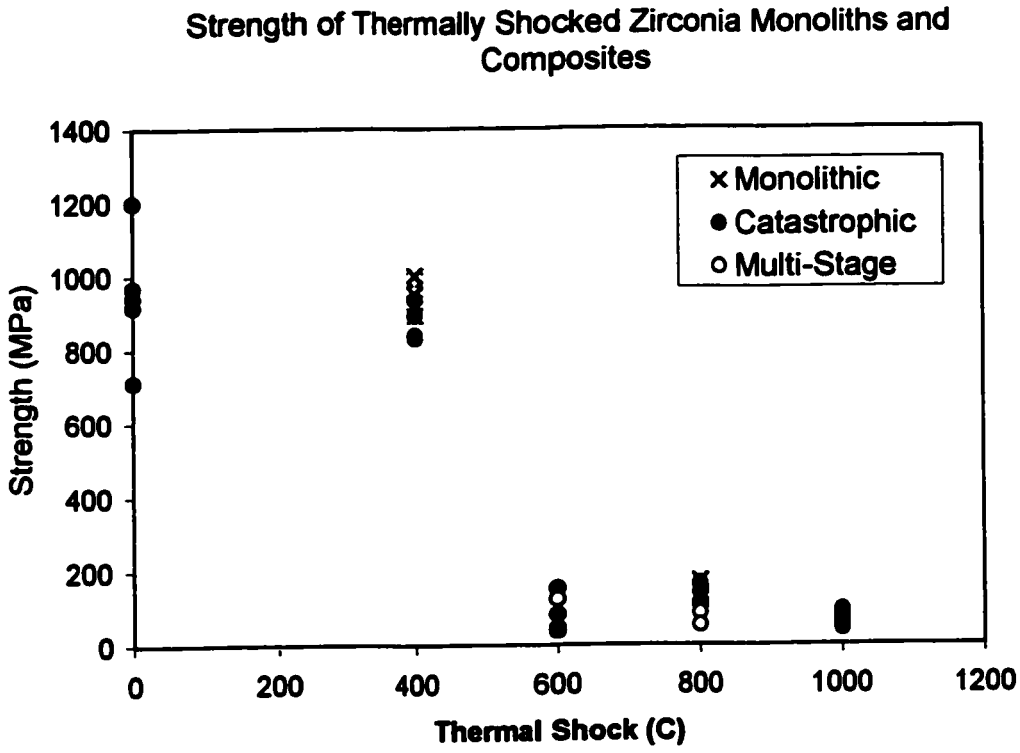

Figure 5.1.2-8. Strength of zirconia monoliths and composites as a function of thermal shock.

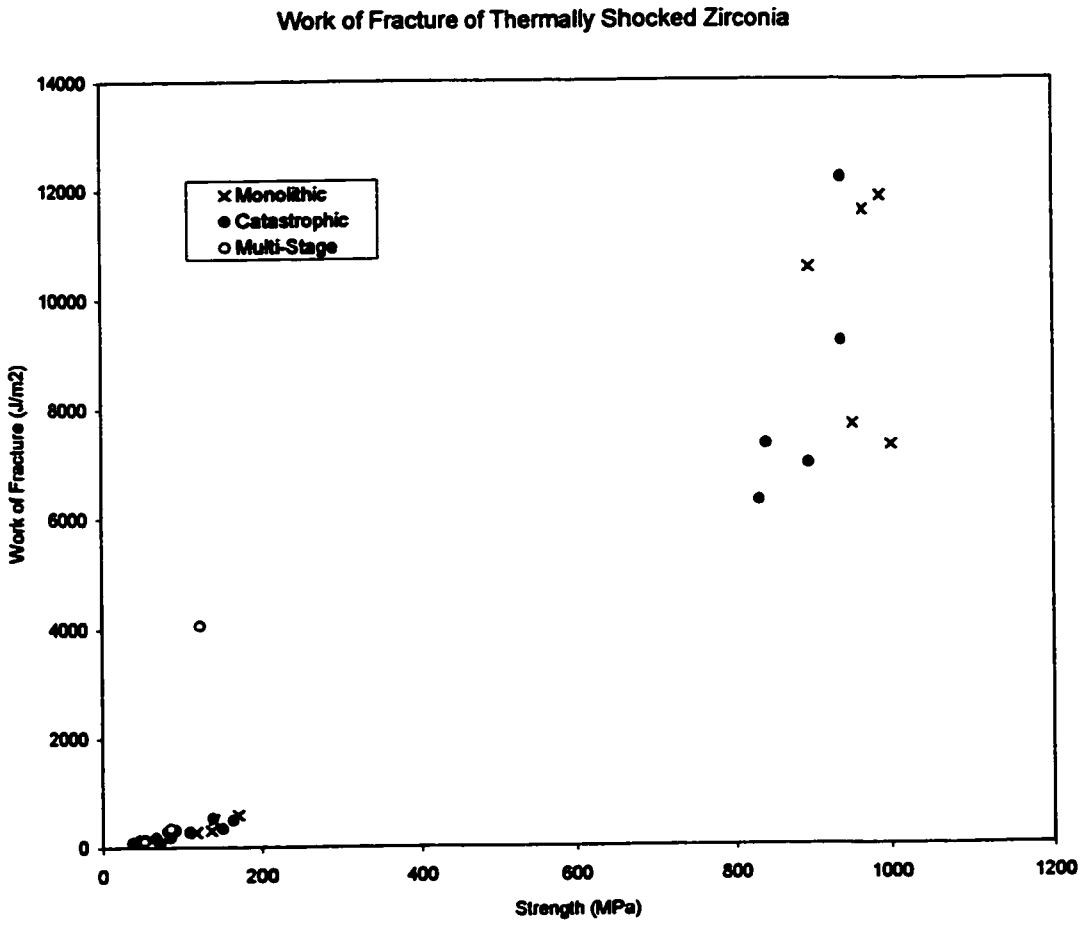

Figure 5.1.2-9. The work of fracture of the quenched zirconia and composite samples.

Thermal stresses are important because they can cause cracking and weaken an otherwise strong material. The interlayer weakness is critical to the fracture mechanism. The work of Lange may have shown a different trend if the initial flaw size and/or surface layer thickness ratio had been varied. The work of Hatton (1998) also showed a variation of fracture behaviour with changing layer thickness.

5.1.3 Glass

The strength of the microscope slide glass was 97.5MPa, with a Weibull modulus of 7.0(±0.3). The hardness was 4.9(±0.3)GPa, and the indentation crack length toughness K_{IC}=0.66(±0.05)MPa$\sqrt{m}$. The cover slides were significantly stronger, but less reliable. The strength was 182(±65)MPa.

The indented strength of the glass was more consistent than the equivalent monolithic zirconia samples (Figure 5.1.3-1). Regression yielded A=58.2(±0.54)MPa·kg^{-n}, and n=-0.27(±0.0005). The measurement error on individual data points is ±1.5%. The indentation-strength-in-bending toughness was also consistent, with K_{IC}=1.0(±0.02)MPa$\sqrt{m}$ (Figure 5.1.3-2).

The work of fracture is plotted versus strength as Figure 5.1.3-3. The measurement error on individual data points is ±2.4%. The relation between strength and work of fracture is comparable to that of the zirconia monoliths and catastrophic composite samples.

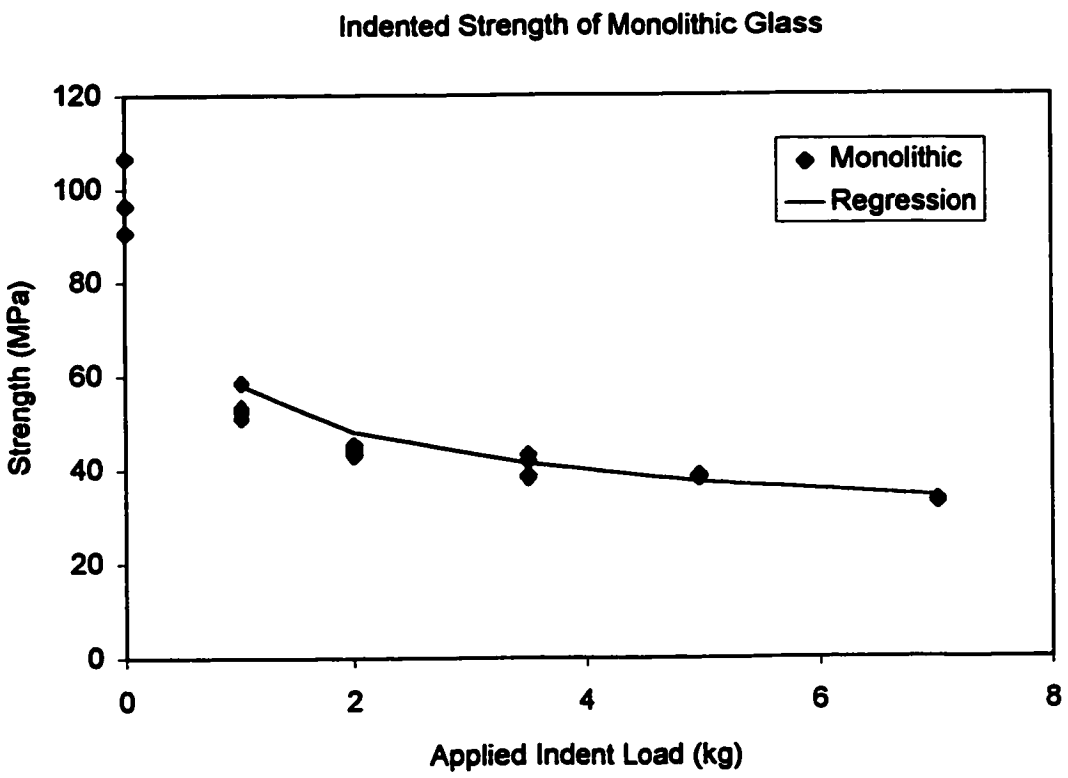

Figure 5.1.3-1. The strength-indent load relationship of the glass samples.

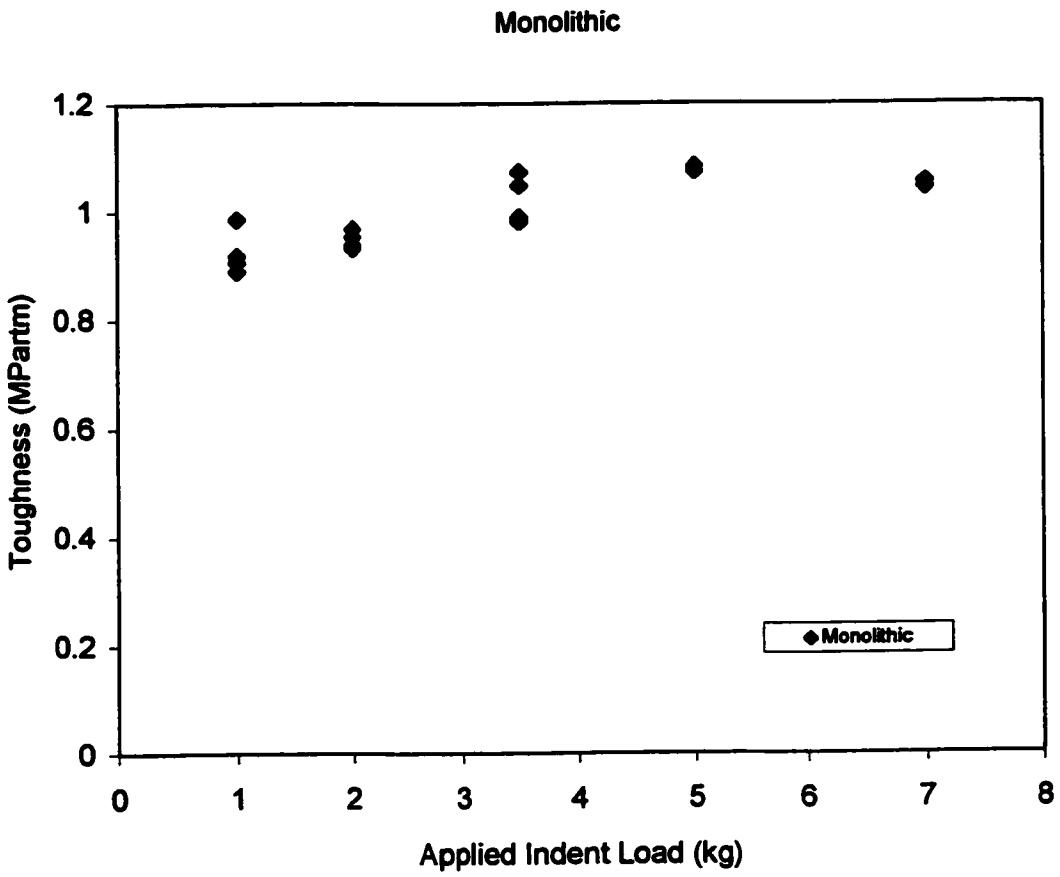

Figure 5.1.3-2. The indentation-strength-in-bending toughness of the glass samples.

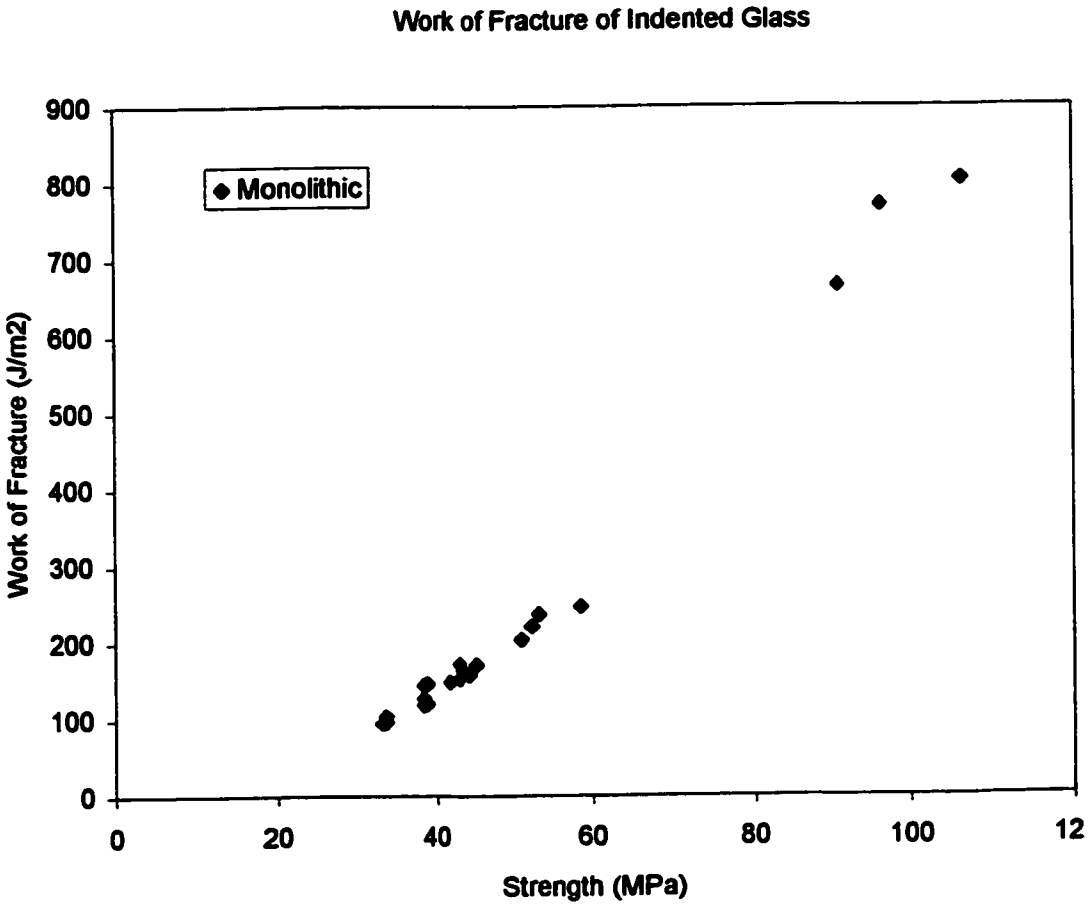

Figure 5.1.3-3. The work of fracture of the glass as a function of strength.

5.1.4 Glass/Epoxy Composites

The delamination tests yielded a critical strain energy release rate of G=305(±110)J/m^2, equivalent to K_C=4.8(±1.7)MPa$\sqrt{m}$. The epoxy (or the glass/epoxy interface) is *tougher* than the glass. This implies the "weak" interlayer fracture mechanism will not work. The epoxy had a fine dispersion of bubbles, with an estimated diameter ~0.5mm. Though epoxy is not as brittle as glass, the effective flaw size makes it substantially weaker. This concept is contrary to the toughness ratio predictions developed by Cook and Gordon (1994), Kendall (1975), and He and Hutchinson (1989). Flaw size must be considered.

The strength of the glass was not affected by lamination. Figure 5.1.4-1 shows the strength of the composites as a function of applied indent load. The data includes composites in which an indent was applied to the "next" strong layer. Strength is independent of the "inner" indent load, but a significant effect is expected on the fracture behaviour, residual strength and work-of-fracture.

Figure 5.1.4-2 shows the results of bend tests compared with the present crack deflection model. In this case cover slides were used as layers in the composites, so the ℓ/h ratios are *not* all ½. Each symbol on the figure is the result of eight tests. Any group of samples in which zero, one or two samples failed in a multi-stage manner is shown as a black symbol. If six, seven or eight samples failed in a multi-stage manner, a white symbol is used. A grey symbol represents an even mixture of multi-stage and catastrophic behaviour.

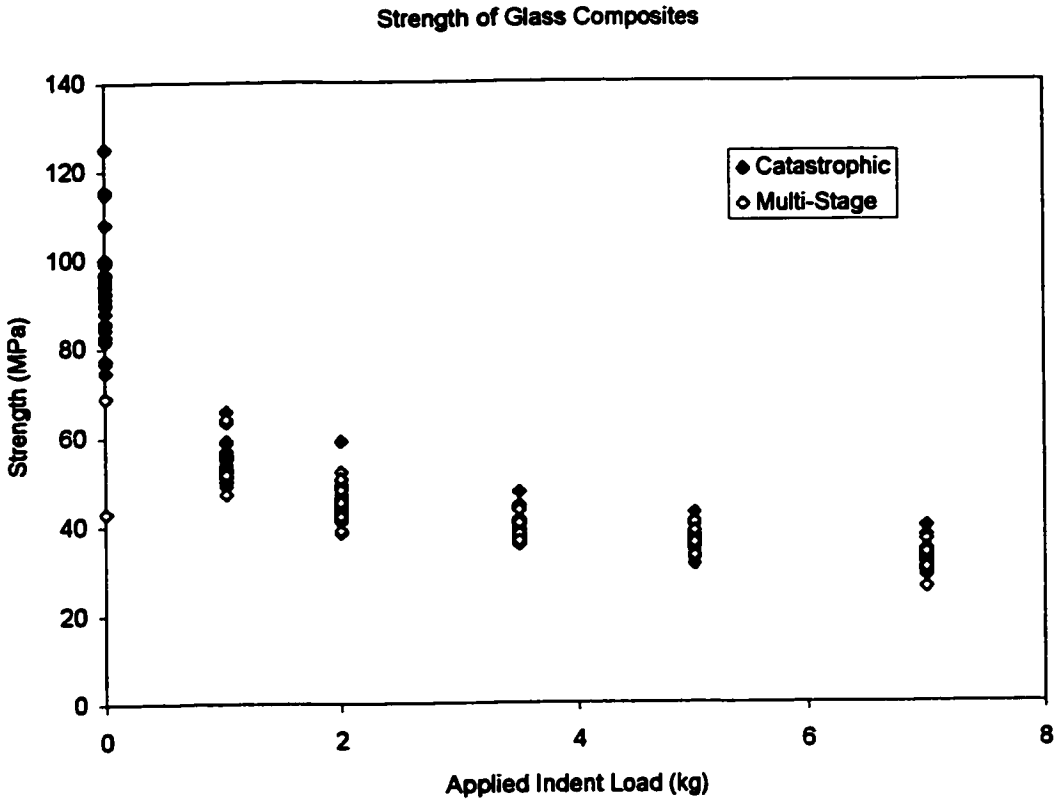

Figure 5.1.4-1. The strength of the glass and glass/epoxy composites as a function of applied indent load.

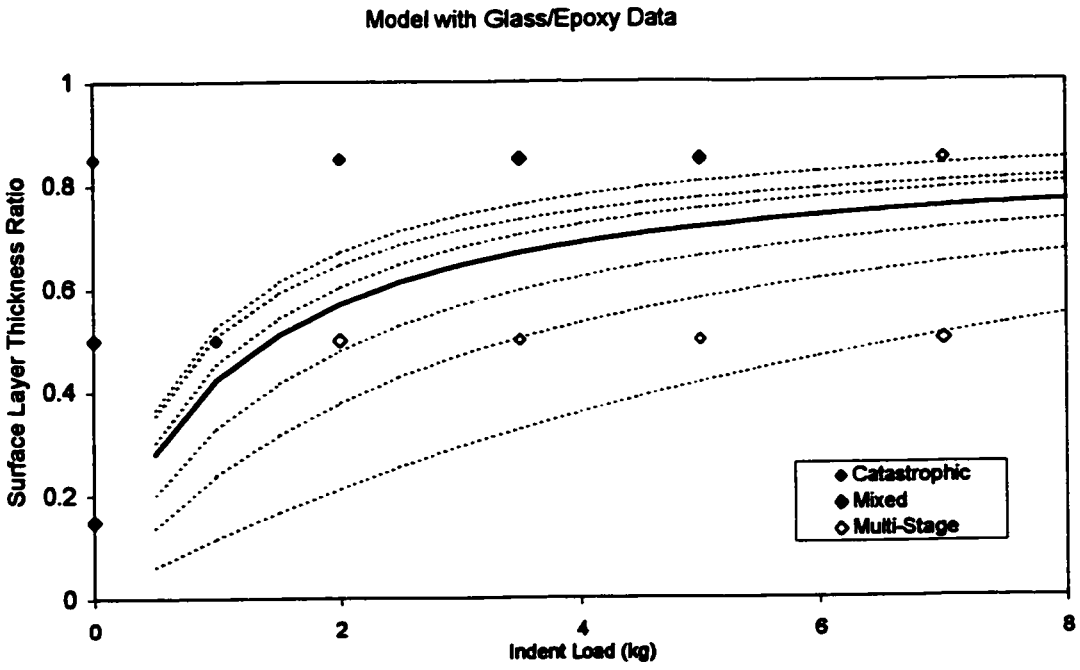

Figure 5.1.4-2. The results of the glass/epoxy bend tests compared to the crack deflection model.

The glass/epoxy results are consistent with the predictions of the present crack deflection model. The pattern is very similar to that of the zirconia/lanthanum aluminate composite tests. This confirms the trend of the model is good.

The ability to pre-indent the second glass layer in the composite (the "inner" indent) allows other trends in fracture behaviour to become apparent. The premise of the model is the strength of the next layer in the composite is critical to the fracture behaviour. Figure 5.1.4-3 shows the proportion of samples that failed in a multi-stage manner as a function of outer indent load. Both the inner and outer indent loads influenced the fracture behaviour of the composites. A large outer flaw and small inner flaw were necessary for consistent multi-stage fracture behaviour. The trend is consistent with the basis of the modeling.

A trend is also expected if the data is plotted with respect to both inner and outer indent loads. Figure 5.1.4-4 shows that multi-stage fracture is likely if the surface layer is weaker and the next layer is stronger. A zone boundary, similar to that determined by the modeling work, was constructed to show regions of predicted fracture behaviour. The boundary is based on Figure 5.1-4-2. A horizontal line drawn through $\ell/h=1/2$ intercepts the model zone boundary and its error lines at several points. The intercepts relate to next layer strengths and probabilities, which can be related to equivalent inner indent loads using Equations 2.1.3-1 and 3.1-14. The data follows the trend predicted.

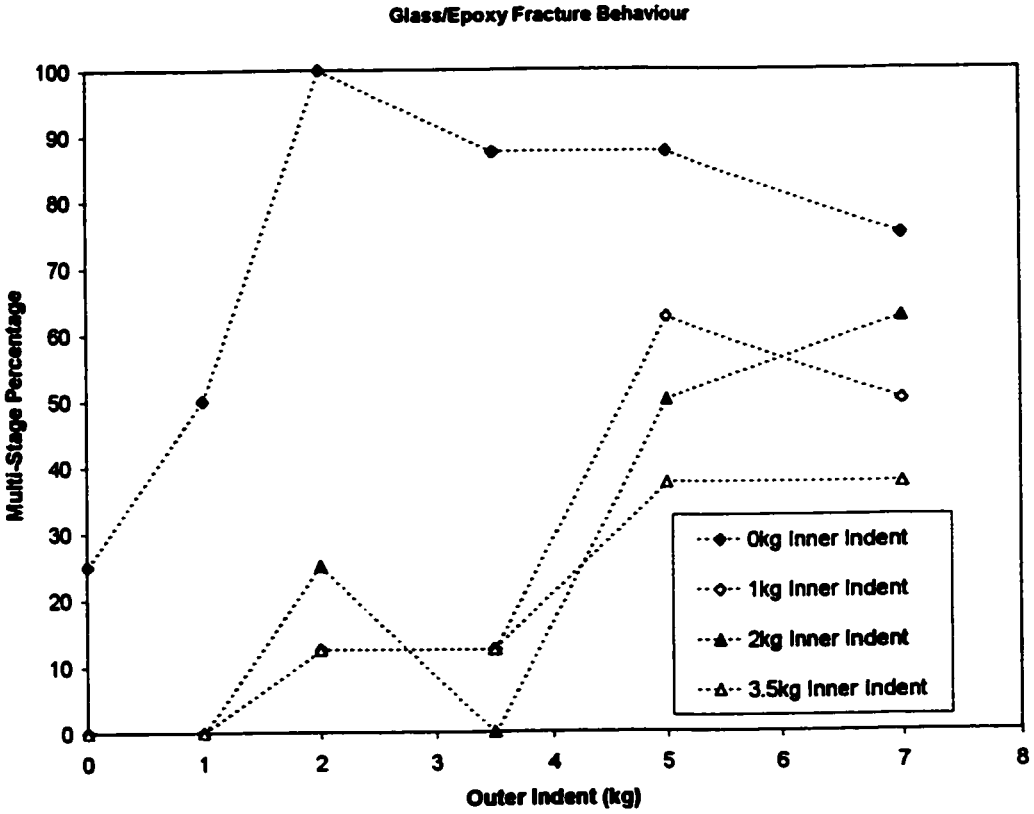

Figure 5.1.4-3. Proportion of multi-stage fractures in glass/epoxy composites as a function of outer indent load.

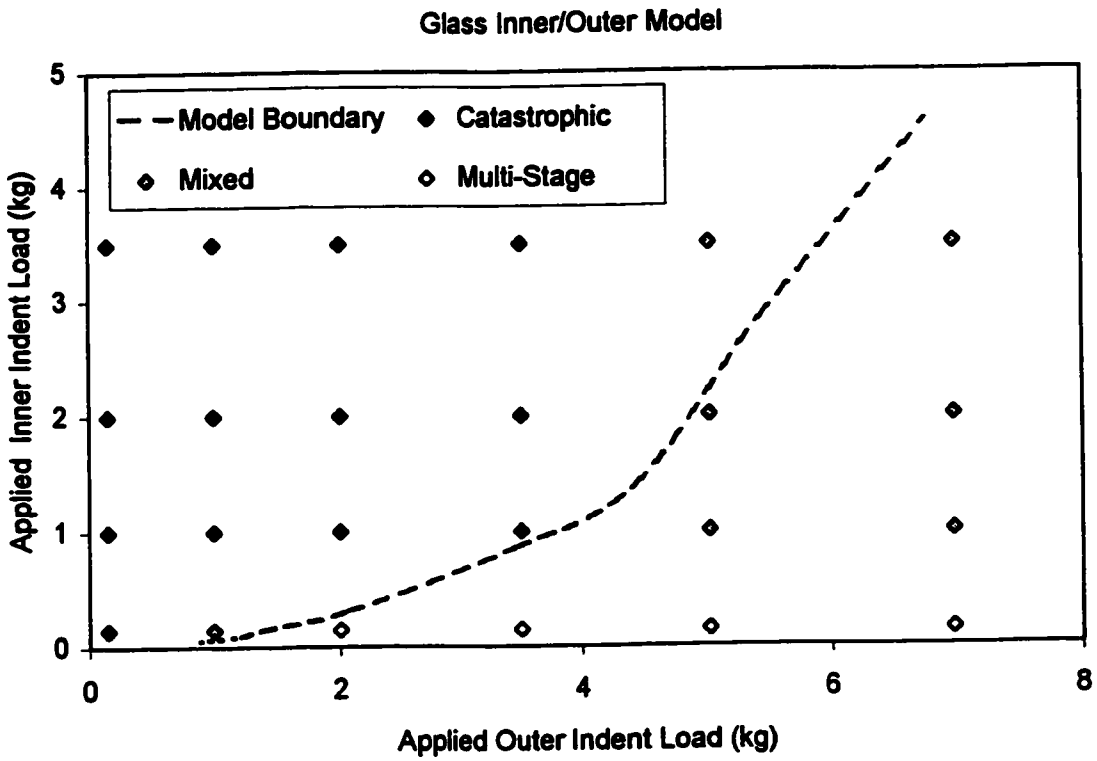

Figure 5.1.4-4. Fracture behaviour as a function of inner and outer applied indent load.

The difference in strength of the two strong layers in the composite has a strong influence on its fracture behaviour. The proportion of multi-stage fractures was plotted against the layer-strength-difference (inner minus outer) – in Figure 5.1.4-5. The strength difference was calculated from the monolithic glass strengths in Figure 5.1.3-1. Composites with stronger outer layers than inner layers (negative values in the figure) failed catastrophically. Composites with stronger inner layers than outer layers (positive values in the figure) showed some multi-stage fracture behaviour. The greater the (positive) difference, the more likely the fracture was non-catastrophic.

The nominal residual strength in the glass/epoxy composites was expected dependent on the inner indent load. The consistency of sample geometry and indent strength, make comparisons easier than for the zirconia/lanthanum-aluminate composites. Figure 5.1.4-6 shows the residual strength as a function of inner applied indent load. There is variation in the data, but no indent load dependence is apparent. The nominal residual strength is comparable in all of the samples. The monolith glass sample strengths showed a difference for this range of indent loads, but it is smaller than the variation of strength in Figure 5.1.4-6. This may be due to the extent of interlayer cracking.

The residual strength of the composites is higher than monolithic glass. The nominal residual strength is based on the initial thickness of the samples, but the "true" residual strength is four times higher (for ℓ/h =1/2, and from strength to sample height relation). This is partially due to the Weibull effect in the

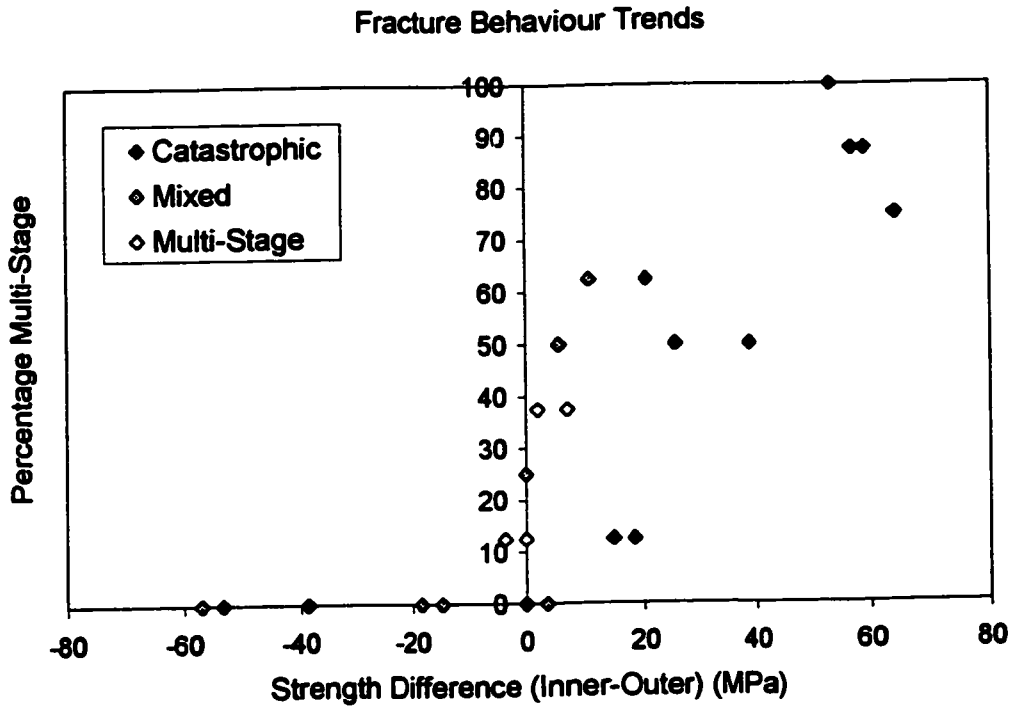

Figure 5.1.4-5. The proportion of multi-stage fractures as a function of layer strength difference (inner-outer).

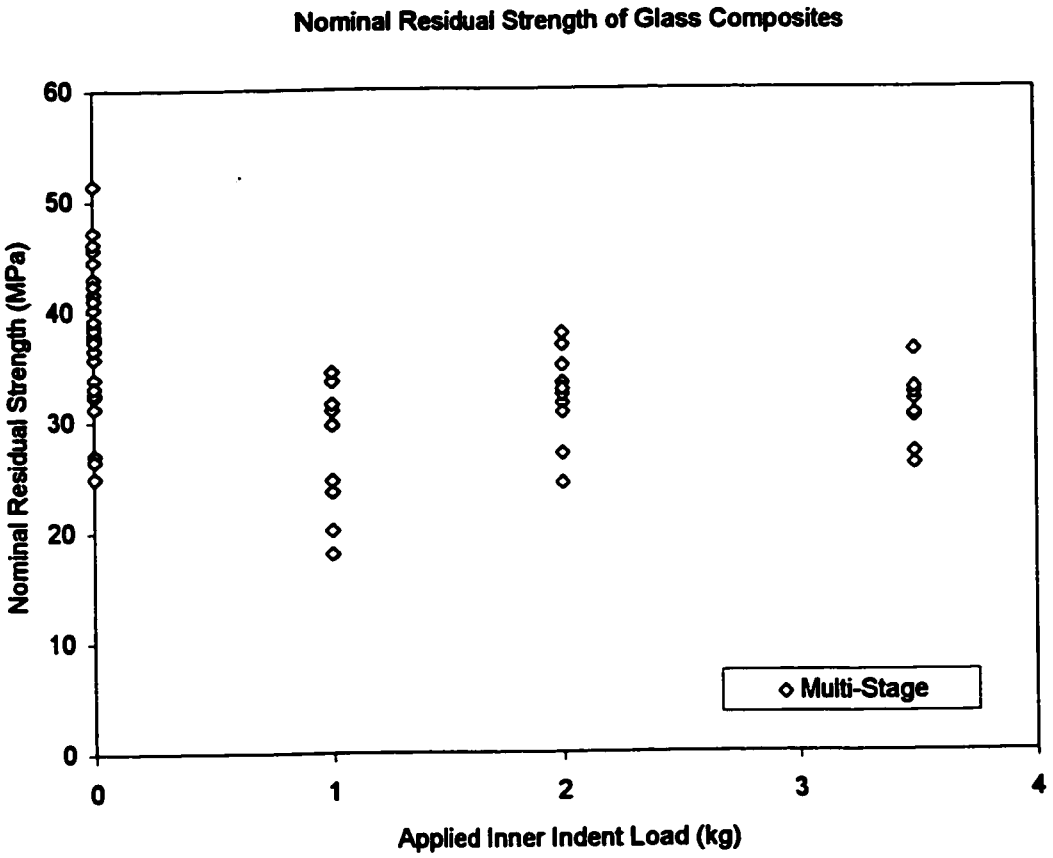

Figure 5.1.4-6. The residual strength of the glass/epoxy composites as a function of inner applied indent load.

samples with non-indented inner layers. A small volume of material is subjected to the maximum stress in the beam, so it is correspondingly stronger. In all samples the strength increase can be attributed to the cracked surface layer bearing some load. The strength reported relies on the remaining layer of the beam, but the surface layer still contributes. The true stress in the next layer is lower than calculated, so the observed strength increase is artificial. This effect also depends on the extent of interlayer fracture.

The extent of interlayer cracking can be estimated from the load drop during fracture of the surface layer, and Equation 3.1-11. Figure 5.1.4-7 shows the calculated value as a function of the nominal residual strength. It is assumed interlayer cracking occurs instantaneously, during fracture of the surface layer. There is no apparent relation between the nominal residual strength and the extent of interlayer cracking, though there may be an effect due to the initial strength.

The work-of-fracture of the glass/epoxy composites was more consistent than the zirconia/lanthanum-aluminate. Figure 5.1.4-8 shows the work-of-fracture as a function of outer indent load. Samples with a smaller indent load have a high work-of-fracture associated with their high strength. Samples subjected to a higher indent load have a low work-of-fracture associated with their low strength, but a high work-of-fracture associated with their high residual strength following multi-stage fracture. Moderate outer indent loads lead to a compromise.

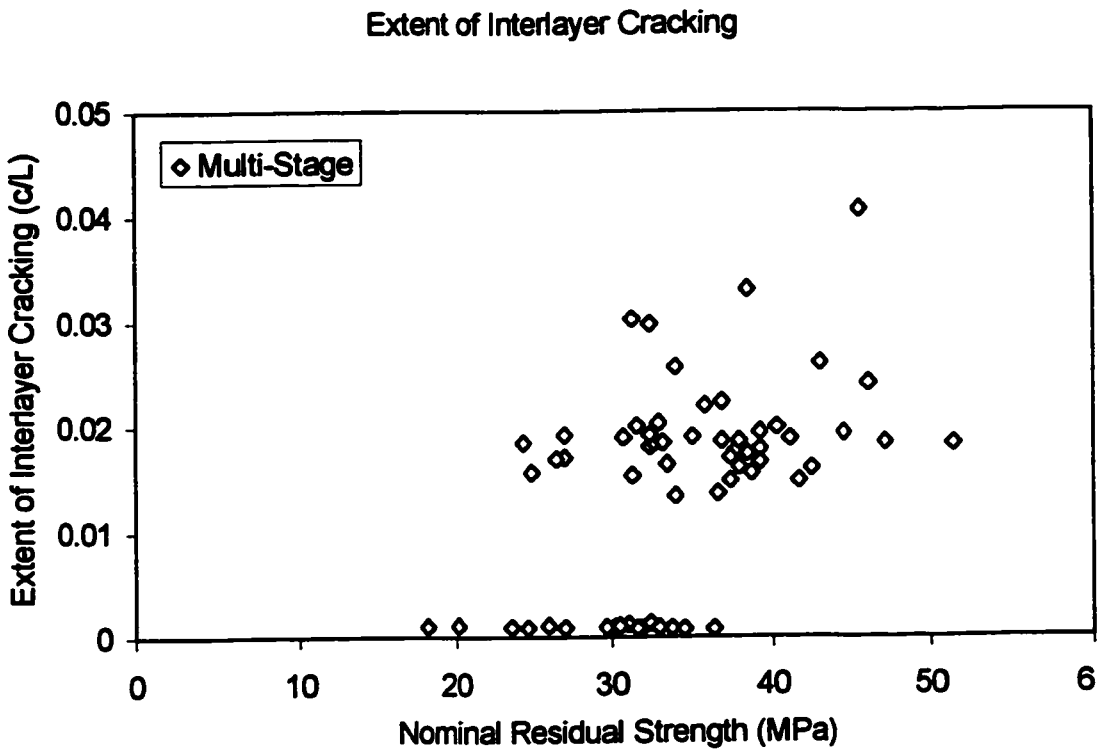

Figure 5.1.4-7. The calculated extent of interlayer cracking as a function of residual strength.

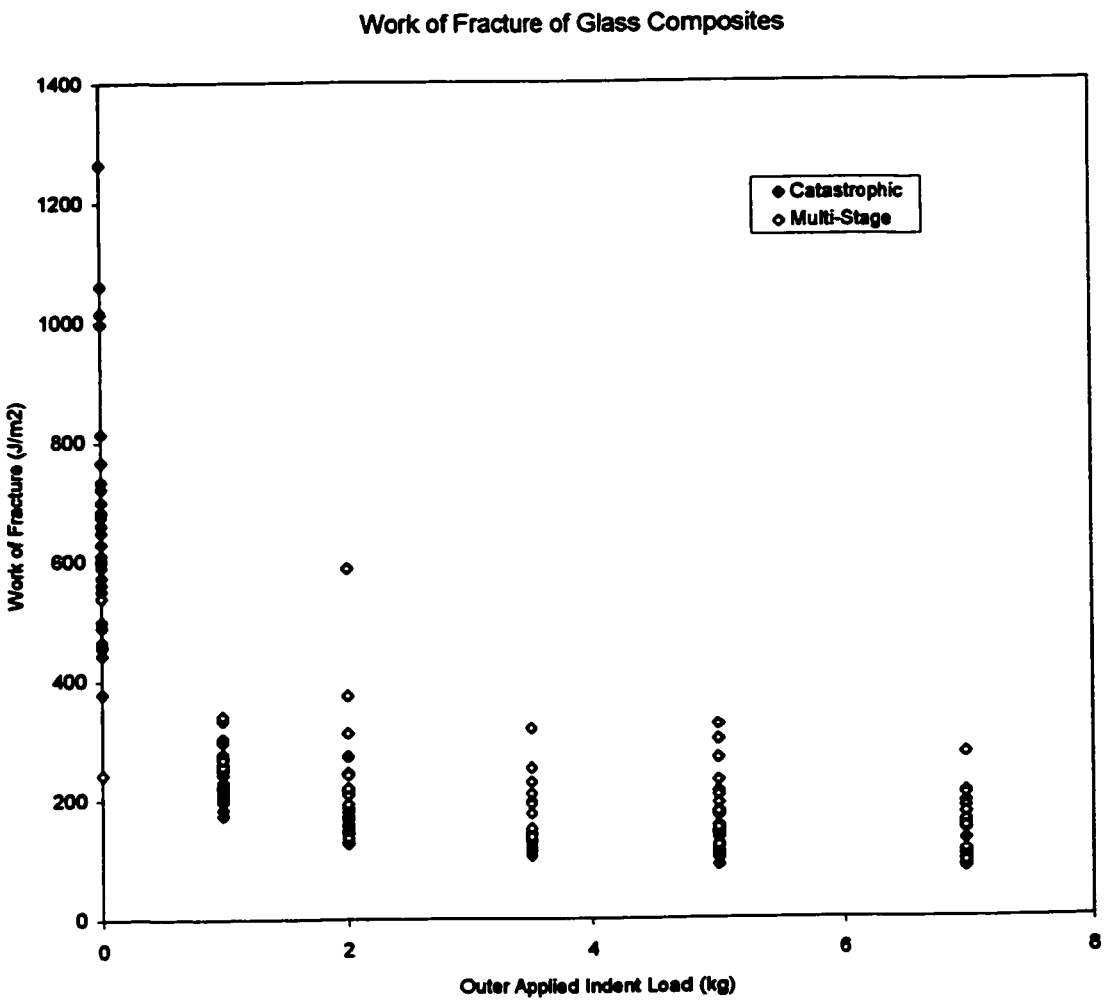

Figure 5.1.4-8. The work of fracture of the glass/epoxy composite as a function of outer applied indent load.

Figure 5.1.4-9 shows the work-of-fracture as a function of the inner indent load. There is a variation in the data due to the range of outer indent loads used in the tests. High works-of-fracture are possible, regardless of the inner applied indent load, but these samples fail catastrophically.

Figure 5.1.4-10 shows the work of fracture as a function of the nominal residual strength. Samples that failed catastrophically have a variation in work of fracture due to the variation of outer applied indent loads. The samples that failed in a multi-stage manner exhibit a relation between work of fracture and nominal residual strength. No multi-stage composites had a work of fracture comparable to the best of the catastrophic samples. This is inconsistent with the zirconia/lanthanum aluminate results, in which some multi-stage fracture samples had higher works-of-fracture than monoliths. The difference is in the surface layer thickness ratios. Some zirconia composites were made with thin surface layers, so had high residual works-of-fracture. The ½ surface layer thickness ratio used in the glass/epoxy composites does not produce a high enough residual work-of-fracture to compensate for the low initial work-of-fracture associated with the large outer indent load. The large outer indent load is necessary to achieve multi-stage fracture. This observation implies multi-stage fracture is not necessarily the optimum way to ensure good mechanical properties.

The results of the glass/epoxy tests are consistent with those of the zirconia/lanthanum aluminate tests. High strength and high work-of-fracture are difficult to achieve in the same material. High strength has no residual work

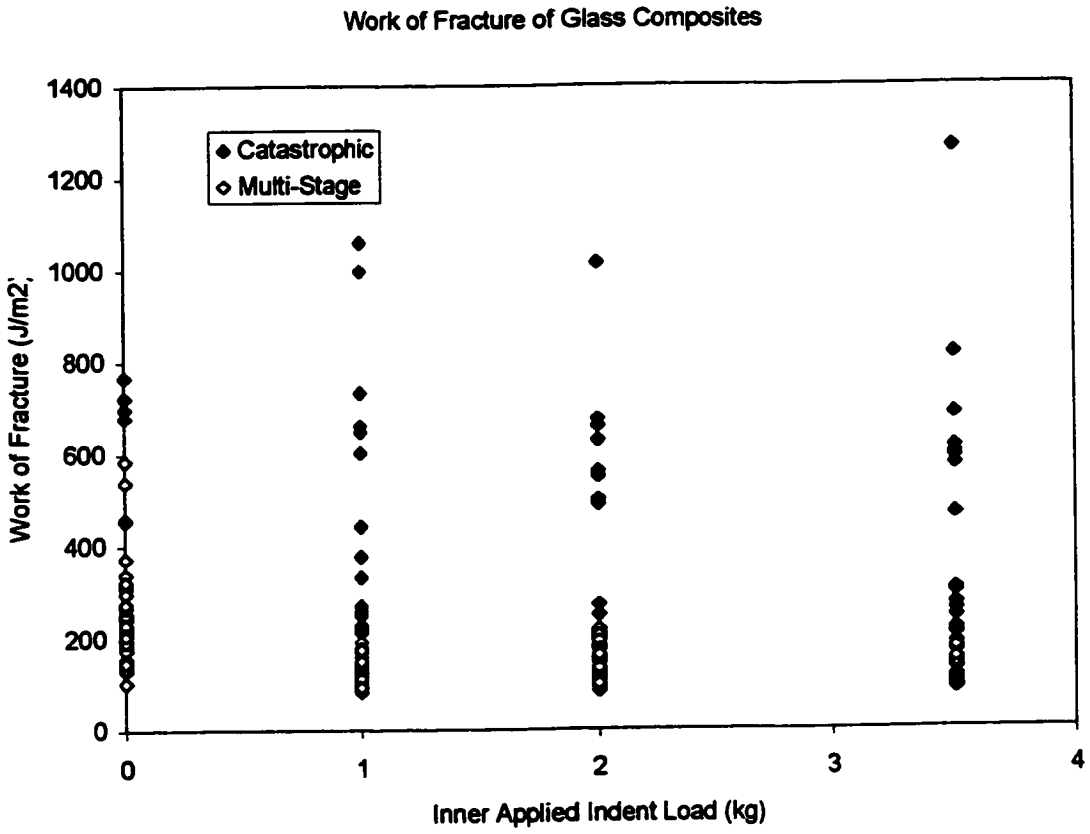

Figure 5.1.4-9. The work of fracture of the glass/epoxy composites as a function of inner applied load.

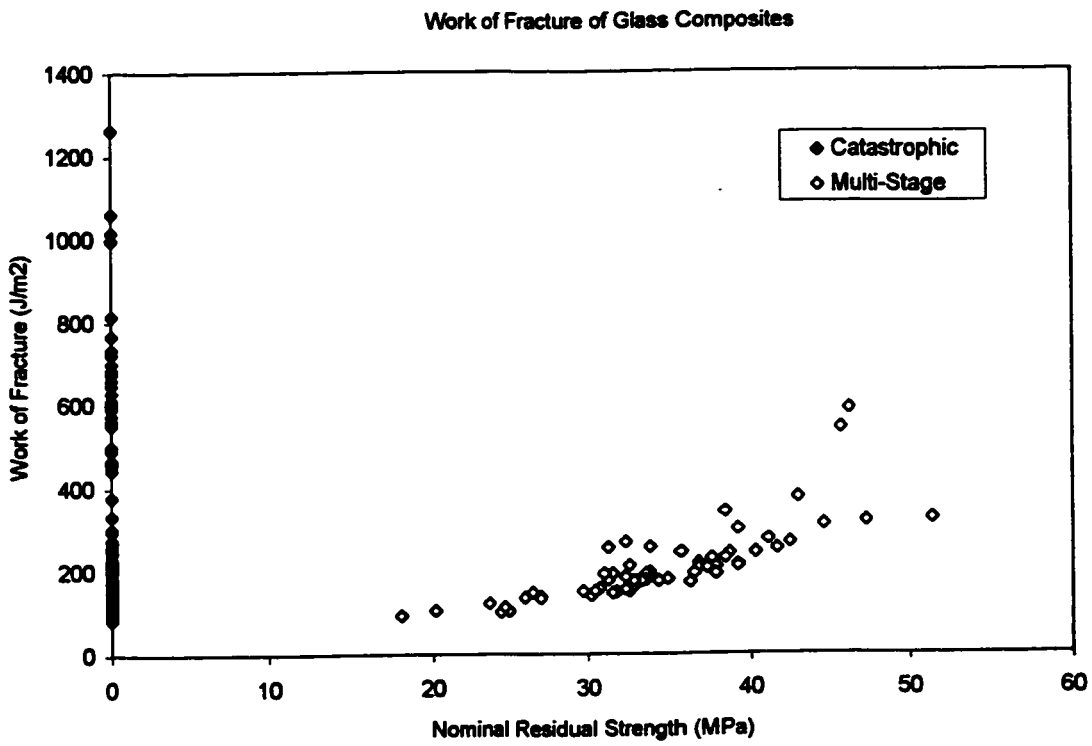

Figure 5.1.4-10. The work of fracture of the glass/epoxy composites as a function of nominal residual strength.

of fracture, but multi-stage fracture requires low strength. Optimization requires a compromise.

5.1.5 Plaster-of –Paris

The highlights of the plaster-of-Paris work were discussed in Section 2.3.4. The pattern of fracture behaviour, shown as Figure 2.3.4-1, is consistent with the fracture mechanics model developed in Section 3.1 and the results of the zirconia/lanthanum-aluminate and glass/epoxy experiments.

5.2 Finite Element Analysis

The accuracy of the analyses was determined by comparing the finite element calculated load and stress values to equivalent theoretical values. Figure 5.2-1 shows the difference as a function of the number of elements used in the calculation. In each case the length/height (slenderness) ratio of the beam was the same.

The accuracy of the finite element calculation improves as more elements are used. Values converge if >600 elements are used. Constant strain quadrilateral elements cannot accurately simulate pure bending conditions, for shear does not exist, so some error is inevitable. The figure shows the error is ~1% for loads, and ~2.5% for stress calculations.

The bulk of this work was based on load calculations. The use of 720 elements was considered as an appropriate balance of calculation accuracy and computation time. Each calculation used the same number of elements, so is expected to have a comparable error. Normalization of all calculated values reduces the problem. There *is* error accrued during the regression analysis.

5.2.1 Catastrophic Failure

The calculated load (for a given, constant displacement) as a function of main crack size is shown as Figure 5.2.1-1. The load required to bend

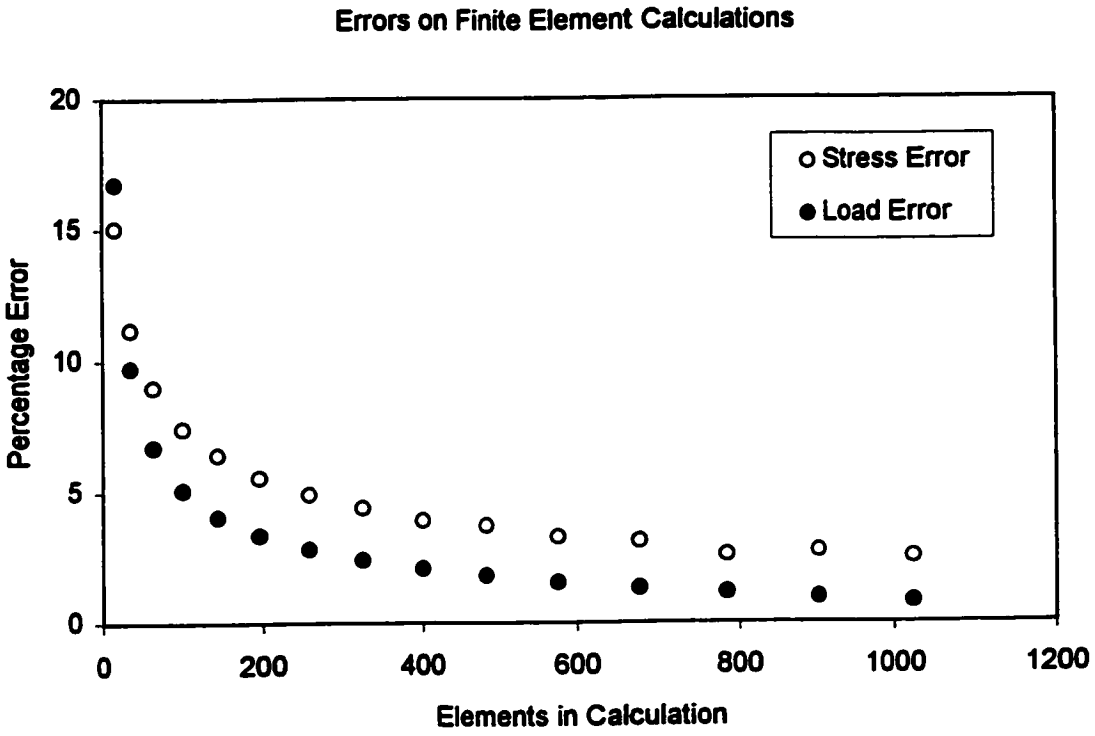

Figure 5.2-1. The error in finite element calculations as a function of the number of elements used in the mesh.

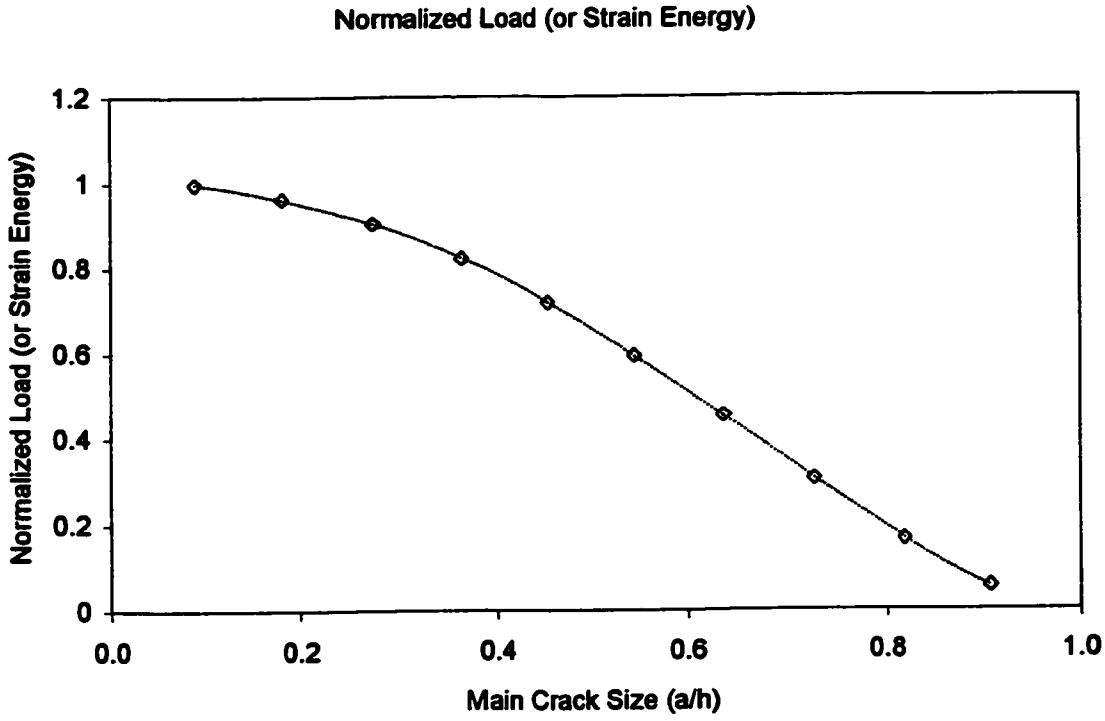

Figure 5.2.1-1. Normalized load (or strain energy) as a function of normalized main crack size during catastrophic failure.

the beam to the given displacement decreases as the crack size increases, because the compliance increases.

Following Equation 3.2.1-12, the calculated load values were compared with stress intensity factors derived from several regression equations; each with an increasing number of terms. The regression equations are plotted in Figure 5.2.1-2, with a standard solution (Brown, 1966) for comparison. An increased number of terms in the regression equation allows a steeper curve to be fit to the data, which increases the calculated stress intensity factor. This figure demonstrates the equations converge to a solution that is slightly lower than the standard one. The standard solution is based on a compliance curve fit to experimental data. The assumptions necessary for this calculation could result in a higher calculated stress intensity.

The load calculations were repeated with different mesh refinements. A fourth order polynomial was fit to each set of values. The data and three of the equations are plotted in Figure 5.2.1-3. The regression equations converge quickly. The use of 720 elements in each calculation was confirmed to be acceptable.

The derivative of the load equation with respect to main crack size gives the strain energy release rate, due to the proportionality of the load and strain energy at constant displacement, and normalization of the values. As the crack propagates the strain energy release rate increases, that is, the magnitude of the slope of the load curve increases. The strain energy release can be considered

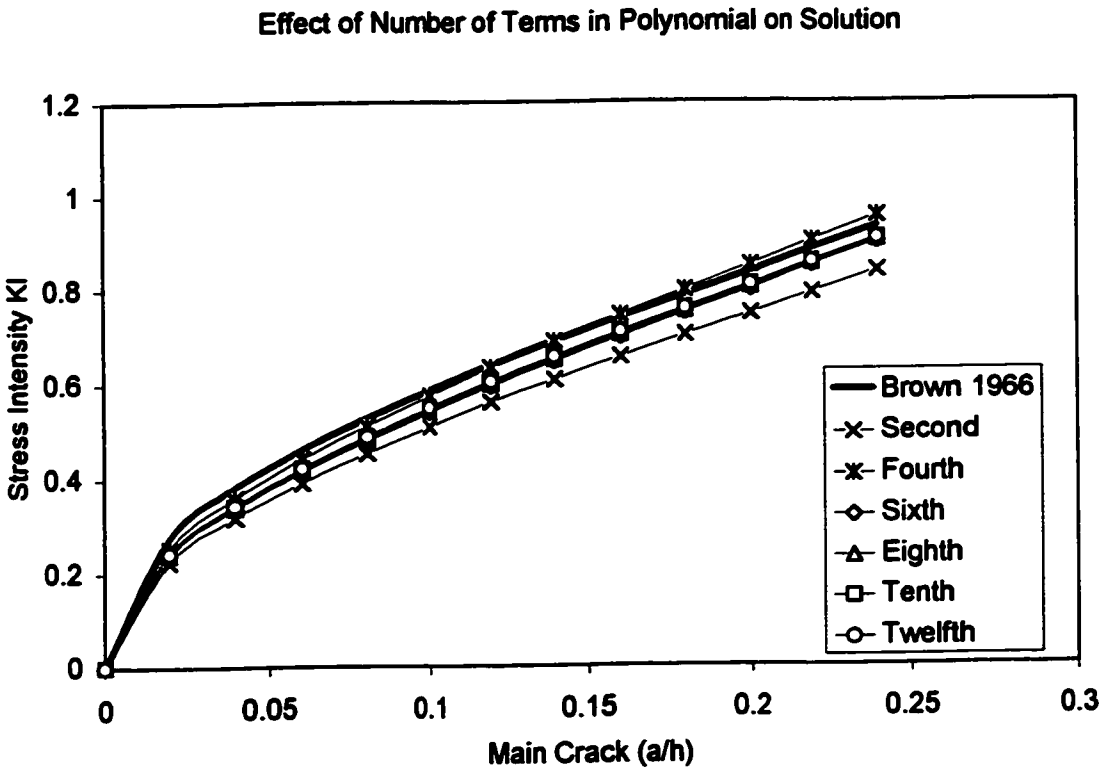

Figure 5.2.1-2. The effect of number of terms in the regression equation on the predicted stress intensity factor.

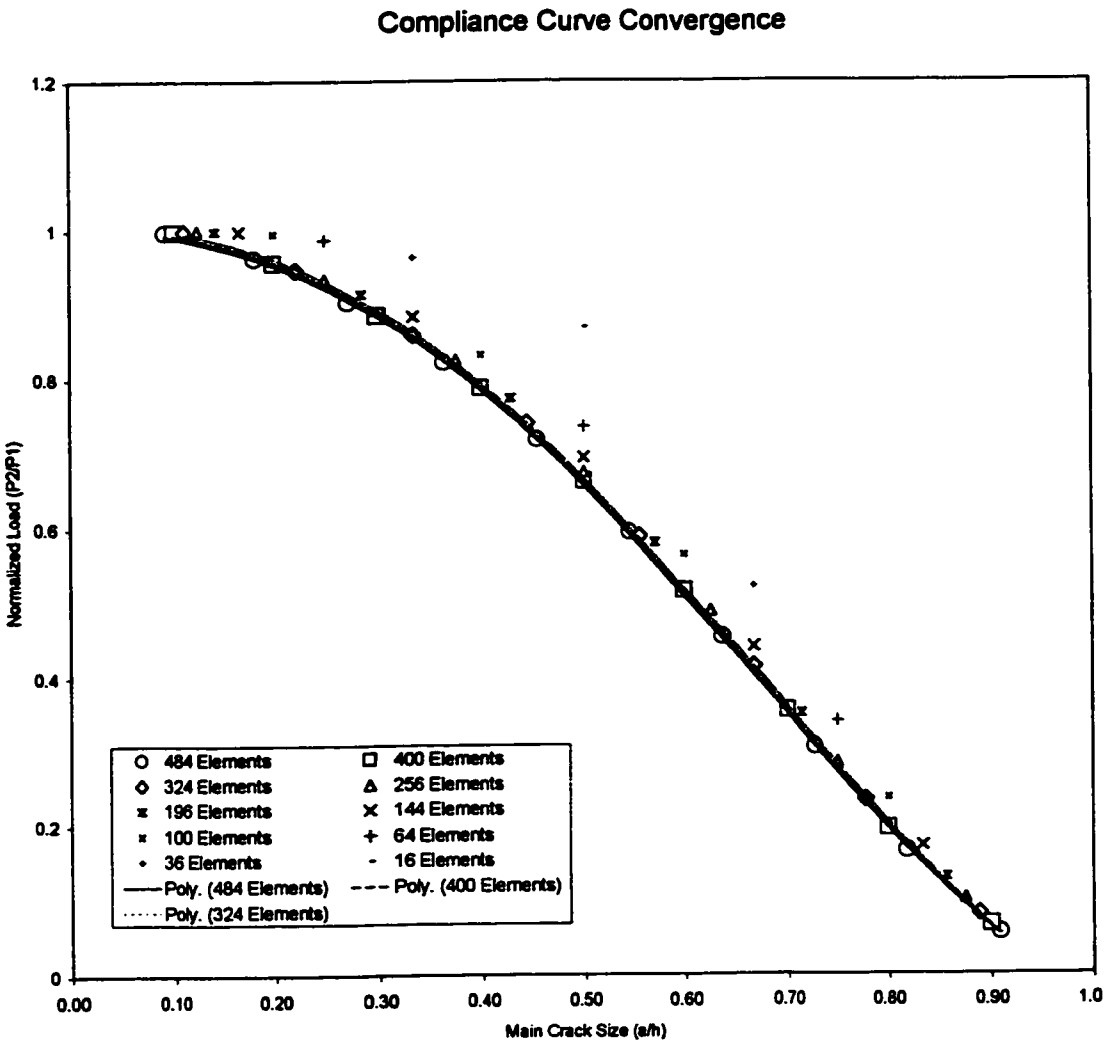

Figure 5.2.1-3. The effect of number of elements in each calculation on the regression equation.

as a sum of surface energy, which is constant for the material, and kinetic energy, which increases.

The crack propagates unstably because the strain energy release rate is higher than (twice) the surface energy of the material, after the onset of propagation. If the surface energy of the material increases across the thickness of the beam more quickly than the strain energy release rate increases, then the crack can be slowed or even arrested. This suggests there are toughening opportunities in fabricating functionally graded materials with a surface energy that increases across a sample that is greater than parabolic. The problem is that a change in surface energy is usually accompanied by a change in elastic modulus, and the parabolic compliance curve becomes invalid. It may be possible to functionally grade both the modulus and surface energy across a sample to achieve stable cracking and increased toughness.

5.2.2 Delamination Fracture

The calculated load (for a given, constant displacement) as a function of interlayer crack size is shown as Figure 5.2.2-1. Values are given for $\ell/h=1/4$, which is representative of the calculations. Similar to catastrophic failure, the load required for a given displacement decreases with increasing crack size, as the compliance of the beam increases. The calculated values are compared with Equation 3.1-11. Derivation of the equation was done assuming zero stress

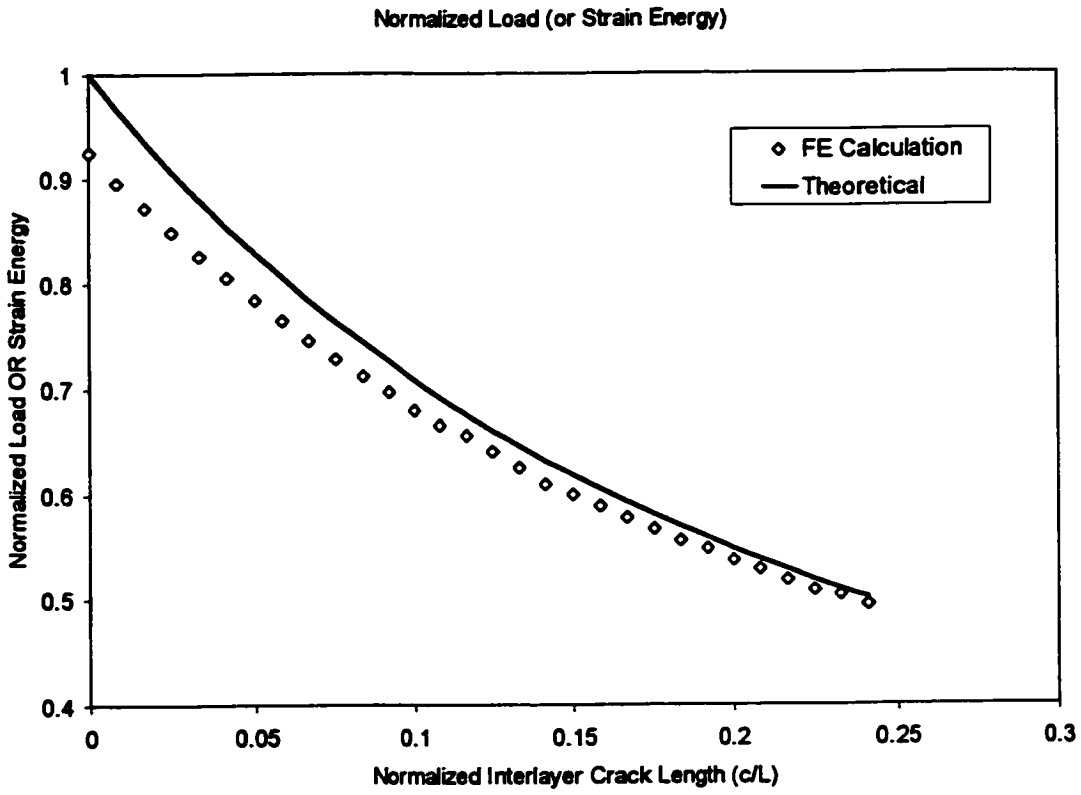

Figure 5.2.2-1. The load as a function of interlayer crack size (during delamination).

in the delaminated layers. This is not the case, so some difference is expected.

A derivative of the load equation with respect to the interlayer crack size gives the strain energy release rate of the interlayer crack. The slope of the calculated values and that of Equation 3.1-11 are comparable, despite the difference in magnitude. Unlike catastrophic failure, the strain energy release rate of the interlayer crack decreases as the crack propagates. This means the secondary crack may stabilize, depending on the surface energy of the material. If the geometry of the beam and the toughness of the interlayer can be controlled, the extent of interlayer fracture can be controlled. This affects the stress distribution in the beam, and therefore the residual strength and work-of-fracture. Note that this scenario does not involve pre-cracking of the interlayer during catastrophic failure of the surface layer. This will later be shown critical to the fracture behaviour of the material.

5.2.3 Pre-Cracking of the Weak Interlayer

The calculated load (for a given, constant displacement) as a function of main and interlayer crack size is shown as Figure 5.2.3-1. The layer thickness ratio is $\ell/h=1/2$. The load decreases as either one of the two cracks propagate. The regression coefficients, β_i's, are given in Table 5.2.3-1, and their calculated errors in Table 5.2.3-2. The R-squared value for each regression was >0.98.

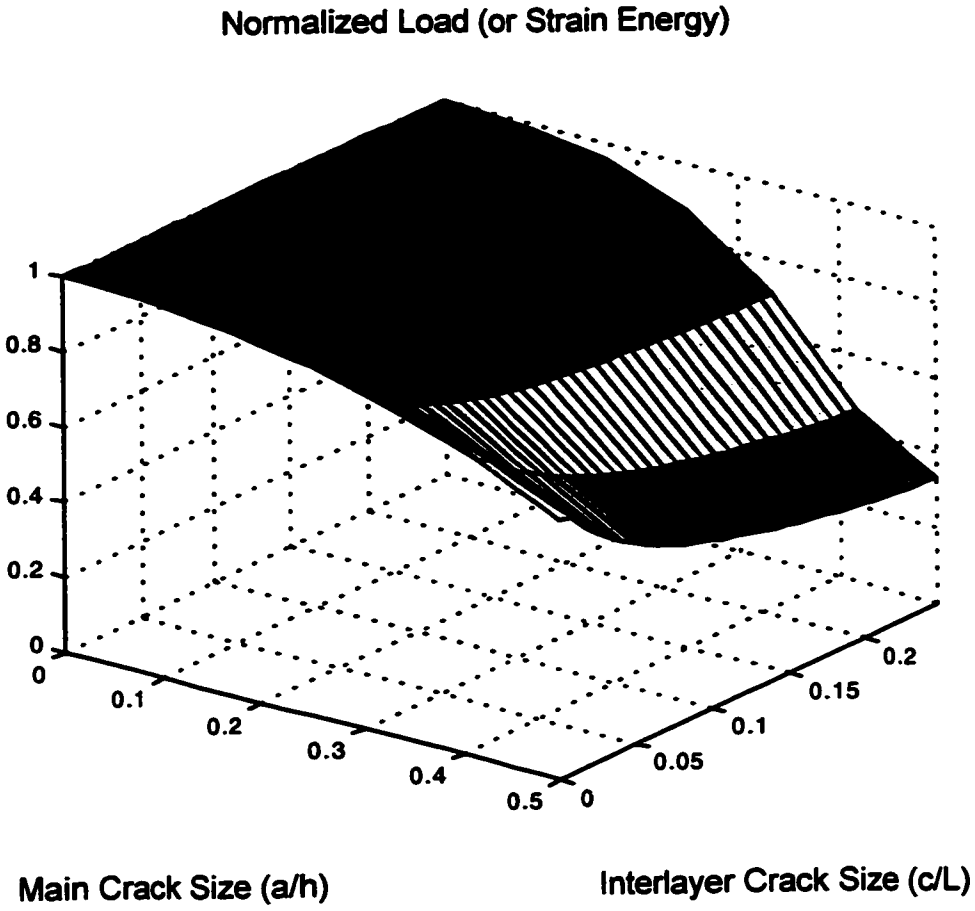

Figure 5.2.3-1. The load as a function of main and interlayer crack size (during pre-cracking of the interlayer).

ℓ/h	β1	β2	β3	β4	β5	β6	β7	β8	β9
1/12	1.00	0	-290	0.0034	-970	0	-0.70	3.1E4	0
1/6	1.00	-1.05	-24	0.055	25	-2.1E4	-3.1	1.4E3	6.2E5
1/4	1.00	-1.3	-4.8	0.32	-130	-4.3E3	-16	7.3E3	1.1E5
1/3	1.00	-1.3	-2.4	0.78	-170	-1.2E3	-33	7.6E3	3.3E4
1/2	1.00	-1.2	-1.3	1.8	-150	-130	-68	-6.2E3	5.6E3
2/3	1.00	-1.2	-0.67	2.6	-121	52	-104	4.7E3	-900

Table 5.2.3-1. The regression coefficients for the load function (during pre-cracking of the interlayer).

ℓ/h	Err1	Err2	Err3	Err4	Err5	Err6	Err7	Err8	Err9
1/12	1.6E-5	2.2E-3	3.2E-1	2.2E-1	3.2E1	4.7E3	3.3E3	4.7E5	6.7E7
1/6	4.3E-5	6.2E-3	8.9E-1	6.2E-1	8.9E1	1.3E4	8.9E3	1.3E6	1.9E8
1/4	9.6E-5	1.4E-2	2.0E0	1.4E0	2.0E2	2.9E4	2.0E4	2.9E6	4.1E8
1/3	2.1E-4	3.1E-2	4.5E0	3.1E0	4.5E2	6.5E4	4.5E4	6.5E6	9.3E8
1/2	6.6E-3	8.1E-2	1.2E1	8.1E0	1.2E3	1.7E5	1.2E5	1.7E7	2.4E9
2/3	8.1E-4	1.2E-1	1.7E1	1.2E1	1.7E3	2.4E5	1.7E5	12.4E7	3.4E9

Table 5.2.3-2. The calculated error on the regression coefficients for the load function (during pre-cracking of the interlayer).

The regression equation is composed of a theoretically derived equation and an empirical equation. If the form of the equation is correct, a plot of the residuals as a function of crack size should have a random pattern. The residual for each point is the difference between the finite element calculated value and the regression equation calculated value. Figures 5.2.3-2 and 5.2.3-3 show the residuals as a function of main crack size and interlayer crack size respectively.

The residual plots show that the form of the equation is not ideal. Residuals increase with increasing main crack size, and there is subtle pattern apparent with increasing interlayer crack size. The regression equation was manipulated by trial and error, and this is the most appropriate relationship found. All of the residuals are ≤1.2%, and this is acceptable. The problem is not likely to have a simple mathematical solution.

The main and weak interlayer crack sizes are important parameters in governing the fracture behaviour of this class of composite. A high, medium and low value of each were selected to simplify comparisons. The values chosen were a/h = 0.005, 0.0125, 0.05 and c/L = 0.0005, 0.00125, 0.005. These crack size ratios correspond to cracks of 10, 25 and 100μm in typical zirconia specimens. Unless specified, both crack sizes are assumed their medium values. One parameter is changed at a time to allow comparisons.

The errors in the regression values vary with crack sizes *a/h* and *c/L*. For the "medium" conditions, the load error is <1%. This is representative of the

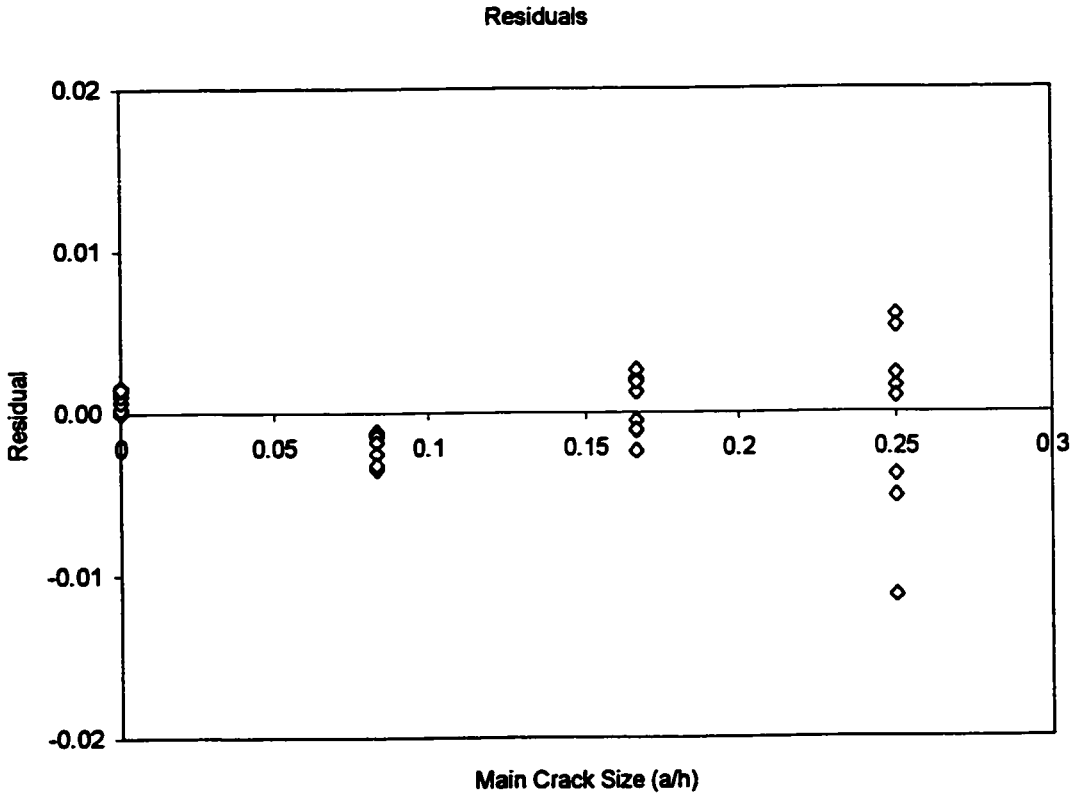

Figure 5.2.3-2. The residuals of the regression plotted as a function of main crack size.

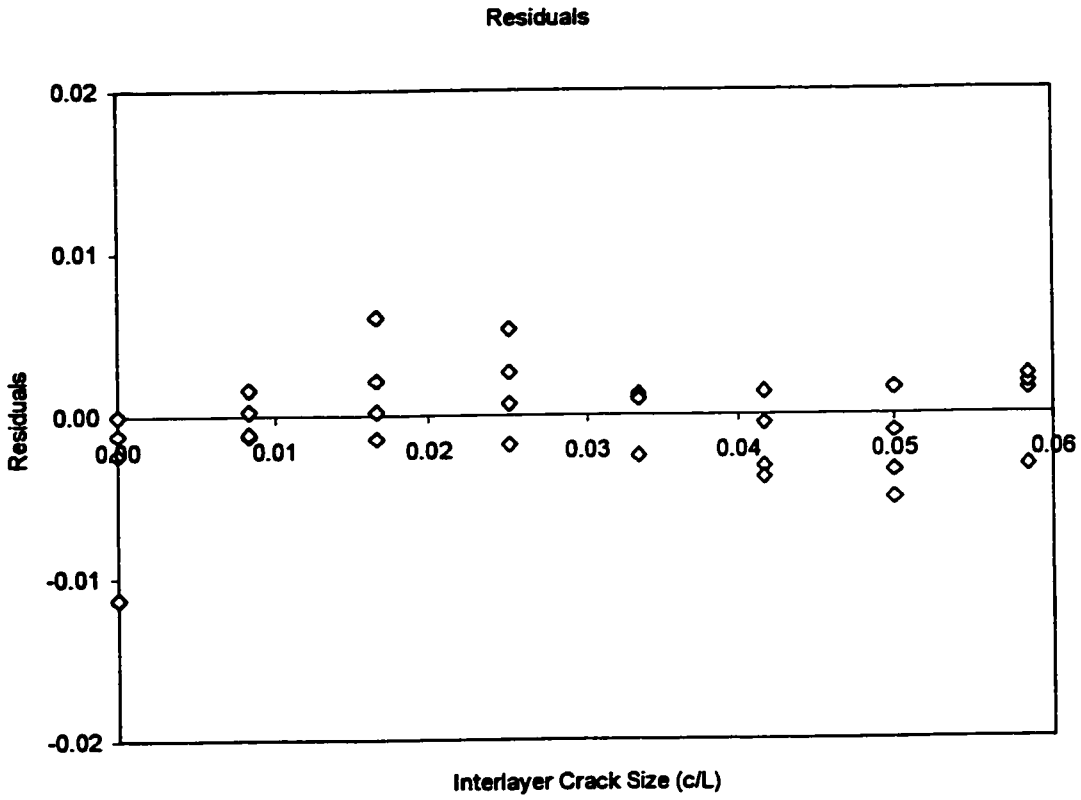

Figure 5.2.3-3. The residuals of the regression plotted as a function of interlayer crack size.

critical calculations. The error on the derivative of the load equation, that is, the strain energy release rate, is ~4%. The error on the derived strength parameter is ~3%. These errors must be considered when examining results.

Figure 5.2.3-4 shows how the strain energy release rate of the main crack changes during its propagation. This figure is based on Equation 3.2.1-2, the negative of the derivative of the load equation with respect to main crack size. The strain energy release rate increases as the crack size increases, so the fracture is catastrophic.

Figure 5.2.3-5 shows how the strength of the composite changes with main crack size. The strength is based on Equation 3.2.3-4. The curve follows theoretical expectations.

Figure 5.2.3-6 shows the strain energy release rate of the interlayer crack as a function of interlayer crack size, plotted for different values of main crack size. Positive values represent crack configurations that may lead to interlayer cracking, provided the interlayer toughness is low. Cracking is possible only if one of the two cracks is large. This is consistent with the premise of the fracture mechanics model. Negative values represent configurations in which the cracks will heal. These are only of theoretical interest.

The shape of the large main crack size curve has implications on the propagation of the weak interlayer crack. The strain energy release rate initially increases, which indicates catastrophic failure of the interlayer. The subsequent decrease indicates the possibility of stabilization. This suggests continued

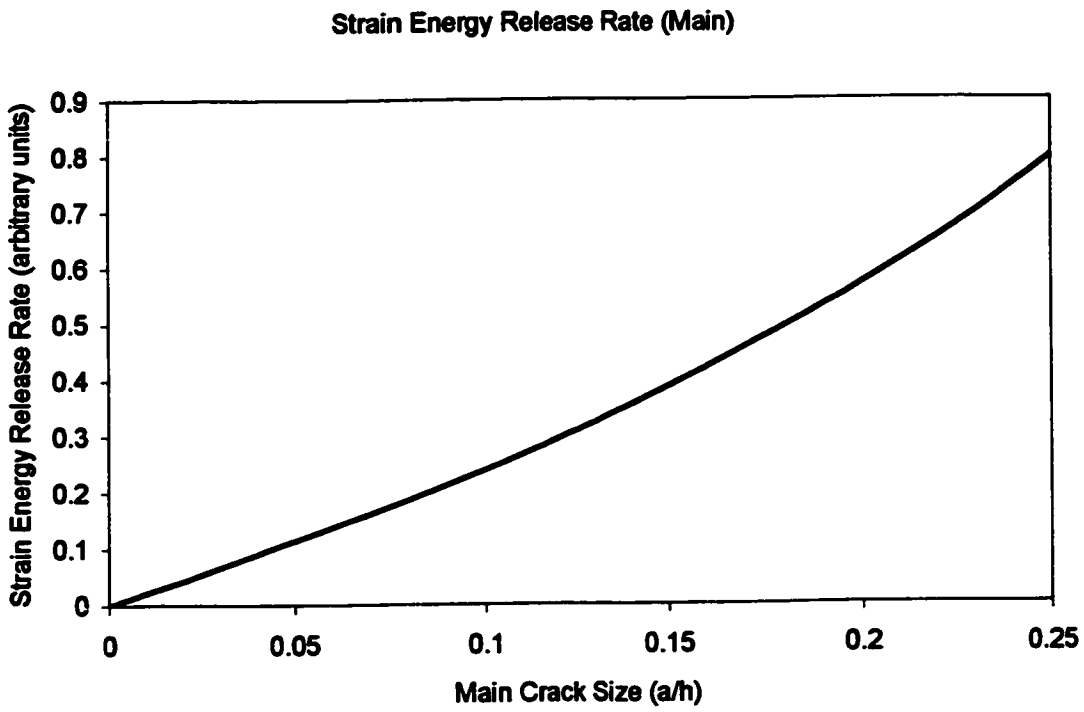

Figure 5.2.3-4. The strain energy release rate as the main crack propagates.

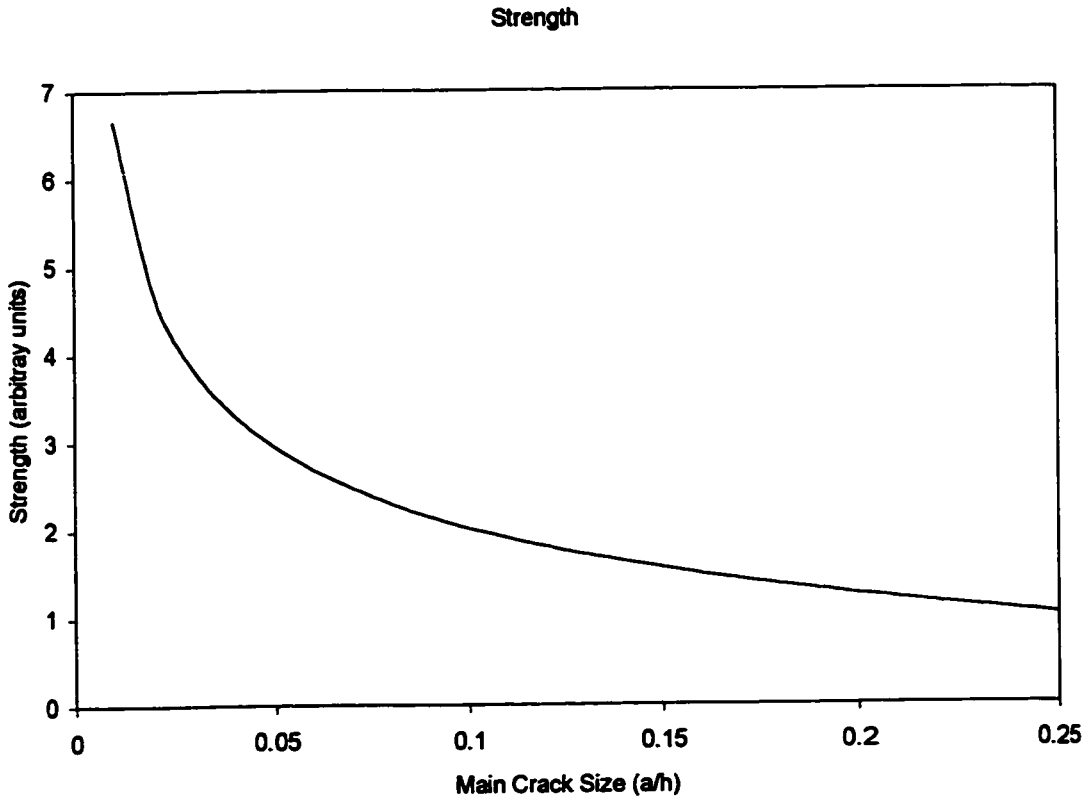

Figure 5.2.3-5. The strength of the composites as a function of main crack size.

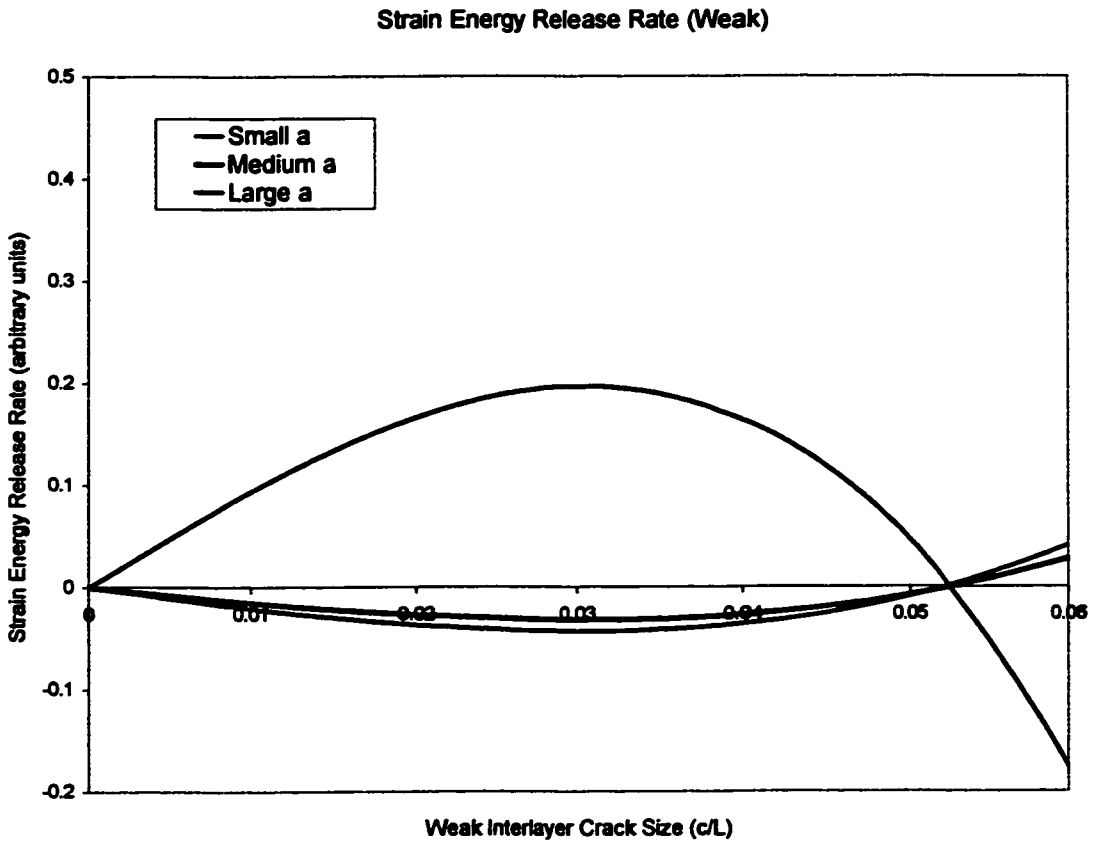

Figure 5.2.3-6. The strain energy release rate of the interlayer crack as a function of interlayer crack size.

cracking of the interlayer relies on continued propagation of the main crack.

The size of the interlayer crack has a minor effect on the strength of the composite, as shown in Figure 5.2.3-7. This is insignificant compared to the effect of the main crack size. No strength difference should be apparent unless both cracks are large. The shallow gradient of the curves indicates there is also no expected effect on the Weibull modulus of composites, when compared to monoliths.

The regression equation was used to predict pre-cracking of the weak interlayer. As the main crack propagates, its strain energy release rate increases. The ratio of strain energy release rates for the main and interlayer cracks also increases. At some point, the combination of crack sizes is sufficient to cause pre-cracking of the weak interlayer. This depends on several factors; the initial main crack size (at the onset of fracture), the initial interlayer crack size, and the ratio of toughness of the two materials. This approach is quasi-static, so is not expected to give exact predictions. Relative comparisons should be similar to the dynamic case.

Figure 5.2.3-8 is a plot of the ratio of the main and interlayer crack strain energy release rates as a function of main crack size, for various initial main crack sizes. The ratio increases rapidly for an initially small main crack and suggests pre-cracking of the interlayer is possible early in the fracture process.

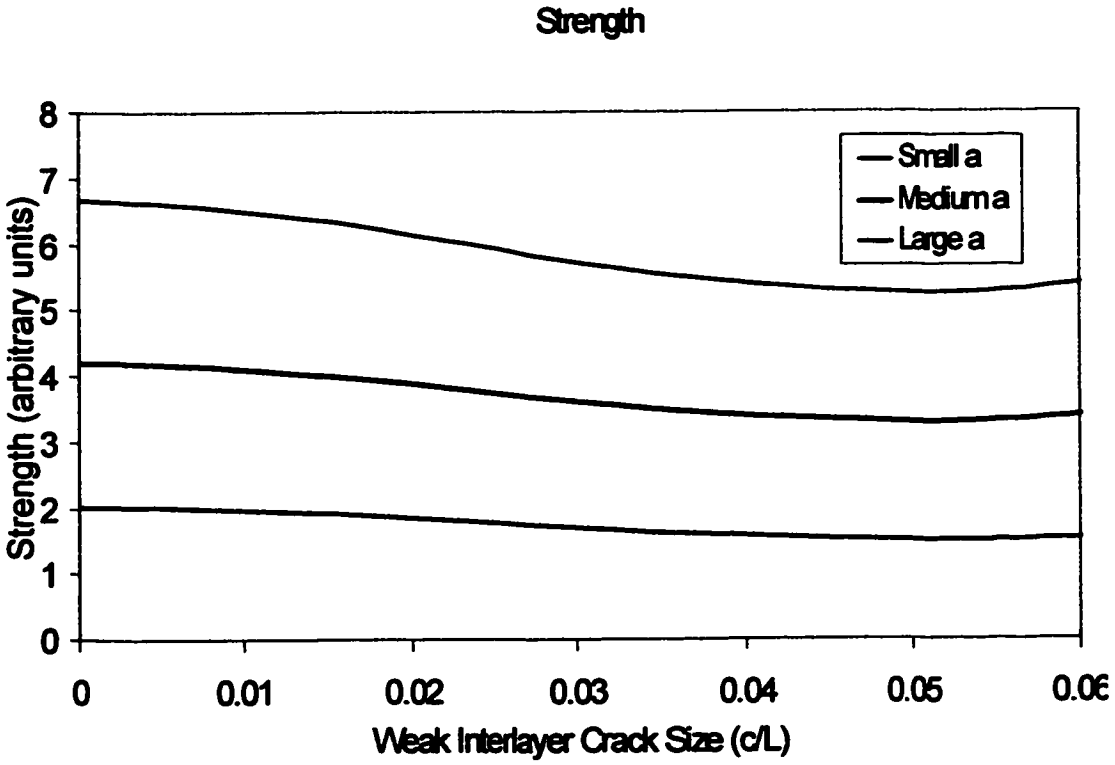

Figure 5.2.3-7. The strength of the composite as a function of interlayer crack size.

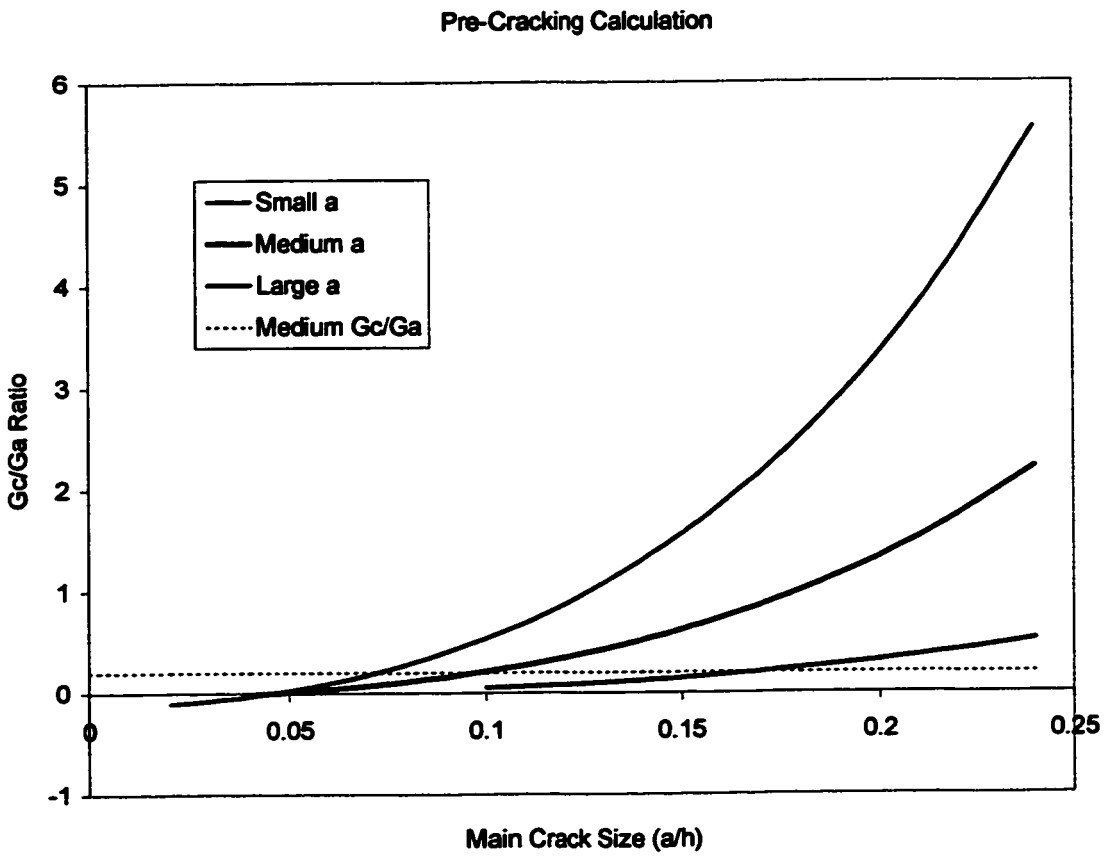

Figure 5.2.3-8. The ratio of main and interlayer crack strain energy release rates as a function of main crack size (l).

Conversely, a larger initial crack leads to pre-cracking later in the process. Values will depend on the ratio of material properties. Figure 5.2.3-9 is a plot of the ratio of main and interlayer crack strain energy release rates as a function of main crack size, for various initial interlayer crack sizes. Large interlayer cracks are predicted to start propagating earlier than small ones. This is consistent with intuition. Both figures are consistent with the fracture mechanics modeling work.

Figure 5.2.3-10 is a plot of the relative velocities of the main and interlayer cracks as a function of main crack size. In each case, the velocity increases as the main crack propagates. At some point during the propagation, the weak interlayer also begins to fracture. The interlayer crack also fails unstably. The form of the two sets of curves is similar. This supports the use of crack velocities as an *estimate* of crack propagation distance.

Figure 5.2.3-11 is a plot of the relative propagation distances of the main and interlayer cracks as a function of main crack size. In each case the interlayer crack propagation distance is a fraction of that of the main crack. The ratios are consistent for each set of curves. Note the approach is quasi-static, so it is not expected be exact, but comparisons should be valid.

Figures 5.2.3-8 to -11 suggest pre-cracking of the interlayer is possible. This is consistent with the literature, and the premise of the fracture mechanics model. The extent of interlayer crack propagation increases with decreasing initial main crack size. This suggests a small initial main crack should lead to more interlayer cracking, which leads to multi-stage fracture behaviour.

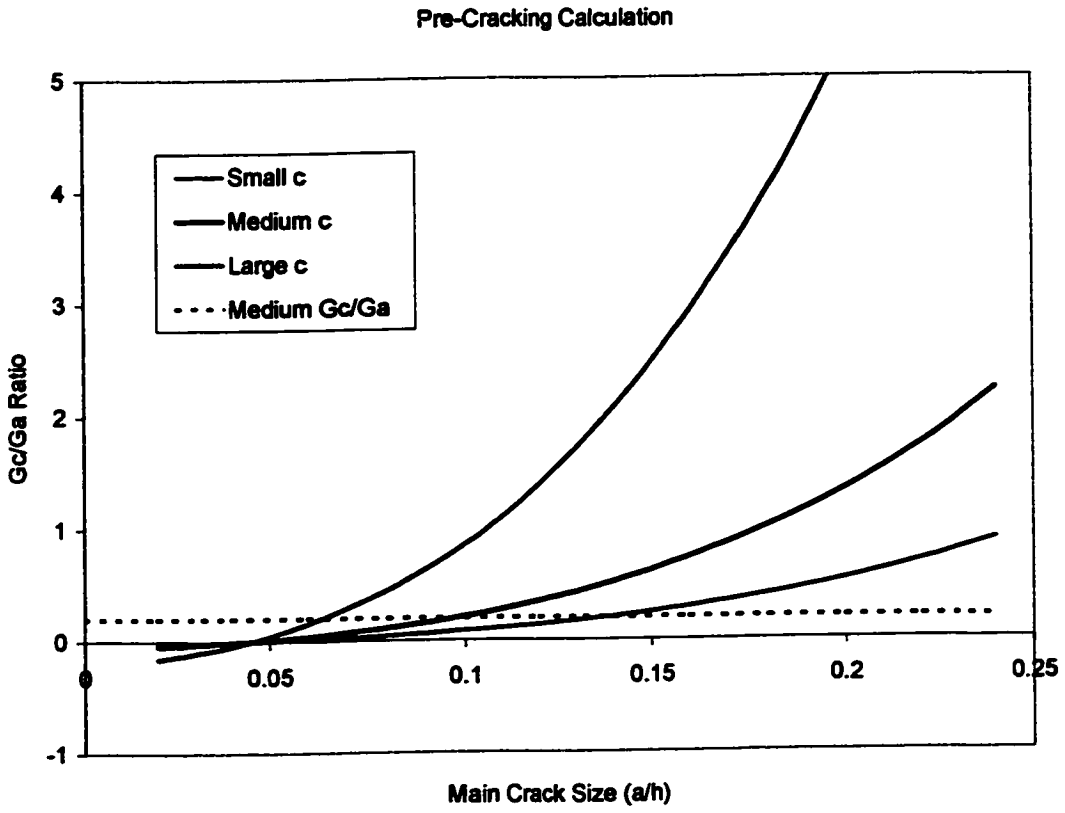

Figure 5.2.3-9. The ratio of main and interlayer crack strain energy release rates as a function of main crack size (II).

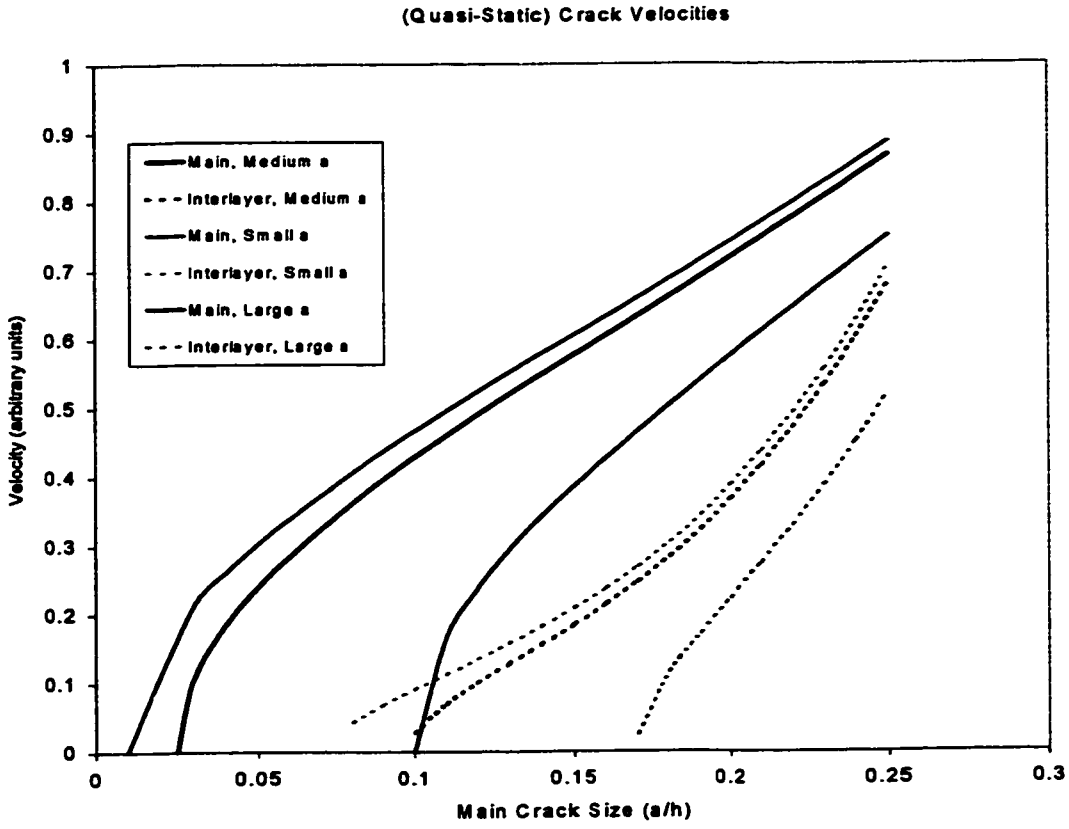

Figure 5.2.3-10. The relative crack velocities of the main and interlayer cracks, as a function of main crack size.

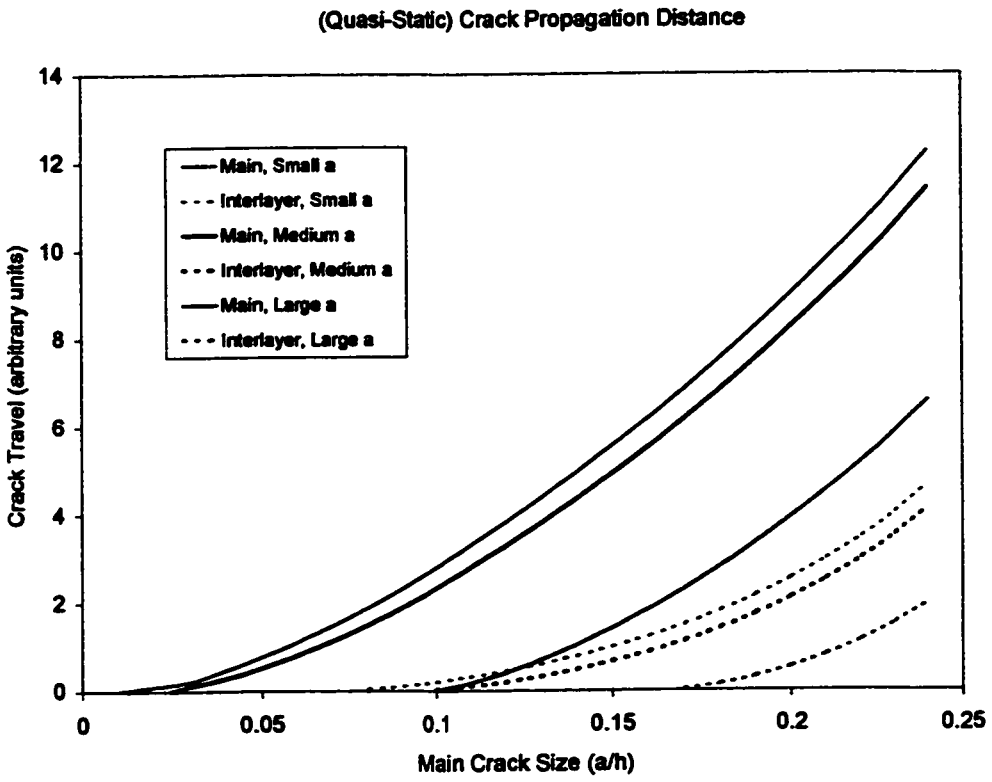

Figure 5.2.3-11. The relative crack propagation distances of the main and interlayer cracks, as a function of main crack size.

This is contrary to the experimental evidence. The discrepancy can be explained by considering Figure 3.1-4, the plot of critical interlayer crack length as a function of (strong) layer strength ratio. The smaller the initial main crack, the greater the extent of interlayer cracking necessary to achieve multi-stage fracture behaviour (for a given "next" layer strength). A large initial main crack leads to less interlayer cracking, but less is required to avoid catastrophic behaviour.

The ratio of the two materials' toughness will also influence the crack deflection behaviour of the composite. A tougher interlayer material delays its pre-cracking, which leads to less interlayer crack propagation distance. The result is a high stress on the next strong layer in the composite, and a greater chance of catastrophic fracture behaviour. A more brittle interlayer encourages its pre-cracking, and therefore multi-stage fracture. This argument relies on consistent initial main and interlayer crack sizes. The toughness ratio required for pre-cracking depends on the initial crack sizes (main and interlayer). This is an important feature of crack deflection.

5.2.4 Crack Tip Mesh Refinement

A typical mesh used for the crack tip mesh refinement is given in Figure 5.2.4-1. The number of elements used in each calculation varied, to a maximum of ~3000. Finer mesh in the vicinity of the crack tip allows more accurate stress intensities to be calculated.

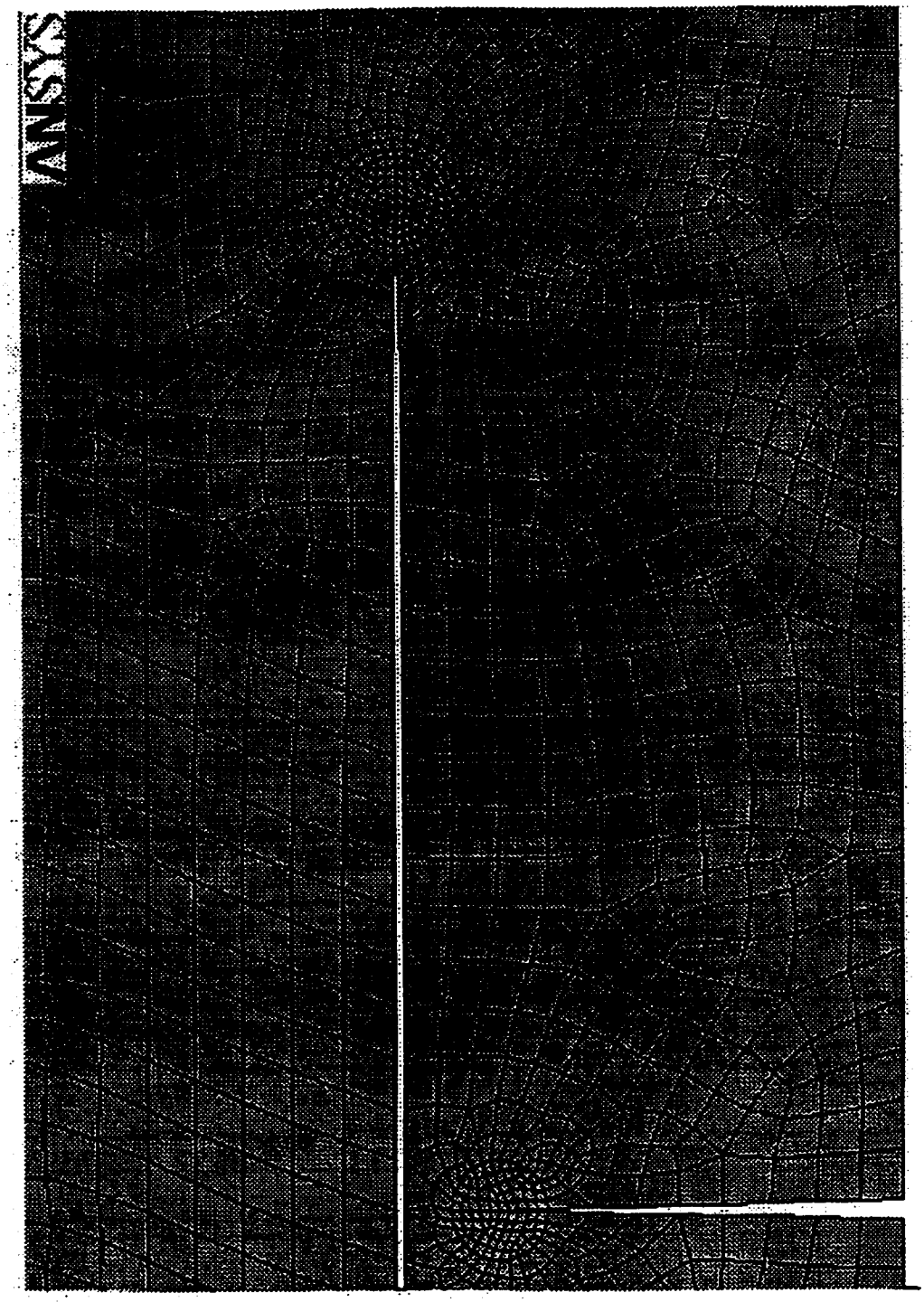

Figure 5.2.4-1. A typical mesh used for the crack tip mesh refinement.

Figure 5.2.4-2 is a comparison of the loads calculated using the commercial software, and the load-regression technique used by the author. The commercial software was used to generate two sets of load values; one using a relatively coarse mesh, and one using the given refined crack tip mesh. The points represent the loads required to apply a 100μm deflection to a 20x2x2mm zirconia sample. Main cracks of 200 and 400μm, and interlayer cracks of 200, 600 and 1000μm (500μm from the tensile surface), were included. The data were normalized to the load for an un-cracked specimen. The load values are similar for each of the three calculation techniques. There is little change in the load values achieved by mesh refinement. There is an error associated with regression.

Figure 5.2.4-3 is a plot of the stresses in the vicinity of the main crack tip calculated using the commercial software. The main crack size was 200μm. The calculated values are compared to equivalent stresses predicted using both the load-regression technique, and a standard solution (Brown, 1966). The stresses were manipulated using Equation 2.1.6-9 and plotted as Figure 5.2.4-4. A crack tip stress intensity factor was calculated by extrapolation. The value *at* the crack tip was not included in this calculation. The three techniques yield similar values.

Figures 5.2.4-5 and 5.2.4-6 are equivalent calculations for the stresses and stress intensity factor for a 1000μm interlayer crack. The values are similar. This supports the load-regression technique for determining loads, stresses near

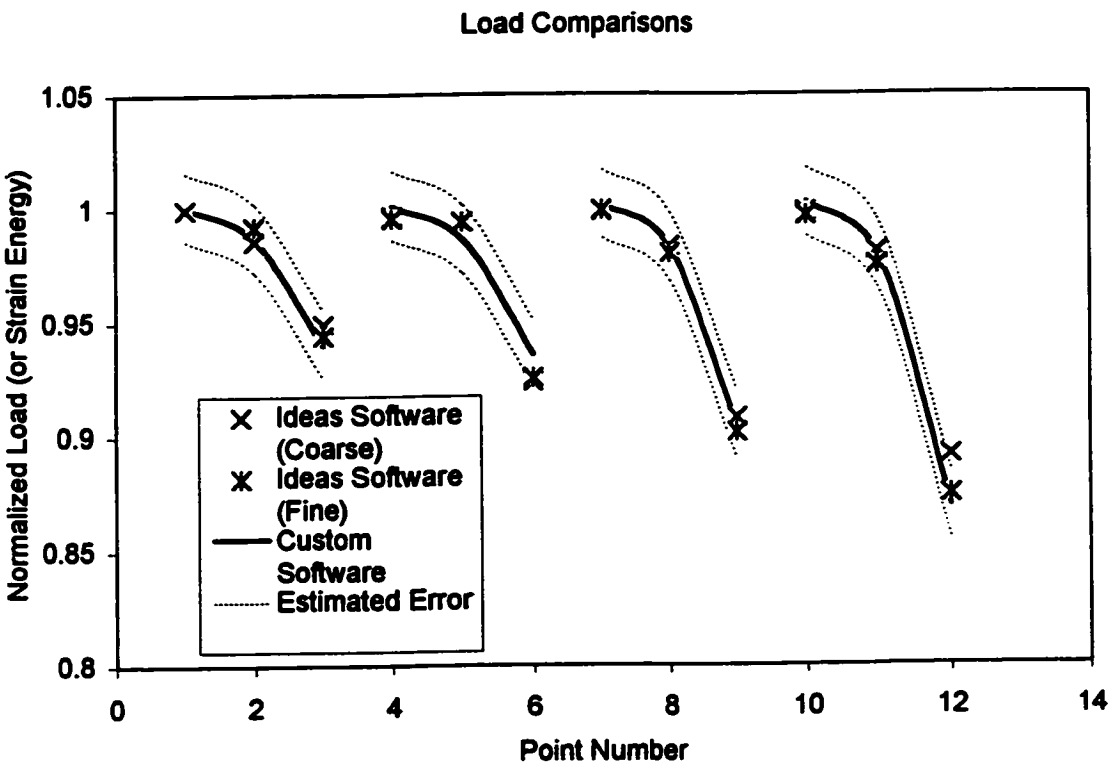

Figure 5.2.4-2. A comparison of the loads calculated using commercial software and the load-regression technique used by the author.

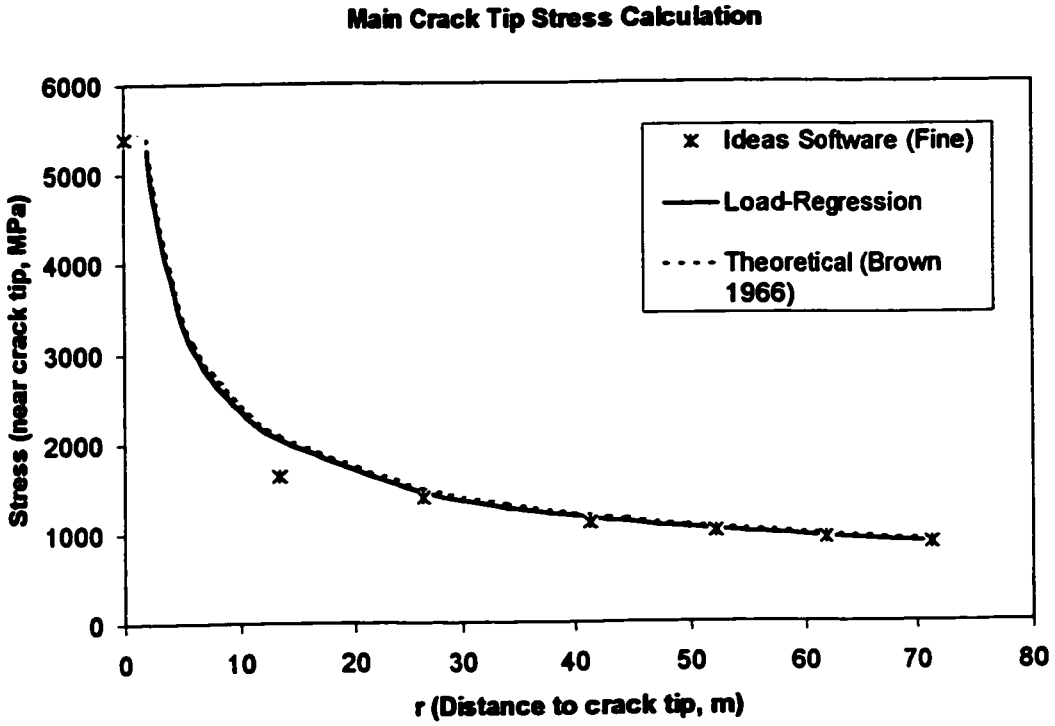

Figure 5.2.4-3. The stress in the vicinity of the main crack tip.

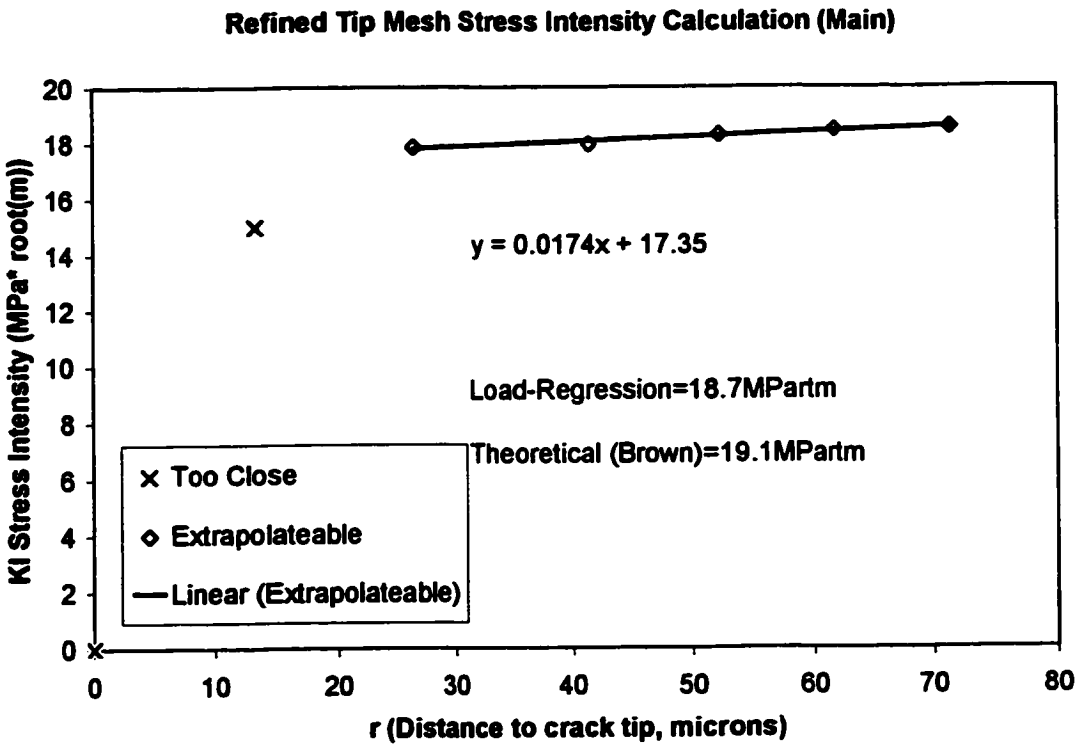

Figure 5.2.4-4. The stress intensity factor at the main crack tip.

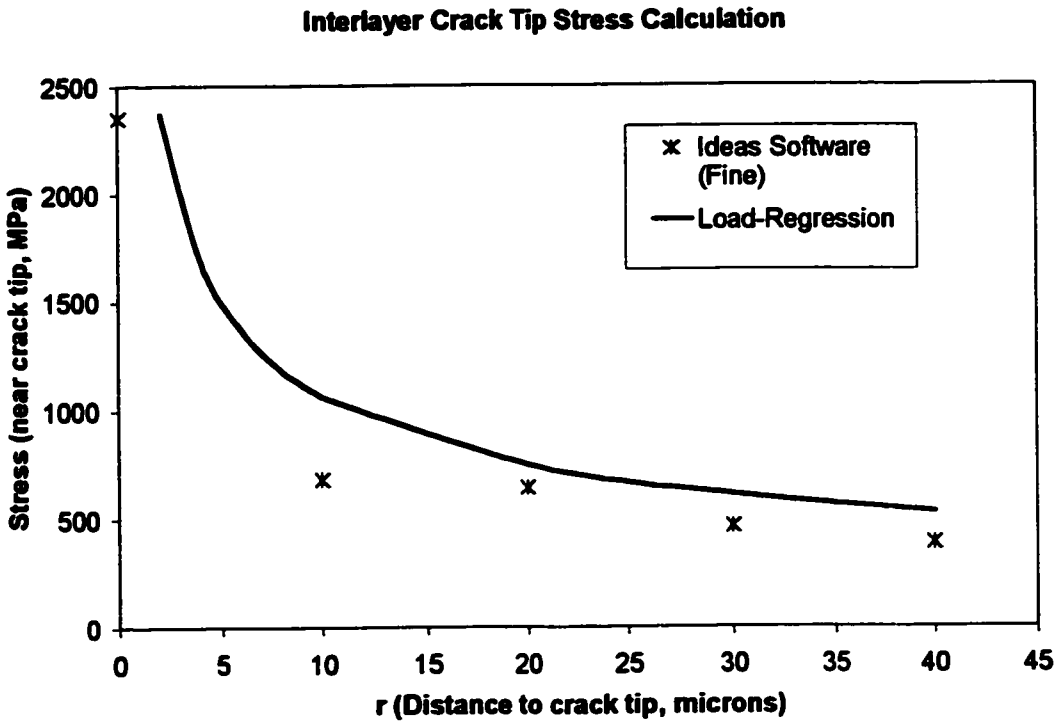

Figure 5.2.4-5. The stress in the vicinity of the interlayer crack tip.

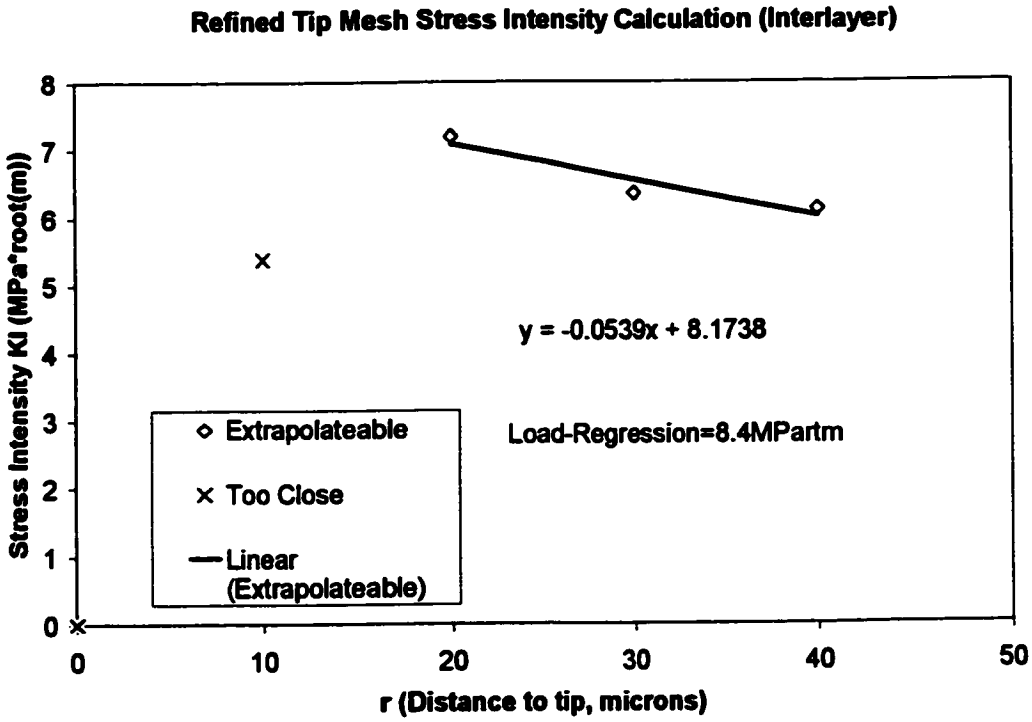

Figure 5.2.4-6. The stress intensity factor at the interlayer crack tip.

crack tips, strain energy release rates, and crack tip stress intensity factors.

The load-regression technique offers several advantages. Mesh generation is relatively simple, as crack tip mesh refinement is not necessary. The method provides equations that can be used to analyze the fracture behaviour of similar composites. It is particularity appropriate for test geometries containing more than one crack. The problems associated with the under-estimation of stresses at the crack tip are avoided. The disadvantage is that judging a suitable regression equation is subjective.

Chapter 6. Conclusions

The aim of this work is to examine the criteria necessary for multi-stage fracture in brittle composites that contain weak interlayers. Non-catastrophic failure of laminates during bend testing increases work of fracture and provides a "safety-net" for brittle materials. The work of others (see Chapter 2) has provided insight into the design of ceramic laminates, but predictions have not been consistent from system to system.

The core of this work is the development of a crack deflection model that can predict flexural fracture behaviour; either catastrophic or multi-stage. The model has required several simplifications and assumptions, which are acknowledged. The main simplification is that composites are treated as two-dimensional beams that contain a single, infinitesmally thin interlayer. The interlayer material has a different toughness than the bulk and contains flaws of known size. The model assumes modulus and/or thermal expansion differences of the two composite materials do *not* play a significant role in crack deflection. The model reveals the size of flaws in the strong (bulk) material and the ratio of surface layer thickness to full sample thickness is more important to the fracture behaviour.

The validity of the model has been confirmed by producing and mechanically testing three types of composites; zirconia/lanthanum-aluminate composites that contain both modulus and thermal expansion differences, glass/epoxy composites that contain a modulus difference, and plaster composites that contain neither. The trends in fracture behaviour of the three systems are consistent with the model's predictions. The flaw distributions in the systems cannot be perfectly controlled, so there is some error. Fracture of brittle composites is ultimately statistical in nature.

Finite element analysis was undertaken to confirm some of the equations used in the fracture mechanics modeling. A load-regression technique was used, which is similar to earlier work of another researcher. The technique was extensively modified to analyze the propagation behaviour of two cracks, and to infer the strength and reliability of composites. The relative velocities of propagating cracks were calculated using a quasi-static analysis. The results are not expected to be the same as for a dynamic approach, which considers shock waves in the material, so only comparisons are considered. The finite element analysis results were consistent with, and reinforced, the results of the fracture mechanics modeling.

The results of the modeling, experiments and finite element analysis have given greater insight into crack deflection phenomena in laminates. The size of flaws in the strong and interlayer materials, the ratio of toughness of the two

materials, and the ratio of strong layer thickness all play a role in achieving multi-stage fracture behaviour.

The size of the flaw in the surface of the strong material of the composite must be considered as it influences the strength, work of fracture and fracture behaviour. A small flaw provides strength and work of fracture, but increases the chance of catastrophic failure. A large flaw reduces the strength, but increases the chance of multi-stage fracture and the associated improvement in work of fracture. The ratio of strengths of the surface and inner strong layers directly affects the likelihood of multi-stage fracture. This is consistent with the experimental results of Oeschner et al (1996), Hatton (1998) and Mawdsley et al (2000), who all noted multi-stage fracture behaviour in samples that contained notches or indents. The role of flaw size in the next strong layer was incorporated into the modeling efforts of Kovar et al (1998) and Mawdsley et al (2000).

The combined effect of the size of the flaw in the interlayer and the interlayer toughness influence the crack deflection behaviour. Earlier work by Cook and Gordon (1964) and He and Hutchinson (1989, I) concentrated on the toughness ratio of the interface and bulk materials. Finite element analysis indicates the size of the interlayer flaw also influences pre-cracking behaviour. Interlayer *strength* becomes more important than interlayer *toughness*, that is, flaw size is critical. This is consistent with the work of Oeschner et al (1996) and Sánchez-Herencia et al (1999), who used thermal residual stresses to generate large flaws in otherwise strong interlayer materials.

The interlayer toughness influences the extent of its cracking, and therefore the fracture behaviour of the material. A brittle interlayer allows extensive delamination, which sheds load and encourages multi-stage fracture behaviour. A tough interlayer reduces the extent of deflection, which sheds less load, but the surface layer continues to support some stress in the composite. Both Phillips et al (1993) and Kovar et al (1998) demonstrated the role of interlayer toughness on energy absorbed.

It has been shown that several factors affect crack deflection and multi-stage fracture behaviour. Strength, work of fracture and non-catastrophic behaviour are difficult to achieve consistently. Strength is governed by the flaw size in the surface of the composite. Work of fracture is influence by both surface flaw size and multi-stage fracture. Multi-stage fracture is influenced by surface flaw size. A concession is necessary in the design of this class of materials.

This work leads to several opportunities for future research. In this work only one weak interlayer was considered. The fracture mechanics model could be modified to incorporate several layers. This could increase the work of fracture if consistent crack deflection was possible in sequential layers. As the number of layers increases, the thermal stresses in the composite will become more important. Thermal stresses will not influence the crack deflection, but they may weaken the surface and next layers. It may be possible to encourage multi-

stage fracture material and improve work of fracture by using a thermally compressed material as the next strong layer.

The work allows other composites to be designed more effectively. Suitable interlayer materials can be selected to toughen other ceramics, at both high and low temperature. The role of modulus differences and thermal residual stresses is less important than other factors, and must be considered accordingly.

The load-regression technique used with finite element analysis has been modified, and used to consider a complex laminate geometry containing two cracks. It can be developed to consider other shapes, loading geometries, layer combinations, and flaw distributions. Different results are expected, but the philosophy should remain consistent.

THE END

References

T.L.Anderson (1995), Fracture Mechanics, Fundamentals and Applications, Second Edition, CRC Press Inc.

G.R.Anstis, P.Chantikul, B.R.Lawn and D.B.Marshall (1981), "A Critical Evaluation of Indentation Techniques for Measuring Fracture Toughness: I, Direct Crack Measurements", *J.Am.Ceram.Soc*, **64** [9] 533-8.

S.J.Bennison, A.Jagota and C.A.Smith (1999), "Fracture of Glass/Poly(vinyl butyral) (Butacite®) Laminates in Biaxial Flexure", J.Am.Ceram.Soc, 82 [7] 1761-70.

J.P.Berry (1960), "Some Kinetic Considerations of the Griffith Criterion for Fracture – I and II", J.Mech.Phys.Solids, Vol 8, 194-216

M.Bissinger (1995), "High Temperature Strength and Toughness of Electrophoretically Deposited Alumina/Lanthanum Aluminate Laminates", M.Eng Thesis, McMaster University.

D.Broek (1982), "Elementary engineering fracture mechanics", Martinus Nijhoff Publishers.

Cambridge Materials Selection Software (1994), V 2.04, Granta Design Ltd.

H.C.Cao and A.G.Evans (1989), "An Experimental Study of Fracture Resistance of Bimaterial Interfaces", *Mech.Mater*, **7** 295-305.

H.Chai (1987), "A note on Crack Trajectory in an Elastic Strip Bounded by Rigid Substrates", *Int.J.Fract*, **32**, 211-3.

S.K.Chan, I.S.Tuba and W.K.Wilson (1970), "On the finite element method in linear fracture mechanics", *Eng.Fract.Mech*, **2** (1970) 1-17.

P.G.Charalambides, J.Lund, A.G.Evans and R.M.McMeeking (1989), "A Test Specimen for Determining the Fracture Resistance of Bimaterial Interfaces", *J.Appl.Mech*, Vol 56, 77-82.

W.J.Clegg, K.Kendall, N.McN.Alford, T.W.Button and J.D.Birchall (1990), "A simple way to make tough ceramics", Nature, Vol 347, 455-7.

J.Cook and J.E.Gordon (1964), " A Mechanism for the Control of Crack Propagation in All-Brittle Systems", *Proc.Roy.Soc.Lon*, **A282**, 508-20.

R.F.Cook and B.R.Lawn (1983), "A Modified Indentation Toughness Technique", *Comm.Am.Ceram.Soc*, November C-200-1.

R.F.Cook, B.R.Lawn and C.J.Fairbanks (1985), "Microstructure-Strength properties in Ceramics: I, Effect of Crack Size on Toughness", *J.Am.Ceram.Soc*, **68** [11] 604-15.

E.N.Dulaney and W.F.Brace (1960), "Velocity Behaviour of a Growing Crack", *J.Appl.Phys*, Vol 31, No 12, 2233-6.

J.Dundurs (1969), "Edge-bonded Dissimilar Orthogonal Elastic Wedges", *ASME J.App.Mech,* Vol 36, 650-2.

N.A.Fleck, J.W.Hutchinson and Z.Suo (1991), "Crack Path Selection in a Brittle Adhesive Layer", *Int.J.Solids Structures*, Vol 27, No 13, 1683-1703.

C.A.Folsom, F.W.Zok and F.F.Lange (1996), "Flexural Properties of Brittle Materials: I, Modeling", *J.Am.Ceram.Soc*, **77** [3] 689-96.

C.A.Folsom, F.W.Zok and F.F.Lange (1996), "Flexural Properties of Brittle Materials: II, Experiments", *J.Am.Ceram.Soc*, **77** [8] 2081-7.

Y.Fukada (2001), PhD Thesis, McMaster University.

R.C.Garvie R.H.Hannink and R.T.Pascoe (1975), "Ceramic Steel?", *Nature* 258 703-4.

D.J.Green (1998), An Introduction to the Mechanical Properties of Ceramics, Cambridge Solid State Science Series.

D.J.Green, R.H.J.Hannink and M.V.Swain (1989), Transformation Toughening in Ceramics", C.R.C. Press.

A.A.Griffith (1920), "The phenomenon of rupture and flow in solids", *Philos.Trans. R.Soc.Lon*, **221A**, 163.

D.A.Hardwick, J.S.Ahearn, A.Desai and J.D.Venables (1986), "Environmental Durability of Phosphoric Acid Anodized Aluminum Adhesive Joints Protected With Hydration Inhibitors", *J.Mat.Sci,* Vol 21, 179-187.

D.P.H.Hasselman (1969), "Unified theory of thermal shock fracture initiation and crack propagation in brittle ceramics", *J.Am.Ceram.Soc*, **52**, 600.

B.D.Hatton (1998), "Flaw Tolerant Alumina/Zirconia Multilayered Composites", M.Eng Thesis, McMaster University.

M-Y.He and J.W.Hutchinson (1989a), "Crack Deflection at an Interface Between Dissimilar Elastic Materials", *Int.J.Solids Struc*, **25** [9] 1053-67.

M-Y.He and J.W.Hutchinson (1989b), "Kinking of a Crack Out of an Interface", J.Appl.Mech, Vol 56, 270-6.

M.Y.He, A.G.Evans and J.W.Hutchinson (1994), "Crack Deflection at an Interface Between Dissimilar Elastic Materials: Role of Residual Stresses", *Int.J.Solids Structures*, Vol 31, No 24, 3443-55.

S.Ho, F.F.Lange and Z.Suo (1995), "Surface Cracking in Layers Under Biaxial, Residual Compressive Stress", *J.Am.Ceram.Soc*, **78** [9] 2353-9.

J-L.Huang, Y-L.Chang and H-H.Lu (1997), "Fabrication of multilaminated Si_3N_4-Si_3N_4/TiN composites and its anisotropic fracture behaviour", *J.Mater.Res*, Vol 12, No 9, 2337-44.

M.Ignat and W.J.Clegg (1995), unpublished work - referenced Lee et al (1996).

C.E.Inglis (1913), " Stresses in a plate due to the presence of cracks and sharp corners", *Trans.Inst.Naval Archit*, **55**, 219.

G.R.Irwin (1958), "Fracture. In *Handbuch der Physik*. Springer-Verlag, Berlin, Vol 6, 551.

F.S.Ji, L.R.Dharani and R.A.Behr (1998), "Damage Probability in Laminated Glass Subjected to Low Velocity Small Missile Impacts", *J.Mat.Sci*, **33**, 4775-82.

M.F.Kanninen and C.H.Popelar (1985), Advanced Fracture Mechanics, Oxford Science Publications.

K.Kendall (1975), "Transition Between Cohesive and Interfacial Failure in a Laminate", Proc.R.Soc.Lond, **A344**, 287-302.

D.Kovar M.D.Thouless and J.W.Halloran (1998), "Crack Deflection and Propagation in Layered Silicon Nitride/Boron Nitride Ceramics", *J.Am.Ceram.Soc*, **81** [4] 1004-12.

D-H.Kuo and W.M.Kriven (1997), "A Strong and Damage Tolerant Oxide Laminate", *J.Am.Ceram.Soc*, **80** [9] 2421-4.

S.G.Larsson and A.J.Carlsson (1973), "Influence of non-singular stress terms and specimen geometry on small-scale yielding at crack tips in elastic-plastic materials", *J.Mech.Phys Solids*, **21**, 263-77.

B.R.Lawn (1993), Fracture of Brittle Solids, Cambridge University Press.

W.Lee (1996), PhD Dissertation, University of Cambridge - referenced Lee et al (1996).

W.Lee, S.J.Howard and W.J.Clegg (1996), "Growth of Interface Defects and its Effect on Crack Deflection and Toughening Criteria", *Acta mater*, Vol 44, No 10 (1996) 3905-22.

A.A.Mammoli, A.L.Graham, I.E.Reimanis and D.L.Tullock (1995), "The Effect of Flaws on the Propagation of Cracks at Bi-Material Interfaces", *Acta.metall.mater*, Vol 43, No 3, 1149-56.

J.R.Mawdsley, D.Kovar and J.W.Halloran (2000), "Fracture Behaviour of Alumina/Monazite Multilayer Laminates", *J.Am.Ceram.Soc*, **83** [4] 802-8.

D.F.Mowbray (1970), "A note on the finite element method in linear fracture mechanics", *Eng.Fract.Mech*, **2**, 173-6.

N.F.Mott (1948), "Brittle fracture in mild steel plates", *Engineering*, Vol 165, 16-17.

R.J.Nuismer (1975), "An Energy Release Rate Criterion for Mixed-Mode Fracture", *Int.Journ. of Fracture*, Vol 11, No 2, 245-50.

J.W.Obreimoff (1930), "The splitting strength of mica", *Proc.Roy.Soc.Lond*, **A217** 290.

M.Oeschner, C.Hillman and F.F.Lange (1996), "Crack Bifurcation in Laminar Ceramic Composites", *J.Am.Ceram.Soc*, **79** [7] 1834-38.

A.J.Phillipps, W.J.Clegg and T.W.Clyne (1993a), "Fracture Behaviour of Ceramic Laminates in Bending-I. Modelling of Crack Propagation", Acta metall.mater, Vol 41, No 3, 805-17.

A.J.Phillipps, W.J.Clegg and T.W.Clyne (1993b), "Fracture Behaviour of Ceramic Laminates in Bending-II. Comparison of Model predictions with Experimental Data", Acta metall.mater, Vol 41, No 3, 819-27.

O.Prakash, P.Sarkar and P.S.Nicholson (1995), "Crack Deflection in Ceramic/Ceramic Laminates with Strong Interfaces", *J.Am.Ceram.Soc*, **78** [4] 1125-27.

W.M.Rainforth and W.E.Lee (1994), Ceramic Microstructures:Property Control by Processing, Chapman and Hall.

D.K.Roberts and A.A.Wells (1954), "The Velocity of Brittle Fracture", *Engineering*, December 24th, 820-1.

A.J.Sánchez-Herencia, C.Pascaul, J.He and F.F.Lange (1999),"ZrO_2/ZrO_2 Layered Composites for Crack Bifurcation", *J.Am.Ceram.Soc*, **82** [6] 1512-8.

P.Sarkar and P.S.Nicholson (1996), "Electrophoretic Deposition (EPD): Mechanisms, Kinetics, and Application to Ceramics", *J.Am.Ceram.Soc*, **79** [8]1987-2002.

D.Stolle (1999), "Introduction to Finite Element Method", McMaster University Custom CourseWare.

Z.Suo and J.W.Hutchinson (1990), *Int.J.Fract*, **43**.

E.K.Szymanski (2000), "Plaster-of-Paris Laminates as Model Materials for the Study of Stable Fracture in Brittle Materials", B.Eng Thesis, McMaster University.

H.Tada, P.Paris and G.Irwin (1973), The Stress Analysis of Cracks Handbook, Del Research Corporation.

S.T.Timoshenko (1953), History of the strength of materials: with a brief account of the history of theory of elasticity and theory of structures, McGraw-Hill.

S.T.Timoshenko and J.M.Gere (1972), Mechanics of Materials, Van Nostrand Reinhold Company, Litton Educational Publishing Inc.

L.Vanderperre, O.Van Der Biest, F.Bouyer and A.Foissy (1998), "SiC-Graphite Laminates Shaped by EPD", *Am.Ceram.Soc.Bull*, January, 53-8.

J-S.Wang and Z.Suo (1990), "Experimental Determination of Interfacial Toughness Curves Using Brazil Nut Sandwiches", *Acta Metall.Mater*, **38,** 1279-90.

P.F.Walsh (1971), "The computation of stress intensity factors by a special finite element technique", *Int.J.Solids and Struct*, **7,** 1333-42.

W.Weibull (1951), "A statistical distribution of wide applicability", *J.Appl.Mech*, **18** 293.

H.M.Westergaard (1939), "Bearing Pressures and Cracks", *J.Appl.Mech*, June, A49-53.

M.W.Whitehead (1994), "Synthesis and Mechanical Properties of Electrophoretically Deposited Alumina/Zirconia Laminated Composites", M.Eng Thesis, McMaster University.

M.L.Williams (1954), "On the Stress Distribution at the Base of a Stationary Crack", J.Appl.Mech, March, 109-14.

Appendix I

The program "mapper" was the program used to perform the fracture mechanics calculations. Only the zirconia/lanthanum-aluminate version is included here. The glass/epoxy version differs only in the material constants used.

The program was written in Pascal v7.0. Notes have been added for clarification. The program iterates through the calculation for a range of values of surface layer thickness and applied outer indent load. Either catastrophic or multi-stage fracture is predicted for each set of conditions, and a "C" or "M" printed as output. An "S" is plotted for the special case that the interlayer crack propagates before the main crack. This region was treated as a multi-stage failure for all subsequent analysis.

A sample of the program output is included. The critical surface layer thickness ratio was determined for each applied indent load by averaging the layer thickness ratios just above and below the boundary between the two zones. The boundary was artificially smoothed by non-linear regression (FitAll v5.7 Non-Linear Regression Analysis, MTR Software) for presentation purposes.

```
program mapper;
{$E+,N+}

uses printer;

const          {These values are changed for different materials}
   KIC=6.6E6;
   sigmaf=895E6;
   gam=938E6;
   m=10;
   czero=4E-6;
   KICW=2.05E6;
   b=0.002;
   h=0.0015;
   L=0.02;

var
  Y, prob: real;
  azero, acrit, ccrit, a, stress, strength, ratio, factor: double;
  P1, P2, check, veloa, veloc, Pind, lay, Keff: double;
```

```
  Pindct, lct: integer;
  result: char;
begin
writeln('Welcome to my fracture zone mapper!!');              {Output to screen}
writeln(lst,'Welcome to my fracture zone mapper!!');          {Output to printer}
writeln('Zirconia - Weibull calculation - mid');
writeln(lst,'Zirconia - Weibull calculation - mid');
prob:=50;          {Failure probability, changed for standard deviation error
curves}
lct:=1400;
Y:=1.12*2/pi;      {Assume semi-circular crack}
while lct>0 do
    begin
    write(lct,'   '); write(lst,lct,'   ');
    if lct<1000 then write(' '); if lct<1000 then write(lst,' ');
    if lct<100 then write(' '); if lct<1000 then write(lst,' ');
    Pindct:=1;
    while Pindct<=20 do          {Iterate for a range of indent loads}
        begin
        Pind:=0.5*Pindct;
        lay:=lct*1E-6;
```

```
        azero:=(1/pi)*sqr(KIC/(Y*gam))*exp(1.1782*ln(Pind));        {Values from
regression of monolithic strength data}
        P1:=(KIC*4*b*sqr(h))/((3*L)*Y*sqrt(pi*azero));
        a:=azero;
        ratio:=czero/(lay-a);
        factor:=ratio;
        if ratio>0.4 then factor:=0.15*ratio+0.35;        {This is an approximation
of the Green integral used, done for simplification of calculation}
        Keff:=factor*KIC*sqrt(a/azero)*(1-sqr(a/h))/(1-sqr(azero/h));
        if Keff>KICW then result:='S'                {Check to see if interlayer cracks
before main}
        else begin
            repeat
            a:=a+1E-6;
            ratio:=czero/(lay-a);
            factor:=ratio;
            if ratio>0.4 then factor:=0.15*ratio+0.35;
            Keff:=factor*KIC*sqrt(a/azero)*(1-sqr(a/h))/(1-sqr(azero/h));
until Keff>=KICW;
            acrit:=a;
            if azero>acrit then acrit:=azero
```

```
        else veloa:=(lay-acrit)+azero*ln(abs((lay-azero)/(acrit-azero)));
        repeat
            ccrit:=ccrit+1E-6;
            veloc:=(ccrit-czero)+czero*ln(abs((ccrit-czero)/(0.01*czero)));
    {Require approximation to avoid singularity in equation}
        until veloc>=veloa;
        strength:=928E6*exp((1/m)*ln(L*(ln(100/prob))/(4*ccrit)));
        P2:=P1*L/(L+3*ccrit*((exp(3*ln(h))-exp(3*ln(h-lay)))/exp(3*ln(h-lay))));
        stress:=(3*P2*L)/(4*b*sqr(h-lay));
        if stress>strength then result:='C'
        else result:='M';
        if azero>lay then result:='S';
        end;
    write(result,' ');
    write(lst,result,' ');
    inc(Pindct)
    end;
writeln(' ');
writeln(lst,' ');
dec(lct,50)
end;
```

```
writeln('Indent load from 0.5 to 10kg.');

writeln(lst,'Indent load from 0.5 to 10kg.');

readln;

end.
```

Sample Output

```
Welcome to my fracture zone mapper!!

Zirconia – Weibull Calculation – mid

1400  C C C C C C C C C C C C C C C C C C C

1350  C C C C C C C C C C C C C C C C C C C

1300  C C C C C C C C C C C C C C C C C C C

1250  C C C C C C C C C C C C C C C C C C C

1200  C C C C C C C C C C C C C C C C C C C

1150  C C C C C C C C C C C C C C C C C C C

1100  C C C C C C C C C C C C C C C C C C C

1050  C C C C C C C C C C C C C C C C C C C

1000  C C C C C C C C C C C C C C C C C C C

950   C C C C C C C C C C C C C C C C C M M M

900   C C C C C C C C C C C C C C C M M M M M M

850   C C C C C C C C C C C C C M M M M M M M M

800   C C C C C C C C C C C M M M M M M M M M M

750   C C C C C C C C C M M M M M M M M M M M
```

700 C C C C C C C M M M M M M M M M M M M

650 C C C C C C M M M M M M M M M M M M M

600 C C C C C M M M M M M M M M M M M M M

550 C C C C C M M M M M M M M M M M M M M

500 C C C C M M M M M M M M M M M M M M M

450 C C C M M M M M M M M M M M M M M S S

400 C C C M M M M M M M M M M M M M S S S

350 C C C M M M M M M M M M M M S S S S S

300 C C M M M M M M M M M M M S S S S S S

250 C C M M M M M M M M M S S S S S S S S

200 C C M M M M M M M S S S S S S S S S S

150 C C M M M M M S S S S S S S S S S S S

100 C M M M S S S S S S S S S S S S S S S

50 C M S S S S S S S S S S S S S S S S S

Indent load from 0.5 to 10kg.

Appendix II

```
% bender.m
% This is a program for calculating the forces, displacements,
% and key stresses in a double cracked beam.
% It uses simple, 4-noded quadrilateral elements

clear all;
format short g;

%Set material properties, in this case zirconia
E=220000000000;
nu=0.31;

% Initialize counter for iterations
ctriii=0;
ctrjjj=0;
counter=0;

for jjj=0:15
for iii=0:3
```

```
  acrack=3;          %note that this is the distance from the surface to the
interlayer
  anew=iii;          %the actual crack size
  ccrack=jjj;

% this part of the program sets the initial mesh for the beam
rows=12;
columns=60;
elmtot=rows*columns;
h=1;
lx=1; ly=1; m=lx/ly;

% Set x,y location for each node.
locx=[];
locy=[];
for i=1:rows+1
  for j=1:columns+1
    nextx=j-1;
    locx=[locx nextx];
    nexty=rows+1-i;
    locy=[locy nexty];
```

```
  end
end

% Set global node numbers for each element.
gln=zeros(elmtot,4);
for i=1:rows
  for j=1:columns
    elm=j+(i-1)*columns;
    nodea=elm+columns+i;
    nodeb=elm+columns+i+1;
    nodec=elm+1+(i-1);
    noded=elm+(i-1);
    next=[nodea nodeb nodec noded];
    gln(elm,:)=gln(elm,:)+next;
  end
end
aaa=max(gln); glntot=max(aaa);

% Set non-zero loads to 1, and known displacements.
loadv=zeros(2*glntot,1);
dispv=ones(2*glntot,1);
```

```
centres=[];


for i=1:gIntot
  if locx(i)==0          % Centre of beam
    loadv(2*i-1)=1;
    dispv(2*i-1)=0;
    centres=[centres i];              % Stores addresses of middle nodes
  end


  if locy(i)==0          % Outer span pin
    if locx(i)==columns
      loadv(2*i)=1;
      dispv(2*i)=0;
    end
  end


  if locy(i)==rows     % Inner span pin
    if locx(i)==0.5*columns          % Must use even number here
      loadv(2*i)=1;
      dispv(2*i)=-0.05;       % Arbitrary displacement
    end
```

```
  end
end

extralv=loadv;
extradv=dispv;

specials       % Separate program to adjust nodes to simulate cracks

% For inner cycle must "re-attach" layer AND the first extra node
if acrack~=0  % Note this is actually layer thickness to interlayer
  for i=1:acrack
    loadv(2*centres(rows+2-i)-1)=1;
    dispv(2*centres(rows+2-i)-1)=0;
  end
end
fexnode=(rows+1)*(columns+1)+1;        %first extra node re-attachment
loadv(2*(fexnode)-1)=1;
dispv(2*(fexnode)-1)=0;

% Re-crack a new acrack ie "anew"
if anew~=0
```

```
  for i=1:anew
    loadv(2*centres(rows+2-i)-1)=0;
    dispv(2*centres(rows+2-i)-1)=1;
  end
end

aaa=max(gln); gintot=max(aaa);
glmatrix=sparse(2*gintot,2*gintot);
glmatrix=zeros(2*gintot,2*gintot);
% Set global stiffness matrix using element stiffness matrix
% defined in quadmatrix.m. Note that the elemental stiffness matrix
% is 8x8 and each value must be put in its correct place
E=220000000000;
nu=0.31;                                        %zirconia
quadmatrix
for i=1:elmtot
  for j=1:4
    index(2*j-1)=2*gln(i,j)-1;
    index(2*j)=2*gln(i,j);
  end
  glmatrix(index,index)=glmatrix(index,index)+kmatrix(:,:);
```

```
end

extraglmat=glmatrix;

addresses=[];
constraints=[];
for i=1:2*glntot
  if loadv(i)~=0
    addresses=[addresses i];
    constraints=[constraints dispv(i)];
    extraglmat(i,:)=zeros(1,2*glntot);
    extraglmat(i,i)=1;
  end
end
extralv(addresses)=constraints;

% Now solve for displacements
dispv=extraglmat\extralv;

% Now solve for loads
loads=glmatrix*dispv;
```

```
%Save some memory
glmatrix=[];
extraglmat=[];



% Loop to extract u and v displacements, and fx and fy loads.
for i=1:glntot
  us(i)=dispv(2*i-1);
  vs(i)=dispv(2*i);
  fxs(i)=loads(2*i-1);
  fys(i)=loads(2*i);
end


% Loop to find the applied force at outer pin
for i=1:glntot
        if locy(i)==0   %outer span pin
     if locx(i)==columns
       force=loads(2*i);
     end
   end
```

```
end

% Print the pin load, set for zero initial crack sizes
maincracksize=anew;
weakcracksize=ccrack;
layerthickness=acrack;
afmat(anew+1,ccrack+1)=force

counter=counter+1
end
end

% Now draw the deformed block - transposed and mirrored
factor = 100;          %input('Factor for magnifying displacements ');
figure(1)
hold on
shift=max(locx)/75;

for i=1:elmtot
nodes=[gln(i,1) gln(i,2) gln(i,3) gln(i,4)];
   x=locx(nodes(:))+factor*us(nodes(:));
```

```
  x(5)=x(1);
  nodes=[gln(i,1) gln(i,2) gln(i,3) gln(i,4)];
  y=locy(nodes(:))+factor*vs(nodes(:));
  y(5)=y(1);
  plot(y,x,'-r');% Note reversal for transpose
  x=-1*x;                    % Mirror down with x-y reversed
       plot(y,x,'-r');
end
hold off;
axis equal
%end
%save('newdelam','rows','columns','jj','counter','initialforce','forcelist','initialbeam','
maxbeamlist','acrack')
% specials.m
% This program specifies the cracked portions of the beam. Base
% values already dealt with in mesh section of code.

if acrack~=0
  for i=1:acrack
    loadv(2*centres(rows+2-i)-1)=0;
    dispv(2*centres(rows+2-i)-1)=1;
```

```
  end
end

if ccrack~=0
  % Specify new nodes, load is zero, disp freedom, loc as other nodes
  for i=1:ccrack
  loadv(2*(gintot+i)-1)=0;
  loadv(2*(gintot+i))=0;
  dispv(2*(gintot+i)-1)=1;
  dispv(2*(gintot+i))=1;
  locx(gintot+i)=locx(centres(rows+1-acrack)-1+i);
  locy(gintot+i)=locy(centres(rows+1-acrack)-1+i);
  gln(((rows-acrack)*columns+i),4)=gintot+i;
  gln(((rows-acrack)*columns+i),3)=gintot+i+1;
       end
  gln(((rows-acrack)*columns+i),3)=...
    gln(((rows-1-acrack)*columns+i),2);
end
aaa=max(gln); gintot=max(aaa);
extraIv=loadv;
extradv=dispv;
```

```
% Here is the m-file for determining the kmatrix.
% Use plain strain, therefore;
E=E/(1-nu^2);
nu=nu/(1-nu);
% These are accepted values, derived for FEA
k1=4*m+(2/m)*(1-nu);          k2=(3/2)*(1+nu);
k3=(4/3)+2*m*(1-nu);          k4=2*m-(2/m)*(1-nu);
k5=(-3/2)*(1-3*nu);           k6=(-4/m)+m*(1-nu);
k7=-2*m-(1/m)*(1-nu);         k8=-4*m+(1/m)*(1-nu);
k9=(-2/m)-m*(1-nu);           k10=(2/m)-2*m*(1-nu);

matterm=E*h/(12*(1-nu^2));
kmatrix=matterm*[k1 k2 k8 k5 k7 -k2 k4 -k5;...
    k2 k1 -k5 k10 -k2 k9 k5 k6;...
    k8 -k5 k1 -k2 k4 k5 k7 k2;...
    k5 k10 -k2 k1 -k5 k6 k2 k9;...
    k7 -k2 k4 -k5 k1 k2 k8 k5;...
    -k2 k9 k5 k6 k2 k1 -k5 k10;...
    k4 k5 k7 k2 k8 -k5 k1 -k2;...
    -k5 k6 k2 k9 k5 k10 -k2 k1];
```